Introduction to Relativistic Heavy Ion Collisions

László P. Csernai

November 14, 2008

Copyright ©by 2005 L.P. Csernai

This book:
L.P. Csernai: "Introduction to relativistic heavy ion collisions" ISBN 0 471 93420 8 (QC794.8.H4C77 1994) was published by Jan. 24, 1994 by Jonh Wiley & Sons Ltd., Chichester, England,

based on the AGREEMENT between the Author and Publisher dated Oct. 10, 1991. The work after sale of near to 500 copies, went out of print on Dec. 31, 2001. Wiley UK has passed the AGREEMENT to Wiley-VCH, Weinheim, Germany on April 25, 2002. The following negotiation between the Author and this branch of the Publisher, regarding reissuing the Work, remained inconlusive, as recognized by both parties in the notice of the Author of March 26, 2005 and counter notice of the Publisher of May 2, 2005.

According to the original, 1991, agreement's
Paragraph 15(b):
"If the Publisher allows the Work to go out of print as aforesaid, the Publisher shall retain the right for a period of 18 months after the date of the aforesaid notice to the Author to decide to reissue or to license the reissue of the Work, and in the event that the Publisher shall make such decision the publisher will give notice to the author." and
Paragraph 15(d):
"If the Publisher shall fail to decide to reissue or to license the reissue of the Work on or before the expiration of the said period of 18 months, the Autor shall be entitled at any time thereafter by notice to the publisher to require the Publisher to reassign to the Author the entire copyright and all other rights in and to the Work hereinbefore assigned to the Publisher subject to, but with the benefit of all such agreements, licences and other encumbrances theretofor entered into by the Publisher with third parties in respect of the Work, and subsisting in the time of reassignment.

In this sense the original, 1991 contract (AGREEMENT) was cancelled by the May 2, 2005 notice of the publisher.

The present electronic version of the book is the true copy of the original, as much as the technology, quality, and typography allows. Corrections, published on the Web in form of an Erratum dated Aug. 1, 2002, are implemented in this version.

No part of this book may be reproduced by any means for use by third parties, however, it is allowed to download and print the book for private, individual use.

Contents

Preface **15**

1 Basic Phenomenology of Heavy Ion Collisions **17**
1.1 Introduction . . . 17
1.1.1 The Quark Gluon Plasma . . . 17
1.1.2 The nuclear Equation of State . . . 18
1.1.3 New collective phenomena . . . 18
1.1.4 Particle production . . . 19
1.2 Energy domains of heavy ion physics . . . 19
1.2.1 Intermediate energy reactions . . . 19
1.2.2 Relativistic heavy ion reactions . . . 20
1.2.3 Ultra-relativistic heavy ion reactions . . . 20
1.3 Heavy ion experiments . . . 21
1.3.1 Acceptance . . . 24
1.3.2 Event selection . . . 24
1.3.3 Physical event tape . . . 25
1.3.4 Detector filters . . . 26
1.3.5 Outline . . . 26
1.4 General features of heavy ion physics . . . 26
1.5 Connections to other fields of physics . . . 27
1.5.1 Nuclear physics . . . 27
1.5.2 Particle physics . . . 29
1.5.3 Statistical physics . . . 29
1.5.4 Relativistic fluid dynamics . . . 30
1.5.5 Astrophysics . . . 30
1.6 Why a theoretical treatment is important? . . . 30
1.7 Outline of the book . . . 31
1.8 Assignment 1 . . . 32
1.8.1 Solutions to Assignment 1 . . . 33
References . . . 33

2 Introduction to Relativistic Kinetic Theory **37**
2.1 Basic definitions of microscopic quantities . . . 37
2.1.1 Phase-space variables . . . 38
2.1.2 Properties of the rapidity . . . 40

2.1.3 Some typical rapidities . . . 41
2.2 Basic definitions of macroscopic quantities . . . 42
2.3 Energy-momentum tensor . . . 46
2.3.1 Hydrodynamic flow . . . 47
2.3.2 Local Rest frame: (LR) . . . 48
2.3.3 Other macroscopic quantities . . . 50
2.3.4 Decomposition of the energy-momentum tensor . . . 52
2.4 Jüttner distribution . . . 53
2.4.1 Normalization . . . 53
2.4.2 Transformation properties of f(x,p). . . . 54
2.5 Mixtures . . . 56
2.6 Assignment 2 . . . 58
2.6.1 Solutions to Assignment 2 . . . 59
References . . . 60

3 Relativistic Boltzmann Transport Equation 65
3.1 Particle conservation . . . 65
3.2 Collisions . . . 66
3.3 Non-relativistic limit . . . 68
3.4 An example for the solution . . . 70
3.5 Relativistic Boltzmann equation for mixtures . . . 74
3.6 Conservation laws . . . 74
3.6.1 Conservation of particle number . . . 76
3.6.2 Conservation of charge . . . 76
3.6.3 Conservation of energy and momentum . . . 77
3.7 Boltzmann H-theorem . . . 78
3.8 Equilibrium distribution function . . . 80
3.9 Zeroth order approximation . . . 80
3.10 Assignment 3 . . . 82
3.10.1 Solutions to Assignment 3 . . . 83
References . . . 86

4 Equation of State 89
4.1 Intermediate Energy EOS . . . 90
4.1.1 Bulk nuclear matter . . . 90
4.1.2 Finite systems and fragment abundances . . . 103
4.2 The Nuclear EOS and Quark Gluon Plasma . . . 107
4.2.1 Hadronic Equation of State . . . 108
4.2.2 QGP Equation of State . . . 111
4.2.3 QGP phase transition and nuclear compressibility . . . 113
4.2.4 Dependence of phase transition on the nuclear EOS . . . 114
4.3 EOS from microscopic theory . . . 116
4.3.1 Momentum dependent interaction . . . 118
4.3.2 Momentum distribution . . . 118
4.3.3 The partition function . . . 119

4.4 Assignment 4 . . . 121
4.4.1 Solutions to Assignment 4 . . . 121
References . . . 123

5 Relativistic Fluid Dynamics 129
5.1 Energy domains, stopping power . . . 129
5.1.1 Stopping energy region . . . 130
5.1.2 Transparent reactions, mid rapidity region . . . 130
5.1.3 Transparent reactions, fragmentation region . . . 131
5.2 Perfect fluid dynamics . . . 131
5.3 Numerical solutions . . . 132
5.3.1 Equation of state . . . 133
5.3.2 Flow characteristics from numerical solutions . . . 134
5.3.3 Conclusions . . . 137
5.4 Numerical methods . . . 138
5.4.1 The Particle in Cell (PIC) method . . . 138
5.4.2 The Flux Corrected Transport algorithm (FCT) . . . 139
5.5 Simple analytic solutions—Shock waves . . . 140
5.5.1 Taub adiabat for finite particle densities . . . 143
5.5.2 Relativistic detonations . . . 147
5.5.3 Detonations to QGP . . . 151
5.5.4 Detonations in baryon free plasma . . . 154
5.5.5 Deflagrations from QGP (*) . . . 155
5.6 Assignment 5 . . . 161
5.6.1 Solutions to Assignment 5 . . . 161
References . . . 163

6 Simple models 169
6.1 Applicability of simple models . . . 169
6.2 The Bjorken model . . . 171
6.2.1 Entropy conservation . . . 174
6.2.2 Multiplicity estimate in ultra-relativistic collisions . . . 174
6.2.3 Inclusion of phase transition in the Bjorken model (*) . . . 175
6.2.4 Baryon recoil in the Bjorken model (*) . . . 180
6.3 Spherical expansion . . . 184
6.3.1 Fireball model . . . 186
6.3.2 Blast-wave model . . . 188
6.3.3 An approximate spherical solution . . . 190
6.4 The Landau model . . . 193
6.4.1 Physical assumptions . . . 193
6.4.2 Quasi-analytic solution . . . 194
6.4.3 Numerical solution . . . 195
6.5 Assignment 6 . . . 198
6.5.1 Solutions to Assignment 6 . . . 199
References . . . 202

7 Measurables **207**
7.1 The freeze out process . . . 207
7.1.1 Formal treatment of the freeze out . . . 208
7.2 Baryon measurables . . . 210
7.2.1 Rapidity distribution . . . 210
7.2.2 Transverse Momentum Spectra . . . 211
7.2.3 Collective Sidewards Flow . . . 211
7.2.4 Average Transverse Momentum . . . 212
7.3 Pion Measurables . . . 212
7.4 Calculation of cross sections . . . 214
7.4.1 Inclusive and exclusive cross sections . . . 214
7.4.2 Double and triple differential cross sections . . . 214
7.4.3 Boosting thermal distributions . . . 214
7.4.4 Spherical expansion . . . 217
7.5 Results of three dimensional calculations . . . 218
7.5.1 Fragment emission at the end of the flow . . . 219
7.6 Global flow analysis . . . 223
7.6.1 Global flow analysis in fluid dynamics . . . 227
7.6.2 Decomposition of the global flow tensor . . . 228
7.7 Transverse Flow Analysis . . . 235
7.7.1 Determination of the reaction plane (A) . . . 236
7.7.2 Self correlations (B) . . . 238
7.8 Assignment 7 . . . 240
7.8.1 Solutions to Assignment 7 . . . 241
References . . . 243

8 Scaling of the hydrodynamical model **247**
8.1 Similarity in classical fluid dynamics . . . 247
8.1.1 Application to heavy ion collisions . . . 249
8.2 Scaling properties of cross sections . . . 250
8.3 Scaling properties of the transverse flow . . . 253
8.3.1 Global flow tensor . . . 253
8.3.2 Transverse Momentum Analysis . . . 255
8.3.3 Fragment flow and scaling . . . 256
8.3.4 Fragment flow - mass dependence (*) . . . 257
8.4 Scaling violations . . . 261
8.4.1 Scaling violation in transverse flow . . . 261
8.4.2 Disappearance of the transverse flow . . . 263
8.5 Assignment 8 . . . 265
8.5.1 Solutions to Assignment 8 . . . 265
References . . . 265

9 Direct Solutions of Kinetic Theory 269
9.1 Viscous Fluid Dynamics . . . 270
9.1.1 Entropy production . . . 271
9.1.2 Shock front profiles . . . 273
9.2 Multi Component Fluid Dynamics . . . 274
9.3 Solutions on microscopic level . . . 277
9.3.1 Intranuclear cascade models . . . 278
9.3.2 Mean field models: BUU - VUU - BN - LV . . . 278
9.3.3 Models of Molecular Dynamics . . . 279
9.4 Assignment 9 . . . 280
9.4.1 Solution to Assignment 9 . . . 280
References . . . 281

10 Search for Quark Gluon Plasma 285
10.1 Introduction . . . 285
10.1.1 Theoretical expectations . . . 286
10.1.2 Experimental facilities . . . 287
10.2 Quarks and gluons . . . 288
10.3 Lattice QCD . . . 289
10.3.1 The lattice formalism . . . 292
10.3.2 The order of the phase transition . . . 294
10.3.3 Critical temperature . . . 295
10.3.4 The Equation of State . . . 295
10.3.5 Screening lengths . . . 297
10.3.6 Summary of present results . . . 297
10.4 Surface tension, viscosity and nucleation . . . 298
10.5 Nuclear stopping power . . . 299
10.5.1 Proton nucleus collisions . . . 300
10.5.2 Heavy ion collisions . . . 301
10.5.3 Stopping in theoretical models . . . 303
10.6 Reaction models . . . 304
10.6.1 Fluid dynamical results . . . 305
10.6.2 Microscopic string models . . . 307
10.7 On some suggested signals . . . 310
10.7.1 Strangeness and Anti-baryon enhancement . . . 312
10.7.2 Heavy quark bound states . . . 313
10.7.3 Exotic signals . . . 313
10.8 Assignment 10 . . . 314
10.8.1 Solution to Assignment 10 . . . 314
References . . . 314

11 Connections of astrophysics and Heavy Ions 321
11.1 Neutron and hybrid stars . . . 321
11.1.1 Pulsars and neutron stars . . . 326
11.1.2 Supernova explosions . . . 326

11.2 Implications on the early universe 327
11.2.1 Strangelets 328
References 328

List of Figures

1.1 F:Kla84-f.2-f.4 . . . 21
1.1 F:Kla84-f.2-f.4 . . . 22
1.2 F:Lud85-f.1 . . . 23
1.3 F:WG76-f.1 . . . 27
1.4 F:SMG80-f.1 . . . 28

2.1 F:CS91 . . . 38
2.2 F:CS91 . . . 39
2.3 F:CS91 . . . 40
2.4 F:CS91 . . . 40
2.5 New . . . 42
2.6 New . . . 43
2.7 F:CS91 . . . 43
2.8 New . . . 47
2.9 F:CS91 . . . 54
2.10 F:CS91 . . . 55
2.11 New . . . 61
2.12 New . . . 61

3.1 F:CS91 . . . 66
3.2 New . . . 70
3.3 New . . . 70
3.4 F:Ra79-f.2a . . . 71
3.5 F:Ra79-f.4 . . . 72
3.6 F:Ra79-f.8 . . . 73
3.7 New . . . 79

4.1 F:CK86-f.3.2 . . . 97
4.2 F:St71-f.5.4 . . . 98
4.3 F:CK86-f.5.9 . . . 105
4.4 F:HS89-f.1 . . . 112
4.5 F:CK86-f.3.3 . . . 113
4.6 F:HS89-f.3 . . . 115

5.1 New . . . 131
5.2 New . . . 133

5.3 F:AH77-f.2-f.3 . . . 134
5.3 F:AH77-f.2-f.3c . . . 135
5.4 F:RR81-f.?? . . . 136
5.5 F:ReG87-f . . . 136
5.6 New . . . 140
5.7 New . . . 141
5.8 New . . . 141
5.9 New . . . 142
5.10 New . . . 144
5.11 New . . . 146
5.12 New . . . 146
5.13 F:CB79p-f.?? . . . 147
5.14 F:BC85-f.4 . . . 148
5.15 New . . . 148
5.16 F:BC85-f.3 . . . 149
5.17 New . . . 150
5.18 F:BC85-f.1 . . . 153
5.19 F:DR87-f.4a . . . 157
5.20 F:DR87-f.4c . . . 158
5.21 F:DR87-f.4d . . . 159
5.22 F:DR87-f.4e . . . 159
5.23 F:GM84-f.1 . . . 160
5.24 New . . . 162

6.1 New . . . 170
6.2 F:Mat87-f.1 . . . 172
6.3 New . . . 173
6.4 F:GM84b-f. . . . 178
6.5 F:KR83-f.2 and Rai84-f1 . . . 179
6.6 F:KR83-f.9a and Rai84-f.6 . . . 181
6.7 F:GC86-f.1 . . . 184
6.8 F:GC86-f.2 . . . 185
6.9 F:CB80-f.1 . . . 188
6.10 F:CB80-f.3 . . . 189
6.11 F:SR79-f.1 . . . 191
6.12 F:CF75-f.1 . . . 196
6.12 F:CF75-f.1c . . . 197
6.13 New . . . 200
6.14 F:BC85-f.5 . . . 201

7.1 F:CB80-f.4 . . . 215
7.2 F:Stoc81-f.1 . . . 218
7.3 F:CS83-f.1 . . . 219
7.4 F:CS83-f.2 . . . 220
7.5 F:CS83-f.4 . . . 222

7.6 F:CG82-f.4 . . . 223
7.7 F:GG84-f.1 . . . 225
7.8 F:GG84-f.2 . . . 226
7.9 F:BG85-f.1 . . . 227
7.10 New . . . 230
7.11 F:CF84-f.1 . . . 232
7.12 F:CF84-f.2 . . . 233
7.13 F:DG83-f.1 . . . 233
7.14 F:DG83-f.3b . . . 234
7.15 F:DG83-f.3a . . . 234
7.16 F:RitS83-f.1 . . . 235
7.17 F:RitS83-f.3 . . . 236
7.18 F:DO85-f.1 . . . 237
7.19 F:DO85-f.2 . . . 239
7.20 F:DO85-f.3abcd . . . 239
7.21 F:Ri85-f.4 . . . 240

8.1 F:BS84-f.1 . . . 252
8.2 F:BS84-f.2 . . . 253
8.3 F:BS84-f.4 . . . 254
8.4 F:BC88-f.4 . . . 259
8.5 F:BC88-f.5 . . . 260
8.6 F:LC91-f.4.3 . . . 262
8.7 F:BC87-f.1 . . . 263
8.8 F:BC87-f.2 . . . 264
8.9 F:BS84-f.3 . . . 265

9.1 F:Da84-f.1 . . . 274
9.2 F:Da84-f.2 . . . 275
9.3 F:CL82-f.5 . . . 276

10.1 F:Pe91-f.6 . . . 296
10.2 F:CK85-f.4 . . . 301
10.3 F:St91-f.3 . . . 302
10.4 F:ACSS92-f.1 . . . 306

11.1 F:RSC92b-f.1 . . . 324
11.2 F:RSC92b-f.2 . . . 325

List of Tables

2.1 New 41

4.1 New 94
4.2 New 99
4.3 New 120

10.1 New 288
10.2 New 290

11.1 New 327

Preface

This book is based on my courses given at the University of Minnesota, Michigan State University and University of Bergen between 1985 and 1992. It is written for advanced undergraduates, or beginning graduate students in physics both for experimentalists and theorists. The book contains more material than necessary for a one semester course to allow for some selection.

The purpose of the book is to give a general introduction to all beginners in the field of high energy heavy ion physics. It tries to cover a wide range of subjects from intermediate to ultra-relativistic energies, so that it provides an introductory overview of heavy ion physics, in order to enable the reader to understand and communicate with researchers of neighbouring or related fields.

Some familiarity with basic nuclear physics, statistical physics and special relativity is assumed. The book is essentially based on a simple introduction to relativistic kinetic theory, with ample examples from the field of heavy ion physics. It introduces the basic variables used in the field. Then collective macroscopic features of the dense and high temperature matter is discussed. Collective fluid dynamical approaches are introduced in a greater detail, and simple (frequently analytically solvable) models are presented. The properties of the nuclear Equation of State are discussed at an introductory level, mentioning some results from the recent years.

The connections between the collective dynamical descriptions and the experimentally measurable quantities are shown, and the mass and energy scaling of data is used to discuss the observability of dissipative properties of the high energy matter. Microscopic an inherently nonequilibrium descriptions are discussed only briefly.

Recent advances in the search for the Quark Gluon plasma are discussed in an extended chapter. Finally a few interesting connections to astrophysics are mentioned.

The book containes assignments with solutions of a wide range of different difficulties. The excercises are important, because some basic information is introduced via the excercises only.

The sections indicated by (*) are recommended for additional reading, and should not be included necessarily in a regular course. The presentation of the subject in the indicated sections is concise, thus the study of the original literature is advised to those who are interested in the subject particularly and in detail.

László P. Csernai

November, 1992

Chapter 1

Basic Phenomenology of Heavy Ion Collisions

1.1 Introduction

In the past decade nuclear physics went through a revolution and its connection to particle physics and statistical physics became more apparent. Initially in late 70's and early 80's some accelerators used by particle physicists earlier, like the Bevatron in Berkeley or the Dubna syncrophasotron, were converted to accelerate heavy ions. At the same time the energies of the accelerators used for nuclear research were increased, so that relativistic beams of heavy nuclei became available at several places in the world. (NSCL/MSU in East Lansing, GSI in Darmstadt, GANIL, Saclay, Celsius ring in Uppsala, etc.)

By the mid 80's the heavy ions were injected into some of the highest energy proton accelerators also, such as the Alternating Gradient Synchrotron (AGS) at Brookhaven National Laboratory (BNL) and to the Super Proton Synchrotron (SPS) at the European Center for Nuclear Research (CERN). By the early 90's the injection of heavy ions is studied already at the planning phase of the new accelerators, like in the case of the Large Hadron Collider (LHC) of CERN. Why did high energy nuclear physics become so much the center of interest again? There are several reasons. The main reason is the exploration of the Quark-Gluon Plasma (QGP).

1.1.1 The Quark Gluon Plasma

Already in the early 70's the deep inelastic electron collision experiments on protons indicated that nucleons have an internal structure, they are built of quarks and gluons. The field theory which describes these quanta is the Quantum Chromodynamics (QCD). This theory leads to the conclusion that single free quarks or gluons cannot be studied or observed in our laboratories, in the so called physical vacuum, because they are confined by the strong interaction which binds them to each other. This strong tie is represented by the quantum number called "color". In our physical world, however, all observable particles are colorless or color neutral. On the other hand, at high energy densities and temperatures the strong tie among the quarks and gluons weakens and

colored objects may propagate longer distances. This was assumedly the situation in the early universe also.

The expectation is that these high energy densities, sufficient to produce QGP, may be reached in laboratory in heavy ion reactions already at relatively modest energies, in the order of 10–100 A·GeV laboratory projectile energy. When these conditions are created, there will be a large number of quarks and gluons in the reaction zone. This is the only possibility to produce unbound quarks and gluons in laboratory in a small volume (10–100 fm^3 for a short time, 2–10 fm/c).

The search for QGP is in progress when this book is written and no clear quantitative conclusions are obtained about the plasma yet. [1, 2, 3] Thus we will discuss briefly the main directions of the search at present.

1.1.2 The nuclear Equation of State

Even if QGP is not formed in a given reaction it is very important to know the behavior of the matter under high densities and temperatures, which can be reached in heavy ion reactions. [4] The intermediate states of a collision may involve as many as 500 particles even at low energies (~ 100 A·MeV) in a small volume. If the energy is increased, so much that particle-antiparticle creation becomes easily possible (at ≈ 100 A·GeV), the number of particles involved in a reaction may go up to several thousand. This system is, although, quite small it can already be sufficiently large for statistical and kinetic physics to be applicable. Since the heavy ion reaction is a highly dynamical process both the equilibrium and non-equilibrium properties of the matter can be studied. Of course equilibrium and non-equilibrium effects are not always easy to separate.

The thermodynamical properties of the matter in statistical equilibrium are described by an Equation of State, (EOS). There are three interesting features of the EOS under investigation now: i) the phase transition from continuous nuclear liquid into a nuclear vapor of fragments and nucleons, the so called nuclear liquid-gas phase transition, or the multifragmentation transition [5, 6], ii) the compressibility of nuclear matter at and higher densities than the density of matter in ground state nuclei (n_0), and finally, iii) the phase transition to QGP mentioned above already.

The nonequilibrium features of matter can also be studied in heavy ion reactions. Transport coefficients can be deduced from experimental results. On the microscopic level these are associated with in-medium nuclear cross sections. The reconciliation of several sorts of experiments and observations leads even to conclusions on the nucleon-nucleon interaction.

1.1.3 New collective phenomena

The most impressive results of high energy heavy ion research so far are the new collective phenomena discovered in these reactions. The hot and compressed nuclear matter behaves like a compressible fluid (not like a dilute gas) and fluid dynamical effects are observed in these reactions.

First the matter was seen to be flowing sidewards in the reaction plane due to the high pressure developed at the impact. Later it was also seen that the matter is

squeezed out of the hot zone between the two nuclei, in the orthogonal direction to the reaction plane also. Finally at lower energies it was observed that the transverse flow decreases with decreasing energy, goes to zero at around 100 A·MeV and turns to a negative angle flow in peripheral reactions below this energy. This is due to the fact that nuclear attraction starts to dominate over the repulsive pressure (which has large thermal pressure contribution).

1.1.4 Particle production

In heavy ion reactions new particles are also produced, with increasing energy an increasing number. Due to the collective effect of several nucleons and due to their Fermi motion, particles can even be produced under their production threshold, i.e. at such low energies where, in free nucleon-nucleon collisions, production is not possible. At very high energies production of exotic particles, which were not known before, such as strangelets, is also predicted.

The wealth of these possibilities provide a unique possibility in physics to study high energy phenomena. Heavy ion beams are the most energetic beams produced by an accelerator and this obviously provides unique possibilities for the research.

1.2 Energy domains of heavy ion physics

In this textbook we try to cover heavy ion physics in the wide range of energies from 100 A·MeV beam energy to 10 A·TeV. Obviously this range involves very different collision processes and physical phenomena, but we will try to concentrate on the features that are common to the whole heavy ion research. These are centered around the relativistic statistical description of these reactions. We will also concentrate more on collective phenomena in heavy ion reactions which can not be studied elsewhere. We will not discuss separately hadron-hadron (h + h), hadron-nucleus (h + A) reactions or light ion reactions, (like $\alpha + \alpha$ or d + D). From the physical point of view the energy region can be divided into three main regions:

i) intermediate energy heavy ion reactions,
ii) relativistic energy heavy ion reactions,
iii) ultra-relativistic heavy ion reactions.

1.2.1 Intermediate energy reactions

This is the energy region where the properties of hot nuclear matter can be studied around the normal nuclear density, n_0. The corresponding beam energies are in the range of 10–100 A·MeV. In this region of the thermodynamic variable space there is an interesting phenomenon the nuclear liquid-gas phase transition. At low excitations the nuclear matter is bound due to the attractive nuclear interaction. In an intermediate energy heavy in collision we may compress the nuclear matter initially (to 1-2 n_0) and heat up the matter to 10–20 MeV. This matter then expands nearly adiabatically to densities below n_0 and to a smaller temperature, 5–10 MeV. Due to the attractive

interaction in this final state smaller nuclear fragments are formed, the nuclear vapor is condensed to form droplets of nuclear liquid. This is the nuclear multi-fragmentation. If the collision energy is low enough the effects of the phase transition, for example critical phenomena, can be studied. The accelerators doing research in this energy domain are for example the NSCL at Michigan State University, UNILAC and SIS at GSI in Darmstadt Germany, GANIL in Caen France, CELSIUS in Uppsala Sweden, etc.

1.2.2 Relativistic heavy ion reactions

In this energy range, 100 A·MeV–10 A·GeV, the nuclear matter is compressed and heated more than at lower beam energies. Here mainly the compressibility and other basic properties of the nuclear EOS and nuclear interactions can be tested. The results in this energy range have astrophysical relevance to neutron stars and supernova explosions. This is the area where the research is most developed and real quantitative questions on the nuclear incompressibility, transport coefficients, in medium cross sections, momentum dependence of the nucleon-nucleon interaction, etc., are studied. Collective processes are well established both experimentally and theoretically, such as different collective flow patterns. The most dominant is the collective sidewards flow in the reaction plane which is used as a tool to extract the EOS and transport properties of nuclear matter. This energy range is studied at some of the accelerators mentioned above and at some others like the BEVALAC at LBL in Berkeley, the heavy ion accelerator in Dubna, SATURN in Saclay France.

1.2.3 Ultra-relativistic heavy ion reactions

This energy region starts around 10 A·GeV beam energy and the most intriguing physics question is the search for Quark Gluon Plasma. The most optimistic theoretical estimates allow QGP formation already at 10 A·GeV. The ultra-relativistic domain can be separated into two regimes with essentially different physics: the *stopping region* where baryons stemming from the projectile and the target are fully or partly stopped by each other, forming a fairly baryon rich matter in the middle of the reaction zone, and the *transparent region* where initial target and projectile baryons are so far apart in the phase space that the heavy ion collision cannot slow them down completely. The boundary between these two regions is not very sharp and experimentally not known yet.

Stopping region

As indicated by the first results from the SPS at CERN and AGS at BNL, up to 60 A·GeVthere is almost complete stopping in reactions with S and Si projectiles. Some theoretical estimates predict that with lead beams even 200 or 800 A·GeVcollisions will result in stopping of the baryons in the middle of the reaction zone and of the phase space [8]. Thus, these reactions provide a tool to study very highly excited baryon rich matter, or eventually baryon rich quark gluon plasma. This area has also astrophysical

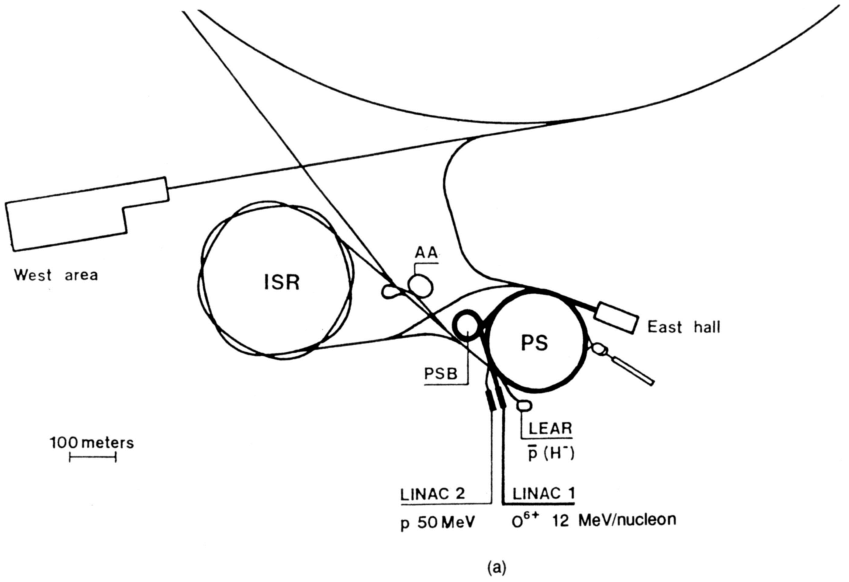

Figure 1.1: The layout of the SPS at CERN, Geneva. Reproduced by permission of Elsevier Science Publishing from [7].

relevance associated with possible hybrid stars, i.e. neutron stars with dense quark matter core.

Transparent region

If we increase the energy further the theoretical expectation is that the initial baryon charge from the projectile and target will not be slowed down completely. The quanta carrying this baryon charge will essentially keep their initial velocities and the middle zone in the reaction will be baryon free. Of course energy will be deposited in this region also. The large energy density matter in the central region may form a baryon free quark gluon plasma, which is of large theoretical interest. The theoretical model calculations are more straightforward for this form of matter than for baryon rich quark gluon plasma, and furthermore, this form of high energy density and low baryon density matter is the one which was present in the early universe before hadrons were formed. The heavy ion accelerators which would be able to reach this energy region are in the planning and construction stage now: the LHC heavy ion collider at CERN, and the RHIC at BNL. The TEVATRON at Fermilab can be mentioned as a proton antiproton collider relevant to this research, where some basic experience can be gained before the heavy ion colliders will be available.

1.3 Heavy ion experiments

Although this textbook does not address the problem of experimental methods and techniques, we have to mention some basic physical features of relativistic heavy ion

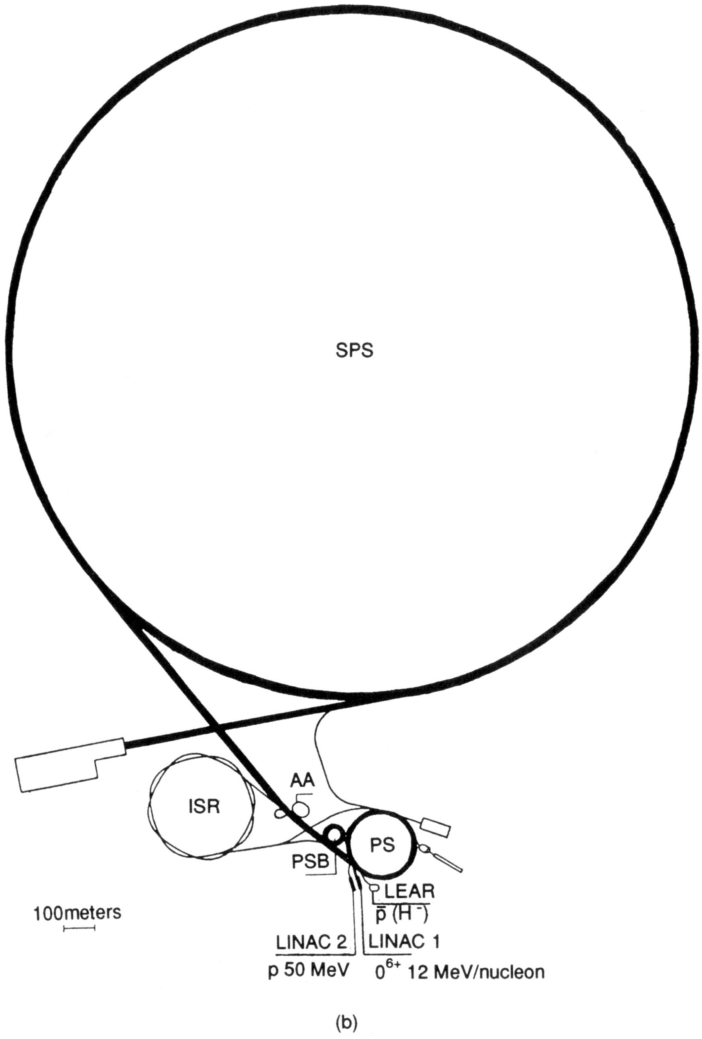

Figure 1.1: continued

collisions, which imply a new experimental approach to the problem also.

At low energy nuclear physics the most frequent event is an elastic collision, where the target and projectile maintain their integrity and even their internal quantum state. In low energy inelastic processes one or both of the outgoing particles may be in excited states, and even some extra third (or fourth) particle(s) are created. But in any case the final multiplicity is rather small. Consequently it is satisfactory at these energies to measure one or at most two outgoing particles. Although in principle there exist a reaction plane in these reactions it cannot be reliably identified in low multiplicity events particularly if some of the particles are not measured (like neutrals). Thus it is customary to measure azimuth averaged cross sections in low energy nuclear and particle collision experiments.

In relativistic heavy ion collisions the multiplicities are large. Already at 100 A·MeV beam energy we can have about 10–100 secondaries, while at 100 A·GeV the number

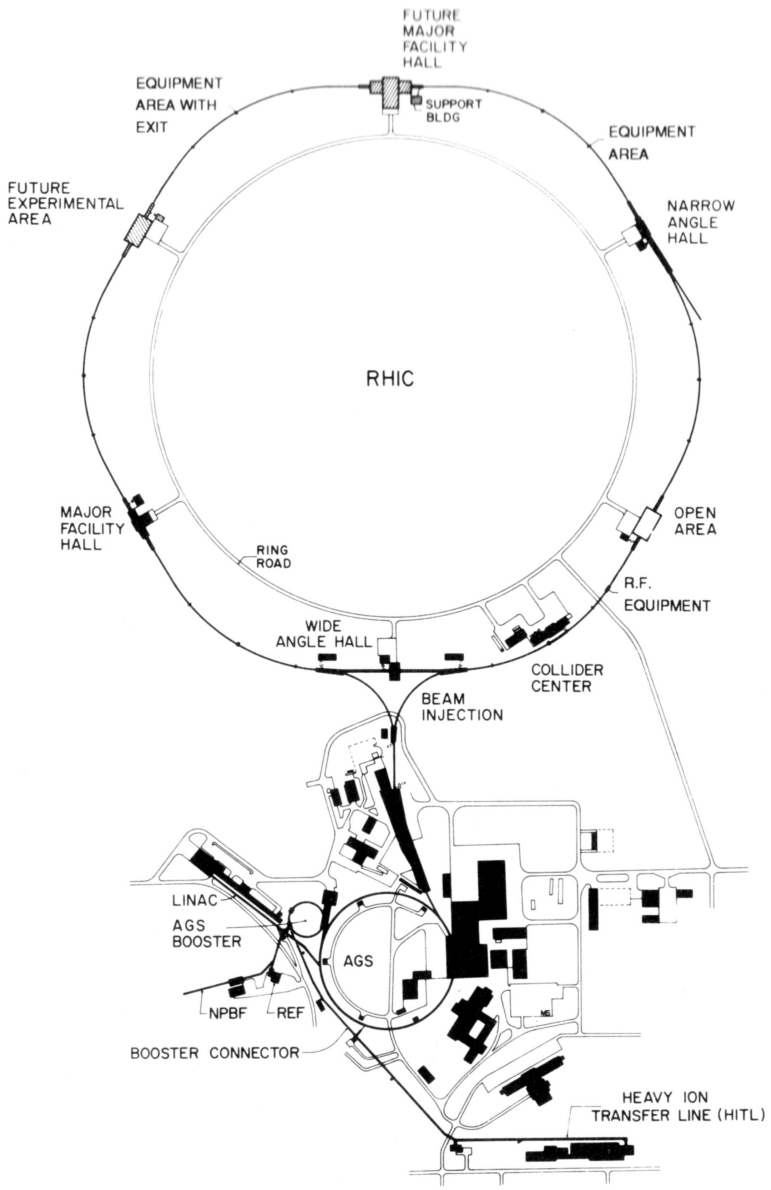

Figure 1.2: The layout of the RHIC at Brookhaven National Laboratory. Reproduced by permission of Elsevier Science Publishing from [9].

of produced particles may exceed 1000, i.e., it can be much more than the number of initial nucleons.

This large multiplicity leads to special experimental requirements not known before in nuclear physics. These multiplicities exceed even the multiplicities of highest energy particle physics experiments. To a general characterization of the event, first of all event by event detection is desirable, and it is also advantageous if we can measure all emitted particles in an event simultaneously. Obviously these requirements led to the introduction of highly segmented detector arrays, like the MSU 4π detector, the BEVALAC Plastic Ball, or the large detector arrays at the CERN-SPS and BNL-AGS heavy ion experiments. Another alternative is a large volume track detector like the streamer chamber, time projection chamber (TPC) or stacks of nuclear emulsion. High energy particle detectors are using top technology, but heavy ion detectors have special extra features. With these advanced detectors the increasing multiplicity does not seem to be an obstacle at the first sight, but the track recognition problem becomes increasingly difficult at very large multiplicities. Recently new techniques are experimented with, like neural networks, to solve the track recognition problem.

The relativistic heavy ion experiments thus are large scale efforts involving several dozen researchers usually and large systems of equipment, similarly to modern particle physics experiments.

The experimental effort is threefold: (i) equipment design and construction, (ii) data taking and (iii) data evaluation. Here we will only concentrate on the last point, but a familiarity with technical limitations and possibilities is necessary if we want to discuss the measurable consequences of the underlying physical processes.

1.3.1 Acceptance

Detectors are of a limited size and given geometry, thus for example they seldom are able to measure sharply forward or backward going particles because the beam vacuum pipe is occupying that region. Also the target is mostly in vacuum also, while the detectors are usually outside the vacuum. Consequently very soft particles (low energy particles of less than 20–30 MeV) cannot penetrate the vacuum vessel, leading to a low energy threshold in the acceptance of the detector system.

The limited geometrical acceptance of the detector system is usually not represented by clear orthogonal cuts in the parallel and orthogonal momenta (with respect to the beam) direction. Thus extrapolations and interpolations are frequently necessary even to construct the transverse momentum, p_t, spectrum of the emitted particles.

1.3.2 Event selection

With heavy ions a collision can be very different if the ions collide head on or only graze each other. Obviously we cannot detect the projectile and the target before the collision, so an evaluation of the final state is necessary to classify the events in some way. It is a common assumption that the more central the collision the more violent it is and it produces more outgoing particles. However, to quantify this aspect of the collision is not easy. It is assumed that *on the average*, decreasing impact parameter (see the definition

later) leads to increasing multiplicity. Thus the most central collisions (these are the most interesting ones) correspond to the highest multiplicity ones. Since the geometrical probability to have a collision of impact parameter $b \pm db$ is increasing proportionally with $2\pi b$. Selecting the 25% highest multiplicity events corresponds *approximately* to selecting collisions with impact parameters less than half of the maximum possible impact parameter. One has to emphasize that this is not an exact impact parameter selection because due to random fluctuations it is possible that the observed multiplicity, M, is higher or lower than the mean value for any given impact parameter. Thus a given selected set of data, $M \in S$, corresponds to a set of events with some distribution of impact parameters, $P_M(b)$. This distribution is not known, it can be estimated in theoretical models. Based on geometrical arguments one can assume that the asymptotic behavior of this distribution for small b is $P_M(b) \sim 2\pi b$.

Event trigger

If we want to select e.g. 25% of the highest multiplicity collisions we have two tasks. First we have to determine how much is 100% of the collisions. In principle if we know all incoming and outgoing particles in an event it is easy to tell if a reaction has happened or not, so that all subsets can be compared to this complete event sample. However, in a real detector system it is possible that some particles are missed, thus some low multiplicity events are not detected at all. Therefore it is important to have an event trigger and an absolute total cross section in an experiment, which is not always an easy task, particularly with limited coverage detectors.

Selection trigger

Having defined a complete sample of measured events, we usually want to select a subset of most violent, most central, or highest multiplicity events. Multiplicity could be measured with a general detector of close to 4π acceptance, but most experimental setups do not have this possibility, therefore some reduced triggering device, or software selection criteria, are used to select a subset of events. The effect of a special triggering may not even select the general highest multiplicity subset of events, furthermore the impact parameter distribution of the subset is basically unknown. Simulations with a given theoretical model may provide an impact parameter distribution for a given trigger condition, but such simulations are costly and even if they are performed very carefully they will be biased by the model used.

1.3.3 Physical event tape

The above mentioned features are quite general in heavy ion experiments. The measured primary data, on the other hand are quite different in different experiments, and a major part of the data evaluation is to convert these primary data to a physical data set which contains the detected particles and their characteristics (species, energy, momentum, etc.) in an event. A set of events with all these characteristic data on each emitted particle can than be stored on a physical data tape. This can then be used to

evaluate the desired cross section, momentum distribution, correlation, or some other measurable.

1.3.4 Detector filters

Some theoretical models can also produce similar "physical data tapes" with a set of particles produced in simulated events. These are usually called *event generators*. It is, however, not possible to compare the two data tapes directly, since the theoretical models are usually not limited by a detector acceptance. Furthermore, the set of events included in the theoretical set might not correspond to the experimentally selected set of events. To circumvent these difficulties some experimental groups provide computer codes to anyone who needs it which simulate their detector acceptance and triggering. The theoretical data tape should then be filtered through the particular detector acceptance program and the resulting *filtered* theoretical data can be compared to experimental data.

This procedure is, however, seldom performed. Mainly experimental groups perform these calculations by simpler theoretical models to enable extrapolations to a given limited region of the phase space. These extrapolated data are then published, which can be directly compared to (non-filtered) theoretical results.

1.3.5 Outline

In this textbook the experimental methods of representing the primary physical data are presented, but experimental techniques are not discussed. There are an almost infinite number of ways to project primary data of an event into a more transparent representation, which gives more insight into the underlying physical phenomena. The most important measurables will be discussed later in this book, after the introduction of basic theoretical aspects of a nonequilibrium, high energy, many-body system.

1.4 General features of heavy ion physics

In all energy ranges mentioned above there are some common aspects of heavy ion reaction dynamics. The energies are large enough and the masses of ions are also large, to consider the heavy ions as classical particles. Their De Broglie wavelength is much less than the typical nuclear sizes. Quantum effects influence the underlying microscopic dynamics only, which can be included in the EOS, in the transport coefficients, or in the kinetic theory describing these reactions.

At relativistic and ultra-relativistic energies even the nucleons can be considered to a large extent as classical particles. This and the short range of the nuclear interaction leads to the fact that geometrical concepts are applicable to a large extent to these reactions. The total reaction cross section can be calculated from the sizes of heavy ions. Furthermore, a simple clear cut geometry is quite well applicable for simple separation of *participant* and *spectator* regions in a heavy ion collision. If we assume that all nucleons propagate along straight line trajectories in a non-central heavy ion

collision, those nucleons which do not meet any other nucleon on their way are the spectators. There can be target and projectile spectators in a collision. The rest of the nucleons may hit each other on the way forming a participant zone with both target and projectile nucleons in it. Of course in reality the separation between spectators and participants is not exact and there is a transition zone between these areas. With increasing energy, however, this transition region becomes smaller. Fig. 1.3.

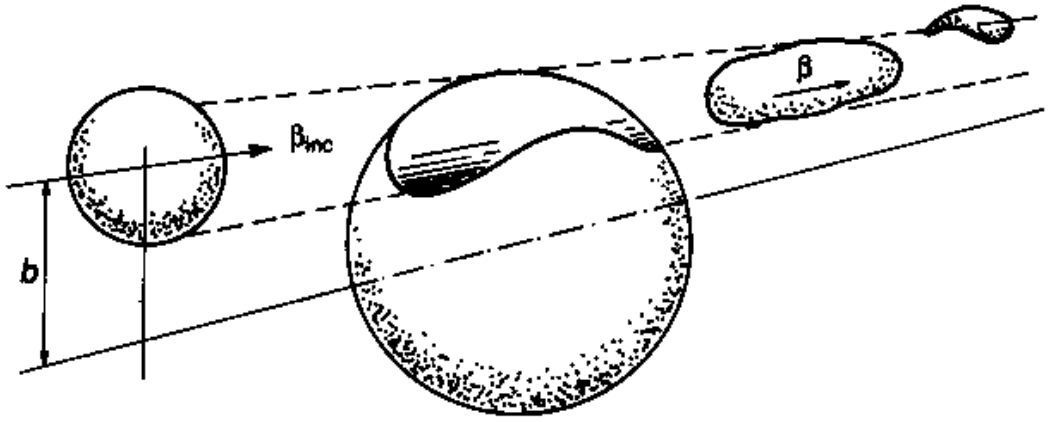

Figure 1.3: Spectators and participants in a heavy ion collision. Reproduced by permission of the American Physical Society from [10].

The most interesting phenomena and the new physics is in the participant zone, but the spectator regions also provide us with interesting phenomena. For example the spectators may form a rest fragment which is somewhat excited due to its irregular shape and the friction to the participants. The study of these fragments is also of great interest. For example extremely neutron rich light fragments can be (and are) created in peripheral heavy ion reactions, which were not produced in laboratory before relativistic heavy ion beams existed. This is the simple consequence of the fact that heavy nuclei are much more neutron rich than light ones, and the remaining light spectator fragment inherits the A/Z ratio of the heavy primordial nucleus.

Realistically the nucleons do not propagate along exactly straight trajectories, deviations from straight propagations are observed even at the highest energies of 200 GeV per nucleon. According to the fluid dynamical model, considerable collective sideward motion is generated [11, 12, 13]. See Fig. 1.4.

1.5 Connections to other fields of physics

1.5.1 Nuclear physics

First of all these events belong to Nuclear Physics obviously, but some subfields of nuclear physics have strong connections to relativistic heavy ions. The most important connection is to the studies on the nuclear equation of state (EOS). In low energy

nuclear reactions the EOS could be studied at essentially zero temperature and at densities very close to the ground state. At relativistic energies Heavy ion reactions map out a much larger domain of the field of thermodynamical variables.

These reactions are strongly influenced by the properties of the nucleon-nucleon interaction, and through this by the non-equilibrium or transport properties of the nuclear matter.

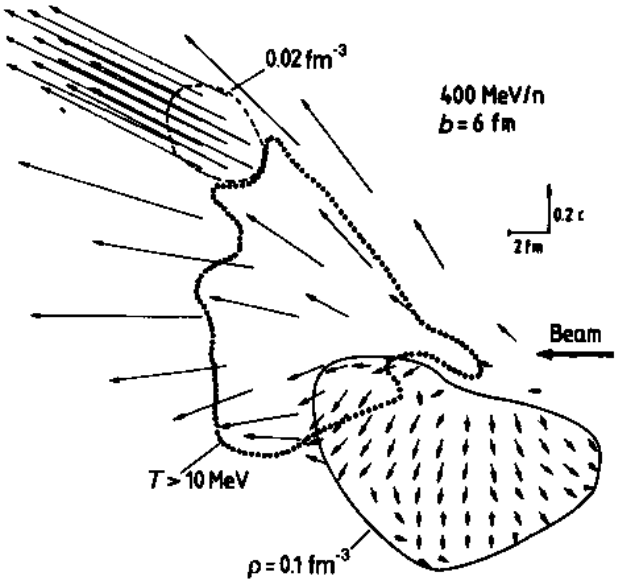

Figure 1.4: Final state in a collision of Ne+U in the fluid dynamical model. The dotted line encloses a region of temperature $T > 10\,\mathrm{MeV}$, other lines are encircling the regions of high density in the target and projectile residues. The arrows indicate the flow velocity field. Reproduced by permission of the American Physical Society from [13].

1.5.2 Particle physics

The connection to particle physics is almost as strong as to nuclear physics. The exact description of many elementary collisions would be needed by the study of heavy ion reactions. Hadronic collision phenomenology is the basis of many reaction models directly (like string Monte Carlo models), and many other models extract features from hadron physics.

Knowledge of hadron physics is a necessity if we want to extract the collective nuclear processes from the simple superposition of many independent hadronic collisions.

On the theoretical side these reactions are testing the features of the nonperturbative QCD, which are not completely known yet. This is an extremely wide field and a large fraction of the researchers works on the study of non-perturbative QCD. Most of these studies are numerical, in the so called "Lattice QCD" which tries to find the equilibrium and nonequilibrium solutions of QCD. In this book we just touch upon this subject. Our aim is just to give some very limited information, necessary to understand the essential basic results of these studies and apply them in reaction models, EOS, etc.

In heavy ion reactions subthreshold particle production may take place also. Not only due to the internal Fermi motion of the nucleons within the nuclei but also due to more interesting collective effects (like cumulative production).

1.5.3 Statistical physics

A heavy ion reaction is a dynamical system of a few hundred nucleons. This is a large number but still far from the continuum, so that deviations from infinite matter limit are important. On the other hand the number of particles participating in a reaction is large enough that the signs of collective matter like behavior can be clearly observed. This is an interesting territory in statistical physics of small but collective systems. The methods developed in this field are unique and may also be applicable in other "small" statistical systems.

When Quark Gluon Plasma is formed the number of quanta increases to a large extent. The plasma can already be considered as a continuum, and finite particle effects should be small.

On the other hand the heavy ion reaction is a rapid dynamical process. The question of phase transitions in a dynamical system is still an open field of research. Heavy ion physics may contribute to this field at two points: i) the dynamics of the phase transitions in "small" systems, and ii) the dynamics of the phase transitions in ultra-relativistic systems where the energy of the system is much higher than the rest mass of the particles.

Finally the heavy ion physics contributes to a large extent to the evolution of the transport theory at high energies. Many numerical reaction models were developed based on transport theory, and the field is in rapid development today.

1.5.4 Relativistic fluid dynamics

Heavy ion reactions are providing a terrestrial possibility to test the solutions of relativistic fluid dynamics. Highly energetic processes like relativistic detonations and deflagrations can be studied theoretically and numerically. Their consequences can be checked by comparing model results to experiments. Considerable development on this field can be attributed to heavy ion physics.

The dynamics of heavy ion reactions is oftentimes better approximated by multicomponent fluid dynamical models. Although such models were known before for partly equilibrated systems (like electron-ion plasmas) the development due to heavy ion physics in this field is also apparent.

1.5.5 Astrophysics

This is maybe the most interesting connection to other fields of physics. For long the information which can be extracted from heavy ion reaction was needed to create adequate models of the early universe, of neutron stars, supernova explosions, quark stars, etc. Some of these questions will be discussed at the end of this book.

The most important common ingredient is the EOS, which is searched for by both astrophysicists and heavy ion researchers. Although astrophysical information provides less constraint on the EOS, conclusions extracted from heavy ion data should be checked against the known astrophysical information. For example, we can extract the compressibility of nuclear matter from heavy ion collision data. This compressibility is, on the other hand strongly related to the mass of the neutron stars. One should pay attention that an EOS extracted from heavy ion data should not support neutron star masses which contradict to the observations; i.e. smaller maximum mass than the observed maximum.

The models of the early universe are strongly influenced by the phase transitions in the highly energetic matter, particularly by the formation of hadrons. We hope to gain important information from heavy ion reactions on the phase transition from Quark-Gluon Plasma to hadronic matter and on the dynamics of this phase transition.

Since heavy ion collisions are highly complex processes connections with other fields of physics may also show up and become important. (One example for such a possibility is the puzzle of electron positron pairs, which show up in a narrow energy peak in relatively low energy heavy ion reactions. There are speculations that nuclear and atomic processes may interact in these phenomena.)

1.6 Why a theoretical treatment is important?

This textbook is written both for theorists and experimentalists as an *introduction* to the field. It tries to present the basic introductory knowledge mainly from the theoretical side.

It is important that to a certain extent both experimentalists and theorists should speak the same language, and theorists should also be aware of experimental possibilities and limitations which are mentioned in the book.

Both experimentalists and theorists should be familiar, on the other hand, with the basic theoretical concepts of the field. Since a heavy ion collision is a rather complex process many areas of physics are necessary for its understanding. The books gives an introduction to most of these fields. Nevertheless, it does not go into the latest details of the more complicated recent research, although a few topics are mentioned indicated with (*). These are advisable for the more theoretically interested reader. For more advanced and theoretically oriented readers more advanced and relatively detailed material can be found in two recent monographs on the field [14, 15]. The proceedings of the Quark Matter series of conferences provides up to date information both for experimentalists and theorists.

1.7 Outline of the book

In Chapters 2 and 3 an introduction is given to the transport theory of relativistic systems. Several examples are taken from the field of heavy ion physics. This part is important to understand the basics of equilibrium and non-equilibrium systems and how the systems evolve towards equilibrium.

Chapter 4 discusses the basic features of the nuclear equation of state (EOS) which characterizes a static equilibrium system. Chapter 5 introduces relativistic fluid dynamics which is able to describe dynamical systems which are locally equilibrated but not globally. Heavy ion reactions in the "ideal" case belong to this category, if the system is sufficiently large (e.g. central or near central collisions with more than 400 particles involved or more than several thousand quanta if QGP is formed). In Chapter 6 the most simple reaction models are presented, widely used both by theorists and experimentalists in the recent years. These are all simple fluid dynamical models.

In Chapter 7 the experimental observables are discussed and their connections to the collective properties of the system. In Chapter 7 the characteristic energy and mass scaling of the observables are discussed, i.e. how can one compare experimental results measured at different beam energy or in different colliding systems.

In Chapter 9 some of the reaction models not assuming a priory equilibrium are introduced. Since most of these are numerical microscopic models we constrain ourselves to the presentation of the basic features and the results of these models.

In Chapter 10 an overview of the search for quark gluon plasma is given. Here more information is given on the EOS based on Lattice QCD, The possible reaction dynamics is discussed in different energy regions, and the results of some reaction models are presented and compared to experiments. Some recent ideas for the possibility to detect the phase transition are mentioned. Since the development particularly in this field is very rapid, the reader should certainly consult the current literature for up to date information.

Finally in Chapter 11 connections between astrophysics and heavy ion reactions are presented.

At the end of each Chapter there are assignments which are important parts of the textbook. Some of the concepts used in the field are introduced in assignments! For those who do not want to solve the assignments a brief solution is also provided. The

difficulty of the assignments gradually increases up to the middle of the book.

1.8 Assignment 1

Participants and Spectators

1.a Calculate the number of participant nucleons in a central S + Pb reaction, assuming that the nuclei have sharp surfaces and their density distribution is uniform, $n_0 = 0.17/\mathrm{fm}^3$.

1.b What is the center of mass kinetic energy of the participants in the laboratory frame if the Sulfur projectile had a beam kinetic energy of $\varepsilon_S^{(kin.)} = 200\,\mathrm{GeV}$ per nucleon in the lab, and the Lead was a fixed target. What is the average excitation energy of the participant nucleons?

1.8.1 Solutions to Assignment 1

1.a The radii of the nuclei can be obtained from $4R^3\pi n_0/3 = A$. If $n_0 = 0.17/\mathrm{fm}^3$, then $R_{Pb} = 6.64\,\mathrm{fm}$ and $R_S = 3.56\,\mathrm{fm}$. The height of the cylinder cut out of the target by the path of the projectile is $H = 2\sqrt{R_{Pb}^2 - R_S^2}$, thus the volume of this cylinder is $V_1 = R_S^2\pi H = 445\,\mathrm{fm}^3$. The height of the spherical slices at the two ends of the cylinder is $h = R_{Pb} - \sqrt{R_{Pb}^2 - R_S^2}$, so the volume of the two spherical slices is $V_2 = 2/3\ \pi h^2(3R_{Pb} - h) = 42\,\mathrm{fm}^3$. I.e. the total number of target participants is $A_T = n_0(V_1 + V_2) = 83$, and the total number of participants is $A_{Part.} = 115$.

1.b The momentum of the projectile is conserved and will be carried by all participants, $\vec{P}_S = \vec{P}_{Part.}$. If the average nucleon mass is $m_Nc^2 = 0.939\,\mathrm{GeV}$, the total projectile energy is $E_S = A_S(200\,\mathrm{GeV} + m_Nc^2) = 6.430048\,\mathrm{TeV}$, and the total projectile momentum is $P_S = (A_S/c)\sqrt{200.939^2\,\mathrm{GeV}^2 - (m_Nc^2)^2} = 6.429978\,\mathrm{TeV}/c$. Consequently the total participant energy is $E_{Part.} = \sqrt{P_S^2 + s} = \sqrt{P_S^2 + A_{Part.}^2(m_Nc^2 + \varepsilon^*)^2} = 6.507985\,\mathrm{TeV}$, and the excitation energy of the participant nucleons is $\varepsilon^* = \sqrt{s}/A_{Part.} - m_Nc^2 = m_Nc^2[\sqrt{A_T^2 + A_S^2 + 2A_TE_S/(m_Nc^2)}/A_{Part.} - 1] = 7.797\,\mathrm{GeV}$

Bibliography

[1] QM'87, Nordkirchen, FRG, Z. Phys. **C38** (1988) 1-370.

[2] QM'89, Lenox, USA, Nucl. Phys. **A498** (1989) 1c-628c.

[3] QM'90, Menton, France, Nucl. Phys. **A525** (1991) lc-741c.

[4] Proc.: "The Nuclear Equation of State, Parts A & B; ed. by W. Greiner, and H. Stöcker, eds.) NATO ASI Series, **Peniscola**, Spain, May 21 - June 3, 1989; (Plenum, 1990).

[5] L.P. Csernai and J. Kapusta, Phys. Rep. **131** (1986) 223.

[6] A.R. DeAngelis and A.Z. Mekjian, in "Relativistic Heavy Ion Physics", eds. L.P. Csernai and D.D. Strottman (World Scientific, Singapore 1991) Vol. 6 p. 354.

[7] R. Klapisch, Nucl. Phys. **A418** (1984) 347c.

[8] N.S. Amelin, E.F. Staubo, L.P. Csernai, V.D. Toneev, K.K. Gudima and D. Strottman, Phys. Lett. **B261** (1991) 352.

[9] T. Ludlam, Nucl. Phys. **A447** (1985) 349c.

[10] G.D. Westfall, J. Gosset, P.J. Johansen, A.M. Poskanzer, W.G. Meyers, H.H. Gutbrod, A. Sandoval and R. Stock, Phys. Rev. Lett. **37** (1976) 1202.

[11] H. Stöcker, W. Greiner and W. Scheid, Z. Phys. **A286** (1978) 121.

[12] H. Stöcker, G. Graebner, J. Maruhn and W. Greiner, Z. Phys. **A295** (1980) 401.

[13] H. Stöcker, J. Maruhn and W. Greiner, Phys. Rev. Lett. **44** (1980) 725.

[14] Quark-Qluon Plasma, ed. R. Hwa, (World Sientific Publishing Co. Pte. Ltd., 1990), Advanced series on directions in high energy physics vol. **6**.

[15] Relativistic Heavy Ion Physics Eds. L.P. Csernai and D.D. Strottman – Int. Rev. of Nucl. Phys. Vol. 5-6 (World Scientific, 1991).

Chapter 2

Introduction to Relativistic Kinetic Theory

Our aim is to describe non-equilibrium relativistic (classical) many body systems, e.g. Relativistic Heavy Ion Collisions (RHIC). Several reaction models exist for this purpose, most of them are based on kinetic theory. The fluid dynamical model, the cascade model, the so called VUU-BUU approach, and different classical and quantum molecular dynamics models can all be related to basic transport theory. These models will be discussed later in this textbook.

In the following we assume that the reader is familiar with the basic concepts of special relativity, elementary statistical physics, and has some initial knowledge of basic classical nuclear and/or particle physics. Thus, we start with a short introduction to kinetic theory. Our discussion is based on the book of S. R. de Groot, W. A. van Leeuwen and Ch. G. van Weert [1]. Those interested may find further information in this excellent textbook. A somewhat shorter introduction than here can be found in ref. [2]. First we have to introduce our basic variables which we use to describe these phenomena.

- Microscopic variables: particle mass, momentum, energy, position
- Macroscopic variables: flow, velocity, density, temperature, etc.

The kinetic theory establishes a relationship between macroscopic and microscopic properties, by using a one-particle distribution function $f(x,p)$. The function $f(x,p)$ describes the phase space density of the particles and a kinetic equation or transport equation governs the time development of $f(x,p)$ (usually for dilute systems). We may have seen this at the discussion of the non-relativistic Boltzmann equation in standard courses of statistical physics.

2.1 Basic definitions of microscopic quantities

Here we briefly repeat some basic definitions and notations of special relativity. A detailed introduction to special relativity can be found in several basic textbooks. In this book we will most of the time use the convention $c = k_B = 1$.

2.1.1 Phase-space variables

- Space-time coordinates.
  The 3 spatial coordinates and the time span a 4 dimensional space, the space-time. Its coordinates are composed of the time t and position 3-vector $\vec{r}$. See Fig. 2.1.

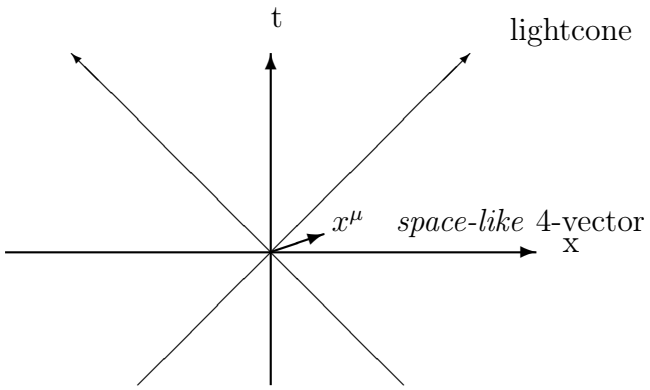

Figure 2.1: Coordinates of a point (or event) in space-time are denoted by a 4-vector: $x^\mu = (t, \vec{r})$. Reproduced by permission of World Scientific Publishing Co. from [2].

- Four momentum.
  The four momentum of a particle in space-time is: $p^\mu = (p^0, \vec{p})$, where $p^0 = \sqrt{(\vec{p})^2 + m^2}$, $(p^0 = E$, as usual at relativistic energies). The 4-momentum is a time-like vector with the normalization $(p^0)^2 - (\vec{p})^2 = m^2$. This can be written in the form:

$$p^\mu p_\mu \equiv \sum_\mu p^\mu p_\mu = m^2, \tag{2.1}$$

  where p^μ's are called the *contravariant*, and p_μ's are the *covariant* components of a 4-vector:

$$p_\mu = g_{\mu\nu} p^\nu, \tag{2.2}$$

  where $g_{\mu\nu} = g^{\mu\nu} = \mathrm{diag}(1, -1, -1, -1)$ is the *metric tensor*. So, $p^\mu = (p^0, \vec{p})$, and $p_\mu = (p^0, -\vec{p})$. The square of the 3-momentum, $(\vec{p})^2$, is also denoted by $p^2 (= (\vec{p})^2)$, while $p^\mu p_\mu = m^2$. Four vectors may be space-like, $q_\mu q^\mu < 0$ or time-like $q_\mu q^\mu > 0$.

- Four velocity.
  (The 3-velocity is $\vec{v} \equiv \vec{p}/p^0$.) The 4-velocity is a unit vector which points in the direction of the motion. It is a *time-like* unit vector:

$$u^\mu u_\mu = +1, \tag{2.3}$$

$$u^\mu = (\gamma, \gamma\vec{v}), \quad \text{and} \quad u_\mu = (\gamma, -\gamma\vec{v}), \tag{2.4}$$

  where $\gamma = 1/\sqrt{1 - \vec{v}^{\,2}}$. This velocity 4-vector is normalized, i.e. $u^\mu u_\mu = \gamma^2(1 - \vec{v}^{\,2}) = +1$. The proper time of an object moving with 4-velocity u^μ is $\tau = t/\gamma$.

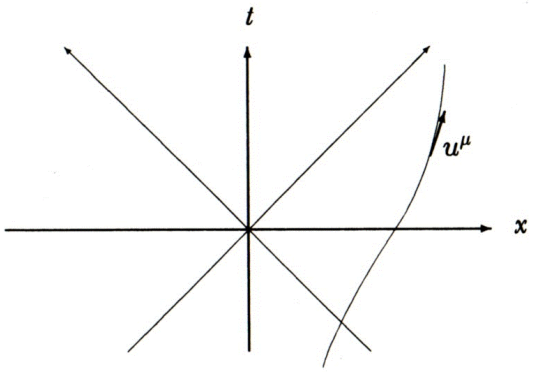

Figure 2.2: u^μ is tangent to the world-line. This means that $u^\mu = dx^\mu/d\tau$. Reproduced by permission of World Scientific Publishing Co. from [2].

- World-line of a particle in space-time is illustrated in Fig. 2.2.

  For a *space-like* unit four vector Λ^μ: $\Lambda^\mu\Lambda_\mu = -1$, while for a *time-like* unit vector Ω^μ : $\Omega^\mu\Omega_\mu = +1$. Space-like and time-like vectors cannot be transformed into each other by a proper Lorentz-Transformation!

- Coordinate system.
  In particle and nuclear physics it is practical to introduce a special coordinate system, where the spatial z-axis is parallel to the beam of the accelerator. In general, not exactly central (not head on) collisions, the 3-vector connecting the centers of a beam particle and a target particle points out an other direction. The component of this vector orthogonal to the beam is the impact vector $\vec{b}$, which is a two dimensional vector. The direction of this vector is denoted usually as the x direction. These two axes, x and z, span the so called reaction plane of a given collision $[x, z]$. See Fig. 2.3.

- Rapidity.
  The rapidity is a generalization of the velocity. The definition of rapidity is:

$$y \equiv \operatorname{arcth} v_\parallel = \operatorname{arcth} \frac{p_\parallel}{p^0} = \frac{1}{2} \ln \frac{p^0 + p_\parallel}{p^0 - p_\parallel} \tag{2.5}$$

  This definition uses the components of vectors $\vec{v}$ and $\vec{p}$ that are parallel to the particle beam of the accelerator. This implies that we use a special coordinate system.

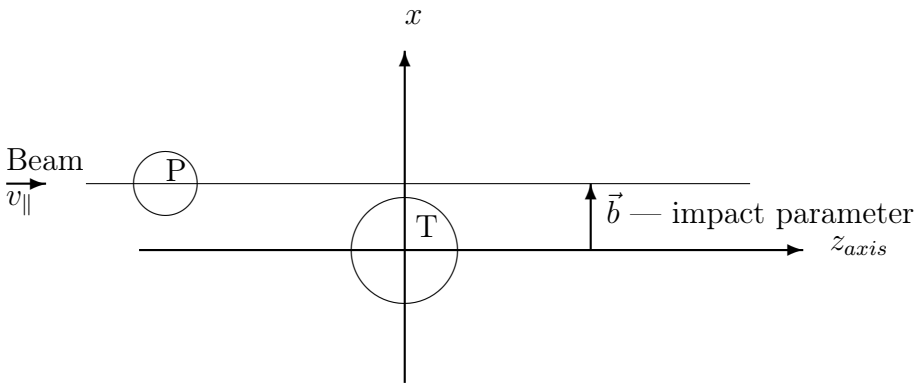

Figure 2.3: The z component of a vector is also denoted as its parallel, ($\parallel$), component. Thus, any vector (three-vector) can be decomposed as: $\vec{v} = (v_\parallel, \vec{v}_\perp)$. Here $\vec{v}_\perp$ is a two-vector which can rotate in the *azimuthal* (ϕ) direction. Reproduced by permission of World Scientific Publishing Co. from [2].

2.1.2 Properties of the rapidity

For small velocities: $y \approx v_\parallel$. If a particle is moving after the collision into some direction $\vec{v}$ it is customary to give its phase space position by the coordinates $(y, \vec{p}_\perp/m)$. Thus the momentum vector can also be decomposed in this coordinate system as $p^\mu = (p^0, p_\parallel, \vec{p}_\perp)$. The limit of rapidity coordinates for non-relativistic velocities: $(y, \vec{p}_\perp/m) \longrightarrow (v_\parallel, \vec{v}_\perp)$. While the velocity is limited to 1 (c), the rapidity y may vary between $(-\infty, \infty)$. See Fig. 2.4

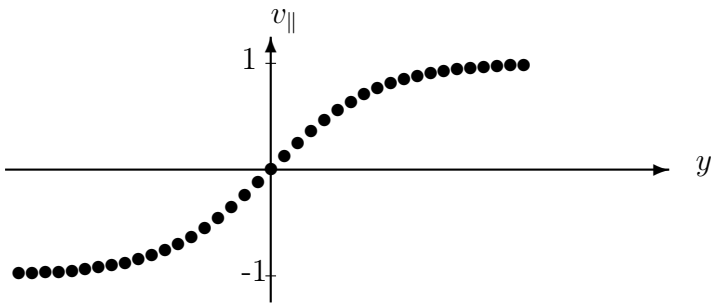

Figure 2.4: The beam-parallel component of the velocity as function of the rapidity y. Reproduced by permission of World Scientific Publishing Co. from [2].

Lorentz transformation properties of rapidity:
If y_1 is the rapidity of a particle in frame K_1, and y_2 is the rapidity of frame K_1 in frame K_2, *then*: $y = y_1 + y_2$ is the rapidity of the particle in frame K_2. Assignment No. 2.a is to prove this.

Assignment No. 2 also includes the definitions of further important quantities like the transverse mass, the pseudo-rapidity and the light-cone variables!

E_{Lab} [AGeV]	p^0 [GeV]	$\mid \vec{p} \mid$ [GeV/c]	Δy -	v [c]	Place -
0.1	1.03	0.445	0.458	0.428	MSU-K800
0.5	1.44	1.09	0.99	0.758	LBL-BEVALAC
1.0	1.94	1.69	1.35	0.875	LBL-BEVALAC
2.0	2.94	2.78	1.81	0.947	LBL-BEVALAC
4.1	5.04	4.95	2.36	0.982	DUBNA
10	-	-	3.06	-	BNL-AGS
14	-	-	3.4	-	BNL-AGS
60	-	-	4.9	-	CERN-SPS
200	-	-	6.0	-	CERN-SPS
1800 (30+30)	-	-	8.2	-	BNL-RHIC*
(100+100)	-	-	10.7	-	BNL-RHIC*
(900+900)	-	-	15.1	-	$(p\bar{p})$ FNAL-Tevatron*
(3500+3500)	-	-	17.8	-	CERN-LHC*
(8TeV+8TeV)	-	-	19.5	-	(pp) CERN-LHC*
(20TeV+20TeV)	-	-	21.2	-	(pp) SSC*

*planned

Table 2.1: Typical rapidities and beam energies of some proton or heavy ion accelerators. The planned accelerators are colliders. At higher energies, $E_{Lab} \gg m_p$, the velocity tends to the velocity of light, and p^0 and $|\vec{p}|$ approach each other.

2.1.3 Some typical rapidities

Here we give some examples for nucleons ($m = 0.939$GeV). The beam energies for some accelerators are given in Table 2.1. In case of colliders the energies of both beams are given separately as 30+30 AGeV.

2.2 Basic definitions of macroscopic quantities

Here we introduce some of the elementary macroscopic quantities and their definitions within the kinetic theory. Several essential macroscopic quantities are presented in the subsequent sections.

(i) Local density $\mathsf{n} = \mathsf{n}(\vec{r}, t) = \mathsf{n}(x)$ as a function of the space time coordinate x $(\equiv x^{\mu})$; $(N = \mathsf{n}\ \Delta^3 x)$. So this density n is not an invariant scalar because the 3-volume element, $\Delta^3 x$, is not invariant under Lorentz transformation. The total number of particles in a fixed volume element, N, is obviously independent of the reference frame, so it is an invariant scalar.

EXAMPLE: DENSITY (Fig. 2.5).

Density profile of a nucleus at rest
$\mathsf{n}(r)$, $\mathsf{n}_0 = 0.145/fm^3$
$(1\ fm\ =\ 1\ F\ =\ 1\ fermi\ =\ 10^{-13}\ cm)$
$(10\ mbarn\ = 1\ fermi^2\ )$
$R \approx\ 7\ fm$, for Pb.

The nucleus at rest is characterized by this density profile where the bulk of the matter is at density n_0 except the relatively narrow surface region.

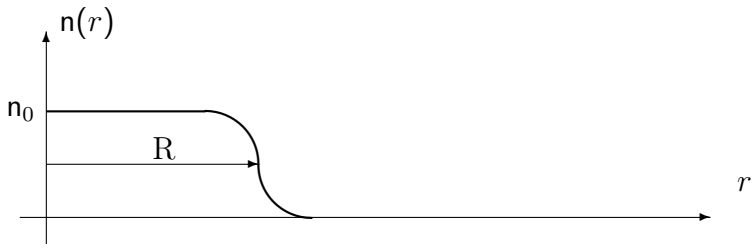

Figure 2.5: Schematic density profile of a large nucleus of radius R and central density n_0

(ii) Local particle flow $\vec{j} = \vec{j}(\vec{r}, t) = \vec{j}(x)$, i.e.: particle current across unit area in unit time.

EXAMPLE: FLOW (Fig. 2.6).

The current $\vec{j}$, depends on $(\vec{r}, t)$.

When two equal size nuclei collide in their center of mass system the currents are directed along the beam (z-axis) and they are opposite to each other in the projectile and target regions. In the overlap region (hatched area) the two currents cancel each other and the resulting current vanishes (if sidewards flow and squeeze out of the matter are neglected).

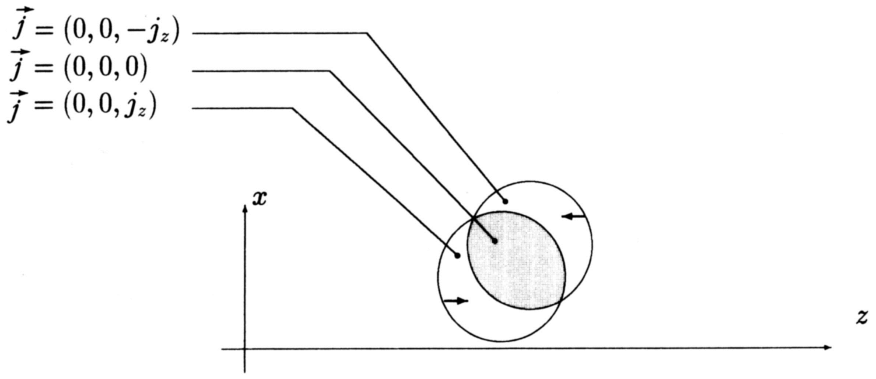

Figure 2.6: Baryon currents in different spatial regions of a heavy ion collision in the center of mass (c.m.) system.

(iii) Particle four flow. From the above two quantities we can formally create a 4-vector. At this stage we do not know its transformation properties yet.

$$N^\mu(x) = (\mathsf{n}(x), \vec{j}(x)) \tag{2.6}$$

(iv) Particle distribution, f, in μ-space, i.e. in the 6-dimensional (x, p)-space

It gives the number of particles, N, in a phase space volume element:

$$f(x,p) \ : \quad N = f(x,p)\ \Delta^3 x\ \Delta^3 p. \tag{2.7}$$

EXAMPLE $f(x, p)$ (Fig. 2.7).

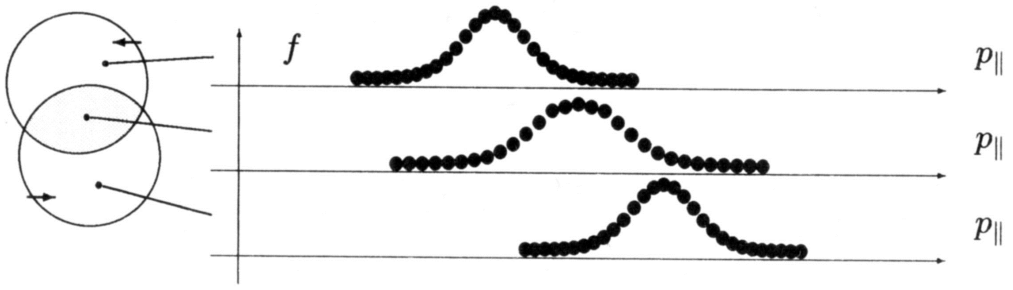

Figure 2.7: Longitudinal component of the momentum distribution in different spatial regions of a heavy ion collision. Reproduced by permission of World Scientific Publishing Co. from [2].

In a given reference frame the density and current can be expressed in terms of the distribution function:

$$\mathsf{n}(x) = \int d^3p\, f(x,p), \tag{2.8}$$

$$\vec{j}(x) = \int d^3p\, \vec{v}\, f(x,p). \tag{2.9}$$

It is not trivial to see what the transformation properties of these quantities are. We know, however, that $\vec{v} = \vec{p}/p^0$, so the above two equations can be united as $N^\mu(x) = (\mathsf{n}(x), \vec{j}(x))$

$$N^\mu(x) = \int \frac{d^3p}{p^0}\, p^\mu\, f(x,p). \tag{2.10}$$

Here p^μ is a 4-vector, so if we want N^μ to be a 4-vector also, then $f(x,p)$ times $\int \frac{d^3p}{p^0}$ should be an invariant scalar. As we will see later this is satisfied, because both of them are invariant scalars.

Aside:
Let us show that d^3p/p^0 is invariant scalar: In four dimensional p^μ space (p^0, p^1,-p^2, p^3), $(d^3p)^\mu$ is the normal four vector of a surface element (of a 3-dimensional hypersurface in 4-space) for which the constraint $p^\mu p_\mu = m^2$ is satisfied and it is centered at some point p^μ. This hypersurface element is then represented by its normal vector (4-vector). It is pointing into the direction of p^μ.

2-dim. hypersurface in a 3-dim space $\longrightarrow$
Sphere with constant
radius: $p^\mu p_\mu = m^2$.

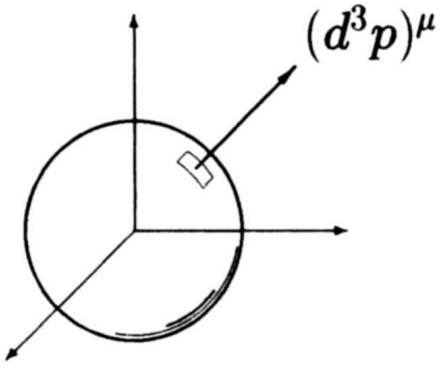

We can visualize the invariance of the phase space volume element as follows: d^3p is the 0th component of the normal vector, $(d^3p)^\mu$. If we divide it by the 0th component of another 4-vector p^μ parallel to it, then the ratio is an invariant scalar :d^3p/p^0.

Strictly we can see this in the following way:

$$\int 2\delta(p^\mu p_\mu - m^2)\Theta(p^0)\, d^4p = \int_{-\infty}^{\infty} dp^3 \int_{-\infty}^{\infty} dp^2 \int_{-\infty}^{\infty} dp^1 \int_{-\infty}^{\infty} dp^0 2\delta(p^\mu p_\mu - m^2)\Theta(p^0) \quad (2.11)$$

Using

$$\delta[\phi(x)] = \sum_i \frac{1}{\mid \phi'(a_i) \mid}\delta(x - a_i), \quad (2.12)$$

where a_i is the root of $\phi(x)$, (i.e. $\phi(a_i) = 0$), we can cast the δ-function in the form $\delta(p^\mu p_\mu - m^2) = \delta((p^0)^2 - (\vec{p})^2 - m^2) = \delta((p^0)^2 - \varepsilon^2) = \frac{1}{2\varepsilon}\,[\delta(p^0 - \varepsilon) + \delta(p^0 + \varepsilon)]$ where $\varepsilon = \sqrt{(\vec{p})^2 + m^2}$. Thus:

$$\int_{-\infty}^{\infty} 2\,\frac{1}{2\varepsilon}\,[\delta(p^0 - \varepsilon) + \delta(p^0 + \varepsilon)]\Theta(p^0)\, dp^0 = \frac{1}{\varepsilon} = \frac{1}{p^0(\vec{p})}, \quad (2.13)$$

where $p^0(\vec{p}) = \varepsilon = \sqrt{(\vec{p})^2 + m^2}$ and

$$\Theta(p^0) = \begin{cases} 1: & \text{if} p^0 \geq 0 \\ 0: & \text{if} p^0 < 0 \end{cases}$$

Therefore

$$N^\mu(x) = \int d^4p\; 2\; \delta(p^2 - m^2)p^\mu f(x,p)\; \Theta(p^0) = \int \frac{d^3p}{p^0}\; p^\mu\; f(x,p), \quad (2.14)$$

where $\Theta(p^0)$ is the step function. Conclusion: $f(x,p)$ is an invariant scalar, and consequently N^μ is a contravariant 4-vector. Furthermore $\mathsf{n}(x)$ and $\vec{j}(x)$ are transformed as components of a 4-vector.

The other macroscopic quantities are more involved. They will be introduced via the distribution function $f(x,p)$ in sections (2.3-4).

2.3 Energy-momentum tensor

The energy-momentum tensor is another macroscopic quantity characterizing the matter (see ref. [3]). $T^{00}(x)$ is the energy density. Since the energy of a particle is p^0 in the kinetic theory

$$T^{00}(x) = \int d^3p\, p^0\, f(x,p) \tag{2.15}$$

The energy flow is: cT^{0i}.
The momentum density: $\frac{1}{c}T^{i0}, \quad (i = 1,2,3)$.
These can be expressed by the distribution function $f(x,p)$:

$$\begin{array}{rcll} T^{0i} & = & \int d^3p\, p^0\, v^i\, f(x,p) & : \text{ energy flow,} \\ T^{i0} & = & \int d^3p\, p^i\, f(x,p) & : \text{ momentum density.} \end{array} \tag{2.16}$$

where v^i is the i^{th}-component of the flow 3-velocity. The momentum flow tensor or pressure tensor can be written as:

$$T^{ik} = \int d^3p\, p^i\, v^k\, f(x,p) \tag{2.17}$$

All these can be combined into the form (by using $\vec{v} = \vec{p}/p^0$):

$$\begin{array}{lcllll} T^{\mu\nu}(x) & = & \int \frac{d^3p}{p^0} & p^\mu p^\nu & f(x,p), \\ tensor & & scalar & tensor & scalar \end{array} \tag{2.18}$$

i.e. the energy-momentum tensor is the second moment of the distribution function $f(x,p)$. It is symmetric: $T^{\mu\nu} = T^{\nu\mu}$. This energy momentum tensor *does not* include fields and potential energy of the particles. Only the rest mass and the kinetic energy are included.

This energy momentum tensor includes the contribution of the particles with their kinetic energies. If for example they interact via electromagnetic fields the contribution of these fields should be added to the energy momentum tensor.

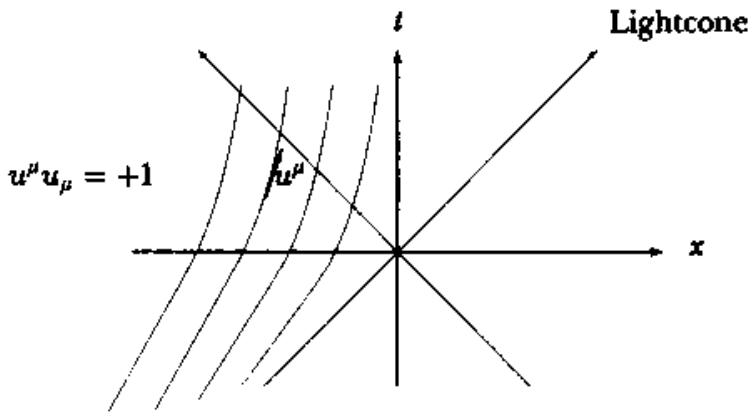

Figure 2.8: Flow velocity

2.3.1 Hydrodynamic flow

The flow velocity of a medium, u^μ, is a time-like unit vector parallel to the world-line of the particles (if there are particles in the matter, otherwise is parallel to the energy flow as we will see this later!), Fig. 2.8.

We define a projector, $\Delta^{\mu\nu}$, which projects a 4-vector into the plane (3-dimensional hypersurface) orthogonal to u^μ.

Aside:
Construct $\Delta^{\mu\nu}$ orthogonal projection to any time-like 4-vector u^μ. The unit vector parallel to u^μ is: $\frac{u^\mu}{(u^\mu u_\mu)^{1/2}}$. The projected length of any vector A^μ in this direction is $\frac{A_\mu u^\mu}{(u^\mu u_\mu)^{1/2}}$, and so the vector projection into the direction of u^μ is

$$\frac{A_\mu u^\mu}{(u^\mu u_\mu)^{1/2}} \times \frac{u^\tau}{(u^\tau u_\tau)^{1/2}}. \tag{2.19}$$

We have to subtract this from the total A^μ in order to get the orthogonal projection. Thus the orthogonal projector is:

$$\Delta^{\mu\nu} \equiv g^{\mu\nu} - \frac{u^\mu u^\nu}{(u^\nu u_\nu)}. \tag{2.20}$$

The projector acting on the flow velocity thus yields: $\Delta^{\mu\nu} u_\mu = 0$.

2.3.2 Local Rest frame: (LR)

This is the reference frame where $u^\mu = u^\mu_{(LR)} = (1,0,0,0)$. Since u^μ is time-like there is always a Lorentz transformation which leads to the Local Rest frame (LR). In this frame:

$$\Delta^{\mu\nu}_{(LR)} = \Delta_{\mu\nu\ (LR)} = diag\ (0,-1,-1,-1), \tag{2.21}$$

and

$$\Delta^{\mu}_{\nu\ (LR)} = diag\ (0,1,1,1). \tag{2.22}$$

How do we find the Local Rest frame? There are two usual ways!

Eckart's Definition

According to this definition the Local Rest frame is tied to conserved particles, or conserved charges like baryon charge (if there are any!) We know the particle 4-flow

$$N^\mu = \int \frac{d^3p}{p^0}\, p^\mu\ f(x,p), \tag{2.23}$$

so a unit vector in this direction is

$$u^\mu = \frac{N^\mu}{(N^\nu N_\nu)^{1/2}}. \quad (\mathsf{Eckart}) \tag{2.24}$$

If we decompose the four components of the flow velocity: $u^\mu = (\gamma, \gamma\vec{v})$, we can see that the 3-vector of the flow velocity, $\vec{v}$, is parallel to the particle current, $\vec{j}$, according to Eckart's definition. N^μ is always a time-like 4-vector. Consequently, if we use Eckart's definition, there is no particle flow in LR in the spatial directions

$$N^i_{(LR)} = 0; \quad i = 1,2,3. \quad (\mathsf{Eckart}) \tag{2.25}$$

In other form this definition means that $\Delta_{\mu\nu}N^\mu = 0$. This definition is not very suitable for ultra-relativistic heavy ion reactions or for the early universe where radiation energy density is high, and the baryon density is low or zero. If the baryon density is approaching zero the flow velocity, eq. (2.24), becomes ill defined because the mass or energy flow becomes independent of the vanishing particle flow. It is also interesting to mention that a coherent flow of particles and antiparticles would yield vanishing flow according to Eckart's definition.

Landau's definition

According to this definition the LR is tied to energy flow: in the LR frame the spatial component of the energy flow and the momentum density should vanish:

$$T^{0i}_{(LR)} = T^{i0}_{(LR)} = 0; \quad i = 1, 2, 3. \quad (\mathsf{Landau}). \tag{2.26}$$

Since the energy-flow 4-vector is $T^{\mu\nu}u_\nu$ and this should be parallel to u^μ according to eq.(2.20), consequently

$$\Delta_{\sigma\mu}T^{\mu\nu}u_\nu = 0 \quad (\mathsf{Landau}) \tag{2.27}$$

This definition is hardly usable (because u^μ is implicit), but it shows that u^μ is the normalized eigenvector of $T^{\mu\nu}$, since $T^{\mu\nu}u_\nu$ is parallel to u^μ. Consequently:

$$u^\mu = \text{constant} \times T^{\mu\nu}u_\nu \tag{2.28}$$

where from the normalization of u^μ the constant $(u_\rho T^{\rho\nu}u_\nu)^{-1}$.

2.3.3 Other macroscopic quantities

We can now introduce covariant macroscopic quantities.

(i) Invariant scalar density n:

$$n \equiv N^\mu u_\mu, \tag{2.29}$$

is the density in the local rest frame.

$$n = N^0_{(LR)}. \tag{2.30}$$

The previously introduced n was not an invariant scalar, it is equal to n only if we are in the local rest frame.

(ii) Invariant scalar energy density e:

$$e \equiv u_\mu T^{\mu\nu} u_\nu, \tag{2.31}$$

so that in the local rest frame

$$e = T^{00}_{(LR)}. \tag{2.32}$$

In the literature the notation ϵ for the energy density is frequently used ($\epsilon = e$). We should, however, note that the specific energy is $\varepsilon = e/n = \epsilon/n$.

(iii) Pressure tensor $P^{\mu\nu}$:

$$P^{\mu\nu} \equiv \Delta^\mu_\sigma T^{\sigma\tau} \Delta^\nu_\tau \tag{2.33}$$

so that $P^{00}_{(LR)} = P^{i0}_{(LR)} = P^{0i}_{(LR)} = 0$, and $P^{ij}_{(LR)} = T^{ij}_{(LR)}$ for $i, j = 1, 2, 3$.

We will see later that $P^{\mu\nu}$ can be split up into two parts:

$$\begin{array}{rcllll} P^{\mu\nu} & = & -P\Delta^{\mu\nu} & + & \Pi^{\mu\nu}, \\ & & \textit{hydrostatic} & & \textit{viscous} \\ & & \textit{pressure} & & \textit{stress} \\ & & \textit{tensor} & & \textit{tensor} \end{array} \tag{2.34}$$

where P is the hydrostatic pressure.

(iv) Heat flow:

$$\begin{array}{rllllll} I^\mu_q \equiv & [u_\nu T^{\nu\sigma} & - & (\frac{e+P}{n}) & N^\sigma] & \times & \Delta^\mu_\sigma \\ & \textit{energy} & & \textit{enthalpy} & \textit{particle} & & \\ & 4-\textit{current} & & \textit{per} & \textit{current} & & \\ & \textit{vector} & & \textit{particle} & \textit{vector} & & \end{array} \tag{2.35}$$

The enthalpy per particle or specific enthalpy is denoted sometimes by h, sometimes by w in the literature, $h = w = e + P$. In the local rest frame the heat flow has spatial components only

$$I^0_{q\ (LR)} = 0; \quad I^i_{q\ (LR)} = T^{0i}_{(LR)} - \left(\frac{w}{n}\right) N^i_{(LR)}, \tag{2.36}$$

the covariant expression is:

$$I_q^\mu u_\mu = 0, \tag{2.37}$$

i.e. the heat flow, I_q^μ, and the four velocity, u^μ, are orthogonal! Definition (2.35) is rather complicated if, however, we choose one of the above mentioned usual definitions of the flow velocity the definition of the heat flow will be greatly simplified as we will see it below.

Special cases

Eckart's definition $(\Delta_\sigma^\mu N_\mu = 0)$:

$$I_q^\mu = u_\nu T^{\nu\sigma} \Delta_\sigma^\mu, \tag{2.38}$$

Landau's definition $(u_\mu T^{\mu\nu} \Delta_\nu^\sigma = 0)$:

$$I_q^\mu = -(\frac{e+P}{n}) N^\sigma \Delta_\sigma^\mu, \tag{2.39}$$

If the particle distribution, $f(x,p)$, is known from kinetic theory (see the next Chapter), $T^{\mu\nu}$, and N^ν can be evaluated and both the static matter properties like the hydrostatic pressure, P, and the energy density, e, as well as the transport properties like the viscous stress tensor, $\Pi^{\mu\nu}$, and the heat flow, I_q^μ can be obtained. For small deviations from static equilibrium the transport properties can be approximated as linearly dependent on the changes of flow velocity and temperature. In these cases the non-static matter can be characterized by *transport coefficients* like the shear and bulk viscosity, η, and ζ, and the heat conductivity, κ. We do not evaluate η, ζ, κ or $\Pi^{\mu\nu}$, and I_q^μ in terms of these transport coefficients here, but for some situations the calculation of these quantities is presented in refs. [1, 4] and in the current literature.

2.3.4 Decomposition of the energy-momentum tensor

Previously we have defined $T^{\mu\nu}$ and N^{μ} based on microscopic quantities. We have used analogies to usual definitions od baryon and energy density in constructing these variables. If, on the other hand, $T^{\mu\nu}$ and N^{μ} are known the energy and baryon density can be obtained in a straightforward way.

Let us divide the energy momentum tensor into a reversible and an irreversible (dissipative) part.

$$\begin{array}{lll} T^{\mu\nu} = & T^{\mu\nu\ (0)} & + \quad T^{\mu\nu\ (1)} \\ & reversible, & \quad irreversible \\ & part & \quad (dissipative)\ part \end{array} \tag{2.40}$$

where

$$T^{\mu\nu\ (0)} = eu^{\mu}u^{\nu} - P\Delta^{\mu\nu} = (e+P)u^{\mu}u^{\nu} - Pg^{\mu\nu}, \tag{2.41}$$

which in the Local Rest frame yields

$$T^{\mu\nu\ (0)}_{(LR)} = \begin{pmatrix} e & 0 & 0 & 0 \\ 0 & P & 0 & 0 \\ 0 & 0 & P & 0 \\ 0 & 0 & 0 & P \end{pmatrix}. \tag{2.42}$$

The dissipative part is then

$$T^{\mu\nu\ (1)} = \left[\underbrace{\left(I_q^{\mu} + (\frac{e+P}{n}) N^{\sigma}\Delta_{\sigma}^{\mu} \right)}_{\equiv Q^{\mu}} u^{\nu} + \underbrace{\left(I_q^{\nu} + (\frac{e+P}{n}) N^{\sigma}\Delta_{\sigma}^{\nu} \right)}_{\equiv Q^{\nu}} u^{\mu} \right] + \Pi^{\mu\nu} \tag{2.43}$$

Similarly the particle four flow can also be divided into two parts

$$N^{\mu} \quad = \quad N^{\mu\ (0)} + N^{\mu\ (1)} \quad = \quad n\ u^{\mu} - \frac{n}{w} I_q^{\mu}\ . \tag{2.44}$$

If $T^{\mu\nu}$ and u^{μ} are given this decomposition can be constructed by using the equations below:

$$e \equiv u_{\mu}T^{\mu\nu}u_{\nu} \tag{2.45}$$

$$-P\Delta^{\mu\nu} + \Pi^{\mu\nu} \equiv \Delta^{\mu}_{\sigma}T^{\sigma\tau}\Delta^{\nu}_{\tau} \tag{2.46}$$

$$Q^{\mu} \equiv u_{\nu}T^{\nu\sigma}\Delta^{\mu}_{\sigma} \tag{2.47}$$

Special cases The (1) component of the energy-momentum tensor takes the simple forms if we use one of the definitions below.

(Landau):

$$T^{\mu\nu\ (1)} = \Pi^{\mu\nu} \qquad N^{\mu\ (1)} = -\frac{n}{w} I_q^{\mu}\ . \tag{2.48}$$

(Eckart):

$$T^{\mu\nu\ (1)} = I_q^{\mu}u^{\nu} + I_q^{\nu}u^{\mu} + \Pi^{\mu\nu} \qquad N^{\mu\ (1)} = 0\ . \tag{2.49}$$

2.4 Jüttner distribution

A question frequently asked is how can $f(x,p)$ be an invariant scalar if the volume element, $\Delta^3 x$, is Lorentz contracted? Yes, $\Delta^3 x$, is Lorentz contracted indeed, but the momentum space, $\Delta^3 p$, is Lorentz elongated! To see this we introduce the "Relativistic Boltzmann", or "Jüttner" distribution function (See refs. [5, 6]):

$$f^{Juttner}(p) = \frac{1}{(2\pi\hbar)^3} \exp\left(\frac{\mu - p^\mu u_\mu}{T}\right), \tag{2.50}$$

In this definition μ is the chemical potential and it should not be mistaken for the covariant and contravariant summation indices, which are also denoted by μ! Since in the (LR) $u^\mu_{(LR)} = (1,0,0,0)$ it follows that $(p^\mu u_\mu)_{(LR)} = p^0 = E$, and since $p^\mu u_\mu$ is an invariant scalar it is the same in all reference frames. Thus $f^{Juttner}(p)$ is the distribution of particle momenta, p^μ, in a thermal system, which is moving with velocity u^μ, has a chemical potential μ, and temperature parameter T. We will see later that these parameters correspond to the usual thermodynamical state variables. Note our convention that the Boltzmann constant is unity, $k = 1$.

2.4.1 Normalization

If we know the invariant scalar density

$$n = N^\mu u_\mu = u_\mu \int \frac{d^3p}{p^0} p^\mu f(x,p) = \int \frac{d^3p}{p^0} p^\mu u_\mu \; e^{\left(-\frac{p^\mu u_\mu}{T}\right)} \frac{e^{\mu/T}}{(2\pi\hbar)^3}, \tag{2.51}$$

we may determine the chemical potential μ. Since n is an invariant scalar it can be evaluated in any frame (n = const.). In the (LR), $u^\mu = (1,0,0,0)$, so

$$n = \frac{e^{\mu/T}}{(2\pi\hbar)^3} \int \frac{d^3p}{p^0}\, p^0 \; e^{-p^0/T} = \frac{e^{\mu/T}}{(2\pi\hbar)^3} 4\pi \int_0^\infty dp \; (\vec{p})^2 \; e^{-\frac{\sqrt{m^2+\vec{p}^2}}{T}}. \tag{2.52}$$

Let us introduce $\tau = \frac{1}{T}\sqrt{m^2+\vec{p}^2}$, $d\tau = \frac{1}{T}\frac{|\vec{p}|}{\sqrt{m^2+\vec{p}^2}} dp$ and $p^2 = T^2\tau^2 - m^2$, then

$$n = \frac{4\pi \; e^{\mu/T}}{(2\pi\hbar)^3} T^3 \int_{m/T}^\infty d\tau \; \tau\sqrt{\tau^2 - \left(\frac{m}{T}\right)^2} e^{-\tau} = \frac{e^{\mu/T}}{(2\pi\hbar)^3} 4\pi m^2 T \; K_2(\frac{m}{T}), \tag{2.53}$$

where K_2 is the Modified Bessel function of the second kind (see ref. [7]). This relation gives a connection between the chemical potential, μ, and the density, n.

2.4.2 Transformation properties of f(x,p).

In the configuration space

First let us see the relatively well known Lorentz contraction. This indicates that a fast moving object seems to be shorter to a stationary observer than the same object when it is standing still in the reference frame of the observer. The distribution function has a spatial component, and this should exhibit the above Lorentz contraction. For now we want to disregard the momentum dependence of our distribution function. This can be done in two ways: Either we can assume that $f(x,p)$ is constant as a function of p (i.e. "homogeneous in p"), or we can integrate it over the momentum space $\mathsf{n}(x) = \int d^3p\ f(x,p)$. In both cases we will have a distribution function in the configuration space, $\mathsf{n} = \mathsf{n}(x)$, which is independent of p. Figure 2.9 illustrate the transformation properties of a distribution function in the configuration space.

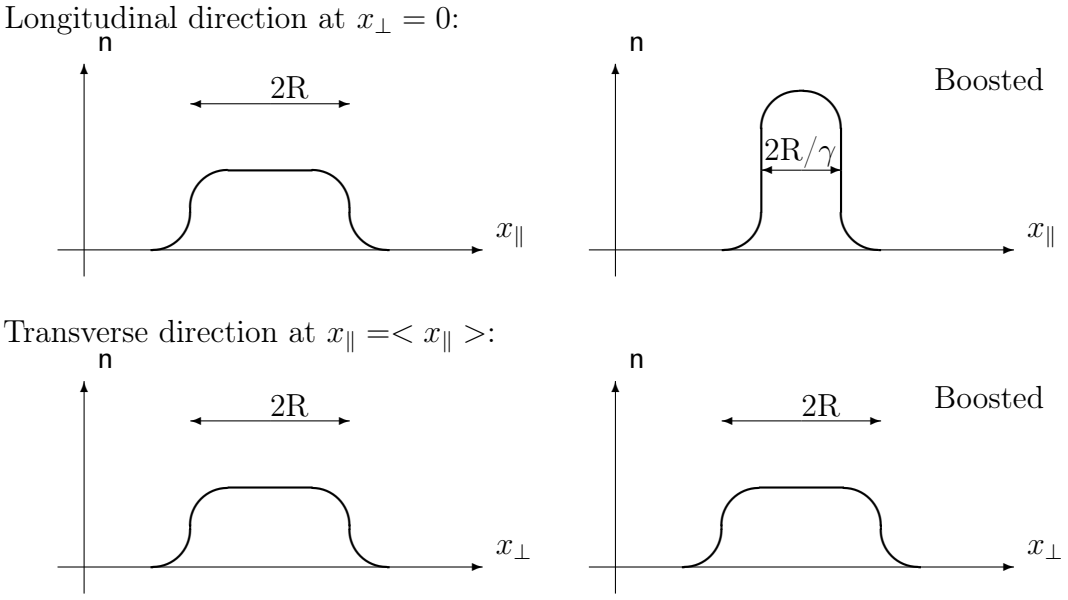

Figure 2.9: Lorentz transformation in the configuration (x) space. Reproduced by permission of World Scientific Publishing Co. from [2].

In the momentum space:

Let us assume that the distribution is uniform in x or integrate the distribution over the whole configuration space. For the latter case assume $f(x,p) = const. \times e^{\left(-\frac{p^\mu u_\mu}{T}\right)}$, where $u^\mu = (\gamma, \gamma v_\parallel, 0, 0)$. This results

$$p^\mu u_\mu = p^0\gamma - p_\parallel \gamma v_\parallel = (\sqrt{m^2 + (\vec{p}_\perp)^2 + (p_\parallel)^2} - p_\parallel v_\parallel)/\sqrt{1-(v_\parallel)^2}. \tag{2.54}$$

So the momentum distribution, $F(p) = \int d^3x f(x,p) = const. \times e^{\left(-\frac{p^\mu u_\mu}{T}\right)}$, can be plotted for $m = 1$ GeV, $T = 0.1$ GeV at $p_\perp = 0$, for different velocities, $v_\parallel = 0,\ 0.5,\ 0.9$. Figure 2.10.

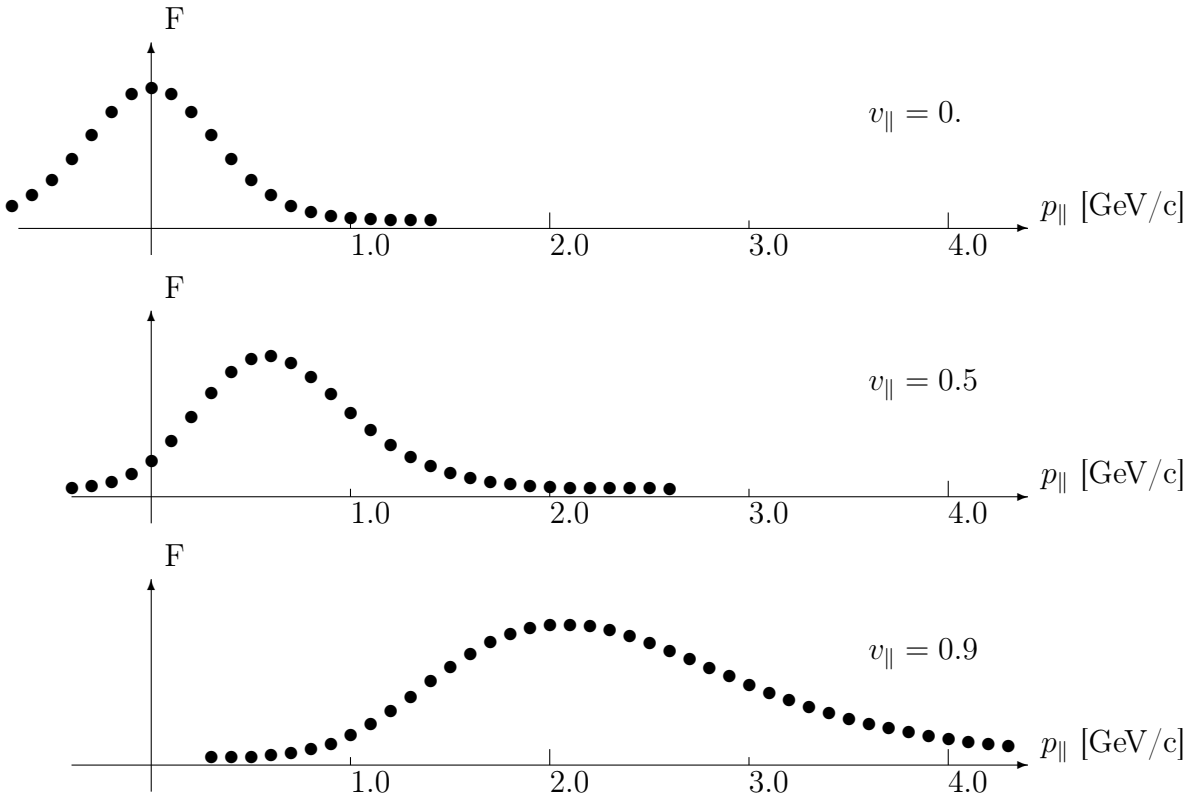

Figure 2.10: Longitudinal momentum distributions Lorentz-boosted with velocity, $v_\parallel$. The boosted distribution is not symmetric! This is due to the fact that the width of the original distribution is not negligible compared to the boost. Reproduced by permission of World Scientific Publishing Co. from [2].

The constant in front of the exponential does not depend on the boost velocity and it is the same in all cases.

2.5 Mixtures

We have introduced the flow velocity for a medium, but in non-equilibrium systems there can be problems, and it may happen that the introduction of a flow velocity is not possible or at least not practical because it does not reflect the essential physical features of our system.

Examples:

- In heavy ion reactions at high energies it is possible that the target and projectile nuclei penetrate somewhat into each other before the collisions among the nucleons will slow down the incoming matter. If the random velocities of nuclei (due to the Fermi motion) are much smaller than the relative velocity of the projectile with respect to the target in the overlap region the local momentum distribution may be very far from any thermalized distribution.

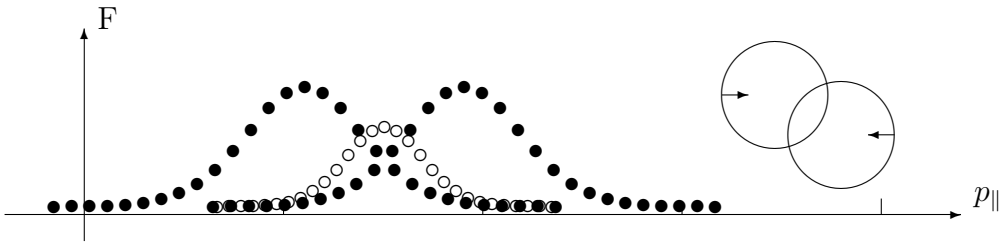

  If x is in the overlap region the distribution is $f(x,p) = f_{Projectile}(x,p) + f_{Target}(x,p) + f_{Therm.}(x,p)$, and the total distribution function may have two peaks in momentum space. This makes it somewhat unphysical to introduce one single flow velocity although it is possible. Later on during the reaction the distributions approach each other and a united thermalized momentum distribution develops where the original Target and Projectile nucleons cannot be separated any more. This situation is usually handled by introducing more fluid components (see e.g. ref. [8]).

- In Electron-Ion plasmas in TOKAMAK's the situation is somewhat similar. The two plasmas show different temperatures and move with different velocities due to external electric and magnetic fields. Unlike the previous example here the two components never get thermalized with each other. The two fluid dynamics (or magneto hydrodynamics) is a well known theoretical method in this field.

- The introduction of more fluid components is not new in nuclear physics either.In a classical collective excitation of nuclei, protons and neutrons oscillate against each other. This is the well known Giant Dipole Resonance. In the *Jensen-Steinwedel* model [9] this resonance is described by a two component distribution function, i.e. one for the protons $f_p(x,p)$, and one for the neutrons $f_n(x,p)$.

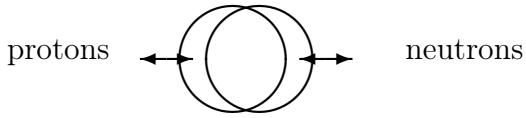

- Nucleons and light fragments at the final stage of a Relativistic Heavy Ion Collision (RHIC) may also be considered as two components. It is usually assumed that before the breakup they are all in thermal and chemical equilibrium. Temperature measurements rely on this assumption! This assumption is, however, not true, it should only be considered as an approximation. Different fragments, and the single nucleons may have very different temperatures, and the internal temperature of the fragments may also differ from the temperature exhibited by the kinetic energies. These differences are due to the relatively fast breakup process compared to the microscopic processes which act in the direction of thermalization.

- Another example may be two coexisting phases in a gas or a fluid. The kinetic motion in this case is usually thermalized due to the enhanced cross sections at the phase transition. Thus the assumption of a common flow velocity and temperature is usually a reasonable approximation for phase mixtures. The chemical potential may, however, be different in the two phases because inelastic reactions converting one phase into another are less frequent. Consequently a two component nonequilibrium mixture may characterize such matter adequately.

In kinetic theory a mixture of several components may be described similarly to the theory we introduced for the one particle component above.

The distribution function of more (N) components is denoted as:

$$f_k(x, p_k) \qquad\qquad k = 1, 2, 3, ..., N \tag{2.55}$$

The rest masses of the components may be different: $p_k^\mu p_{\mu k} = m_k^2$.

The four flow of component k is

$$N_k^\mu = \int \frac{d^3 p_k}{p_k^0} p_k^\mu f_k(x, p_k), \tag{2.56}$$

and similarly to the one component case the energy momentum tensor can be evaluated for the components separately

$$T_k^{\mu\nu} = \int \frac{d^3 p_k}{p_k^0} p_k^\mu p_k^\nu \; f_k(x, p_k). \tag{2.57}$$

Important: there is always one common flow velocity u^μ, although the component distributions may be centered around different velocities u_k^μ. This common flow velocity

can be connected to the total particle current or to the total energy momentum tensor:

$$N^\mu = \sum_{k=1}^{N} N_k^\mu, \tag{2.58}$$

$$T^{\mu\nu} = \sum_{k=1}^{N} T_k^{\mu\nu}. \tag{2.59}$$

If particles of a component are not conserved, but there is one (or more) conserved charge, q_k, (like baryon charge) carried by these particles we can introduce a total current for this charge:

$$Q_k^\mu = \int \frac{d^3p_k}{p_k^0} q_k \; p_k^\mu \; f_k(x, p_k), \qquad Q^\mu = \sum_{k=1}^{N} Q_k^\mu. \tag{2.60}$$

In mixtures one can define the scalar density as $n = \sum n_k$, and the concentrations as $x_k = n_k/n$, which satisfy $\sum x_k = 1$. Note that these are valid only if the flow velocities of the components are the same or if n_k is defined as $n_k \equiv N_k^\mu u_\mu$ and not via the component velocities u_k^μ. If the components have different flow velocities we can introduce the diffusion current:

$$D_k^\mu \equiv N_k^\mu - x_k N^\mu \tag{2.61}$$

so that

$$\sum_{k=1}^{N} D_k^\mu = 0. \tag{2.62}$$

2.6 Assignment 2

Properties of the Rapidity

2.a Prove that the rapidity is additive under Lorentz transformation

2.b Show that the energy of a particle of rapidity, y, and transverse momentum, $p_\perp$, is $E(= p^0) = m_\perp \; \cosh(y)$, where $m_\perp$ is the transverse mass : $m_\perp = \sqrt{m^2 + p_\perp^2}$.

2.c Show that if $E \to \infty$ then $y \to \eta \; = \; \ln(\cot \frac{\Theta}{2})$ (pseudorapidity), where Θ is the polar angle of the emitted particle.

2.d Plot the contour lines belonging to $E = 2, 4, 8$ GeV/nucleon energy in the $[y, p_\perp/m]$ plane. $(m = 1 \; GeV)$.

Plot also the lines in the same plane, corresponding to constant polar angles $\Theta = 0^o, 30^o, 60^o, 90^o$.

2.6.1 Solutions to Assignment 2

2.a A Lorentz transformation into a frame moving with velocity $-u$ along the $z-$axis is:

$$v' = \frac{v+u}{1+vu}$$

Then the rapidity is:

$$y_i = \operatorname{arcth} v_i \quad or \quad v_i = \tanh y_i.$$

$$v' = \frac{\tanh y_v + \tanh y_u}{1 + \tanh y_v \tanh y_u} = \tanh(y_v + y_u).$$

Since $v' = \tanh y_{v'}$ it follows that $\tanh y_{v'} = \tanh(y_v + y_u)$. So in conclusion

$$y_{v'} = y_v + y_u.$$

Note that this goes in one direction only! (By definition the beam axis is selected!)

2.b According to the definition of the rapidity:

$$y = \operatorname{arcth} v_{\parallel} = \operatorname{arcth} \frac{p_{\parallel}}{p^0} = \operatorname{arcth} \frac{p_{\parallel}}{E}.$$

Using that

$$\operatorname{arcth} x = \frac{1}{2} \ln \frac{1+x}{1-x}$$

if ($|x| < 1$) we can write that

$$y = \frac{1}{2} \ln \frac{E + p_{\parallel}}{E - p_{\parallel}}.$$

Let us now define the light cone variables:

$$p^+ = E + p_{\parallel} \quad \textit{and} \quad p^- = E - p_{\parallel}.$$

It follows then

$$p^+ p^- = E^2 - p_{\parallel}^2 = m^2 + p_{\perp}^2 + p_{\parallel}^2 - p_{\parallel}^2 = m^2 + p_{\perp}^2 \equiv m_{\perp}^2.$$

This is the definition of the *transverse mass*, $m_{\perp}$. Then by using these (so called light-cone) variables

$$y = \frac{1}{2} \ln \frac{p^+}{p^-} = \frac{1}{2} \ln \frac{(p^+)^2}{p^+ \, p^-} = \frac{1}{2} \ln \frac{(p^+)^2}{m_{\perp}^2} = \ln \frac{p^+}{m_{\perp}} = -\ln \frac{p^-}{m_{\perp}}.$$

Inverting these last two equations

$$p^+ = m_{\perp} \, e^{+y}, \quad \textit{and} \quad p^- = m_{\perp} \, e^{-y}.$$

Summing up these two and dividing by 2:

$$p^0 \equiv E = m_{\perp} \cosh y,$$

$$p_{\parallel} = m_{\perp} \sinh y.$$

q.e.d.

2.c If $E \to \infty$ then $[m^2 + (\vec{p})^2] \to \infty$ so it follows that $p \to \infty$ (if $m \ll |\vec{p}|$). Thus if $E \to \infty$, it means that $E \to |\vec{p}| \to \infty$. So that

$$y \to \frac{1}{2} \ln \frac{|\vec{(}p)| + p_{\parallel}}{|\vec{(}p)| - p_{\parallel}} = \ln \left(\frac{1 + p_{\parallel}/|\vec{(}p)|}{1 - p_{\parallel}/|\vec{(}p)|} \right)^{1/2}$$

Since $\cos \Theta = p_{\parallel}/|\vec{(}p)|$, so we obtain the required relation

$$y \to \ln \sqrt{\frac{1 + \cos \Theta}{1 - \cos \Theta}} = \ln \left(\cot \frac{\Theta}{2} \right) \equiv \eta,$$

which is at the same time the definition of the *pseudo-rapidity*, η.

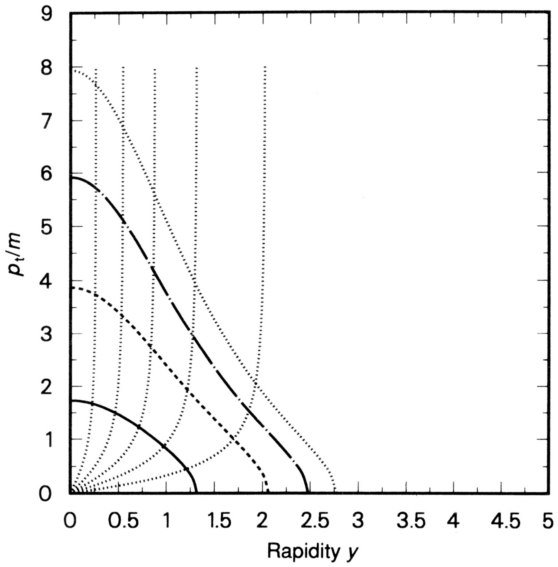

2.d

Figure 2.11: Constant angle (15^0, 30^0, 45^0, 60^0 and 75^0) and constant energy (E = 2, 4, 6, 8 GeV/nucl.) contour lines in the rapidity–transverse momentum plane

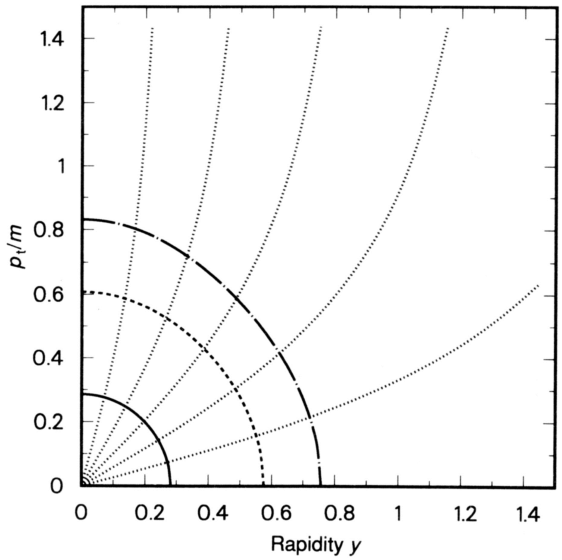

Figure 2.12: Constant angle and constant energy contour lines in the rapidity - transverse momentum plane at low energies

Bibliography

[1] S. R. de Groot, W. A. van Leeuwen and Ch. G. van Weert: Relativistic Kinetic Theory (North-Holland, Amsterdam 1980).

[2] L.P. Csernai and D. Strottman; in Relativistic Heavy Ion Physics Eds. L.P. Csernai and D.D. Strottman – Int. Rev. of Nucl. Phys. Vol. 5-6 (World Scientific, 1991) p. 1.

[3] L.D. Landau and E.M. Lifshitz: Classical Field Theory (Nauka, Moscow, 1973).

[4] K. Huang: Statistical Mechanics (Wiley, New York, 1963).

[5] F. Jüttner, Ann. Phys. und Chemie, **34** (1911) 856.

[6] I. Abonyi, Acta Phys. Hungarica, **23** (1967) 247.

[7] M. Abramovitz and I.A. Stegun: Handbook of Math. Functions (Dover, New York, 1968).

[8] L.P. Csernai, H.W. Barz and W. Greiner, Phys. Rev. **C26** (1982) 740.

[9] H. Steinwedel and J. H. D. Jensen, Z. Naturforschung, **5a** (1950) 413.

Chapter 3

Relativistic Boltzmann Transport Equation

The relativistic Boltzmann Transport Equation (BTE) describes the time evolution of the single particle distribution function $f(x,p)$. It is based on the following assumptions:

1. Only two-particle collisions are considered, the so called binary collisions.
2. "Stoßzahlansatz" or assumption of "Molecular Chaos": Number of binary collisions at x is proportional to $f(x,p_1) \times f(x,p_2)$.
3. $f(x,p)$ is a smoothly varying function compared to the mean free path (m.f.p.)

3.1 Particle conservation

The number of particles in a small 3-dimensional volume element around $\vec{x}$ at time t, $\Delta N(x)$, is identical to the number of world-lines crossing a 3-dimensional (time-like) hyper surface:

$$\Delta N(x) = \int_{\Delta^3\sigma} d^3\sigma_\mu \; N^\mu(x') = \int_{\Delta^3\sigma}\int_{\Delta^3 p} d^3\sigma_\mu \; \frac{d^3p}{p^0} \; p^\mu \; f(x',p). \tag{3.1}$$

Here $d^3\sigma_\mu$ is a time-like 4-vector, which is orthogonal to the surface $\Delta^3\sigma$. In the (LR) $d^3\sigma_\mu = (d^3x', 0, 0, 0)$. In the (LR) $\Delta N(x) = \int_{\Delta^3 x}\int_{\Delta^3 p} d^3x' \; d^3p \; f(x',p)$ is the number of world-lines crossing $\Delta^3\sigma$, with momenta in the range $\Delta^3 p$ around p.

If particles are conserved, the number of world-lines is constant, i.e. they cross both $\Delta^3\sigma$ and later $\Delta^3\sigma'$. (see Figure 3.1.) So

$$\int_{\Delta^3\sigma}\int_{\Delta^3 p} d^3\sigma_\mu \; \frac{d^3p}{p^0} \; p^\mu \; f(x',p) - \int_{\Delta^3\sigma'}\int_{\Delta^3 p} d^3\sigma_\mu \; \frac{d^3p}{p^0} \; p^\mu \; f(x',p) = 0. \tag{3.2}$$

Since the edges of the 4-volume element are negligibly small it follows that the integral over the total surface of the volume element, S, should vanish:

$$\int_{S(\Delta^4 x)}\int_{\Delta^3 p} d^3\sigma_\mu \; \frac{d^3p}{p^0} \; p^\mu \; f(x',p) = 0. \tag{3.3}$$

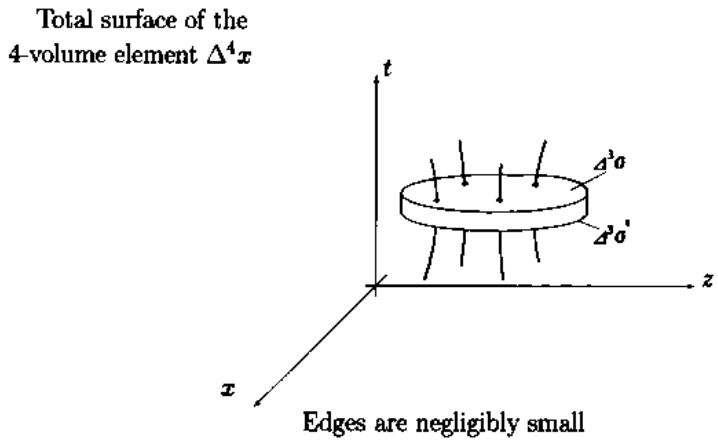

Figure 3.1: World-lines penetrating through a 4-volume element. Reproduced by permission of World Scientific Publishing Co.

Using then Gauss'es theorem, (keeping in mind that $\frac{\partial}{\partial x^\mu}(p^\mu f) = (p^\mu f)_{,\mu} = p^\mu f_{,\mu}$, because p^μ does not depend on x):

$$\int_{\Delta^4 x}\int_{\Delta^3 p} d^4x \; \frac{d^3p}{p^0} \; p^\mu \; f_{,\mu}\,(x,p) = 0. \tag{3.4}$$

Here we used the notation $\partial_\mu \equiv_{,\mu} \equiv \frac{\partial}{\partial x^\mu} \equiv (\partial_t, \nabla)$. Since x, p and $\Delta^4 x$, $\Delta^3 p$ are arbitrary:

$$p^\mu f_{,\mu} = 0, \quad or \quad p^\mu \partial_\mu f(x,p) = 0. \tag{3.5}$$

This is the relativistic transport equation for the collisionless case in non-relativistic notation. Now dividing eq.(3.5) by p^0,:

$$(\partial_t + \vec{v}\;\nabla_x) f(x,p) = 0, \tag{3.6}$$

since $\vec{v} = \vec{p}/p^0$. This is the known form of the continuity equation. This derivation did not take into account an external force.

3.2 Collisions

Collisions among particles lead to a change of $f(x,p)$. The number of particles in $\Delta^4 x$, $\Delta^3 p$ changes by $\Delta^4 x \frac{\Delta^3 p}{p^0} C(x,p)$, where $C(x,p)$ is the collision integral. A general binary

collision can be characterized by the momenta:

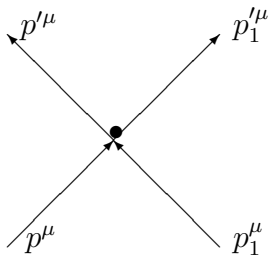

The number of such collisions is proportional to:

(i) The number of nucleons (particles) around $\vec{p}$: $\Delta^3 p\, f(x,p)$.

(ii) The number of nucleons (particles) around $\vec{p}_1$: $\Delta^3 p_1\, f(x,p_1)$.

(iii) The final state and configuration volume intervals $\Delta^3 p'$, $\Delta^3 p_1'$, and $\Delta^4 x$. The proportionality factor is:

$$\frac{W(p,p_1|p',p_1')}{p^0\, p_1^0\, p'^0\, p_1'^0} \tag{3.7}$$

The quantity $W(p,p_1|p',p_1')$ is the transition rate. It is an invariant scalar. Its x dependence is assumed to be weak.

Thus the number of particles scattering out of $\Delta^3 p\, \Delta^4 x$ is

$$\frac{1}{2}\Delta^4 x\ \frac{\Delta^3 p}{p^0}\int \frac{d^3p_1}{p_1^0}\frac{d^3p'}{p'^0}\frac{d^3p_1'}{p_1'^0}\ f(x,p)\, f(x,p_1)\, W(p,p_1|p',p_1'). \tag{3.8}$$

The factor $\frac{1}{2}$ in front of the integral is there because it is symmetric under the exchange $p,p_1 \leftrightarrow p_1', p'$, and we correct for double counting. Similarly the change due to the gain term is:

$$\frac{1}{2}\Delta^4 x\ \frac{\Delta^3 p}{p^0}\int \frac{d^3p_1}{p_1^0}\frac{d^3p'}{p'^0}\frac{d^3p_1'}{p_1'^0}\ f(x,p')\ f(x,p_1')W(p',p_1'|p,p_1). \tag{3.9}$$

Thus the total transport equation is:

$$p^\mu \partial_\mu f(x,p) = C(x,p), \tag{3.10}$$

where

$$C(x,p) = \frac{1}{2}\int \frac{d^3p_1}{p_1^0}\frac{d^3p'}{p'^0}\frac{d^3p_1'}{p_1'^0}\left[f' f_1' W(p',p_1'|p,p_1) - f f_1 W(p,p_1|p',p_1')\right], \tag{3.11}$$

where we introduced the notation

$$f' \equiv f(x,p'),\quad f_1' \equiv f(x,p_1'),\quad f \equiv f(x,p),\quad f_1 \equiv f(x,p_1). \tag{3.12}$$

3.3 Non-relativistic limit

We can rewrite the above equation in another form

$$(\partial_t + \vec{v}\,\nabla_x) f(x,p) = \frac{1}{2}\int d^3p_1\, d^3p'\, d^3p'_1\, [f' f'_1 w(p', p'_1|p, p_1) - f f_1 w(p, p_1|p', p'_1)]\,, \quad (3.13)$$

where

$$w = \frac{W(p, p_1|p', p'_1)}{p^0\ p_1^0\ p'^0\ p'^0_1} \quad (3.14)$$

Since W is a Lorentz scalar depending on p^μ 's of a collision, it may depend on the invariants of the collision only: (Due to the energy conservation in a collision $p^\mu + p_1^\mu = p'^\mu + p_1'^\mu$). There are only 2 independent invariants we can use

$$s \equiv (p + p_1)^2, \quad (3.15)$$
$$t \equiv (p - p')^2. \quad (3.16)$$

In the c.m. frame of the collision if $P^\mu \equiv p^\mu + p_1^\mu = p'^\mu + p_1'^\mu$, then $P^\mu = (\sqrt{s}, 0, 0, 0)$; i.e. $\sqrt{s}$ is the total c.m. energy. t is related to the scattering angle Θ

$$\cos\Theta \equiv \left[\frac{(\vec{p}\ \vec{p}')}{|\vec{p}|\ |\vec{p}'|}\right]_{cm} = \frac{(p^\mu - p_1^\mu)(p'_\mu - p'_{\mu_1})}{(p - p_1)^2} = \frac{2t}{s - 4m^2} + 1. \quad (3.17)$$

Thus the transition rate can be expressed as

$$W(p, p_1|p', p'_1) = s\ \sigma(s, \Theta)\ \delta^{(4)}(p + p_1 - p' - p'_1) \quad (3.18)$$

where the delta function enforces energy conservation and s is introduced to have the proper non-relativistic limit as we will see it later; (By dimensional analysis: [W] = [fm^2/GeV^2]; from eqs.(3.10) and (3.11), and $c = 1$.) Here $\sigma(s, \Theta)$ is some function having the dimension of fm^2 .

We will see that $\sigma(s, \Theta)$ is in fact the differential cross-section by calculating the non-relativistic limit. Insert eq.(3.18) into eq. (3.11) and for example for the gain term of the collision integral will have the form

$$I = \int \frac{d^3p_1}{p_1^0}\frac{d^3p'}{p'^0}\frac{d^3p'_1}{p'^0_1}\ f(x,p')\ f(x,p'_1)\ s\ \sigma(s,\Theta)\ \delta^{(4)}(p + p_1 - p' - p'_1). \quad (3.19)$$

In the c.m. system $P^\mu = p^\mu + p_1^\mu = p'^\mu + p_1'^\mu = (\sqrt{s}, 0, 0, 0)$, so the integration over $\frac{d^3p'_1}{p'^0_1}$ can be carried out. There is only the ^{0}th component left then.

$$\int \frac{d^3p'}{p'^0}\frac{d^3p'_1}{p'^0_1}\ \delta^{(4)}(p + p_1 - p' - p'_1) = \frac{1}{2}\int \frac{d^3p'}{p'^0}\ \frac{1}{p'^0}\ \delta(\frac{1}{2}\sqrt{s} - p'^0), \quad (3.20)$$

i.e. $p'^0 = \frac{1}{2}\sqrt{s}$ in the c.m. frame. Then

$$I = 2\int d^3p' \frac{d^3p_1}{p_1^0}\ \delta(\frac{1}{2}\sqrt{s} - p'^0)\sigma(s,\Theta)\ \ f(x,p')\ f(x,p'_1)\ , \quad (3.21)$$

where $d^3p' = |\vec{p}'|^2\ dp'\ d\Omega$. Now using the relations for $\delta(\phi(x))$ (see Chapter 2)

$$\delta(\frac{1}{2}\sqrt{s} - \sqrt{(\vec{p}')^2 + m^2}) = \sqrt{\frac{s}{s-4m^2}}\ \ \delta(|\vec{p}'| - \frac{1}{2}\sqrt{s-4m^2}). \tag{3.22}$$

Thus the integral is:

$$I = 2\int dp' \frac{d^3p_1}{p_1^0} d\Omega\ \ |\vec{p}'|^2 \sqrt{\frac{s}{s-4m^2}}\ \delta(|\vec{p}'| - \frac{\sqrt{s-4m^2}}{2})\sigma(s,\Theta) f' f_1' = \tag{3.23}$$

$$\int \frac{d^3p_1}{p_1^0} d\Omega\ \ \underbrace{\frac{1}{2}\sqrt{s(s-4m^2)}}_{\equiv F}\sigma(s,\Theta) f' f_1', \tag{3.24}$$

where the part indicated by F is the so called *Invariant Flux*. Remember that the flux was $|\vec{v}_2 - \vec{v}_1|$ in the non-relativistic transport theory. F corresponds to this quantity

$$F = \frac{1}{2}\sqrt{s(s-4m^2)} = \sqrt{(p_1^\mu p_\mu)^2 - m^4}_{|in\ \ c.m.} = \left|\frac{\vec{p}}{p^0} - \frac{\vec{p_1}}{p_1^0}\right| p^0 p_1^0 = |\vec{v} - \vec{v_1}|_{c.m.}\, p^0 p_1^0. \tag{3.25}$$

The two 0^{th} components of the momenta are present in the relativistic expression to balance the invariant scalar volume elements of the integration, $\frac{d^3p}{p^0}$. Using this quantity

$$I = \int \frac{d^3p_1}{p_1^0}\ d\Omega\, |\vec{v} - \vec{v_1}|_{c.m.}\, p^0 p_1^0 \sigma(s,\Theta)\ f(x,p')\ f(x,p_1'). \tag{3.26}$$

And finally using the symmetry relations of W or σ we can write down the complete collision integral and then the full BTE:

$$p^\mu f_{,\mu} = \frac{1}{2}\int d^3p_1\ d\Omega\, |\vec{v} - \vec{v_1}|_{c.m.}\, p^0 \sigma(s,\Theta)\ [f(x,p')\ f(x,p_1') - f(x,p)\ f(x,p_1)]. \tag{3.27}$$

By expressing the conmoving derivative in the usual non-relativistic way

$$(\partial_t + \vec{v}\ \nabla) f(x,p) = \frac{1}{2}\int d^3p_1\ d\Omega\, |\vec{v} - \vec{v_1}|_{c.m.}\, \sigma(s,\Theta)\ [f(x,p')\ f(x,p_1') - f(x,p)\ f(x,p_1)]. \tag{3.28}$$

This is the form of the Boltzmann equation we learned in the statistical physics course. The definition of the cross section via the transition rate is then

$$\sigma(s,\Theta)d\Omega = \frac{1}{F} W(p,p_1|p',p_1') \frac{d^3p'}{p'^0} \frac{d^3p_1'}{p_1'^0} \tag{3.29}$$

One important difference is the factor $\frac{1}{2}$! In the non-relativistic theory (see ref. [1]) there is no such factor. This means that in the classical theory $\sigma_{cl} = \frac{1}{2}\sigma$, and the factor one half takes into account the identical particles. The total cross section should be calculated here as $\sigma_{tot} = \frac{1}{2}\int d\Omega \sigma(s,\Theta)$, while in the classical theory $\sigma_{tot} = \int d\Omega \sigma_{cl}(s,\Theta)$.

3.4 An example for the solution

This example is taken as an illustration from the work of J. Randrup [2]. Randrup solved the Boltzmann transport equation for a spatially uniform distribution. This example may represent the overlap region of a heavy ion collision. The initial condition was such as in the overlap region (Fig. 3.2) of a heavy ion reaction initially, before the nucleon-nucleon collisions result in an approach to thermalization. The question was: how fast can we approach a thermalized momentum distribution.

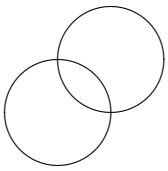

Time dependence of $f(p)$ in the overlap region

Figure 3.2: The overlap region of two nuclei in a heavy ion collision

The Pauli principle for the nucleons was also taken into account in this work. If at a given location x the $p_1, p \to p_1', p'$ scattering would populate a momentum state which is already occupied then this is forbidden. Thus the rate is not proportional to ff_1, but to

$$\underbrace{f(x,p)}_{\equiv f}\underbrace{f(x,p_1)}_{\equiv f_1}\underbrace{[1-f(x,p')]}_{\equiv \bar{f}'}\underbrace{[1-f(x,p_1')]}_{\equiv \bar{f}_1'}.$$

These terms were introduced by Nordheim [3] and by Uehling and Uhlenbeck [4]. Randrup, thus, solved numerically the equation:

$$p^0 f_{,0} = const. \int d^3p_1 \; d\Omega \, |\vec{v} - \vec{v_1}| \, p^0 \sigma(s,\Theta) \; [f' f_1' \bar{f} \bar{f}_1 - f f_1 \bar{f}' \bar{f}_1']. \tag{3.30}$$

The initial state was given by a two-peaked momentum distribution representing a heavy ion collision before the thermalization. Fig. 3.3.

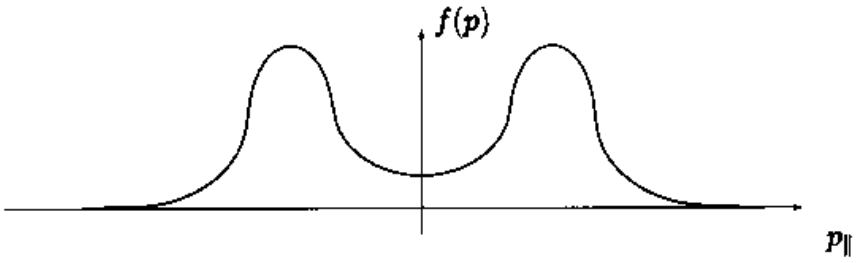

Figure 3.3: Momentum distribution in the longitudinal direction in the overlap region

The time development of momentum distribution was calculated for several beam energies. The result is illustrated in Fig. 3.4 (from ref. [2]).

The entropy can also be calculated. By using the usual definition the entropy 4-current is

$$S^\mu \equiv -\int p^\mu \frac{d^3p}{p^0}\left[f(x,p)\ln f(x,p) - f(x,p)\right] \ , \tag{3.31}$$

where the additive $-f(x,p)$ term ensures the appropriate entropy constant for joining smoothly low temperature quantum statistical results (See also assignment 3.e). Also, the argument of the function $\ln(z)$ should be dimensionless. This is ensured by inserting the elementary phase space volume next to f in the argument, $(2\pi\hbar)^3$. In eqs. (3.31-3.32) we drop this factor for simplicity. If we want to take into account the Pauli principle in high temperature limit

$$S^\mu \equiv -\int p^\mu \frac{d^3p}{p^0}\left[f\ln f + \bar{f}\ln\bar{f}\right] . \tag{3.32}$$

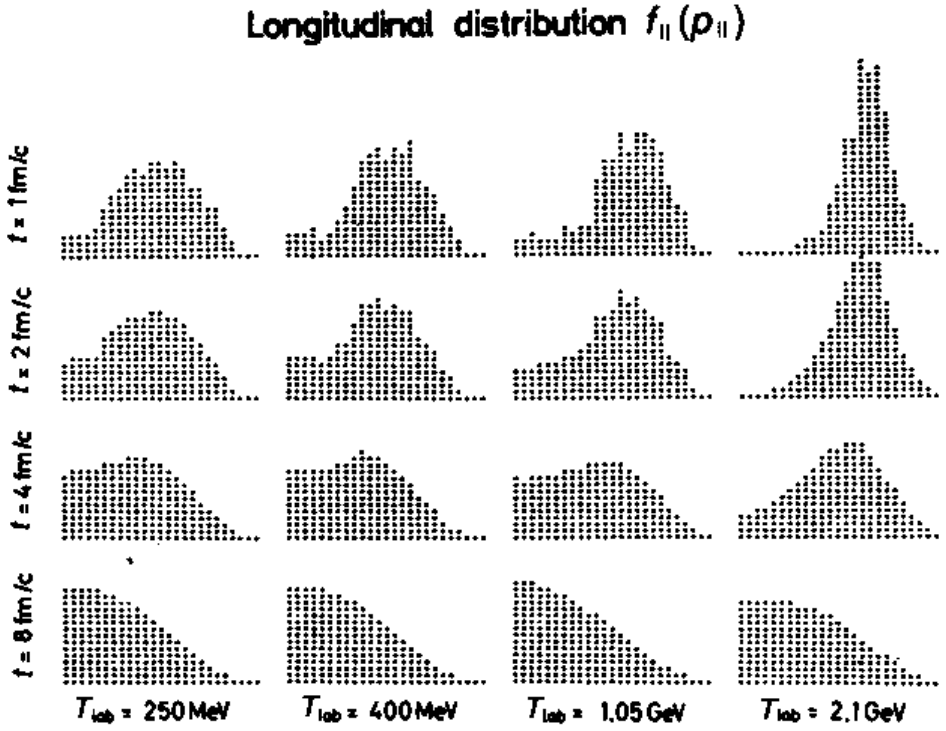

Figure 3.4: The time development of longitudinal momentum distribution $f(p_\parallel)$ which is obtained from the phase occupancy $f(p)$ by projecting onto the beam axis. The normalization is arbitrary but common. $p_\parallel$ runs from 0 to the c.m. beam momentum, p_0. Reproduced by permission of Elsevier Science Publishing from [2].

Randrup used this latter definition. We will see later that these definitions coincide with the thermodynamic definitions for equilibrium systems! The Lorentz scalar entropy density is then defined as

$$s = S^\mu u_\mu, \tag{3.33}$$

while the specific entropy is

$$\sigma = \frac{s}{n}. \tag{3.34}$$

Randrup calculated the time dependence of entropy production and this way the speed of equilibration or thermalization. See Fig. 3.5 (from ref. [2]).

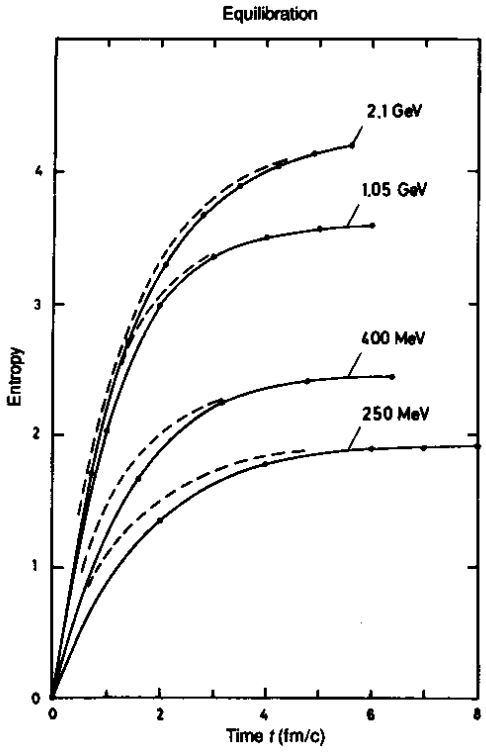

Figure 3.5: Specific entropy production as a function of time The role of Pauli principle in the process of equilibration is shown in the figure: dashed lines are without, full lines with Pauli principle. Reproduced by permission of Elsevier Science Publishing from [2].

The role of Pauli principle is not too large in entropy production! The population of the momentum space is qualitatively different in elastic and in inelastic collisions. The elastic collisions populate essentially a sphere in the c.m. momentum space because of energy conservation. Fig. 3.6 from ref. [2]

Inelastic collisions populate mid rapidities. This leads to thermalization faster than expected!!

There is a large number of works where the collective mean field formed by the nuclear matter is also taken into account. These are called as BUU, VUU or Landau–Vlasov models. These models proved to be very effective in explaining heavy ion collisions up to a few 100 MeV/nucleon colliding energy. [5, 6, 7, 8]

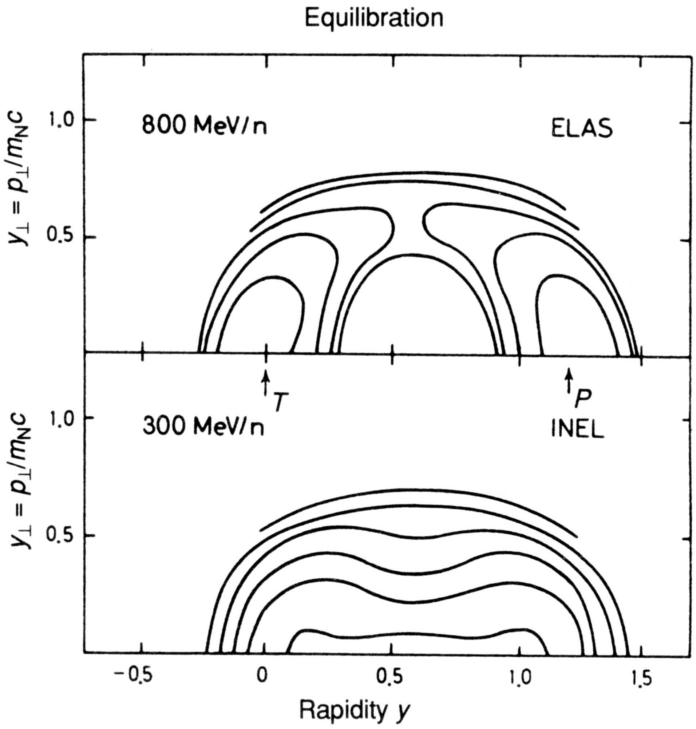

Figure 3.6: Contour plots of the distribution of nucleons in rapidity space after their first collision. The upper portion is for elastic collisions only. In the lower portion inelasticity is included via delta formation. The nucleons resulting from the isotropic decay of the deltas have been added to the plot. Reproduced by permission of Elsevier Science Publishing from [2].

3.5 Relativistic Boltzmann equation for mixtures

Let us assume that we have N components and their distribution is described by

$$f_k(x, p_k), \quad k = 1, 2, ..., N. \tag{3.35}$$

The BTE is then

$$p_k^\mu f_{k,\mu} = \sum_{l=1}^{N} C_{kl}(x, p_k) \tag{3.36}$$

where

$$C_{kl}(x, p_k) = (1 - \frac{1}{2}\delta_{kl}) \int \frac{d^3p_l}{p_l^0} \frac{d^3p_k'}{p_k'^0} \frac{d^3p_l'}{p_l'^0} \left[f_k' f_l' W_{kl}(p_k', p_l'|p_k, p_l) - f_k f_l W_{kl}(p_k, p_l|p_k', p_l') \right]. \tag{3.37}$$

This is the BTE for elastic collisions only. The δ_{kl} in front of the collision integral serves to distinguish mixtures composed of identical particles, $k = l$, and of non-identical particles, $k \neq l$. For inelastic collisions the final states may belong to different components: $k + l \ \rightarrow \ i + j$. (We will neglect the possibility now, that the particle number may change in an inelastic collision like: $k + l \ \rightarrow \ i + j + s + ...$) In such a more general case we have a transition rate $W_{kl\rightarrow ij}$ or $W_{kl|ij}$. In this case the collision integral is:

$$C_{kl}(x, p_k) = \frac{1}{2} \sum_{i,j=1}^{N} \int \frac{d^3p_l}{p_l^0} \frac{d^3p_i}{p_i^0} \frac{d^3p_j}{p_j^0} \left[f_i f_j W_{ij|kl}(p_i, p_j|p_k, p_l) - f_k f_l W_{kl|ij}(p_k, p_l|p_i, p_j) \right]. \tag{3.38}$$

In the following discussion we will omit the arguments of the transition rates W, keeping the indices only (similarly as we do it for the distribution function f). The transition rates have some simple symmetries. First the sequence of the final states is irrelevant:

$$W_{kl|ij} = W_{kl|ji}, \tag{3.39}$$

and from the time reversal symmetry of the microscopic processes $W_{ij|kl} = W_{kl|ij}$.

3.6 Conservation laws

According to macroscopic (phenomenological) theories the macroscopic quantities, $n, e, P, ...$ change according to given dynamical equations (e.g. in hydrodynamics) which are postulated. In the transport theory the conservation laws connect the microscopic properties of the system to the equations governing the development of the macroscopic quantities.

Lemma

1. Ψ_k is a microscopic quantity determined by the particle type (k), position (x) and momentum (p_k) as:

$$\Psi_k(x, p_k) = a_k(x) + b_\mu(x) p_k^\mu.$$

2. This quantity is conserved in a binary collision $kl \to ij$, such that:

$$\Psi_k + \Psi_l = \Psi_i + \Psi_j.$$

One example for such a conserved quantity is the mass in an elastic collision, $a_k = m_k$, and then the energy and momentum conservation leads to $b_\mu = 1$, because p^μ is a conserved quantity also.

Statement: If assumptions 1 and 2 are valid then the quantity, F, is

$$F = \sum_{k,l=1}^{N} \int \frac{d^3p_k}{p_k^0} \Psi_k C_{kl}(x, p_k) = 0, \tag{3.40}$$

where

$$C_{kl}(x, p_k) = \frac{1}{2} \sum_{i,j=1}^{N} \int \frac{d^3p_l}{p_l^0} \frac{d^3p_i}{p_i^0} \frac{d^3p_j}{p_j^0} \left[f_i f_j W_{ij|kl}(p_i, p_j|p_k, p_l) - f_k f_l W_{kl|ij}(p_k, p_l|p_i, p_j) \right]. \tag{3.41}$$

Let us calculate F

$$F = \frac{1}{2} \sum_{i,j,k,l=1}^{N} \int \frac{d^3p_i}{p_i^0} \frac{d^3p_j}{p_j^0} \frac{d^3p_k}{p_k^0} \frac{d^3p_l}{p_l^0} \Psi_k \left[f_i f_j W_{ij|kl} - f_k f_l W_{kl|ij} \right]. \tag{3.42}$$

Let us exchange the summation and integration variables in the loss term as $k, l \leftrightarrow i, j$. This yields

$$F = \frac{1}{2} \sum_{i,j,k,l=1}^{N} \int \frac{d^3p_i}{p_i^0} \frac{d^3p_j}{p_j^0} \frac{d^3p_k}{p_k^0} \frac{d^3p_l}{p_l^0} (\Psi_k - \Psi_i) f_i f_j W_{ij|kl}. \tag{3.43}$$

Using the symmetry $W_{ij|kl} = W_{ij|lk} = W_{ji|lk}$, F can be written as:

$$F = \frac{1}{2} \sum_{i,j,k,l=1}^{N} \int \frac{d^3p_i}{p_i^0} \frac{d^3p_j}{p_j^0} \frac{d^3p_k}{p_k^0} \frac{d^3p_l}{p_l^0} (\Psi_l - \Psi_j) f_j f_i W_{ij|kl}. \tag{3.44}$$

Summing up the last two expressions and multiplying by $\frac{1}{2}$

$$F = \frac{1}{4} \sum_{i,j,k,l=1}^{N} \int \frac{d^3p_i}{p_i^0} \frac{d^3p_j}{p_j^0} \frac{d^3p_k}{p_k^0} \frac{d^3p_l}{p_l^0} (\Psi_k + \Psi_l - \Psi_i - \Psi_j) f_i f_j W_{ij|kl}. \tag{3.45}$$

Since Ψ is conserved in a collision the expression in parentheses vanishes, and so $F = 0$. q.e.d.

3.6.1 Conservation of particle number

In this case $\Psi_k = 1$. Let us take the BTE

$$p_k^\mu f_{k,\mu} = \sum_{l=1}^{N} C_{kl}(x, p_k), \tag{3.46}$$

and multiply it with Ψ_k, sum it over k and integrate it over $\int \frac{d^3p_k}{p_k^0}$:

$$\sum_{k=1}^{N} \int \frac{d^3p_k}{p_k^0} p_k^\mu f_{k,\mu} = \sum_{k,l=1}^{N} \int \frac{d^3p_k}{p_k^0} C_{kl}(x, p_k). \tag{3.47}$$

According to the Lemma the right hand side vanishes. Since the particle four-current is $N_k^\mu = \int \frac{d^3p_k}{p_k^0} p_k^\mu f_k$ equation (3.47) means that the 4 divergence of the particle current vanishes:

$$N^\mu{}_{,\mu} = \sum_{k=1}^{N} N_k^\mu{}_{,\mu} = 0. \tag{3.48}$$

This is the Continuity Equation. It expresses the fact that the particle number is conserved if it is conserved in a microscopic collision.

3.6.2 Conservation of charge

We can choose any conserved charge, like baryon charge, strangeness, or electric charge. In this case $\Psi_k = q_k$ can be taken as the charge. The corresponding 4-current is then

$$Q_k^\mu = \int \frac{d^3p_k}{p_k^0} \, q_k \, p_k^\mu \, f_k. \tag{3.49}$$

Thus the Charge Conservation can be expressed similarly to the previous case as

$$Q^\mu{}_{,\mu} = \sum_{k=1}^{N} Q_k^\mu{}_{,\mu} = 0. \tag{3.50}$$

3.6.3 Conservation of energy and momentum

Choose in this case $\Psi_k = p_k^\nu$. Let us take the BTE again

$$p_k^\mu f_{k,\mu} = \sum_{l=1}^{N} C_{kl}(x, p_k), \tag{3.51}$$

and multiply it with Ψ_k, sum it over k and integrate it over $\int \frac{d^3p_k}{p_k^0}$:

$$\sum_{k=1}^{N} \int \frac{d^3p_k}{p_k^0} p_k^\mu p_k^\nu f_{k,\mu} = \sum_{k,l=1}^{N} \int \frac{d^3p_k}{p_k^0} p_k^\nu C_{kl}(x, p_k). \tag{3.52}$$

According to the Lemma the right hand side vanishes. Since the energy-momentum tensor is $T_k^{\mu\nu} = \int \frac{d^3p_k}{p_k^0} p_k^\mu p_k^\nu f_k$, equation (3.52) means that the 4 divergence of the energy-momentum tensor vanishes:

$$T^{\mu\nu}{}_{,\mu} = \sum_{k=1}^{N} T_k^{\mu\nu}{}_{,\mu} = 0. \tag{3.53}$$

This is the energy and momentum conservation. Equations (3.48-3.53) are also the equations of the relativistic fluid dynamics. In the fluid dynamics these equations are postulated and not derived. As a matter of fact equations (3.48-3.53) are not a closed set of equations, because the energy-momentum tensor and the particle 4-current should be defined too. In the transport theory this is done through the distribution function, which is known only if the solution of the BTE is known. Thus within the transport theory these equations do not provide us the solution of a dynamical problem.

In Eulerian (perfect) fluid dynamics we postulate that the form of the energy-momentum tensor is given by $T^{\mu\nu\ (0)}$ (see section 2.3.4) and the Equation of State (EOS) gives the relation $P = P(e, n)$. This provides a closed set of solvable partial differential equations.

In the case of Navier–Stokes (viscous) fluid dynamics we assume that the energy-momentum tensor contains $T^{\mu\nu\ (1)}$ also, and not only the EOS but the transport coefficients that occur in the dissipative part of the energy momentum tensor also have to be given.

3.7 Boltzmann H-theorem

We have seen that the definition of the entropy 4-current in transport theory is

$$S^\mu = -\sum_k \int \frac{d^3p_k}{p_k^0} p_k^\mu f_k[\log f_k - 1]. \tag{3.54}$$

Here we assume that $c = \hbar = k = 1$. The entropy should be a non-decreasing function of time, i.e. $S^\mu{}_{,\mu} \geq 0$.

We want to see if this is a consequence of the BTE or not. Let us calculate the 4 divergence of the entropy current according to the definition

$$S^\mu{}_{,\mu} = -\sum_k \int \frac{d^3p_k}{p_k^0} p_k^\mu [\log f_k] f_{k,\mu}\,. \tag{3.55}$$

From the Boltzmann Transport Equation $p_k^\mu f_{k,\mu} = \sum_l C_{kl}(x, p_k)$. Inserting this into the equation above

$$S^\mu{}_{,\mu} = -\sum_{k,l} \int \frac{d^3p_k}{p_k^0} [\log f_k] C_{kl}(x, p_k). \tag{3.56}$$

We can now repeat the steps of the Lemma in the previous section, with $\Psi_k = \log f_k$, although $\log f_k$ is not a collision invariant. Thus the integral will not necessarily vanish, but we still can get it into a symmetrized form by using the same steps:

$$S^\mu{}_{,\mu} = -\sum_{ijkl} \frac{1}{4} \int \frac{d^3p_i}{p_i^0} \frac{d^3p_j}{p_j^0} \frac{d^3p_k}{p_k^0} \frac{d^3p_l}{p_l^0} \left[\log \frac{f_k f_l}{f_i f_j}\right] f_i f_j W_{ij|kl}. \tag{3.57}$$

Aside:
The transition rate has also the following symmetry:

$$\sum_{ij} \int \frac{d^3p_i}{p_i^0} \frac{d^3p_j}{p_j^0} W_{kl|ij} = \sum_{ij} \int \frac{d^3p_i}{p_i^0} \frac{d^3p_j}{p_j^0} W_{ij|kl}. \tag{3.58}$$

This is a consequence of the unitarity of the scattering matrix. Now multiply the above equation by $f_k f_l$, then sum it over k and l, and integrate it over $\frac{d^3p_k}{p_k^0}$ and $\frac{d^3p_l}{p_l^0}$.

$$\sum_{ijkl} \int \frac{d^3p_i}{p_i^0} \frac{d^3p_j}{p_j^0} \frac{d^3p_k}{p_k^0} \frac{d^3p_l}{p_l^0} (f_k f_l W_{kl|ij} - f_k f_l W_{ij|kl}) = 0. \tag{3.59}$$

In the first term we make an index change: $i, j \leftrightarrow k, l$. This yields

$$\frac{1}{4} \sum_{ijkl} \int \frac{d^3p_i}{p_i^0} \frac{d^3p_j}{p_j^0} \frac{d^3p_k}{p_k^0} \frac{d^3p_l}{p_l^0} (f_k f_l - f_i f_j) W_{ij|kl} = 0. \tag{3.60}$$

Summing up equations (3.57) and (3.60) we obtain the relation

$$S^{\mu}{}_{,\mu} = \frac{1}{4}\sum_{ijkl}\int \frac{d^3p_i}{p_i^0}\frac{d^3p_j}{p_j^0}\frac{d^3p_k}{p_k^0}\frac{d^3p_l}{p_l^0}[\frac{f_kf_l}{f_if_j} - \log\frac{f_kf_l}{f_if_j} - 1]f_if_jW_{ij|kl}. \tag{3.61}$$

The expression in parentheses is a function, $g(x) = x - \log(x) - 1$, which is depicted in Figure 3.7

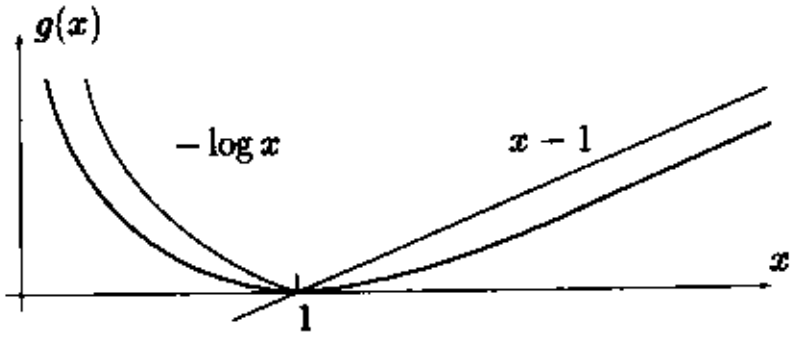

Figure 3.7: The $g(x) = x - \ln(x) - 1$ function

Since the distribution function is never negative, the argument of function $g(x)$ is also non-negative, thus it follows that $g(x) \geq 0$. This means that the above equation then yields

$$S^{\mu}{}_{,\mu} \geq 0, \tag{3.62}$$

and it vanishes only if $x = 1$, i.e. if $f_kf_l = f_if_j$.

Consequence: If irreversible processes are present the entropy increases. In equilibrium the distribution, $f = f^{eq.}$, is constant, so $S^{\mu}{}_{,\mu} = 0$, i.e. the entropy is constant, but it reached its maximum when the equilibrium was reached.

Special case for one component only: Since $S^{\mu}{}_{,\mu} = 0$ it follows

$$f^{eq.}(x,p)f^{eq.}(x,p_1) = f^{eq.}(x,p')f^{eq.}(x,p_1'), \tag{3.63}$$

so, $\log f$ is a collision invariant:

$$\log f^{eq.}(x,p) + \log f^{eq.}(x,p_1) = \log f^{eq.}(x,p') + \log f^{eq.}(x,p_1'). \tag{3.64}$$

3.8 Equilibrium distribution function

In a collision $p, p_1 \to p', p'_1$, where $p^\mu + p_1^\mu = p'^\mu + p_1'^\mu$ the most general collision invariant is $\Psi = a(x) + b_\mu(x)p^\mu$. This means that if $\log f^{eq.}(x,p)$ is a collision invariant it should be expressible via Ψ,

$$\log f^{eq.}(x,p) = a(x) + b_\mu(x)p^\mu, \quad \text{so that,} \quad f^{eq.}(x,p) = \exp(a(x) + b_\mu(x)p^\mu). \tag{3.65}$$

If there is no external force the distribution should be homogeneous:

$$f^{eq.}(x,p) = f^{eq.}(p). \tag{3.66}$$

Since there are no gradients it follows that there are no transports. This way Landau's and Eckart's definitions are equivalent. We can determine constants a and b^μ by calculating macroscopic expectation values from this distribution $f^{eq.}(p)$. Let us start with the flow velocity, $u^\mu = const. \times N^\mu$, where

$$N^\mu = const. \times \int \frac{d^3p}{p^0} p^\mu \exp(a + b_\mu p^\mu) = const. \times \int \frac{d^3p}{p^0} p^\mu \exp(b_\mu p^\mu). \tag{3.67}$$

This integral converges only if b^μ is a time-like four-vector (and $b_\mu p^\mu < 0$). Then from (3.67) N^μ will be parallel to b^μ. Consequently

$$b^\mu = const. \times u^\mu = -\frac{1}{T} u^\mu, \tag{3.68}$$

where T is just a constant. This yields

$$f^{eq.}(p) = const. \times e^{-u_\mu p^\mu / T}, \tag{3.69}$$

where the normalization constant can be obtained from the requirement $n = u_\mu N^\mu$ and it yields $const. = n/[4\pi m^2 T K_2(m/T)]$. This is just the Jüttner distribution that was introduced in sect. 1.8.

Thus we have seen that the Jüttner distribution is the stationary solution of the relativistic Boltzmann equation. If f is a solution of the BTE, it tends to $f^{Juttner}$. This was illustrated in the example in sect. 2.4.

This is the relativistic extension of the Boltzmann distribution. The approach to equilibrium is fast: 3-8 fm/c! Most of the time the local distribution $f(x,p)$ is close to $f^{Juttner}$.

3.9 Zeroth order approximation

Perfect fluid dynamics

Assumption: Our system is not homogeneous, but the gradients are small, so local distributions can be written as

$$f(x,p) = \frac{1}{(2\pi\hbar)^3} \exp\left(\frac{\mu_{ch}(x) - p^\mu u_\mu(x)}{T(x)}\right), \tag{3.70}$$

now the local $n(x), P(x), e(x), s(x)$ are also known (from $f(x,p)$ by using the definitions), and we assume (!) that in the (LR), $T^{\mu\nu}$ is diagonal. This is also a consequence of the assumption since we have neglected the gradients of the flow velocity and of the thermodynamical variables:

$$T^{\mu\nu}_{LR} = T^{\mu\nu\ (0)}_{LR} = (e+P)u^\mu_{LR}u^\nu_{LR} - Pg^{\mu\nu} = \begin{pmatrix} e & 0 & 0 & 0 \\ 0 & P & 0 & 0 \\ 0 & 0 & P & 0 \\ 0 & 0 & 0 & P \end{pmatrix}_{LR} \tag{3.71}$$

The equations of Perfect Fluid Dynamics are the conservation laws under the assumption that $f(x,p) = f^{Juttner}(x,p)$

$$N^\mu{}_{,\mu} = 0 \quad \text{or} \quad \partial_\mu(nu^\mu) = 0, \tag{3.72}$$

and

$$T^{\mu\nu}_{\ ,\mu} = 0 \quad \text{or} \quad \partial_\mu(T^{\mu\nu}) = 0. \tag{3.73}$$

Using $u^\mu = (\gamma, \gamma\vec{v})$, $T^{ik} = w\gamma^2 v_i v_k + P\delta_{ik}$, $T^{0i} = -T_{0i} = w\gamma^2 v_i$, $T^{00} = T_{00} = (e + Pv^2)\gamma^2$, $(i,k = 1,2,3)$, the equation of continuity takes the form

$$\partial_t(n\gamma) + \mathrm{div}(n\gamma\vec{v}) = 0, \tag{3.74}$$

or

$$(\partial_t + \vec{v}\,\mathrm{grad})(n\gamma) + n\gamma \mathrm{div}\vec{v} = 0. \tag{3.75}$$

Now introducing the apparent density

$$\mathcal{N} \equiv n\gamma = \mathsf{n}, \tag{3.76}$$

the continuity equation takes the familiar form

$$(\partial_t + \vec{v}\,\mathrm{grad})\mathcal{N} = -\mathcal{N}\mathrm{div}\vec{v}. \tag{3.77}$$

Similarly introducing

$$\vec{\mathcal{M}} \equiv T^{0i} = w\gamma^2\vec{v}, \tag{3.78}$$

$$\mathcal{E} \equiv T^{00} = (e + P\vec{v}^{\,2})\gamma^2, \tag{3.79}$$

the energy and momentum conservation will take the form

$$(\partial_t + \vec{v}\,\mathrm{grad})\vec{\mathcal{M}} = -\vec{\mathcal{M}}(\mathrm{div}\vec{v}) - \mathrm{grad}P, \tag{3.80}$$

$$(\partial_t + \vec{v}\,\mathrm{grad})\mathcal{E} = -\mathcal{E}\mathrm{div}\vec{v} - \mathrm{div}(P\vec{v}). \tag{3.81}$$

The last two equations are the Euler equation of fluid dynamics and the energy conservation. Equations (3.77,3.81) have the familiar form of the equations of non-relativistic perfect fluid dynamics. The difference is that

the quantities $\mathcal{N}$, $\mathcal{E}$, $\vec{\mathcal{M}}$ are not related directly to the EOS, but one has to solve a set of algebraic equations, (3.76,3.78,3.79) to obtain the thermodynamical quantities.

3.10 Assignment 3

3.a Show that, if u^μ is the flow velocity: $u^\mu u_{\mu,\nu} = 0$. (The notation is such that: $,_\mu \equiv \frac{\partial}{\partial x^\mu} \equiv \partial_\mu \equiv (\partial_t, \nabla_{\vec{r}})$.

3.b Prove that $\Delta^{\mu\nu}\Delta_{\nu\sigma} = \Delta^\mu_\sigma$, and $\Delta^\mu_\mu = 3$.

3.c Determine the chemical potential μ from the normalization $n = N^\mu u_\mu$. (Will be done in class too!)

3.d Determine the energy-momentum tensor for the equilibrium distribution function $f^{Juttner}(x,p)$, (i.e.: determine e and p). Show that T tends to the temperature in the non-relativistic limit (i.e.: $e \approx n(m + \frac{3}{2}T + ...)$).

3.e Determine the entropy density and show that the basic thermodynamical relation

$$Ts = e + p - \mu n$$

holds for the Jüttner distribution.

3.10.1 Solutions to Assignment 3

3.a Show that $u^\mu u_{\mu,\nu} = 0$.

u^μ is a time-like unit vector: $u^\mu u_\mu = +1$, so it follows that $(u^\mu u_\mu)_{,\nu} = 0$. Thus,

$$(u^\mu u_\mu)_{,\nu} = u^\mu{}_{,\nu}\, u_\mu + u^\mu u_{\mu,\nu} = (g^{\mu\sigma} u_\sigma)_{,\nu}\, u_\mu + u^\mu u_{\mu,\nu} = g^{\mu\sigma} u_{\sigma,\nu}\, u_\mu + u^\mu u_{\mu,\nu} =$$

$$g^{\mu\sigma} u_\mu u_{\sigma,\nu} + u^\mu u_{\mu,\nu} = u^\sigma u_{\sigma,\nu} + u^\mu u_{\mu,\nu} = 2 \times u^\mu u_{\mu,\nu} = 0.$$

q.e.d.

3.b Prove that $\Delta^{\mu\nu}\Delta_{\nu\sigma} = \Delta^\mu_\sigma$, and $\Delta^\mu_\mu = 3$.

$$\Delta^{\mu\nu}\Delta_{\nu\sigma} = (g^{\mu\nu} - u^\mu u^\nu)(g_{\nu\sigma} - u_\nu u_\sigma) = g^{\mu\nu} g_{\nu\sigma} + u^\mu u^\nu u_\nu u_\sigma - g^{\mu\nu} u_\nu u_\sigma - g_{\nu\sigma} u^\mu u^\nu =$$

$$g^\mu_\sigma + u^\mu u_\sigma - u^\mu u_\sigma - u^\mu u_\sigma = g^\mu_\sigma - u^\mu u_\sigma = \Delta^\mu_\sigma$$

$$\Delta^\mu_\mu = g^\mu_\mu - u^\mu_\mu = \delta^\mu_\mu - u^\mu u_\mu = 4 - 1 = 3$$

other solution: Δ^μ_μ is invariant scalar. In the LR $\Delta^\mu_{mu_{LR}} = 3$. Hence $\Delta^\mu_\mu = 3$.
q.e.d.

3.c This is important, students should solve it or it should be presented in class!

$$n = N^\mu u_\mu = C \int \frac{d^3p}{p^0} p^\mu u_\mu \exp(-p^\mu u_\mu / T).$$

This integral is an invariant scalar, therefore it can be evaluated in any frame. We will take the LR frame. Here $u^\mu = (1,0,0,0)$, so $p^\mu u_\mu = p^0 = \sqrt{\vec{p}^{\,2} + m^2}$. Using this

$$n = C \int d^3p \frac{p^0}{p^0} \exp(-\sqrt{\vec{p}^{\,2} + m^2}\ /T).$$

Introducing spherical polar coordinates $d^3p = |\vec{p}|^2\, d|\vec{p}|\, d\Omega$, and performing the integration over $d\Omega$ we obtain

$$n = 4\pi C \int_0^\infty d|\vec{p}||\vec{p}|^2 \exp(-\sqrt{|\vec{p}|^2 + m^2}\ /T).$$

Introducing new variables

$$\tau = \frac{\sqrt{|\vec{p}|^2 + m^2}}{T}, \quad z = \frac{m}{T},$$

leads to

$$|\vec{p}|^2 = (T\tau)^2 - m^2, \ \ d|\vec{p}| = \frac{T^2\tau}{\sqrt{(T\tau)^2 - m^2}} d\tau \quad = \frac{T^3\tau}{T|\vec{p}|} d\tau,$$

and consequently

$$n = 4\pi T^3 C \int_z^\infty d\tau \tau \frac{|\vec{p}|}{T} \exp(-\tau) = 4\pi T^3 C \int_z^\infty d\tau \tau \sqrt{\tau^2 - z^2}\ \exp(-\tau).$$

Comparing this with the integral expression of the modified Bessel function of the second kind:

$$K_n(z) = \frac{2^{n-1}(n-1)!}{(2n-2)!} z^{-n} \int_z^\infty d\tau (\tau^2 - z^2)^{n-3/2}\ \tau \exp(-\tau),$$

the particle number density can be written as

$$n = 4\pi C \frac{m^2}{T^2} T^3 K_2(\frac{m}{T})$$

and from here the normalization constant C can be expressed:

$$C = \frac{n}{4\pi m^2 T K_2(m/T)}.$$

Thus the complete distribution function is

$$f^{eq}(p) = \frac{n\ e^{-p^\mu u_\mu / T}}{4\pi m^2 T K_2(m/T)}.$$

We can determine the chemical potential μ. From the definition $C = e^{\mu/T}\ /\ (2\pi\hbar)^3$, so it follows that

$$n = \frac{4\pi m^2 T e^{\mu/T}\ K_2(m/T)}{(2\pi\hbar)^3},$$

and then

$$\mu = T \ln \left[\frac{n(2\pi\hbar)^3}{4\pi m^2 T K_2(m/T)} \right].$$

3.d The energy-momentum tensor $T^{\mu\nu}$ is diagonal in the LR frame, and

$$e = u_\mu T^{\mu\nu} u_\nu = C \int \frac{d^3p}{p^0} (p^\mu u_\mu)^2 e^{-p^\mu u_\mu / T},$$

$$P = -\frac{1}{3} T^{\mu\nu} \Delta_{\mu\nu} = -\frac{1}{3} C \int \frac{d^3p}{p^0} \left[\underbrace{p^\mu p_\mu}_{(p^0)^2 - |\vec{p}|^2} - (p^\mu u_\mu)^2 \right] e^{-p^\mu u_\mu / T}.$$

Evaluating this second integral in the LR frame

$$P = -\frac{1}{3} C \int \frac{d^3p}{p^0} \left[(p^0)^2 - |\vec{p}|^2 - (p^0)^2 \right] e^{-p^0/T} = \frac{4\pi}{3} C \int_0^\infty d|\vec{p}| \; |\vec{p}|^2 \frac{1}{p^0} |\vec{p}|^2 e^{-\sqrt{|\vec{p}|^2 + m^2} \; /T}.$$

Using the same variable transformations as in the solution of problem 2.d:

$$P = \frac{4\pi}{3} C \int_z^\infty d\tau \frac{T\tau}{\sqrt{\tau^2 - z^2}} T^4 \frac{[\tau^2 - z^2]^2}{\tau T} e^{-\tau} = \frac{4\pi}{3} C T^4 \int_z^\infty d\tau (\tau^2 - z^2)^{3/2} e^{-\tau}.$$

Now using the definition:

$$K_n(z) = \frac{2^n \; n!}{(2n)!} z^{-n} \int_z^\infty d\tau \; (\tau^2 - z^2)^{n-1/2} \; e^{-\tau},$$

we obtain

$$P = \frac{4\pi}{3} C T^4 3 z^2 K_2(z) = 4\pi C \frac{m^2}{T^2} T^4 K_2(m/T).$$

Now using the normalization expressed in terms of n above:

$$P = nT.$$

This is the Equation of State (EOS) of the relativistic ideal gas of classical particles. It is the same as that of the non- relativistic ideal gas!! **Consequently T can be identified with the temperature!** This can be done only now, before it was just a parameter of the distribution function characterizing the width of the distribution.

Similarly the energy density, e, can be obtained in a straightforward calculation following the same procedure as we did it for the pressure.

$$e = 4\pi C m^4 \left[3 \frac{K_2(z)}{z^2} + \frac{K_1(z)}{z} \right].$$

Thus the energy per particle, $\varepsilon = \frac{e}{n}$ is

$$\varepsilon = 3T + m \frac{K_1(m/T)}{K_2(m/T)}.$$

Making use of the asymptotic formula for $z \to \infty$:

$$K_n(z) = \sqrt{\frac{\pi}{2z}} \; e^{-z} \left[1 + \frac{4n^2 - 1}{8z} + \frac{(4n^2 - 1)(4n^2 - 9)}{2! \; (8z)^2} + \; ... \right],$$

the second term in the expression of the specific energy tends to

$$\frac{K_1}{K_2} \to \frac{1 + \frac{3}{8} z^{-1} - \frac{15}{2 \cdot 64} z^{-2} + ...}{1 + \frac{15}{8} z^{-1} + \frac{15 \cdot 7}{2 \cdot 64} z^{-2} + ...} \approx$$

(Using $(1+x)^{-1} = 1 - x + x^2 - ....$)

$$\approx \left(1 + \frac{3}{8}z^{-1} - \frac{15}{2\cdot 64}z^{-2} + ...\right)\left(1 - \frac{15}{8}z^{-1} + \frac{15\cdot 7}{2\cdot 64}z^{-2} + ... + (\frac{15}{8})^2 z^{-2} + ...\right) =$$

$$1 - \frac{3}{2}z^{-1} - \left(\frac{2\cdot 3\cdot 15}{2\cdot 64} + \frac{15}{2\cdot 64} + \frac{7\cdot 15}{2\cdot 64} + \frac{15^2}{64}\right)z^{-2} + ... = 1 - \frac{3}{2}z^{-1} + \frac{15}{8}z^{-2} + ...$$

Using this low temperature limit the specific energy is:

$$\varepsilon = m + \frac{3}{2}T + \frac{15}{8}\frac{T^2}{m} + ...$$

The first two terms give the well known non-relativistic expression, the third term is a relativistic correction for gases where the temperature is still not too high but it is comparable with the rest mass.

3.e

$$s = S^\mu u_\mu = -\int \frac{d^3p}{p^0} p^\mu u_\mu f^{eq}(p)\left[\ln\left((2\pi\hbar)^3 f^{eq}(p)\right) - 1\right] =$$

$$-\int \frac{d^3p}{p^0} p^\mu u_\mu f^{eq}(p)\left[\frac{\mu - p^\mu u_\mu}{T} - 1\right] = -\int \frac{d^3p}{p^0} f^{eq}(p)\left[\frac{\mu}{T}p^\mu u_\mu - \frac{1}{T}(p^\mu u_\mu)^2 - p^\mu u_\mu\right].$$

Comparing this with the previous results,

$$s = -\frac{\mu}{T}n + \frac{1}{T}e + n,$$

and using the EOS, $P = nT$:

$$Ts = e + P - \mu n.$$

Thus the entropy density, s, as we defined it satisfies the well known thermodynamical relations. Thus at this point we can state that the entropy, $s = S^\mu u_m u$, is really the parameter we are familiar with from equilibrium thermodynamics. This definition, however, is applicable for non-equilibrium situations also!

Bibliography

[1] K. Huang: Statistical Mechanics (Wiley, New York, 1963).

[2] J. Randrup, Nucl. Phys. **A314** (1979) 429.

[3] L. Nordheim, Proc. Roy. Soc. **A119** (1928) 689.

[4] E.A. Uehling and G.E. Uhlenbeck, Phys. Rev. **43** (1933) 552.

[5] J. Cugnon, Phys. Lett. **135B** (1984) 374.

[6] J. Aichelin and H. Stöcker, Phys. Lett. **176B** (1986) 14.

[7] J. Aichelin, A. Rosenhauer, G. Peilert, H. Stöcker, and W. Greiner, Phys. Rev. Lett. **58** (1987) 1926.

[8] G.M. Welke, M. Prakash, T.T.S. Kuo, S. Das Gupta, and C. Gale, Phys. Rev. **C38**, 2101 (1988).

Chapter 4

Equation of State

In this chapter we will study two regions of the nuclear equation of state (EOS): the energy and density region which is reachable in intermediate energy heavy ion collisions up to a few GeV/nucl. energy, and some aspects of the Quark-Gluon Plasma (QGP) phase transition. In the intermediate energy region we will pay particular attention to the compressibility of nuclear matter and to the liquid–gas phase transition. Some basic facts about the nuclear multifragmentation will also be mentioned. Here we will discuss the features of the phase transition to QGP only from the EOS view point, and the sensitivity of the phase transition to the nuclear compressibility. We will concentrate on the connections between experimental data and the EOS rather than on theoretical derivation of a particular EOS in the framework of a particular theoretical model.

The EOS provides only limited information about the nuclear matter: the static thermal equilibrium properties. Before we proceed it has to be mentioned that in heavy ion collisions non-equilibrium processes are very important, thus nuclear transport properties will play an equally important role. It is also possible to extract transport coefficients from the data. An example of this is given in refs. [1, 2] where scaling properties of the data were studied and this led to conclusions about the Reynolds number (i.e. viscosity).

4.1 Intermediate Energy EOS

4.1.1 Bulk nuclear matter

Nuclear compressibility

From conventional nuclear physics we know that there is a stable equilibrium state at the normal nuclear density $n_0 = 0.145 - 0.17 fm^{-3}$ [3, 4] with a compressibility which was earlier assumed to be in the range of $K = 180 - 240\ MeV$ [5] and a binding energy of 16 $MeV/nucleon$. If we want to learn about the EOS at high densities and high temperatures we have to rely mostly on theoretical estimates. The high density high temperature part of the equation of state is decisive in the first, compression stage of the collision. The low density behavior of nuclear matter determines the observables and the reaction mechanism of the final expansion stage in a collision before the breakup. In this first part of the lecture we will concentrate on the low density part of the nuclear equation of state, which is directly related to the final fragmentation, nuclear compressibility, momentum dependence, etc.

After an energetic nucleus-nucleus collision, many light nuclear fragments, a few heavy fragments and a few mesons (mainly pions) are observed in the 100 MeV − 4 $GeV/nucleon$ beam energy region. Thus the initial kinetic energy of the projectile leads to the destruction of the ground state nuclear matter and converts it into a dilute gas ($n << n_0$) of fragments, which then loses thermal contact during the breakup or freeze-out stage. These frozen-out fragments and their momentum distributions can be measured by the detectors. Some excited fragments can of course decay while reaching the detectors.

One of the most standard methods to calculate the nuclear EOS is in the mean field theory. We start out with a Lagrangian including the nucleon field, ψ, a scalar meson field, ϕ and a vector meson field, V_μ. Customarily the contribution of the scalar field is described by a quartic polynomial. The coefficients and the coupling constants determine the behavior of the calculated EOS. Not all the parameters are free obviously, since basic nuclear parameters like the binding energy and the saturation density should be reproduced by the model. Also the compressibility, K, and the effective nucleon mass, m^*, are sometimes considered as known parameters.

However, based on a mean field theoretical calculation Waldhauser *et al.*, pointed out recently that the characterization of the EOS with the ground state compressibility is sometimes very misleading [6]. For example at $T = 100\ MeV$, and if the effective mass is $m^* = 0.55m$ the EOS at $n = 2-3n_0$ is practically the same for different compressibilities like $K = 210,\ 300,\ 400\ MeV$. On the other hand the EOS is very sensitive to the effective mass at high densities. This finding explains the earlier experience that if some phenomenon, which is sensitive to the EOS at high densities, is satisfactorily described in a theoretical model with one given $K(n_0, T = 0)$, it is still possible that other models have to use a different constant value for the ground state K. So to debate about the nuclear compressibility is meaningful only if apart of the value of K also the particular model or parametrization is also discussed.

The nuclear compressibility is in the focus of an international debate recently. With

the advancement of the relativistic heavy ion physics we reached the stage where *quantitative* conclusions about the high temperature high density EOS became possible. The compressibility

$$K_\sigma = 9\frac{\partial P(\sigma, n)}{\partial n}$$

influences a great number of experimental observables. These were summarized recently by Glendenning [7]. Following his work we can briefly summarize the different phenomena leading to some conclusions about the EOS.

Landau Sum Rule. In the Landau theory of Fermi liquids the compressibility is given by $K = 3\hbar^2 k_F^2(1 + F_0)/m^*$, where F_0 is one of the Landau parameters characterizing the liquid. Brown and Osnes [8] determined F_0, and thus K, from the Landau sum rule which connects the Landau parameters. Collecting the information available for them the authors concluded that the compressibility is $K = 106\ MeV$. Glendenning, on the other hand analyzing the accuracy of this estimate found that since the Landau parameters are not known really well the compressibility can be in the range of $K = 74 - 371\ MeV$.

Pion Multiplicities in Relativistic Heavy Ion Collisions. One of the first attempts to determine the EOS from high energy experiment was done by Stock *et al.* [9]. The idea was that there are less pions observed than one would expect based on a cascade calculation, or on a (noninteracting) ideal gas model. So, some kinetic energy should be missing during the collision, and this causes the smaller pion production rate. This missing energy should then be the compressional energy. In several subsequent works this effect was studied in more sophisticated models. First the compression was calculated by using the EOS from the Rankine-Hugoniot relations for shock compression. Then it turned out that the final expansion should also be taken into account because pion reabsorption is also important. These calculations are quite involved but in most of them a large compressibility, $K > 200\ MeV$ was needed to reproduce the pion multiplicity data. A basic problem was pointed out recently by Maruhn and Stöcker [10]. The pion multiplicities were measured at high energies only, and there is a sizeable energy gap between the ground state and the lowest energy data. This leads to an essential uncertainty if we want to calculate the EOS directly from the data using the Rankine-Hugoniot relations. Most authors do not realize this because they assume some given parametrization of the EOS which connects the two regions in an arbitrary way. To avoid this problem the measurement of K around the ground state would be needed, or in other words the first and second derivative of K (versus n and T) at the ground state.

Sidewards Flow in High Energy Nuclear Collisions. The existence of shock waves and the collective "bounce off" of nuclei of each other was predicted [11, 12] long before the first really convincing experiments [13]. By now the flow analysis is one of the well-established methods to extract information about the EOS, and even about the transport properties of the hot nuclear matter. Earlier it was described satisfactorily in the fluid dynamical model but the more recent transport theoretical models (VUU-BUU-LV) [14, 15] have the advantage of being able to incorporate finite particle number and non-equilibrium effects. The nuclear mean field potential is an organic constituent of these models, so the nuclear compressibility can be explicitly read off from the calculations. The most recent model calculations include also momentum dependent interactions

which are especially important in the initial, not completely equilibrated stage of the collision. These calculations indicate that the compressibility should be in the range of $K = 200 - 400\ MeV$ to fit the flow data. The momentum dependence of the potential allows for the lower compressibility values in this range while momentum-independent interactions lead to stiffer EOS.

Supernova Explosions. A very interesting contribution to the nuclear EOS has been provided by theoretical calculations of Supernova explosions. At late stages of star evolution a star of about $10M_\odot$ may explode if its iron core is in the range of $1.3 - 1.35M_\odot$. Baron *et al.* found that, if the EOS is sufficiently soft at high densities, a successful prompt supernova explosion may occur due to the shock wave which develops after the gravitational collapse of the core [16]. The compression modulus depends on the proton fraction Z/A, which is smaller in supernova than in nuclei. The EOS which led to the explosion had $K(Z/A = 1/3) = 138\ MeV$ and this corresponds to a $K(1/2) = 180\ MeV$.

Neutron Stars. Glendenning [7] used the same EOS [16] to calculate the maximum mass of a neutron star by solving the Tollman–Oppenheimer–Volkov equation. The stiffer the EOS the heavier neutron star can be supported by it. He found that with $Z/A = 1/3$ the maximum neutron star mass would be $1.25M_\odot$. However, the neutron stars are more neutron rich, so $Z/A = 1/5$ might be more appropriate value. In this case the maximum neutron star mass would be only $1M_\odot$. Since there is a neutron star with $M = 1.451 \pm 0.007M_\odot$ (PSR1913+16), and another where the mass is less accurately measured with $M = 1.85^{+0.35}_{-0.30}M_\odot$, these indicate that the EOS may be more stiff than the supernova calculations predicted. According to Glendenning's calculations at least $K = 200\ MeV$ is necessary to account for the observed neutron star masses.

Giant Monopole Resonance. New results for K have been reported by the Groningen group who made precision measurements of the breathing mode of 5 Sn and 4 Sm isotopes [17, 18]. These data were analyzed in conjunction with the already existing data on ^{208}Pb and ^{24}Mg nuclei. They determined the compressibility of infinite nuclear matter, the surface, the isospin and the Coulomb contribution to the data:

$$K_A = K_\infty + K_s A^{-1/3} + K_\tau (\frac{N-Z}{A})^2 + K_C Z^2 A^{-4/3}.$$

The resulting value for K_∞ was $299 \pm 25\ \ MeV$, much more than the value extracted from the earlier data.

The above mentioned cases are not complete, there are still other ways to gain information about the EOS and the compressibility. The most accurate measurements of course still apply to the ground state nuclear matter (Giant Monopoles) or to the cold matter (Neutron Stars). The other data deal with more dynamic situations and with hot and compressed matter so it is not surprising that there is still room for improving the present estimates.

Thermodynamical variables

Before we continue the discussion of the EOS, let us repeat the definitions and notations of the most important thermodynamical variables, particularly because these notations are not completely unique in the literature. Thermodynamics is usually discussed for macroscopic systems of given volume, V, and given particle number, N. If, however, we have a continuum like a fluid where the parameters change from place to place, it is useful to introduce local quantities instead of the global extensives. There are two usual ways to do this: either we introduce *specific extensives* by dividing each extensive by N, or by introducing *extensive densities* by dividing each extensive by V.

Here we will denote all specific extensives by Greek letters and all extensive densities by lower case latin letters. This notation is quite usual but we have to keep in mind that the energy density, denoted here by e is frequently denoted by ϵ. Here we use ϵ for the specific energy. The thermodynamics and the EOS can be formulated in all three formalisms. See Table 4.1.

If one thermodynamical potential in terms of its proper variables is given, all other quantities can be derived immediately by simple derivations. If the microscopic properties of a system are known along with the statistics of the particles, one can calculate the *partition function*. This is related directly to one of the thermodynamical potentials, usually to the Helmholz free energy (Canonical Partition Funct.) or to the Grand-potential (Grand-Canonical Partition Function).

A simplified Equation of State

Considering the most essential properties of the nuclear equation of state for densities below n_0, theoretically a liquid gas phase transition is clearly predicted with $T_c = 15 - 20\ MeV$ and $n_c = 0.3 - 0.5 n_0$. More accurate information and further details can be obtained only from thorough experimental research and by comparing experimental and theoretical results. Before we discuss the properties of the nuclear equation of state let us introduce the general notation of thermodynamic variables (Table 3.1). If we have defined one of the "state functions" or "thermodynamical potentials" in terms of its proper variables like $e(s,n)$, $F(T,V,N)$ or $\mu(T,P)$, all other thermodynamical variables can be obtained by differentiating the thermodynamical potential. For example: The equation of state $P = P(T,n)$ can be obtained from the Helmholtz free energy density as $P(T,n) = n\ f_{,n} - f$. (The comma denotes the partial derivative: $a_{,x} \equiv \partial a/\partial x$.)

THERMODYNAMICAL VARIABLES		
Extensives $S = entropy$	Specific Extensives$(1/N)$ $N = particle\ number$ $\sigma = S/N$	Extensive densities$(1/V)$ $V = volume$ $s = S/V$
$E(S,V,N) = TS - PV + \mu N$ $dE = TdS - PdV + \mu dN$	$\epsilon(\sigma,\nu) = T\sigma - P\nu + \mu$ $d\epsilon = Td\sigma - Pd\nu$	$e(s,n) = Ts + \mu n - P$ $de = Tds + \mu dn$ eg.: $P = -e + se_{,s} + ne_{,n}$
One intensive replaces an extensive:		
Enthalpy:		
$H(S,P,N) = E + PV = TS + \mu N$ $dH = TdS + VdP + \mu dN$	$\chi(\sigma,P) = \epsilon + P\nu = T\sigma + \mu$ $d\chi = Td\sigma + \nu dP$	$w(s,n) = e + P = Ts + \mu n$ $dw = Tds + \mu dn$ (redundant)
Helmholtz free energy:		
$F(T,V,N) = E - TS =$ $= \mu N - PV$ $dF = -SdT - PdV + \mu dN$	$\Phi(T,\nu) = \epsilon - T\sigma = \mu - P\nu$ $d\Phi = -\sigma dT - Pd\nu$	$f(T,n) = e - Ts =$ $= \mu n - P$ $df = -sdT + \mu dn$
X - potential:		
$X(S,V,\mu) = E - \mu N = TS - PV$ $dX = TdS - PdV - Nd\mu$	$-$	$x(s,\mu) = e - \mu n = Ts - P$ $dx = Tds - nd\mu$
Two intensives replace two extensives:		
Gibbs free energy:		
$G(T,P,N) = E + PV - TS = \mu N$ $dG = -SdT + VdP + \mu dN$	$\mu(T,P) = -T\sigma + P\nu$ $d\mu = -\sigma dT + \nu dP$	$-$
Grand potential Ω:		
$\Omega(T,V,\mu) = -PV =$ $= E - TS - \mu N$ $d\Omega = -SdT - PdV - Nd\mu$	$-$	$z(\mu,T) = -P =$ $= e - Ts - \mu n$ $dz = -sdT - nd\mu$
Y-potential:		
$Y(S,P,\mu) = E + PV - \mu N$ $dY = TdS + VdP - Nd\mu$		
Gibbs–Duhem relation		
$E + PV - TS - \mu N = 0$ $-SdT + VdP - Nd\mu = 0$	$d\mu = -\sigma dT + \nu dP$	$dP = sdT + nd\mu$

Table 4.1: Thermodynamical potentials

As an example which is used widely in the literature [19, 20, 21, 22, 23, 24, 25, 26, 27], let us define an analytic parametrization for the nuclear equation of state. The thermodynamical potential $e = e(n, s)$ as a function of baryon density n, and entropy density s is given by:

$$e(n, s) = e_c(n) + e^*_F(n, s) - e^*_F(n, 0),$$

where $e_c(n)$ is the ground state energy density, and $e^*_F(n, s)$ is the energy density of an ideal Fermi-gas. We can parametrize the ground state energy density as [25]

$$e_c(n) = n_0 \sum_{i=2}^{5} a_i \ (\frac{n}{n_0})^{\frac{i}{3}+1},$$

where $a_i = +21.1, -38.3, -26.7, +35.9\ MeV$ for $i = 2, ..., 5$ respectively. This parametrization yields a binding energy $\epsilon_0(n_0) \equiv \epsilon(n_0) = e_0(n_0)/n_0 = -8\ MeV$ (instead of the usual infinite nuclear matter value of -16MeV to simulate finite size effects) and a nuclear compressibility $K = 210\ MeV$ at $n_0 = 0.15 fm^{-3}$. Note that this parametrization is used for small nuclear densities $n < 2n_0$. At high densities the sound speed exceeds the speed of light. For the thermal part of the energy density we use the non-relativistic ideal Fermi-gas approximation because for the low density and temperature at the break-up, relativistic corrections are negligible. Then the energy density e depends on the density n and specific entropy $\sigma = s/n$ as [28]:

$$e^*_F(n, s) = (\frac{n^{5/3}}{m}) y(\sigma),$$

where y is a dimensionless quantity and it depends on the dimensionless specific entropy σ (or μ/T). $y(\sigma)$ can be given in integral form [28], but in actual calculations usually practical analytic parametrizations are used [25, 29]. A parametrization for the inverse function, $\sigma(y)$ given in ref. [25] is

$$\sigma(y) = 0.5213 + 1.5 \ln(y + 0.7064) + \frac{1.809 y^{1/2}}{1 + 1.139 y^{1/3} + 1.417 y + 1.014 y^{3/2}}.$$

Other thermodynamical quantities can then be calculated from standard thermodynamical relations:

$$T(n, s) = e_{,s} = \frac{n^{2/3}}{m} y'(\sigma),$$

$$\mu(n, s) = e_{,n} = \frac{1}{3} \sum_{i=2}^{5} (i + 3) a_i (\frac{n}{n_0})^{i/3} \ + \ \frac{5}{3n} e^*_F(n, s) \ - \ T(n, s)\sigma,$$

$$P(n, s) = P_c(n) + \frac{2}{3} e^*_F(n, s),$$

where $P_c(n) = \frac{n_0}{3} \sum_{i=2}^{5} i a_i (\frac{n}{n_0})^{i/3+1}$. The equation of state represents a stable equilibrium configuration only if the energy has a minimum. This condition is satisfied if the matrix $M_{ik} = e_{,ik}$ (where $k, i = n, s$) is positive definite. This requirement leads to two

independent constraints on the derivatives of the thermodynamical parameters [28], (Section 21):

$$c_\nu = Ts(T,\nu)_{,T} > 0, \quad \text{and} \quad \kappa_T = -\frac{1}{\nu}\nu(P,T)_{,P} > 0,$$

where κ_T is the isothermal compressibility, and c_ν is the isochoric (under constant specific volume) specific heat. In nuclear physics the compressibility is customarily characterized by another positive quantity:

$$K_\sigma = 9P(\sigma,n)_{,n}\,, \quad \text{and} \quad K_T = 9P(T,n)_{,n}\,.$$

If these requirements are satisfied then the adiabatic sound speed is positive and larger than the isotherm sound speed: $u_\sigma^2 = (c_p/c_\nu)u_T^2 > u_T^2 > 0$.

There are regions in the $[T,n]$ plane where these stability conditions are not satisfied. That is, our equation of state does not represent a stable equilibrium. The region where the isotherm sound speed, $u_T^2 < 0$ is contained within the unstable region. There are speculations [19, 30] that the matter in a relativistic heavy ion collision might penetrate into the unstable region because of rapid expansion during the collision.

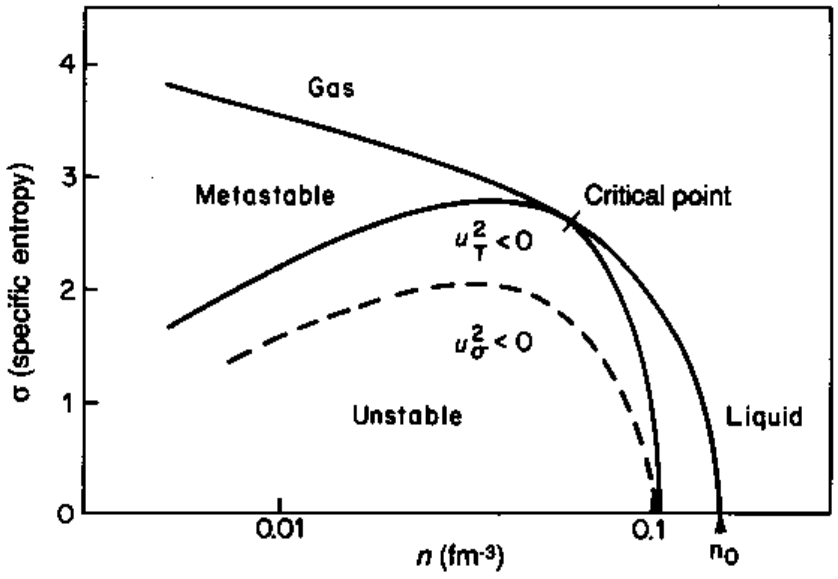

Figure 4.1: Phase diagram on the entropy density plane. Phase equilibrium is possible above the critical entropy too! u_σ and u_T are the adiabatic and isotherm sound speeds. The stable gas and liquid phases are separated from the metastable region by the Maxwell construction line. Reproduced by permission of Elsevier Science Publishing from [29].

Phase coexistence between liquid and gas phases

If the temperature and density of our system falls into the unstable region, or even close to this region, it may split up into two phases. Theoretically this is also a consequence of the stability requirements. If we allow for two co-existing liquid (L) and gas (G) phases we have one more free parameter in our thermodynamical problem, the volume fraction of the phases $i = L, G$:

$$\lambda_i = V_i/V,$$

or equivalently the particle number fractions:

$$\alpha_i = N_i/N.$$

The sum of both is normalized to 1, $\alpha_L + \alpha_G = 1$, $\lambda_L + \lambda_G = 1$ and there is a relation among α and λ:

$$\lambda_i = \frac{n}{n_i}\alpha_i, \quad \text{and} \quad \lambda_L = \frac{n - n_G}{n_L - n_G}.$$

Now the requirement of the energy minimum leads to Gibb's criteria of phase equilibrium: $P_L = P_G = P$, $T_L = T_G = T$, and $\mu_L = \mu_G = \mu$. For a two phase system these requirements restrict the region of stability on the $[n, s]$ plane to a line! This is the Maxwell construction line, and it lies in the stable region of the previous stability study. Fig. 4.1.

Outside the region confined by this line the matter is stable in one single phase. Within this line but outside the $u_T^2 < 0$ region the matter is mechanically stable if formation of the other phase is hindered or delayed. The region between the Maxwell construction line and the boundary of instability $u_T^2 < 0$ is metastable, matter can be stable in this region if the other phase is not present. These are the phenomena of superheating and supercooling which are quite common in relatively slow thermodynamic processes, so we expect these phenomena to occur in the much faster relativistic heavy ion collisions too. If we solve the Gibb's criteria for our equation of state the extensive thermodynamic quantities are given along the Maxwell construction line as functions of one intensive parameter, say T. In a heavy ion reaction in principle we might reach the phase mixture region with arbitrarily high energy collisions in the subsequent quasi-adiabatic expansion [21] if the break-up density is sufficiently low.

Critical exponents

It will be imperative to mention a few results about critical phenomena. The critical opalescence in liquid gas phase transition was observed more than a century ago and in the 1940's Guggenheim [31] realized that several fluids behave similarly around the critical point of the liquid-gas phase transition. This lead to the extended study of the critical exponents which started in the 1960's. (see ref. [32]). Let us introduce the "order parameter" $n_L^{eq}(T) - n_G^{eq}(T)$, $(= n_L - n_G)$ and the relative deviation from the critical temperature

$$\varepsilon = (T - T_c)/T_c.$$

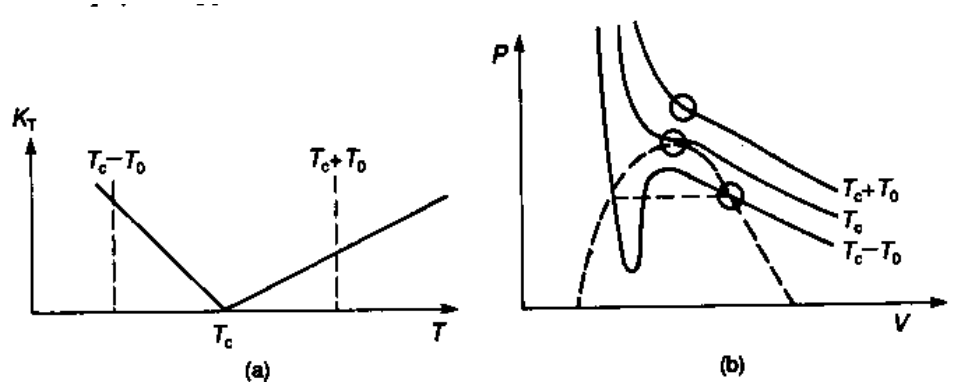

Figure 4.2: Determination of the critical behavior. Reproduced by permission of Oxford University Press from [32].

Guggenheim's observation was that just below the critical point

$$n_L - n_G \propto (-\varepsilon)^\beta,$$

where β is a *critical exponent*, which was found to be universally $\beta = 1/3$ for the liquids he studied. Similarly, another critical exponent δ is defined at $T = T_c$ by

$$P - P_c \propto (n - n_c)^\delta \mathrm{sign}(n - n_c).$$

At the critical point the isotherm compressibility, κ_T, diverges and at the same time K_T tends to zero. See Fig. 4.2. This divergence can be parametrized by a critical exponent also:

$$\kappa_T \propto (-\varepsilon)^{-\gamma'}, \quad \text{if}: \ \varepsilon < 0,$$
$$\kappa_T \propto (\varepsilon)^{-\gamma}, \quad \text{if}: \ \varepsilon > 0,$$

below and above the critical point, respectively. Similarly the specific heat can be parametrized around the critical point as:

$$c_\nu \propto (-\varepsilon)^{-\alpha'}, \quad \text{if}: \ \varepsilon < 0,$$
$$c_\nu \propto (\varepsilon)^{-\alpha}, \quad \text{if}: \ \varepsilon > 0.$$

The critical exponents can be calculated for a given equation of state. So far in nuclear physics applications, however, the critical exponents were seldom evaluated. In Table 4.2 (from [32]) some critical exponents are listed for different models and systems:

	α	α'	β	γ	γ'	δ
	$T > T_c$	$T < T_c$	$T < T_c$	$T > T_c$	$T < T_c$	$T = T_c$
Fluids	~ 0.1	~ 0.1	~ 0.34	1.35	~ 1	4.2
3 dim Ising model	$\sim 1/8$	$\sim 1/8$	$\sim 5/16$	$\sim 5/4$	$\sim 5/4$	~ 5
Classical mean field (Van der Waals)	0	0	1/2	1	1	3

Table 4.2: Values of critical-point exponents for selected systems.

In [24] for a simple analytic equation of state the above mentioned critical exponents were evaluated and the same values were obtained as in the Van der Waals theory.

A discussion of the critical point properties of a Skyrme interaction is given in [33, 34]. The similarity between the nuclear liquid gas transition and a ferromagnetic system is studied in [35].

Fragment mass distributions

There are numerous models describing fragment mass distributions. A concise review is given in ref. [29]. The overwhelming majority of the models describe a static situation at the "freeze-out moment". It is possible that at this moment some excited nuclear fragments exist and their final decay by particle emission is also considered in the most sophisticated calculations [19, 36, 37, 38]. Most models are of statistical origin and in principle they would yield an equation of state. (This is not so in some percolation models where the connection between the bond-breaking probability and physical quantities like energy and density is not defined.) The evaluation of the equation of state is, however, not a trivial task and in practice it is very seldom performed. Thus it is not always clear whether a statistical model which satisfactorily describes the experimental data exhibits a liquid- gas phase transition or not. Here, only some very basic facts will be mentioned about the fragment distributions, and a few of the recent works not mentioned in ref. [29] will be discussed.

At high beam energies the system breaks up after the collision with considerable excitation energy, so that the system is rather dilute at freeze out. In this case the description of fragment mass distribution is simpler because we are close to an ideal gas behavior. This situation will be discussed in the next section. At lower accelerator energies the situation might get more involved, due to the influence of the liquid gas phase transition. Both in equilibrium and in non-equilibrium expansion, if finally two phases exist, they are very different. The gas phase is very dilute and has a large entropy $\sigma = 3.5 - 4$, while the liquid phase has low entropy $\sigma = 1 - 2$ and density close to n_0. What is the fragment distribution in such a phase mixture? The gas phase, having large entropy, consists of very light fragments with an exponentially decreasing mass spectrum. In this limit there is not much difference in the model estimates. From the experimentally observed light fragment (proton to alpha) abundances all previously discussed models extract an entropy value on the order of $3 - 4$, down to a few 100 MeV beam energy or even lower [25, 39].

The prediction of the mass distribution of heavier fragments representing the liquid phase is a more involved problem. The thermodynamical limit does not yield a definite prediction. Surface effects, nuclear size, reaction geometry, fission, final state decays and even the collective flow pattern may influence the intermediate and heavy fragment mass distribution. The light fragment distributions are not independent of the liquid phase. The final decay or fission of the heavier fragments can change the light fragment distributions too. While for the light fragments the grand canonical treatment is acceptable, the behavior of intermediate mass fragments is already strongly influenced by the limited nucleon number. These finite size and surface effects will be discussed later in sect. 3.1.2.

Law of Mass Action

The law of mass action as applied to ideal gases is the most basic law describing the fragment distributions. The application of Law of Mass Action for Relativistic Heavy Ion Reactions was first proposed by Mekjian in 1978 [40]. Ignoring relativistic, quantum and isospin effects the number density of ground state nuclei, n_g, of mass number A is

$$n_g(A) = g_A(\frac{mTA}{2\pi})^{3/2}\ e^{A(\mu+W_0)/T} \tag{4.1}$$

where g_A is the spin degeneracy, m is the nucleon mass, and $W_0 > 0$ is the binding energy per nucleon. The non-relativistic chemical potential per nucleon, μ, is related to the relativistic chemical potential by $\mu = \mu_{rel.} - m$. If $\mu < -W_0$ then the number density is an exponentially decreasing function of A. Once $\mu = -W_0$ the nuclei would like to coalesce, to form uniform liquid nuclear matter.

Using Eq.(4.1) for p and d, and neglecting the binding energy difference, the deuteron to proton ratio is: $x \equiv n_d/n_p = \frac{3}{2}\ 2^{3/2}e^{\mu/T}$. It follows that $\mu/T = lnx - 1.445$. Now from $e = Ts + \mu n - p$ by inserting the Boltzmann ideal gas expressions $e = n\frac{3}{2}T$ and $p = nT$, we get $\sigma = s/n = -\mu/T + 2.5$. Using the expression of μ/T in terms of x we can express the entropy by the d/p ratio:

$$\sigma = 3.945 - \ln x.$$

This result was first obtained by Siemens and Kapusta [41], and it served as the basis for experimental measurements of entropy later.

At the freeze out, however, not only nuclei in their ground states but also nuclei in various excited states will be present. To explicitly count them we should additively include

$$n_i(A) = \frac{g_i}{g_A} n_g(A) e^{-E_i^*/T},$$

where g_i is the degeneracy of the excited state and E_i^* is its excitation energy above the ground state. If the total baryon density is known as usual, μ can be obtained from the total nucleon density of the system at break-up

$$n = \sum_A \sum_{g,i} A n_i(A).$$

There are several large numerical models which calculate the nuclear fragment mass distribution based on the law of mass action for ideal gases. In [42, 43, 36, 44] all known nuclear states with $A < 16$ having a width $\Gamma < 1\ MeV$ were included explicitly, and these levels for $A > 4$ were supplemented by an effective level density formula for the higher lying states which are not known experimentally [36, 45]. Since this model includes an excluded volume approximation, the equation of state belonging to this is somewhat different from the ideal gas equation of state, the pressure increases sharper at higher densities as $n \to n_0$. It does not show a first order phase transition because only repulsive interactions are included, long-range attraction is not. This code has recently been named FREESCO [45]. It is an approximate microcanonical event generator where the exact microcanonical fragment distribution is calculated recursively by approximating the one-fragment inclusive distributions in each step by the grand canonical distribution. Another fragmentation model is the Quantum Statistical Model (QSM) [46, 19] which calculates the grand canonical one-fragment inclusive distribution functions, but it includes as a special feature quantum statistics. The known particle-stable and metastable nuclear states with $A < 20$ are included in this model, and the repulsive interactions are simulated by the excluded volume approximation also.

Both models are based on the same physical picture: namely a first fast explosion creating light and medium mass fragment according to the law of mass action followed by sequential evaporation from these products in a final decay step. These two models, which can be regarded as different implementations of a general statistical model for nuclear disassembly, were compared to each other and to experimental results recently [38]. It was found that in the breakup temperature range of $T = 30 - 90\ MeV$ there is an essentially unique relationship between the "d-like/p-like" fragment ratio, X, and the specific entropy of the ideal gas mixture σ. The lower temperature isotherms begin to deviate from the universal curve at low entropies. At high entropies and low X the "Siemens–Kapusta" formula [41] $\sigma = 3.945 - \ln X$ is a good approximation to the results of the more sophisticated statistical models. The experimentally determined values of X at the maximum charged particle multiplicity for different experiments ranging from 400 to 1050 $MeV/nucleon$ beam energy [47] are between 0.48 and 0.68. According to

both above mentioned models this corresponds to entropy values of $\sigma = 3.45 - 3.9$ at the break-up.

In intermediate energy heavy ion reactions temperatures extracted from the energy spectra of different fragments with a moving source fit.[1] The temperatures are impressively constant independently of the particle type[48]! This might suggest thermal and phase equilibrium. The above-mentioned experiments [47] are of relatively high energy and we do not expect the system to reach the nuclear liquid-gas phase transition before breakup. Therefore the above theoretical models which neglect attractive interactions yield satisfactory results. At lower energies the same is not true anymore. While the light fragments show a relatively high entropy according to the analysis, the intermediate fragments have an entropy value by almost one unit smaller [49]. This indicates that the above model cannot yield satisfactory results at lower energies, and other effects like the nuclear liquid-gas phase transition [50], microcanonical statistics, attractive and Coulomb interactions should be considered.

[1] The moving source fit first locates the c.m. of the emitted fragments in the phase space, and then an ideal thermal source moving with this speed is fitted to the energy spectra of the fragments to determine the temperature, T.

4.1.2 Finite systems and fragment abundances

Phase transition in finite systems

For a system with a finite number of particles, in a very strict sense no phase transitions exist and fluctuations can be important. Could it be that nuclear systems are so small that these fluctuations completely wash out the first order liquid-gas phase transition below T_c? This question was first addressed in the context of heavy ion reactions in ref. [51]. Consider a system held at fixed temperature and pressure. We are interested in density fluctuations of this system. Instead of a nuclear system it may be helpful to think of a finite number of particles placed in a cylinder which is maintained at a fixed temperature T, with a movable piston at one end which exerts a constant pressure, P, on the gas particles. Only a finite number of particles per unit time collide with the piston, so the position of the piston will fluctuate with time about some mean position. Thus the density of the gas will also fluctuate.

The ratio of probabilities for a system to be at density n_1 or n_2 is

$$p(n_2)/p(n_1) = \exp[-(G(n_2) - G(n_1))/T]$$

where $G(n)$ is the Gibbs free energy at p and T. For an infinite system in equilibrium the density n is determined by the EOS once p and T are specified. We want to know, however, the probability of having the system at a non-equilibrium density. It is necessary therefore to know $G(n)$ for densities not permitted by the equation of state. This is provided by the Landau theory [28] in which n is treated as an independent variable not restricted by p and T. Such an analysis was carried out in ref. [51]. A simple form for the nuclear EOS was chosen

$$p = -a_0 n^2 + 2a_3 n^3 + nT, \tag{4.2}$$

($a_0 = 293\ MeVfm^3$, $a_3 = 666\ MeVfm^6$, $n_0 = 0.15fm^{-3}$, $W_0 = 8\ MeV$) which has a critical point at $n_c = a_0/(6a_3)$, $T_c = a_0 n_c$, $P_c = \frac{1}{3}T_c n_c$. One can expand the EOS (4.2) around the critical point by introducing $t = T - T_c$ and $\eta = n - n_c$ so that,

$$P - P_c = n_c t + t\eta + 2a_3\eta^3. \tag{4.3}$$

This equation of state behaves similarly to the Van der Waals EOS, for negative t the phase equilibrium points can be found by the Maxwell construction [33, 34, 51]:

$$\eta_L = -\eta_G = \sqrt{-t/2a_3}.$$

The essential feature of the Landau approach is the construction of the free energy in terms of a power series in the order parameter η. Thus $G(p, T, \eta)$ will be defined at nonequilibrium values of η too, for a fixed p and T. In the neighborhood of the critical point the Gibbs free energy is then:

$$G(p, T, \eta) = G_0(p, T, \eta) + \alpha(p, T)\eta + A(p, T)\eta^2 + C(p, T)\eta^3 + B(p, T)\eta^4 + ... \tag{4.4}$$

The EOS (4.3) can be used to obtain the coefficients in (4.4) since the equilibrium value of η can be obtained from the requirement that G has an extremum in equilibrium:

$$\frac{\partial G}{\partial \eta} = \alpha + 2A\eta + 3C\eta^2 + 4B\eta^3 = 0. \tag{4.5}$$

This should be the EOS (4.3). Comparing (4.3) and (4.5) we obtain for the coefficients: $\alpha = -(P - P_c - n_c t)D$, $A = \frac{1}{2}tD$, $B = \frac{a_3}{2}D$, $C = 0$, where $D = N/n_c^2$ and N is the total number of nucleons in the system. This choice of D gives the correct G for equilibrium states. So the G in the order parameter expansion is

$$G = G_0(p,T) + \frac{N}{n_c^2}[-(P - P_c - n_c t)\eta + \frac{1}{2}t\eta^2 + \frac{a_3}{2}\eta^4].$$

The density or η values at the phase equilibrium η_L and η_G are the solutions of the EOS (4.3) if $P = P_c + n_c t$. At this pressure, P, the probability distribution $p(n)$ of the density of the system is given by

$$R(n) = \frac{p(n)}{p(n_L)} = \exp[-(G(p,T,\eta) - G(p,T,\eta_L))/T]. \tag{4.6}$$

This probability is plotted in Fig. 4.3 (from [29]).

For T not too close to T_c there are two well defined peaks corresponding to a separation of liquid and gas phases, thus exhibiting a reasonably sharp first order phase transition. As T approaches T_c from below, the valley separating the two peaks gets filled in and the distinction between liquid and gas gets washed out. At T_c the distribution is flat at the top. These large density fluctuations at the critical point give rise to the phenomenon of critical opalescence in atomic systems.

To find the relative probability for a system composed of N nucleons, N not necessarily 100, one simply scales the results of Fig. 4.3 to the power $N/100$, $R^{N/100}$, because in Eq. (4.6) the Gibbs free energy was taken to be proportional to the total number of particles. For the density midway between n_L and n_G, the relative probability assumes the simple form $R(\frac{1}{2}(n_L + n_G)) = \exp(-0.75(T - T_c)^2 N/(TT_c))$. Thus a larger number of nucleons sharpens the distinction between liquid and gas phases.

Droplet and bubble formation

Let us now consider the surface effects. Suppose that in a central collision between heavy nuclei an intermediate state of high temperature and density is reached and that subsequently it undergoes an adiabatic expansion. Then, no matter what the entropy per baryon is, it will eventually intersect the Maxwell curve separating liquid and gas phases if it does not break up before. (See Fig. 4.1). What happens next depends on whether the system hits the Maxwell curve from the liquid side ($n > n_c$) or from the gas side ($n < n_c$). If from the liquid side, bubbles begin to form, and if from the gas side, droplets begin to form. For definiteness we shall consider the formation of droplets in a gas.

The probability of droplet formation is estimated by calculating the change in the Gibbs free energy of the system when a droplet appears in the gas [28, 52]. Suppose

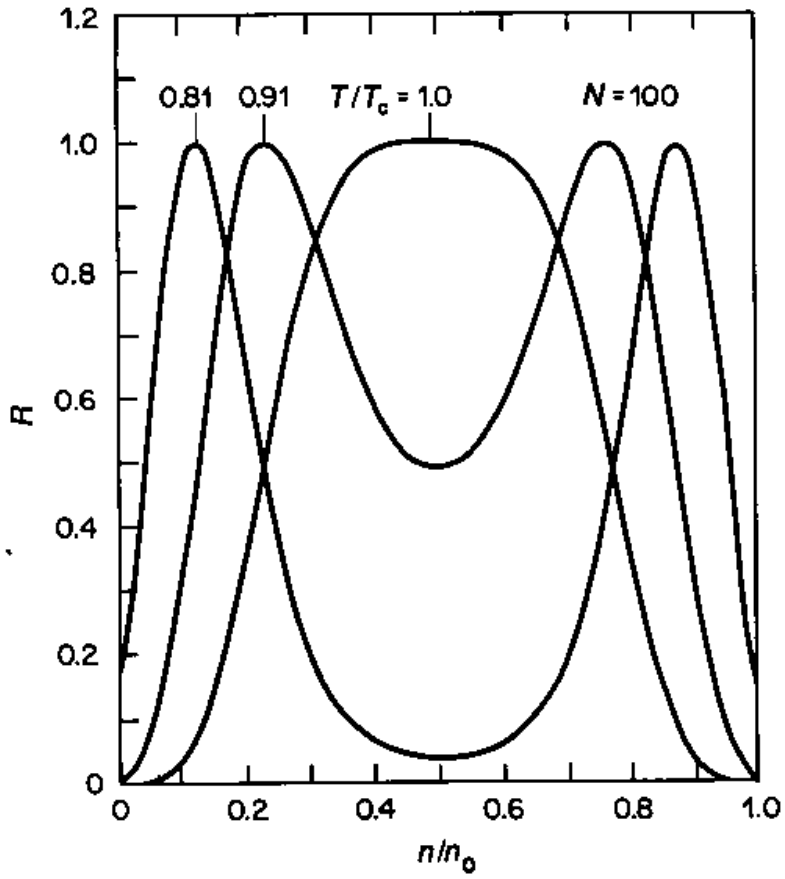

Figure 4.3: The relative probability for the system to be at density n compared to the thermodynamically favored values n_L or n_G. The number of nucleons is $N = 100$. The pressure is the equilibrium pressure. Reproduced by permission of Elsevier Science Publishing from [29].

that a spherical droplet containing A nucleons spontaneously forms in a gas consisting originally of a total number $A + B$ nucleons.

$$G_{no\ drop} = \mu_G(A + B), \tag{4.7}$$

$$G_{drop} = \mu_L A + \mu_G B + 4\pi R^2 \sigma_s + T\tau \ln A. \tag{4.8}$$

Here μ_G and μ_L are the nucleon chemical potentials in the gas and liquid phase respectively at pressure p and temperature T. The third term in Eq. (4.8) is the surface free energy for a droplet of radius R and with surface tension $\sigma_s = \sigma_s(T)$. The last term in Eq. (4.8) was introduced by Fisher [53] in his droplet model. It takes into account the fact that the droplet surface closes on itself which reduces the total entropy associated with surface fluctuations. He introduced the critical exponent τ based in the critical exponent δ as $\tau = 2 + 1/\delta$, and since in mean field theories $\delta = 3$, thus $\tau \equiv 2 + 1/\delta = 7/3$.

The probability of formation of the droplet is proportional to $\exp(-\Delta G/T)$, where ΔG is the difference between Eqs. (4.8) and (4.7). The yield of a fragment of mass A is

$$Y(A) = Y_0 \exp[\frac{\mu_G - \mu_L}{T} A - \frac{4\pi r_0^2 \sigma_s}{T} A^{2/3} - \tau \ln A]. \tag{4.9}$$

Here Y_0 is a normalization constant and r_0 is related to the droplet radius by $R = r_0 A^{1/3}$ and to the density by $n_L^{-1} = 4\pi r_0^3/3$. The importance of the surface effects was first observed by the Purdue–Fermilab group [54, 55, 56] and applied to high energy, $80 - 350\ GeV$, proton-nucleus reactions. Mass and charge distributions for A up to 30 were measured with higher precision than ever before possible because of the use of an in-beam gas jet target. Arguments based on emulsion experiments and on temperature measurements suggested that these fragments come from a common thermalized source. It was noticed that a power law $A^{-2.65}$ fits the data better than an exponential $e^{-\alpha A}$. The novel interpretation was that the target nucleus was almost instantaneously heated by the passage of the ultra-relativistic proton, and that subsequently the heated nucleus expanded in size until it passed through the critical point, $T = T_c$ and $n = n_c$, of the liquid-gas phase transition. At that point the distribution of droplets is $Y(A) = Y_0 A^{-\tau}$ because in Eq. (4.9) $\mu_G = \mu_L$ and $\sigma_s = 0$ at the critical point, so the volume and surface free energy terms vanish. There is no distinction between liquid and gas at the critical point, only long range fluctuations.

There are at least two difficulties with the above interpretation. First, why should one be so lucky to hit the critical point of nuclear matter accidentally with proton energies ranging from 80 to 350 GeV and with targets so different in size as krypton and xenon? Second, according to Fisher's version of the droplet model, $2 < \tau < 2.5$, whereas the data were outside this range.

The group recently remeasured the mass distributions depending on the proton energy in the range of $E_p = 1 - 20\ GeV$ [57]. Based on Eq. (4.9) they introduced a parametrization

$$Y(A) = Y_0\ x^{A^{0.6386}}\ y^A\ A^{-\tau}.$$

Thus if the system would approach the critical point x and y, should tend to 1, according to (4.8). They determined x and y by fitting the experimental mass yields at different energies and found that x and y tend to 1 monotonically from below (above) respectively! At $E_p = 2\ GeV$, $x = 0.2, y = 1.4$ and around 10 GeV both reach 1 already. At this fit τ was kept constant at 2.2. These data indicate that the path in the thermodynamical space is really energy dependent and it gets in the vicinity of the critical point only at higher proton energies. When τ was independently fitted to the data it showed a similar convergence to $\tau \approx 2.1$ from below.

These recent results of the group are consistent with the liquid gas phase transition picture. With increasing bombarding energy multifragmentation occurs first in the mechanical instability region, then in the supersaturated vapor region and finally at energies above 10 GeV in the critical region.

To draw a conclusive opinion about the nuclear fragmentation models would be too premature now. One remark, however, is probably important to make: The connection between the nuclear fragmentation models and the nuclear EOS should be firmly

established before a final conclusion about the nuclear liquid- gas phase transition can be drawn. So far the EOS underlying the statistical models was seldom calculated (apart from some simple cases [36]). In statistical fragmentation models the evaluation of the EOS is in principle possible although it may be very cumbersome. We may be confident, however, that in the near future a consistent nuclear EOS and fragmentation theory will arise form the large scale theoretical effort.

On the experimental side the problems are to separate central heavy ion collisions and eliminate geometric effects arising in peripheral reactions. The most promising development in the near future will be provided by the 4π detector at Michigan State University (MSU) with good mass and energy resolution. This will lead to a major step in understanding the mechanism of heavy ion reactions in the nuclear liquid gas phase transition region.

4.2 The Nuclear EOS and Quark Gluon Plasma

In the field of the equation of state of the quark gluon plasma most of the theoretical work is invested in the study of pure SU(N) Yang-Mills theory on the lattice. These calculations, however, are so far restricted to zero net baryon density or zero chemical potential [58].

Lattice QCD calculations will be discussed later in the Chapter on the Search for Quark Gluon Plasma. To form a low or "zero" baryon density matter in the deconfined phase one expectedly needs extremely high energy. Relatively simple "phenomenological" theories on hand, are able to provide us with an equation of state (EOS) in the phase transition region for cold matter [59, 60, 61], for zero baryon charge at finite temperature [62], or in the complete phase space for finite density and temperature [16, 63, 64, 65, 66, 67, 68]. These phenomenological equation of state studies can yield a good qualitative insight into the phase transition problem until a priori QCD calculations will be available in the complete density-temperature domain. There are even some advantages in the phenomenological approach: The results of these nuclear EOS studies can easily be incorporated into the phenomenological phase transition models.

4.2.1 Hadronic Equation of State

We discussed the nuclear equation of state extensively in these lectures. Similar phenomenological EOS can be used here too, however, more attention to high temperature and high density behavior is necessary.

In sect. 4.1.1 we introduced a simple parametrization of the nuclear EOS. In the literature several other parametrizations are also used. In one other parametrization the energy density e in terms of density n and temperature T is parametrized as

$$e = n[m - W_0 + K(n/n_0 - 1)^2/18 + 3T/2], \tag{4.10}$$

where m is the nucleon rest mass, $W_0 > 0$ is the binding energy, the third term is the compressional energy e_c, usually called "quadratic", and the last term is the thermal energy described as that of a Boltzmann ideal gas. (This approximation must be sufficient at high temperatures). At high temperatures at least pion pairs should also be taken into account. Otherwise the energy density would be zero in baryon free matter. The simplest way to take this additive mesonic component into account, is by neglecting their rest mass:

$$e_m = g_1(\pi^2/30)T^4, \quad P_m = e_m/3, \quad s_m = \frac{4}{3}e_m/T,$$

where g_1 is the degeneracy of states. If we consider only pions, $g_1 = 3$ and so:

$$e_\pi = \pi^2 T^4/10, \quad P_\pi = \pi^2 T^4/30, \quad s_\pi = 4\pi^2 T^3/30.$$

At high temperatures some nucleons can be excited. The most important contribution is coming from delta resonances. Since the total baryon charge is conserved, $n = n_N + n_\Delta$, in the Boltzmann approximation the delta to nucleon ratio is given by

$$n_\Delta/n_N = 4(m_\Delta/m_N)^{3/2} \exp(-[m_\Delta - m_N]/T).$$

This causes a change in the energy density where the rest mass term is now $n_\Delta m_\Delta + n_N m_N$, and also influences the other thermodynamical variables. The sum of two or more of the above mentioned combinations provides the total hadronic (h) EOS. In the simplest case $e_h = e_n + e_\pi$.

Compressional part of the nuclear EOS

The requirement of causality provides several theoretical constraints on the EOS [69] at high densities and limits the choice of the functional form of the compressional energy that can be used in a phenomenological EOS. Very *hard* equations of state may lead to a superluminal speed of sound (see ref. [70]). However, this is not a problem if the acausality occurs in a region of the phase diagram where matter is in the mixed or plasma phase, because the phase transition softens the matter. The specific energies $\epsilon = e/n$ at high densities for some phenomenological parametrizations are:

- "Linear" and "Quadratic" (Ref. [71])

$$\epsilon_L(n;K) = E_B + \frac{K}{18}\frac{(n-n_0)^2}{nn_0},$$

$$\epsilon_Q(n;K) = E_B + \frac{K}{18}\frac{(n-n_0)^2}{n_0^2}.$$

- "Sierk–Nix" (Ref. [20])

$$\epsilon_{SN}(n;K) = E_B + \frac{2K}{9}\left(\sqrt{\frac{n}{n_0}} - 1\right)^2.$$

- "Grant–Kapusta" (Ref. [70])

$$\epsilon_{GK}(n;K,a) = \epsilon_{SN}(n;K) + a\left(\sqrt[3]{\frac{n}{n_0}} - 1\right)^3.$$

The corresponding density of the free energy is

$$f_{compr}(n;K) = n\epsilon_{compr}(n;K).$$

All of these parametrizations are acausal at sufficiently high densities. Fortunately the acausality occurs well within or beyond the mixed or plasma phase for all the parametrizations except the "Quadratic". The basic parameter is the (isothermal) compressibility K, which is defined as

$$K = 9\left(\frac{\partial P}{\partial n}\right)_{n=n_0,T=0}.$$

The value of K can be determined in several different ways (see [72] and references therein). It is usually around $K = 100 - 400\ MeV$ but depends on the parametrization chosen [70] and the point in the phase diagram at which the data are fitted. We have chosen in most calculations the "Sierk–Nix" parametrization with $K = 550\ MeV$ which reproduces the pion multiplicity data of Stock *et al.*,[73] if one assumes that the pion properties are the same as in vacuum. This is higher than the generally acceptable compressibility of nuclear matter in the ground state, but it corresponds

to $K = 275\ MeV$ in the "Quadratic" parametrization! The two parametrizations with different compressibilities yield essentially the same EOS [70] for densities of interest. So, it should be regarded as a simple parametrization simulating the effect of momentum-dependent interactions which also make nuclear matter stiffer at high temperatures.

It is important to emphasize that the nuclear EOS strongly influences the phase transition and the phase diagram. The compressional energy is particularly important. When it is neglected [68] the resulting phase diagram may lead to pathological behavior, the matter at n_0, and $T = 0$ being in the mixed phase. (Also the possibility of a first order phase transition is restricted to a very small range of bag constants: $\sqrt[4]{B} = 149 - 154\ MeV$ [68].) One way of including the compressional energy into the hadronic phases is the excluded volume approximation [65], which is a standard way of treating nuclear matter in relativistic nuclear collisions, first introduced in ref. [46]. This approximation leads to a phase diagram [65] similar to the nuclear EOS-s with explicit compressional energy.

4.2.2 QGP Equation of State

The QCD Lagrangian leads to an equation of state which should in principle describe both the nuclear and quark-gluon plasma phase. Due to the nonlinear interactions it is not easy to find this EOS. At high energy densities, however, the coupling tends to zero between quarks and gluons and an "asymptotic freedom" sets in. In this limit, i.e. at high enough temperatures and densities, the EOS of the quark world [74] would be quite trivial. It would correspond to a non-interacting gas of N_f flavor quarks that come in N_c colors, and $(N_c^2 - 1)$ spin 1 gluons. In this case the EOS is given by the Stefan–Boltzmann type expressions:

$$e_{SB}(T,\mu) = \frac{\pi^2}{15}(N_c^2 - 1 + \frac{7N_cN_f}{4})T^4 \ + \ \frac{N_cN_f}{2}(T^2\mu^2 + \frac{\mu^4}{2\pi^2}),$$

$$P_{SB}(T,\mu) = \frac{1}{3}e_{SB}(T,\mu),$$

$$n_{SB}(T,\mu) = \frac{N_cN_f}{9\pi^2}(\mu^3 + \pi^2T^2\mu),$$

where T and $\mu = \mu_q$ are the quark temperature and chemical potential ($\mu_b = 3\mu_q$), and $n_{SB} = n_b$ is the *baryon charge* density in the quark phase.

It is plausible that the vacuum in which the ideal gas of quarks and gluons exist differs from our everyday vacuum. Since we do not see the quarks and gluons in our nonperturbative physical vacuum [75] , this vacuum should have an energy lower than the QCD perturbative vacuum where they can exist. Phenomenologically, we can try to take this effect into account by adding a constant $Bg^{\mu\nu}$ to the energy momentum tensor of the "quark world". This leads to the EOS :

$$e_q(T,\mu) = e_{SB}(T,\mu) + B,$$

$$P_q(T,\mu) = P_{SB}(T,\mu) - B,$$

where B is called the bag constant and this EOS is the "Bag Model" EOS. Usually for applications in heavy ion physics we can restrict ourselves to two flavors (u and d) in the quark-gluon phases, so $N_f = 2$ and $N_c = 3$ (for $u,\ d,\ s$ quarks $N_f = 3$). In zero'th order of perturbation theory then the pressure P_q in terms of T and μ_b is

$$P_q = 37\pi^2T^4/90 + \mu_b^2T^2/9 + \mu_b^4/162\pi^2 - B,$$

where μ_b is the chemical potential associated with the baryon charge. For phase transition studies this simple form is frequently used. In some cases 1-loop [65, 66] or 2-loop [67, 76] perturbative corrections are also included. The introduction of these perturbative terms leads to a 10-20% increase of the critical temperature and to a similar decrease of the critical densities n_{cq} and n_{ch}.

Phase mixture

Having defined both the Hadronic and QCD plasma EOS one can create a complete EOS by Maxwell construction, containing pure phases and a region where the above two phases coexist. If the plasma has zero baryon charge, 2 of Gibb's criteria, $P_q = P_h,\ T_q = T_h$, and in baryon-rich plasma an additional one, $3\mu_q = \mu_h$, should be satisfied in the mixed phase region. For baryon free plasma $P_q = 37\pi^2T^4/90 - B$ and for a pionic gas $P_h = 3\pi^2T^4/90$, thus from the requirement that $P_q(T_c) = P_h(T_c)$ we can get the critical temperature T_c :

$$T_c^4 = 90B/(34\pi^2)$$

The phase transition is first order. At T_c the coexisting hadronic and quark phase have different energy and entropy densities. For example if $B = \Lambda_B^4/(\hbar c)^3 = 0.397$ GeV/fm^3[2], then the critical temperature and pressure are $T_c = 169\ MeV$, $P_c = 35\ MeV/fm^3$, and the critical energies at T_c are $e_h(T_c) = 106\ MeV/fm^3$, and $e_q(T_c) = 1.695\ GeV/fm^3$.

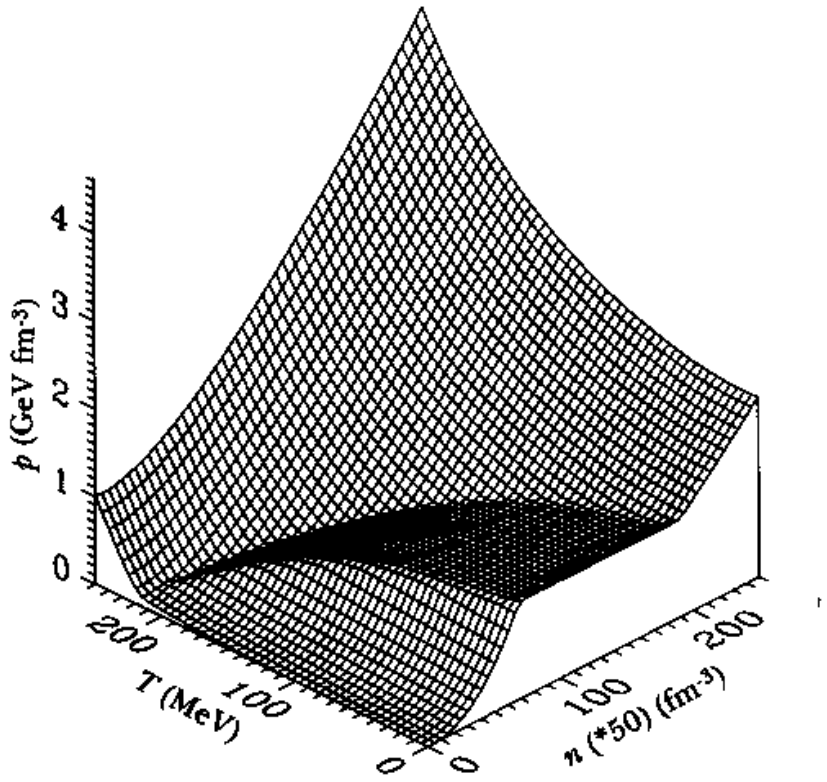

Figure 4.4: The pressure is drastically reduced by the phase transition, when the density and temperature reach the mixed phase region. The pressure increases again only when the pure quark-gluon phase is reached. Thus the phase transition effectively softens the EOS. Reproduced by permission of the American Physical Society from [77].

[2]The bag constant, B, is frequently parametrized by Λ_B also

For baryon-rich matter in this approach the Maxwell construction can be done relatively easily since $P_q(\mu, T)$ is given and the chemical potential of the hadronic phase is also well known. For the EOS (10) in the Boltzmann approximation

$$\mu_b = T \ln(\frac{n_b C}{dT^{3/2}}) + \ m_N + \ W_0 + \ K(n_b - n_0)(3n_b - n_0)/(18n_0^2),$$

where $C = (2\pi(\hbar c)^2/(mc^2))^{3/2}$, and d is the degeneracy of the nucleon gas, $d = 4$. Now the phase equilibrium at a given temperature T_c can be found from the Gibbs criteria, i.e. by solving a single equation (numerically) for n_b. A typical phase diagram arising from this construction is shown in Fig. 4.5 (from [29]).

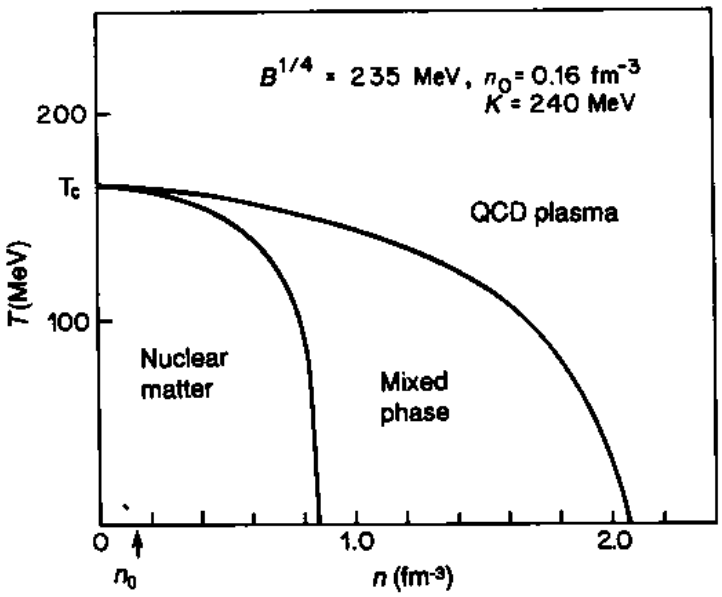

Figure 4.5: Phase diagram of the nuclear matter quark matter phase transition from a simplified phenomenological model. Reproduced by permission of Elsevier Science Publishing from [29].

4.2.3 QGP phase transition and nuclear compressibility

The phase diagram of the first order phase transition is sensitive to both the nuclear and plasma parameters. The increase of compressibility K leads to a decrease of both critical densities, n_{cq} and n_{ch} while increase of the bag constant B leads to the increase of the critical temperature, and densities. The inclusion of hadronic resonances has negligible effect on the phase diagram at $T = 0$ or $\mu = 0$ but it pushes the phase boundaries to higher n and T values in the intermediate region, leading to an increase of the pure nuclear matter domain on the $[\mu, T]$ plane. The equilibrium pressure at fixed intermediate chemical potentials also increases due to the inclusion of hadronic resonances. The equilibrium pressure is higher at $T = 0$ than at T_c which is an interesting feature first observed in ref. [67].

The energy density where the mixed phase formation becomes possible is about $1-2\ GeV/fm^3$ at finite densities, and it decreases below $1\ GeV/fm^3$ when the density tends to zero. To form pure QCD plasma one should, however, reach $2-6\ GeV/fm^3$ energy density at finite densities and $1-4\ GeV/fm^3$ at $n=0$. This of course does not mean that $n=0$ QCD plasma can be formed with less beam energy! For comparison the energy density of the normal nuclear matter is $0.134\ GeV/fm^3$.

4.2.4 Dependence of phase transition on the nuclear EOS

The so called "Sierk–Nix" parametrization gives the critical baryon densities in cold, baryon-rich plasma as $n_{cH}(T=0)=1.39\ fm^{-3}$ and $n_{cQ}(T=0)=3.80\ fm^{-3}$. The corresponding energy densities are $e_{cH}(T=0)=2.04\ GeV/fm^3$ and $e_{cQ}(T=0)=7.53\ GeV/fm^3$[77].

The parameters of EOS influence the phase diagram in the way shown in Figure 4.6 (from ref. [77]), where the phase boundaries are plotted in the (n,T) plane for different equations of state.

Bag parameter: Decreasing B makes it easier to get into the perturbative vacuum. This leads to a decrease in both the critical temperature at zero baryon density and the critical baryon densities at zero temperature. The net effect is thus to decrease the (n,T) domain of hadronic matter.

Compressibility: Decreasing K gives a "softer" EOS and increases the critical baryon densities in cold matter. Figure 4.6c shows the "Sierk–Nix" EOS with $K=350\ MeV$.

Parametrization of compressional energy: The type of the parametrization also influences the transition region. To get almost identical behavior up to $n=3-4n_0$ one can use [70] "Quadratic" with $K=275\ MeV$, "Sierk–Nix" with $K=550\ MeV$ (Fig. 4.6a) or "Grant–Kapusta" with $K=200\ MeV$ and $a=400\ MeV$. If the compression is neglected [68], the critical baryon density of hadronic matter is lowered to just about twice the baryon density of normal nuclear matter $n_0=0.145\ fm^{-3}$ and the bag parameter is restricted to a small interval $B=149-154\ MeV/fm^3$.

Δ-resonances: Including Δ-resonances makes no changes at low temperatures or baryon densities, but the chemical potential is lowered slightly at intermediate n and T. This pushes the phase boundary outward (see Fig. 4.6d).

"Massive" pions: Lowers the pressure (as a function of T) in the hadronic phase and reduces the critical temperature by half a MeV (at $T_c=215.9\ MeV$).

Nucleon–anti-nucleon pairs: Increases the pressure (as a function of T) in the hadronic phase and increases the critical temperature at $n=0$ by about one MeV.

Relativistic nucleon gas: Almost negligible increase in the pressure of the hadronic phase and the critical temperature at $n=0$ (approximately $0.5\ MeV$).

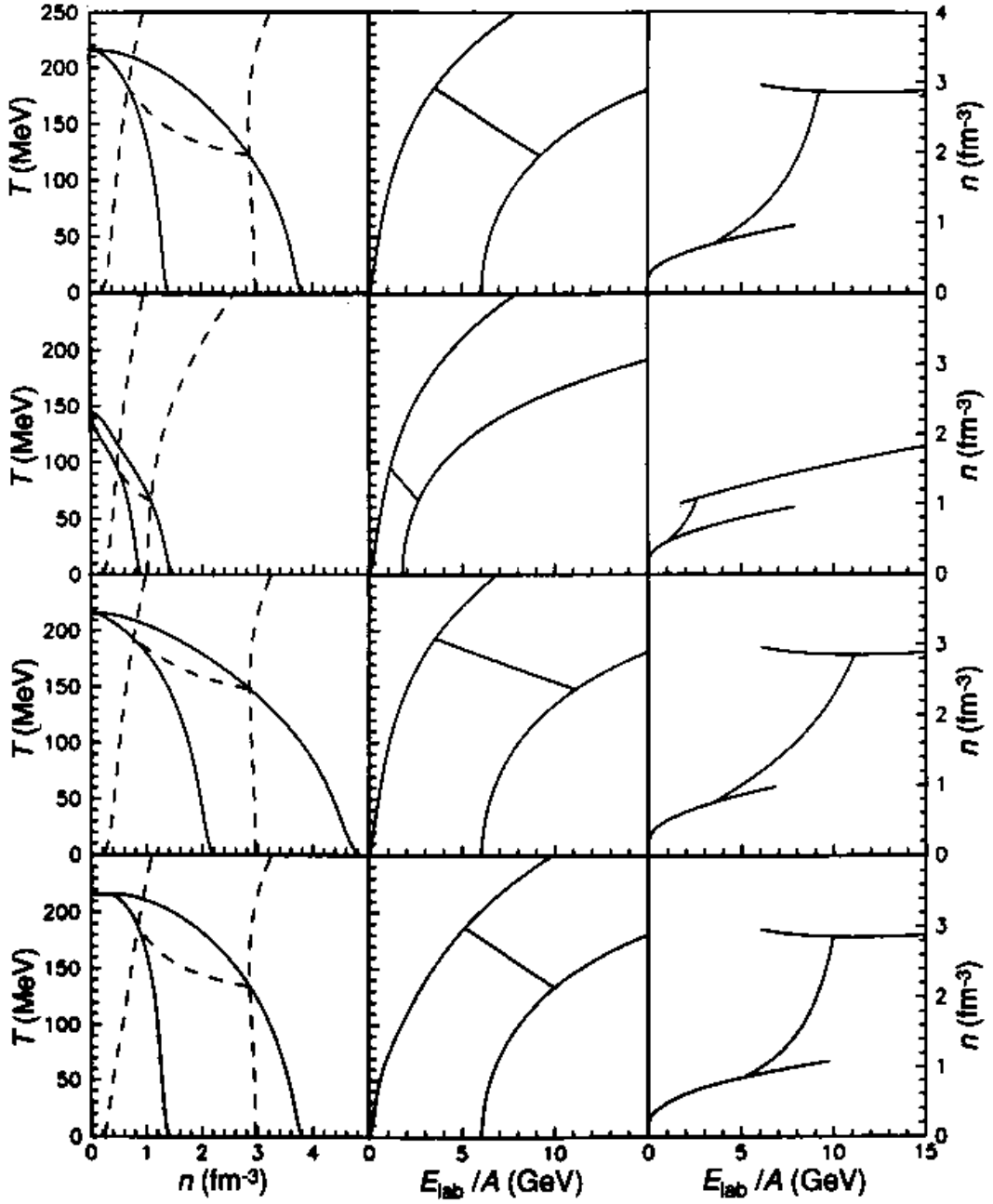

Figure 4.6: Shock adiabats and phase boundaries for different equations of state. From top to bottom a, b, c, d. Reproduced by permission of the American Physical Society from [77].

4.3 EOS from microscopic theory

In elementary statistical physics we have learned, how to calculate the partition function and the thermodynamical potentials for a statistical microscopic system. An introduction to this approach can be found e.g. in Chapters 6, 7, 9, and 10 of ref. [52]. We present here this approach based on an example of nuclear matter [78].

In Chapter 10 further applications of this approach will be mentioned related to the EOS of quark gluon plasma. An introduction to the calculation of EOS in quantum field theories can be found in ref. [79].

The most general Hamiltonian for an A-nucleon system with two-body interaction v_{ij}, three-body interaction v_{ijk}, etc., is

$$H = \sum_{i=1}^{A} \frac{p_i^2}{2m} + \frac{1}{2}\sum_{i,j=1}^{A} v_{ij} + \frac{1}{6}\sum_{i,j,k=1}^{A} v_{ijk} + \ \ldots\ , \tag{4.11}$$

where m is the nucleon mass. In terms of the non-relativistic phase space distribution function, $f(\mathbf{r},\mathbf{p})$, we can write the total energy of the system as

$$\begin{aligned} E \ &= \int d^3r d^3p\ \tfrac{p^2}{2m} f(\mathbf{r},\mathbf{p}) + \tfrac{1}{2}\int d^3r d^3p\ d^3r' d^3p' f(\mathbf{r},\mathbf{p}) f(\mathbf{r}',\mathbf{p}')\ v_{ij}(\mathbf{r},\mathbf{r}',\mathbf{p},\mathbf{p}') + \ldots \\ &= \int d^3r d^3p\ \tfrac{p^2}{2m} f(\mathbf{r},\mathbf{p}) + V[f]. \end{aligned} \tag{4.12}$$

Clearly, the one-body term of the Hamiltonian depends on one distribution function, while the two-body term contains two distribution functions, etc. In general, the potential energy, $V[f]$, (in addition to its complicated momentum dependence) is explicitely nonlocal, as a consequence of the single-particle distribution functions appearing in it.

In the *local approximation*, the potential energy density, $u[f]$, contains delta–functions for the coordinates, so that one non-trivial integral over one single position coordinate, r is left in the potential energy, $V[f]$:

$$V[f] = \int d^3r\ u[f(\mathbf{r},\mathbf{p}), f(\mathbf{r},\mathbf{p}'),\ \ldots\ ]\,. \tag{4.13}$$

For example, if we assume a momentum-independent two body interaction,

$$v_{ij}(\mathbf{r},\mathbf{r}',\mathbf{p},\mathbf{p}') = v_{ij}^{(0)}(\mathbf{r}-\mathbf{r}'), \tag{4.14}$$

then

$$\begin{aligned} V \ &= \tfrac{1}{2}\int d^3r d^3p\ d^3r' d^3p'\ f(\mathbf{r},\mathbf{p}) f(\mathbf{r}',\mathbf{p}')\ v_{ij}^{(0)}(\mathbf{r}-\mathbf{r}') \\ &= \tfrac{1}{2}\int d^3r d^3r'\ n(\mathbf{r}) n(\mathbf{r}')\ v_{ij}^{(0)}(\mathbf{r}-\mathbf{r}'). \end{aligned} \tag{4.15}$$

Furthermore, with a local (contact) two-body interaction,

$$v_{ij}^{(0)}(\mathbf{r}-\mathbf{r}') = \frac{a}{n_0}\delta(\mathbf{r}-\mathbf{r}'), \tag{4.16}$$

where n_0 is the normal nuclear matter density and a is a constant of energy dimension, the potential energy takes the form

$$V = \frac{1}{2}\int d^3r d^3p\; d^3r' d^3p'\; f(\mathbf{r},\mathbf{p}) f(\mathbf{r}',\mathbf{p}')\; \frac{a}{n_0}\delta(\mathbf{r}-\mathbf{r}') = \int d^3r\; \frac{a}{2}\frac{n^2(\mathbf{r})}{n_0}. \tag{4.17}$$

We adopt the local approximation in the following. Note, that the parameters of the nucleon distribution function, $f(\mathbf{r},\mathbf{p})$, may also be position-dependent, e.g. the local temperature, $T = T(\mathbf{r})$. The distribution function for an interacting gas with a momentum-dependent interaction will contain additional, potentially $\mathbf{r}$-dependent parameters, for example the width $\Lambda = \Lambda(\mathbf{r})$ in eq. (4.18).

Even in the local approximation (as defined above), the exchange part of the two-body interaction gives rise to a momentum-dependent term. This momentum-dependence expresses the effective nonlocality introduced by the Pauli principle [80]. For a Yukawa two-body interaction, the term arising from the exchange part can be written as[81]

$$v_{ij} = v_{ij}^{(0)}(\mathbf{r}-\mathbf{r}') + \frac{2c}{n_0}\frac{\delta(\mathbf{r}-\mathbf{r}')}{1+(\frac{\mathbf{p}-\mathbf{p}'}{\Lambda})^2}\,, \tag{4.18}$$

where c is a constant of energy dimension. The full energy is

$$\begin{aligned} E &= \int d^3r d^3p\; \frac{p^2}{2m} f(\mathbf{r},\mathbf{p}) \\ &+ \frac{1}{2}\int d^3r d^3p\; d^3r' d^3p' f(\mathbf{r},\mathbf{p}) f(\mathbf{r}',\mathbf{p}') \left[v_{ij}^{(0)}(\mathbf{r}-\mathbf{r}') + \frac{2c}{n_0}\frac{\delta(\mathbf{r}-\mathbf{r}')}{1+(\frac{\mathbf{p}-\mathbf{p}'}{\Lambda})^2} \right] \\ &+ \ldots, \end{aligned} \tag{4.19}$$

where we have separated the momentum dependent part of the two body interaction approximated as in eq.(4.18). The $v_{ij}^{(0)}$ is assumed to be momentum independent, as well as the three-body and further terms of the Hamiltonian. For simplicity we consider the two-body and higher order terms of the Hamiltonian to be described in the local approximation as:

$$E = \int d^3r \left[\int d^3p \frac{p^2}{2m} f(\mathbf{r},\mathbf{p}) + \frac{a}{2}\frac{n^2}{n_0} + \frac{b}{\sigma+1}\frac{n^{\sigma+1}}{n_0^\sigma} + \frac{c}{n_0}\int d^3p d^3p' \frac{f(\mathbf{r},\mathbf{p}) f(\mathbf{r},\mathbf{p}')}{1+(\frac{\mathbf{p}-\mathbf{p}'}{\Lambda})^2} \right], \tag{4.20}$$

where the expression in the square brackets is the kinetic energy plus the potential energy density, $u[f]$. By choosing the parameter σ to be greater than one, an effective representation of the three- and more-nucleon interactions is obtained.

The *mean field approximation* can be derived from the potential energy density, $u[f]$, by taking the variational derivative with respect to the distribution function, f,

$$\varphi \equiv \delta u[f]/\delta f(\mathbf{r},\mathbf{p})\,. \tag{4.21}$$

Using eq. (4.21) one obtains for the momentum-dependent part of the mean field

$$\varphi_{mom}(\mathbf{r},\mathbf{p}) = \frac{2c}{n_0}\int d^3p' \frac{f(\mathbf{r},\mathbf{p}')}{1+(\frac{\mathbf{p}-\mathbf{p}'}{\Lambda})^2}\,, \tag{4.22}$$

hence for the momentum-dependent part of the single-particle energy

$$\varepsilon_{mom}(\mathbf{r},\mathbf{p}) = \frac{p^2}{2m} + \varphi_{mom}(\mathbf{r},\mathbf{p})\,. \tag{4.23}$$

With the usual parametrization of the momentum-independent part of the mean field, [82, 15, 81], the full single-particle energy has the form

$$\varepsilon(\mathbf{r},\mathbf{p}) = \frac{p^2}{2m} + a\frac{n}{n_0} + b(\frac{n}{n_0})^\sigma + \frac{2c}{n_0}\int d^3p' \frac{f(\mathbf{r},\mathbf{p}')}{1+(\frac{\mathbf{p}-\mathbf{p}'}{\Lambda})^2}\,. \tag{4.24}$$

4.3.1 Momentum dependent interaction

A simplified momentum-dependent mean field was used in Refs. [82, 78], which can be obtained by replacing $\mathbf{p}'$ in eq. (4.18) by its average, $<\mathbf{p}'>$, yielding

$$\varphi_{mom}(\mathbf{r},\mathbf{p}) = \delta u[f]/\delta f(\mathbf{r},\mathbf{p}) = c\frac{n}{n_0}\left[\frac{1}{1+(\frac{\mathbf{p}-<\mathbf{p}'>}{\Lambda})^2}\right] + c\frac{n}{n_0}\left\langle\frac{1}{1+(\frac{\mathbf{p}-<\mathbf{p}'>}{\Lambda})^2}\right\rangle_p \tag{4.25}$$

Note that the manifest symmetry between $\mathbf{p}$ and $\mathbf{p}'$, reflecting the symmetry of the nucleon-nucleon interaction [see eq.(4.18)] is lost in this approximation. The use of eq. (4.25) is an acceptable approximation for nuclear collisions at sufficiently high energies. We will adopt this approximation in the following.

This momentum dependent mean-field potential will lead to an attraction between nucleons of the same or similar momenta. The potential energy density is written as

$$u[f] = a\frac{n^2}{2n_0} + b\frac{n^{\sigma+1}}{(\sigma+1)n_0^\sigma} + c\frac{n}{n_0}\int d^3p\ \frac{f(\mathbf{p})}{1+(\frac{\mathbf{p}-\mathbf{p}_0}{\Lambda})^2}. \tag{4.26}$$

where $\mathbf{p}_0$ is the local mean momentum, and n_0 is the standard nuclear matter density. In the local rest frame of the matter $\mathbf{p}_0 = 0$. The parameter Λ describes the width of the momentum distribution.

4.3.2 Momentum distribution

If the mean field is independent of the momentum of the nucleon moving in it, the momentum distribution in the classical limit has the usual Maxwell–Boltzmann form:

$$f_0(p) = \frac{n}{g\ (2\pi mT)^{3/2}}\exp\left[-p^2/2mT\right]. \tag{4.27}$$

where n is the baryon density of nuclear matter and g is the degeneracy of nucleons, $g = 4$. With a momentum-dependent mean field, the exponent of the momentum distribution will contain the entire momentum-dependent part of the single-particle energy (4.23), and the corresponding distribution function will no longer be a simple Maxwellian.

The single-particle energy corresponding to eq. (4.26) is:

$$\varepsilon(\mathbf{r},\mathbf{p}) = \frac{p^2}{2m} + a\frac{n}{n_0} + b(\frac{n}{n_0})^\sigma + c\frac{n}{n_0}\frac{1}{1+(\frac{\mathbf{p}-\mathbf{p}_0}{\Lambda})^2} + c\frac{n}{n_0}\left\langle \frac{1}{1+(\frac{\mathbf{p}-\mathbf{p}_0}{\Lambda})^2} \right\rangle_p . \tag{4.28}$$

For static nuclear matter $\mathbf{p}_0$ vanishes and, at zero temperature the integral in the last term of Eq. (4.26) can be carried out to yield

$$\varepsilon^0_{MD}(\mathbf{r};n) = 3c\frac{n}{n_0}\left(\frac{\Lambda}{p_F}\right)^3\left[\frac{p_F}{\Lambda} - \tan^{-1}(\frac{p_F}{\Lambda})\right]. \tag{4.29}$$

where p_F is the Fermi momentum.

The momentum-dependent part of the interaction gives rise to the following distribution (see assignment [4.a]):

$$f(p) = N\exp\left[-\frac{1}{T}\left(\frac{p^2}{2m} - c(\frac{n}{n_0})\frac{p^2}{p^2+\Lambda^2}\right)\right] \tag{4.30}$$

where N is the value of the distribution function at zero momentum, as it should be. (Note that this would not hold true without the absorption of the momentum-independent term in the momentum-independent part of the potential.)

However, it is advantageous for calculational purposes to *approximate* the full distribution with a Maxwellian at a given temperature and density. In the following, we introduce an 'equivalent mass', m^{MB}_{eq}, which can be used at a given temperature and density in a Maxwell–Boltzmann distribution with the closest correspondence to the momentum-distribution obtained with the full momentum-dependent mean field

$$f^{MB}_{eq}(p) = N\exp\left[-p^2/2m^{MB}_{eq}T\right] , \tag{4.31}$$

where $N = n/[(2\pi m^{MB}_{eq}T)^{3/2}\ g]$. The equivalent mass will depend on the temperature and the density, but will be momentum-independent, $m^{MB}_{eq} = m^{MB}_{eq}(n,T)$.

When $f(\mathbf{p})$ is approximated by the equivalent Maxwell–Boltzmann distribution, m^{MB}_{eq} is fixed by the condition

$$f(p=0) \;=\; f^{MB}_{eq}(p=0).$$

This yields an equivalent mass of

$$m^{MB}_{eq}(n,T) = \frac{1}{2\pi T}\left\{\int d^3p\exp\left[-\frac{p^2}{T}\left(\frac{1}{2m} - c\left(\frac{n}{n_0}\right)\frac{1}{p^2+\Lambda^2}\right)\right]\right\}^{2/3}. \tag{4.32}$$

4.3.3 The partition function

In order to utilize the momentum dependent interaction in collective nuclear models one has to evaluate the Equation of State (EOS). It is important to emphasize that the thermal part of the EOS will be modified by the momentum dependent interaction because the equilibrium momentum distribution is also changed. For instance, the

incompressibility will increase more rapidly with the temperature in the presence of the momentum dependent interaction.

To obtain the correction, thermodynamic perturbation theory will be applied [28]. In this approximation the free energy of the system is calculated as

$$F = F_0 + < V > + \frac{1}{2T} \left\langle (V - < V >)^2 \right\rangle ,$$

where we will take the kinetic energy to determine the zeroth order approximation, F_0. Only the first nonvanishing correction will be evaluated here in accordance with the approximations made earlier in the momentum independent part of the interaction energy. This is given by the average of the interaction over the phase space, $< V >$. See Ref. [28] for a general discussion of the second-order correction.

Taking the kinetic energy only as the single particle contribution to the Hamiltonian, $E = \sum_{i=1}^{A} p_i^2/2m$, a calculation of the zeroth order of the free energy yields

$$F_0 = -T \ln Z_0 = -T \ln \left\{ \int' d\Gamma e^{-E/T} \right\} = -AT + AT \ln \left[\frac{n(2\pi\hbar)^3}{g\ (2\pi m T)^{3/2}} \right] , \qquad (4.33)$$

where Z_0 is the canonical partition function and $\int' d\Gamma$ accounts for the proper Boltzmann counting in the phase space integral [52]. The average of the potential energy over the phase space is given by

$$< V >= \frac{\int' d\Gamma\ V}{\int' d\Gamma} = e^{(F_0 - E)/T} \int' d\Gamma\ V . \qquad (4.34)$$

The EOS can be obtained by evaluating the canonical partition function or the free energy, F, (see ref. [78] and assignment [4.b]).

Thermodynamical potential	Partition function	Statistics
$S(E,V,N)$	$\ln Z_{mc}(E,V,N)\ [= \ln \Omega(E)]$	micro canonical
$F(T,V,N)$	$\ln Z_c(T,V,N)$	canonical
$\Omega(T,V,\mu)$	$\ln Z_{gc}(T,V,\mu)$	grand canonical

Table 4.3: Connection between the partition functions and thermodynamical potentials

The thermodynamic potentials and the partition function are connected to each other as shown in Table 4.3. This way, by calculating the partition function in a microscopic theory one can obtain the EOS.

4.4 Assignment 4

4.a Calculate the distribution function, $f(p)$, if the single particle energy is given by eq. (4.28).

4.b Calculate the nuclear EOS for the momentum dependent interaction given by eq. (4.28), using the thermodynamic perturbation theory (up to first order).

4.4.1 Solutions to Assignment 4

4.a The single-particle energy (4.28) can be decomposed into a momentum dependent and a momentum independent part:

$$\varepsilon(\mathbf{r},\mathbf{p}) = \frac{p^2}{2m} + c\frac{n}{n_0}\frac{1}{1+(\frac{\mathbf{p}-\mathbf{p_0}}{\Lambda})^2} + a\frac{n}{n_0} + b(\frac{n}{n_0})^\sigma + c\frac{n}{n_0}\left\langle \frac{1}{1+(\frac{\mathbf{p}-\mathbf{p_0}}{\Lambda})^2}\right\rangle_p \tag{4.35}$$

Let us now focus on static nuclear matter ($\mathbf{p_0}=0$). Then

$$\begin{aligned}\varepsilon(\mathbf{r},\mathbf{p}) &= \frac{p^2}{2m} + c\frac{n}{n_0}\frac{1}{1+(\frac{\mathbf{p}}{\Lambda})^2} + a\frac{n}{n_0} + b(\frac{n}{n_0})^\sigma + c\frac{n}{n_0}\left\langle \frac{1}{1+(\frac{\mathbf{p}}{\Lambda})^2}\right\rangle_p \\ &= \frac{p^2}{2m} - c\frac{n}{n_0}\frac{p^2}{p^2+\Lambda^2} + a'\frac{n}{n_0} + b(\frac{n}{n_0})^\sigma + c\frac{n}{n_0}\left\langle \frac{1}{1+(\frac{\mathbf{p}}{\Lambda})^2}\right\rangle_p \end{aligned} \tag{4.36}$$

where $a' = a + c$. Using the result (4.29), the last term in (4.36) can be separated into a zero-temperature and a T-dependent part as

$$c(\frac{n}{n_0})\left\langle \frac{1}{1+(\frac{\mathbf{p}}{\Lambda})^2}\right\rangle_p = \varepsilon^0_{MD}(\mathbf{r};n) + \frac{c}{n_0}\int d^3p \frac{f(\mathbf{p}) - f^{Fermi}_{T=0}(\mathbf{p})}{1+(\frac{\mathbf{p}}{\Lambda})^2}. \tag{4.37}$$

According to the usual convention, the density-dependent, zero-temperature part of the single-particle energy $\varepsilon(\mathbf{r},\mathbf{p})$ will be referred to as the compressional energy:

$$\begin{aligned}\varepsilon_{comp}(\mathbf{r};n) &= a'(\frac{n}{n_0}) + b(\frac{n}{n_0})^\sigma + \varepsilon^0_{MD}(\mathbf{r};n) \\ &= a'\frac{n}{n_0} + b(\frac{n}{n_0})^\sigma + 3c\frac{n}{n_0}\Big(\frac{\Lambda}{p_F}\Big)^3\Big[\frac{p_F}{\Lambda} - \tan^{-1}(\frac{p_F}{\Lambda})\Big]. \end{aligned} \tag{4.38}$$

In addition to the compressional energy, the total single particle energy contains a density- and temperature-dependent, but momentum-independent (thermal) part

$$\varepsilon_{therm}(\mathbf{r};n,T) = \frac{c}{n_0}\int d^3p \frac{f(\mathbf{p}) - f^{Fermi}_{T=0}(\mathbf{p})}{1+(\frac{\mathbf{p}}{\Lambda})^2}. \tag{4.39}$$

Thus, the total single-particle energy (4.28) is decomposed into three terms,

$$\varepsilon(\mathbf{r},\mathbf{p}) = \varepsilon_{comp}(\mathbf{r};n) + \varepsilon_{therm}(\mathbf{r};n,T) + \varepsilon_{mom}(\mathbf{r},\mathbf{p}). \tag{4.40}$$

Here the momentum-dependent part of the single particle energy is:

$$\varepsilon_{mom}(\mathbf{r},\mathbf{p}) = p^2\left[\frac{1}{2m} - c(\frac{n}{n_0})\frac{1}{p^2+\Lambda^2}\right]. \tag{4.41}$$

This leads to the momentum distribution given by eq. (4.30). qed.

4.b For the Hamiltonian (4.19) this phase space average is

$$< V >= e^{(F_0-E)/T}\ \frac{1}{A!}\frac{1}{(2\pi\hbar)^{3A}}\int d^{3A}r\ d^{3A}p\ f_i(\mathbf{r}_i,\mathbf{p}_i)f_j(\mathbf{r}_j,\mathbf{p}_j)\ \times \left\{\frac{1}{2}\sum_{i\neq j}\left[v_{ij}^{(0)}(\mathbf{r}_i-\mathbf{r}_j)+\frac{2c}{n_0}\frac{\delta(\mathbf{r}_i-\mathbf{r}_j)}{1+(\frac{\mathbf{p_i}-\mathbf{p_j}}{\Lambda})^2}\right]\right\}+\ldots. \tag{4.42}$$

Performing the major part of the phase space integrals leads to factors which will be canceled by $e^{(F_0-E)/T}$. The summations over identical terms give factors of $A(A-1)$. The resulting expression is

$$< V >= \frac{A(A-1)}{2\Omega^2}\int d^3r d^3r' v_{ij}^{(0)}(\mathbf{r}_i-\mathbf{r}_j)\ + \frac{A(A-1)\ c}{n_0\ \Omega\ (2\pi mT)^3}\int d^3p d^3p' \frac{e^{-p^2/2mT}\ e^{-p'^2/2mT}}{1+(\frac{\mathbf{p}-\mathbf{p}'}{\Lambda})^2}, \tag{4.43}$$

where Ω is the total volume of the system.

We now specialize to a sufficiently large system ($A \gg 1$) with a constant (position-independent) density n. Then $(A-1)/\Omega \approx A/\Omega = n$. Further, we apply the approximation introduced in eq. (4.20) for the momentum independent terms to get

$$< V >= \Omega\left[\frac{a}{2}\frac{n^2}{n_0}+\frac{b}{\sigma+1}\frac{n^{\sigma+1}}{n_0^\sigma}+\frac{c\ n^2}{n_0(2\pi mT)^3}\int d^3p d^3p' \frac{e^{-p^2/2mT}\ e^{-p'^2/2mT}}{1+(\frac{\mathbf{p}-\mathbf{p}'}{\Lambda})^2}\right]. \tag{4.44}$$

Observing that $f_0(p)=\frac{n(2\pi\hbar)^3}{g(2\pi mT)^{3/2}}e^{-p^2/2mT}$, expression (4.44) can be reduced to

$$< V >= \Omega\left[\frac{a}{2}\frac{n^2}{n_0}+\frac{b}{\sigma+1}\frac{n^{\sigma+1}}{n_0^\sigma}+\frac{c}{n_0}\frac{g^2}{(2\pi\hbar)^6}\int d^3p d^3p' \frac{f_0(\mathbf{r},\mathbf{p})f_0(\mathbf{r},\mathbf{p}')}{1+(\frac{\mathbf{p}-\mathbf{p}'}{\Lambda})^2}\right]. \tag{4.45}$$

To simplify this expression further, we apply the approximations used in section 4.3.2. First we replace one of the integrands in eq. (4.45) by its average, $\mathbf{p}' \to < \mathbf{p}' >= \mathbf{p}_0$, and then assume that we are in the local rest frame of the matter, $\mathbf{p}_0 = 0$. This leads to

$$< V >= \Omega\left[\frac{a}{2}\frac{n^2}{n_0}+\frac{b}{\sigma+1}\frac{n^{\sigma+1}}{n_0^\sigma}+c\frac{n}{n_0}\frac{g}{(2\pi\hbar)^3}\int d^3p \frac{f_0(\mathbf{r},\mathbf{p})}{1+(\frac{\mathbf{p}}{\Lambda})^2}\right]. \tag{4.46}$$

Let us introduce the notation $I(n,T)$ for the integral in the last term:

$$I(n,T) \equiv \frac{g}{(2\pi\hbar)^3}\int d^3p \frac{f_0(p)}{1+(\frac{p}{\Lambda})^2}\ . \tag{4.47}$$

The total free energy in this approximation is

$$F(n,T)=\Omega\left\{-nT+nT\ln\left[\frac{n(2\pi\hbar)^3}{g(2\pi mT)^{3/2}}\right]+\frac{an^2}{2n_0}+\frac{b}{\sigma+1}\frac{n^{\sigma+1}}{n_0^\sigma}+c\frac{n}{n_0}I(n,T)\right\}. \tag{4.48}$$

The corresponding pressure, entropy, energy and chemical potential are respectively

$$P(n,T) = nT + \frac{an^2}{2n_0} + \frac{b\sigma}{\sigma+1}\frac{n^{\sigma+1}}{n_0^\sigma} + c\frac{n^2}{n_0}\left.\frac{\partial I(n,T)}{\partial n}\right|_T , \tag{4.49}$$

$$\frac{S(n,T)}{A} = \frac{5}{2} - \ln\left[\frac{n(2\pi\hbar)^3}{g(2\pi mT)^{3/2}}\right] - \frac{c}{n_0}\left.\frac{\partial I(n,T)}{\partial T}\right|_n , \tag{4.50}$$

$$E(n,T) = F + TS = \Omega \left\{\frac{3}{2}nT + \frac{an^2}{2n_0} + \frac{b}{\sigma+1}\frac{n^{\sigma+1}}{n_0^\sigma} + c\frac{n}{n_0}\left[I(n,T) - T\left.\frac{\partial I(n,T)}{\partial T}\right|_n\right]\right\} \tag{4.51}$$

$$\mu(n,T) = \left.\frac{\partial(F/\Omega)}{\partial n}\right|_T = \frac{F+P\Omega}{A}. \tag{4.52}$$

A straightforward calculation yields for the derivatives of the integral $I(n,T)$:

$$\left.\frac{\partial I(n,T)}{\partial T}\right|_n = -\frac{3}{2T}I(n,T) + J(n,T), \tag{4.53}$$

$$\left.\frac{\partial I(n,T)}{\partial n}\right|_T = \frac{1}{n}I(n,T)\,. \tag{4.54}$$

The integrals $I(n,T)$ and $J(n,T)$ can be evaluated to give

$$I(n,T) = 2n\chi^2\left\{1 - \sqrt{\pi}\chi e^{\chi^2}\left[1-\Phi(\chi)\right]\right\}, \tag{4.55}$$

$$J(n,T) = \frac{2n\chi^2}{T}\left\{\frac{1}{2} - \chi^2 + \sqrt{\pi}\chi^3 e^{\chi^2}\left[1-\Phi(\chi)\right]\right\}, \tag{4.56}$$

where

$$\chi^2 = \frac{\Lambda^2}{2mT}, \quad \text{and} \quad \Phi(x) = \frac{2}{\sqrt{\pi}}\int_0^x e^{-t^2}\,dt\,,$$

is the error function.

Bibliography

[1] A. Bonasera, L.P. Csernai, Phys. Rev. Lett. **59** (1987) 630.

[2] A. Bonasera, L.P. Csernai and B. Schürmann, Nucl. Phys. **A476** (1988) 159.

[3] W.D. Myers, Atomic Data Nucl. Data Tables **17** (1976) 411.

[4] H.A. Bethe, Ann. Rev. Nucl. Sci., **21** (1971) 93.

[5] J.P. Blaizot, D. Gogny and B. Grammaticos, Nucl. Phys. **A265** (1976) 315.

[6] B. Waldhauser, J. Maruhn, H. Stöcker, and W. Greiner, Phys. Rev. **C38** (1988) in press.

[7] N.K. Glendenning, Phys. Rev. **C** (1988) in press.

[8] G.E. Brown, and E. Osnes, Phys. Rev. Lett. **159B** (1985) 223.

[9] R. Stock, R. Bock, R. Brockmann, J.W. Harris, A. Sandoval, H. Ströbele, K.L. Wolf, H.G. Pugh, L.S. Schroeder, M. Maier, R.E. Renfordt, A. Daca and M.E. Oritz, Phys. Rev. Lett. **49** (1982) 1236.

[10] T. Matsui and H. Satz, Phys. Lett. **B187** (1986) 416.

[11] W. Scheid, H. Müller and W. Greiner, Phys. Rev. Lett. **32** (1974) 741.

[12] G.F. Chapline, M.H. Johnson, E. Teller and M.S. Weiss, Phys. Rev. **D8** (1973) 4302.

[13] H.Å. Gustafsson, H.H. Gutbrod, B. Kolb, H. Lohner, B. Ludewigt, A.M. Poskanzer, T. Renner, H. Riedesel, H.G. Ritter, A. Warwick, F. Weik and H. Wieman, Phys. Rev. Lett. **52** (1984) 1590.

[14] C. Gale, G. Bertsch and S. Das Gupta, Phys. Rev. **C35** (1987) 1666.

[15] J. Aichelin, A. Rosenhauer, G. Peilert, H. Stöcker, and W. Greiner, Phys. Rev. Lett. **58** (1987) 1926.

[16] H.W. Barz, L. P. Csernai, B. Kämpfer and B. Lukács, Phys. Rev. **D32** (1985) 115.

[17] M. M Sharma, W.T.A. Borghols, S. Brandenburg, S. Crona, A. van der Woude and M.N. Harakeh, Phys. Rev. **C38** (1988) 2562.

[18] A. van der Woude, W. T. A. Borghols, S. Brandenburg and M. M. Sharma, Phys. Rev. Lett. **58** (1987) 2383.

[19] H. Stöcker, G. Buchwald, G. Graebner, P.R. Subramanian, J.A. Maruhn, W. Greiner, B.V. Jacak and G.D. Westfall, Nucl. Phys. **A400** (1983) 63c.

[20] A.J. Sierk and J.R. Nix, Phys. Rev. **C22** (1980) 1920.

[21] L.P. Csernai and H.W. Barz, Z. Phys. **A296** (1980) 173.

[22] L.P. Csernai, H. Stöcker, P.R. Subramanian, G. Graebner, A. Rosenhauer, G. Buchwald, J.A. Maruhn and W. Greiner, Phys. Rev. **C28** (1983) 2001.

[23] P. Danielewicz, Nucl. Phys. **A314** (1979) 465.

[24] M. Gyulassy, K. Kajantie, H. Kurki-Suonio and L. McLerran, Nucl. Phys. **B237** (1984) 477.

[25] J. Kapusta, Phys. Rev. **C29** (1984) 1735.

[26] J.R. Nix, Prog. in Part. and Nucl. Phys. **2** (1979) 237.

[27] I.N. Mishustin and L.M. Satarov, Yad. Fiz. **37** (1983) 894.

[28] L.D. Landau and E.M. Lifshitz: Statistical Physics (Nauka, Moscow, 1954).

[29] L.P. Csernai and J. Kapusta, Phys. Rep. **131** (1986) 223.

[30] J. A. Lopez and P. J. Siemens, Nucl. Phys. **A431** (1984) 728.

[31] E.A. Guggenheim, J. Chem. Phys. **12** (1945) 253.

[32] H.E. Stanley: Introduction to phase transitions and critical phenomena (Oxford University Press, 1971).

[33] H.R. Jaqaman, A.Z. Mekjian and L. Zamick, Phys. Rev. **C27** (1983) 2782.

[34] H.R. Jaqaman, A.Z. Mekjian and L. Zamick, Phys. Rev. **C29** (1984) 2076.

[35] A.R. DeAngelis and A.Z. Mekjian, Phys. Rev. **C40** (1989) 105.

[36] G. Fai and J. Randrup, Nucl. Phys. **A404** (1983) 551.

[37] H.W. Barz, J. P. Bondorf, R. Donangelo, and H. Schulz, Phys. Lett. **169B** (1986) 318.

[38] L.P. Csernai, J.I. Kapusta, G. Fai, D. Hahn, J. Randrup, and H. Stöcker, Phys. Rev. **C35** (1987) 1297.

[39] B. V. Jacak, H. Stöcker and G. D. Westfall, Phys. Rev. **C29** (1984) 1744.

[40] A.Z. Mekjian, Phys. Rev. **C17** (1978) 1051.

[41] P.J. Siemens and J.I. Kapusta, Phys. Rev. Lett. **43** (1979) 1486.

[42] J. Randrup and S.E. Koonin, Nucl. Phys. **A356** (1981) 223.

[43] G. Fai and J. Randrup, Nucl. Phys. **A381** (1982) 557.

[44] J. Randrup and G. Fai, Phys. Lett. **115B** (1982) 281.

[45] G. Fai and J. Randrup, Comp. Phys. Comm. **42** (1986) 385.

[46] P. R. Subramanian, L. P. Csernai, H. Stöcker, J. Maruhn, W. Greiner and H. Kruse, J. Phys. **G7** (1981) L241.

[47] P. Danielewicz and M. Gyulassy, Phys. Rev. **D31** (1985) 53.

[48] B. V. Jacak, G. D. Westfall, G. Crawley, D. Fox, C. K. Gelbke, L. H. Harwood, B. E. Hasselquist, W. G. Lynch, D. K. Scott, H. Stöcker, M. B. Tsang, G. Buchwald, and T. J. M. Symons, Phys. Rev. **C35** (1987) 1751.

[49] L.P. Csernai and G. Fai, Acta Phys. Hung. **62** (1987) 355.

[50] L.P. Csernai, Phys. Rev. Lett. **54** (1985) 639.

[51] A.L. Goodman, J. I. Kapusta and A. Z. Mekjian, Phys. Rev. **C30** (1984) 851.

[52] F. Reif: Fundamentals of statistical and thermal physics (McGraw-Hill, 1965).

[53] M.E. Fisher, Physics (N. Y.) **3** (1967) 255.

[54] J.E. Finn, S. Agarval, A. Bujak, J. Chuang, L. J. Gutay, A. S. Hirsch, R. W. Minich, N. T. Porile, R. P. Scharenberg, B. C. Stringfellow, and F. Turkot, Phys. Rev. Lett. **49** (1982) 1321.

[55] R. W. Minich, S. Agarval, A. Bujak, J. Chuang, J. E. Finn, L. J. Gutay, A. S. Hirsch, N. T. Porile, R. P. Scharenberg, B. C. Stringfellow and F. Turkot, Phys. Lett. **118B** (1982) 458.

[56] A. S. Hirsch, A. Bujak, J. E. Finn, L. J. Gutay, R. W. Minich, N. T. Porile, R. P. Scharenberg, and B. Stringfellow, Phys. Rev. **C29** (1984) 508.

[57] M. Mahi, A. T. Bujak, D. D. Charmony, Y. H. Chung, L. J. Gutay A. S. Hirsch, G. L. Paderewski, N.T. Porile, T.C. Sangster, R.P. Scharenberg, and B.C. Stringfellow, Phys. Rev. Lett. **60** (1988) 1936.

[58] F. Karsch, Z. Phys. **C38** (1988) 147.

[59] G. Baym and S.A. Chin, Phys. Lett. **62B** (1076) 241.

[60] G.F. Chapline and M. Nauenberg, Phys. Rev. **D16** (1977) 456.

[61] B. Freedman and L. McLerran, Phys. Rev. **D17** (1978) 1109.

[62] T. Celik and H. Satz, Z. Phys. **C1** (1979) 163.

[63] H.W. Barz, B. Kämpfer, L.P. Csernai and B. Lukács, Phys. Lett. **143B** (1984) 334.

[64] H.W. Barz, B. Kämpfer, B. Lukács and L.P. Csernai, Phys. Rev. **C31** (1985) 268.

[65] P.R. Subramanian, H. Stöcker and W. Greiner, Phys. Lett. **B173** (1986) 486.

[66] U. Heinz, P.R. Subramanian, H. Stöcker and W. Greiner, J. Phys. G: Nucl. Phys. **12** (1986) 1237.

[67] J. Kuti, B. Lukács, J. Polonyi, and K. Szlachányi, Phys. Lett. **B95** (1980) 75.

[68] J. Cleymans, R. Gavai and E. Suhonen, Phys. Rep. **130** (1986) 217.

[69] T. S. Olson and W. A. Hiscock, Phys. Rev. **C39** (1989) 1818.

[70] C. Grant and J. Kapusta, Phys. Rev. **C32** (1985) 663.

[71] H. Stöcker and W. Greiner, Phys. Rep. **137** (1986) 277.

[72] L.P. Csernai, in Proc. of the High En. HI Collisions & Quark Degrees of Freedom in Nuclei int. workshop, Puri, India, Jan. 2-15, 1987, ed. by S.C. Phatak and Satpathy (World Scientific, 1987) p. 69.

[73] P.J. Steinhardt, Phys. Rev. **D25** 2074 (1982).

[74] M. Gyulassy, Progress in Part. and Nucl. Phys. **15** (1985) 403.

[75] E.V. Shuryak, Phys. Rep. **61** (1980) 71.

[76] S.A. Chin, Phys. Lett. **78B** (1978) 552.

[77] A.K. Holme, E.F. Staubo, L.P. Csernai, E. Osnes and D. Strottman, Phys. Rev. **D40** (1989) 3735.

[78] L.P. Csernai, G. Fai, C. Gale and E. Osnes, Phys. Rev. **C46** (1992) 736.

[79] J.I. Kapusta: Finite-temperature field theory, (Cambridge University Press, Cambridge 1989).

[80] A. Bohr and B.R. Mottelson, Nuclear Structure, Vol. 1. W.A. Benjamin, New York (1969).

[81] G.M. Welke, M. Prakash, T.T.S. Kuo, S. Das Gupta, and C. Gale, Phys. Rev. **C38**, 2101 (1988).

[82] C. Gale, G.F. Bertsch, and S. Das Gupta, Phys. Rev. **C35**, 1666 (1987).

Chapter 5

Relativistic Fluid Dynamics

Fluid dynamics is a reaction model frequently used to describe heavy ion reactions in all energy regions. It has the advantage that it is transparent and analytic or quasi analytic solutions are possible, which provide a deeper insight into physical processes. The input of the fluid dynamics is directly the equation of state, so that it provides an excellent tool for the study of the EOS.

On the other hand fluid dynamics is an idealized continuum description assuming local equilibrium. Microscopic numerical models are usually able to describe a heavy ion reaction more closely, and account for fluctuations and finite particle effects.

5.1 Energy domains, stopping power

Before we start to discuss specific models some basic considerations should be made about the different types of collisions anticipated to appear at different energies.

There are two major possibilities for the basic reaction mechanism of heavy ions colliding at ultra-relativistic energies: at lower energies the stopping power of the colliding nucleons or quanta might be sufficient to stop the nuclear matter and create a nearly equilibrated hot and dense system in the C.M. frame, while at very high energies the baryons can penetrate through each other initially. In this latter case the development of the central zones and the side (fragmentation) regions is different.

5.1.1 Stopping energy region

At BEVALAC energies we have seen evidence that a central, highly excited zone with high pressure develops leading to the observed collective flow[1]. The mean free path is not negligibly small at these energies but it is still smaller than the size of the system, so fluid dynamical effects are still observable. With increasing energies the nucleon nucleon cross section becomes more and more forward peaked leading to longer mean free path and more transparency. This observation led to the introduction of the two fluid[2] and three fluid[3] models.

At the threshold of the QCD plasma phase transition, however, the degrees of freedom increase rapidly, and so this can contribute to an increased stopping power. In fact stopping power studies, based on proton nucleus reactions at the 20-100 GeV energy [4, 5, 6, 7, 8, 9] indicate that a heavy target nucleus can slow down the incident proton by about 2.5 units of rapidity[4], which means that we can have stopping for the heaviest nuclei colliding on each other up to about 15-35 GeV/nucleon Lab. beam energy. This indicates to us that we should try to apply a one-fluid description at this energy region, or two-fluid dynamics to allow for a partial transparency at the initial stages of the collision.

5.1.2 Transparent reactions, mid rapidity region

At energies above E=30-100 GeV/nucleon the stopping of the nuclei is not anticipated. Even in central collisions the baryons or the corresponding three valence quarks are expected to slow down only slightly. At the initial impact target and projectile nucleons interact and this interaction, represented by gluon or chromoelectric fields lasts for a considerable time. During this time the leading quanta (e.g. the 3 valence quarks) carrying the baryon charge propagate further due to their large initial momentum. Thus the quanta which carry the baryon charge leave the c.m. region while the interaction still acts between the projectile and the target. There is a large energy density, however, associated with the fields representing this interaction. At later stages the fields neutralize, and pion and other hadron pairs are created. The momentum or rapidity distribution of these particles is expected to be uniform based on the similar result in p+p reactions. This indicates that the energy density is also "uniform" in space time. Namely, it is constant along a curve corresponding to constant proper time away from the reaction. Fig. 5.1.

This region can be described somewhat more easily than the others, since the matter is free of baryon charge and so the EOS is simpler. Furthermore, the uniformity of the rapidity distribution allows for simple and imperative theoretical description as we will see later.

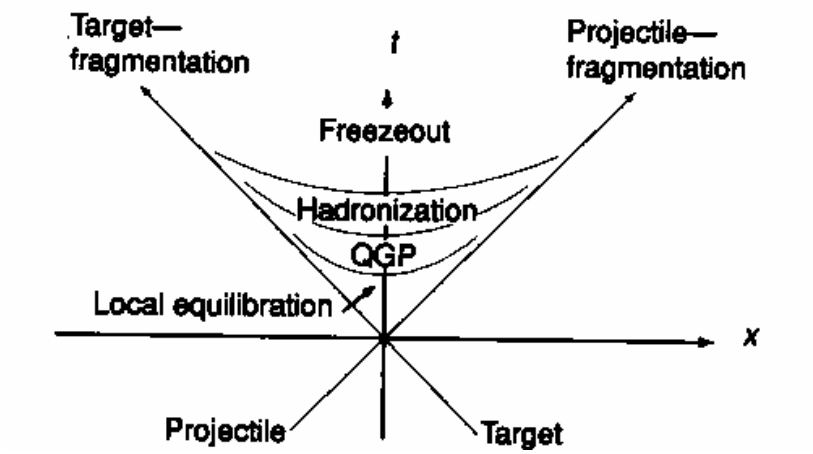

Figure 5.1: Space-time picture of an ultra-relativistic heavy ion collision. The projectile and the target and later their valence quarks propagate close to the light-cone. The thermalized matter in the mid-rapidity region changes its state according to the proper time counted from the event of collision

5.1.3 Transparent reactions, fragmentation region

The most involved is probably the description of the so called fragmentation region. Based on p+p and p+A experiments the expectation is that the baryons after a high energy collision will be emitted in a narrow rapidity range of few units, not far from their original rapidity. The net baryon charge in these reactions is distributed in two peaks, these are the so called fragmentation regions. However, the target nucleons still will be accelerated by the projectile and vice versa, and this and the interaction will lead to an increase in the energy density. The increase of energy density might be sufficient to reach the threshold of the phase transition in the fragmentation region also.

5.2 Perfect fluid dynamics

As we derived it in chapter 2, the conservation laws of a continuum can be expressed in a differential form via the energy-momentum tensor. The validity of these equations is wider than the derivation in chapter 2 may suggest. Dense liquids can also be described by these equations. Here, we will use the perfect relativistic fluid dynamical equations most of the time.

The equations of Perfect Fluid Dynamics are the conservation laws

$$N^{\mu}{}_{,\mu} = 0 \quad \text{or} \quad \partial_{\mu}(nu^{\mu}) = 0, \tag{5.1}$$

and

$$T^{\mu\nu}_{\ ,\mu} = 0 \quad \text{or} \quad \partial_{\mu}(T^{\mu\nu}) = 0. \tag{5.2}$$

Using $u^{\mu} = (\gamma, \gamma\vec{v})$, $w = e + P$, $T^{ik} = w\gamma^2 v_i v_k + P\delta_{ik}$, $T^{0i} = -T_{0i} = w\gamma^2 v_i$,

$T^{00} = T_{00} = (e + Pv^2)\gamma^2$, and introducing the apparent density

$$\mathcal{N} \equiv n\gamma = \mathsf{n}, \tag{5.3}$$

and the momentum current density and apparent energy density:

$$\vec{\mathcal{M}} \equiv T^{0i} = w\gamma^2\vec{v}, \tag{5.4}$$

$$\mathcal{E} \equiv T^{00} = (e + P\vec{v}^{\,2})\gamma^2, \tag{5.5}$$

the equations of fluid dynamics take the more familiar form. The continuity equation

$$(\partial_t + \vec{v}\,\mathrm{grad})\mathcal{N} = -\mathcal{N}\mathrm{div}\vec{v}. \tag{5.6}$$

The energy and momentum conservation will take the form

$$(\partial_t + \vec{v}\,\mathrm{grad})\vec{\mathcal{M}} = -\vec{\mathcal{M}}(\mathrm{div}\vec{v}) - \mathrm{grad}P, \tag{5.7}$$

$$(\partial_t + \vec{v}\,\mathrm{grad})\mathcal{E} = -\mathcal{E}\mathrm{div}\vec{v} - \mathrm{div}(P\vec{v}). \tag{5.8}$$

The last two equations are the Euler equation of fluid dynamics and the energy conservation. The difference between these equations and the non-relativistic perfect fluid dynamics is that the quantities $\mathcal{N}$, $\mathcal{E}$, $\vec{\mathcal{M}}$ are not related directly to the EOS, but one has to solve a set of algebraic equations, (5.3,5.4,5.5) to obtain the thermodynamical quantities. Thus, the equations of fluid dynamics are not complete without an equation of state. The EOS is always needed to obtain a solution.

The viscous fluid dynamics is seldom used in relativistic physics. This is due to the fact that there are still questions around the proper relativistic generalization of viscous fluid dynamics [10]. It was shown that the usual relativistic generalizations of viscous fluid dynamics may lead to unstable solutions. Dissipative effects are, nevertheless, important as many non- relativistic calculations indicate. There exist a few relativistic viscous calculations which can be viewed upon as approximations.

5.3 Numerical solutions

The fluid dynamical equations introduced at the end of the previous chapter were first solved numerically in 1975 in Los Alamos [11, 12, 13, 14] for a heavy ion collision in full complexity. By now several research groups have 3-dimensional relativistic fluid dynamical codes, which are appropriate to model high energy heavy ion collisions. These calculations, however, require considerable computing power and extensive numerical work in developing proper numerical methods. Thus, today there are still less than half a dozen groups able to perform relativistic fluid dynamical calculations in 3 dimensions. A recent review of the fluid dynamical models can be found in refs.: [15, 16].

The equations $N^{\mu}{}_{,\mu} = 0$ and $T^{\mu\nu}{}_{,\nu} = 0$ do not provide a complete system of equations, the number of unknowns is greater than the number of equations. We need some further information. This is provided by the Equation of State (EOS): $P = P(n, T)$ or $P = P(n, e)$.

5.3.1 Equation of state

The nuclear Equation of State (EOS) was discussed in the previous chapter in detail, here we just repeat the most basic information. In the transport theory we discussed so far, the pressure is that of an ideal gas because we neglected all interactions among the particles. Thus, strictly speaking, the fluid dynamical equations we derived from the BTE are valid only under the assumptions we made: our system is in local equilibrium everywhere, and the distribution function is a Jüttner distribution. Consequently, our EOS is necessarily the EOS of a classical relativistic ideal gas.

Nevertheless, this restriction is not really necessary. The fluid dynamical equations can be derived in many different ways, since they express only the energy, momentum and mass conservation. Thus, the only real requirement is that the EOS should satisfy all thermodynamical requirements. In the fluid dynamical model the EOS can be more realistic than a simple ideal gas. For heavy ion collisions it should reflect the known basic properties of nuclear matter.

Some basic features of the EOS are presented in Fig. 5.2. The nuclear matter has a stable ground state at the normal nuclear density, $\mathsf{n}_0 = 0.145\text{-}0.17$ fm^{-3} with -8 MeV/nucleon energy. (The value of -8 MeV instead of -16 MeV is taken to simulate finite size and Coulomb effects.) This is a minimum of the specific energy at zero temperature. At higher temperatures the specific energy is higher. The curvature of the specific energy curve is characterized by the nuclear compressibility. The value of this compressibility is the subject of present heavy ion research, and we will discuss it later.

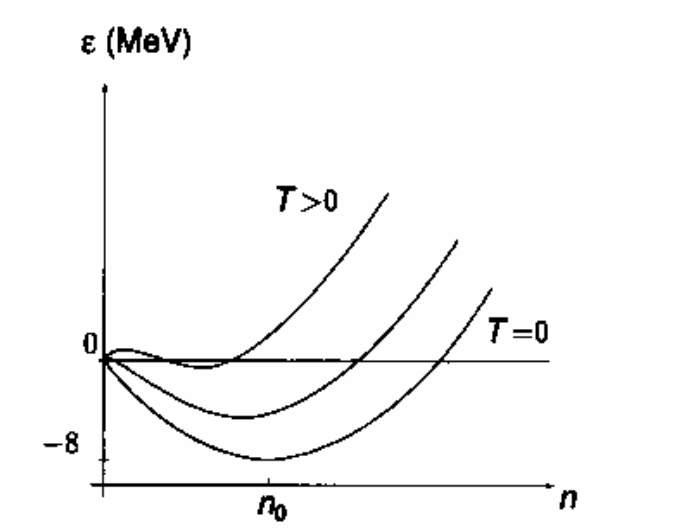

Figure 5.2: The nuclear EOS: the specific energy as function of the nuclear density. The parameter is the temperature, T.

It is customary to represent the EOS via the specific energy, ε:

$$\varepsilon(n,T) = m_0 + \varepsilon_0(n) + \varepsilon_T(n,T),$$

where $\varepsilon_0(n) \equiv \varepsilon(n, T=0)$, and m_0 is the contribution of the rest mass to the specific

energy. This separation of the thermal, ε_T, and compressional, ε_0, energy is unique but it is not necessarily a sensible separation in a given theoretical model. Furthermore, one has to keep in mind that $\varepsilon(n,T)$ is not a thermodynamical potential so this quantity alone does not determine the thermodynamical behavior of the matter completely.

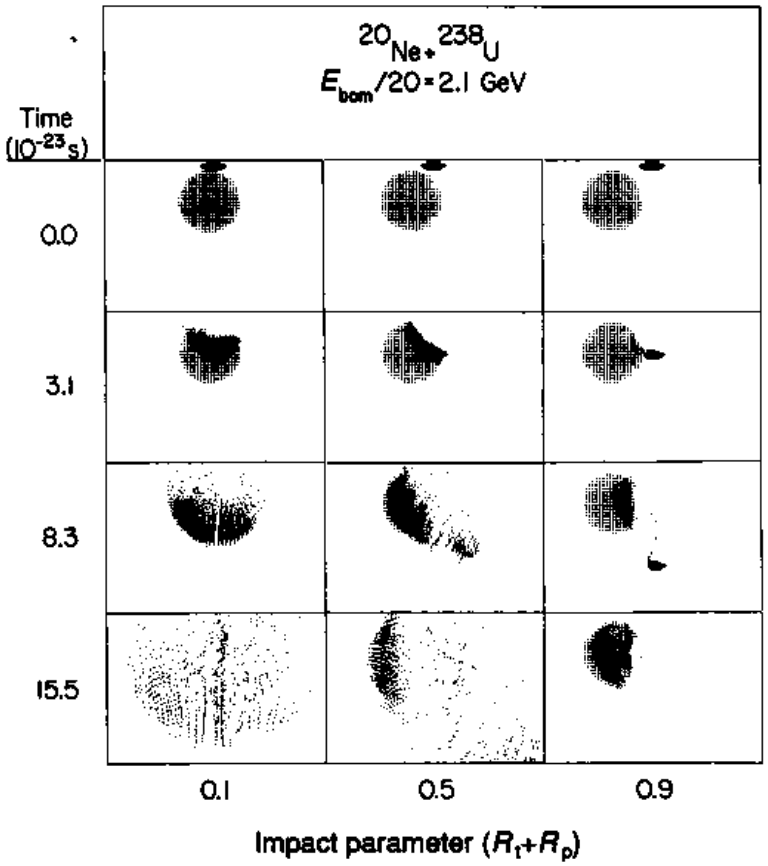

Figure 5.3: Change of density configuration in a relativistic heavy ion collision. The darkness illustrates the density of nuclear matter. (Each dot represents a so called "marker particle" of the PIC numerical method. If several marker particles are exactly above each other we see only one dot as their projection to the reaction plane.) One marker particle represents a fraction of the unit baryon charge, typically 1/100-1/500. The most apparent feature is the relatively sharp shock front at the initial compression stage. Reproduced by permission of the American Physical Society from [12].

5.3.2 Flow characteristics from numerical solutions

Let us first see some examples for the solutions of the relativistic Euler equations. In Figures 5.3,5.4,5.5 there are some examples from numerical results of fluid dynamical calculations. Fig. 5.3 from ref. [12] illustrates heavy ion collisions as calculated in the relativistic fluid dynamical model in Los Alamos.

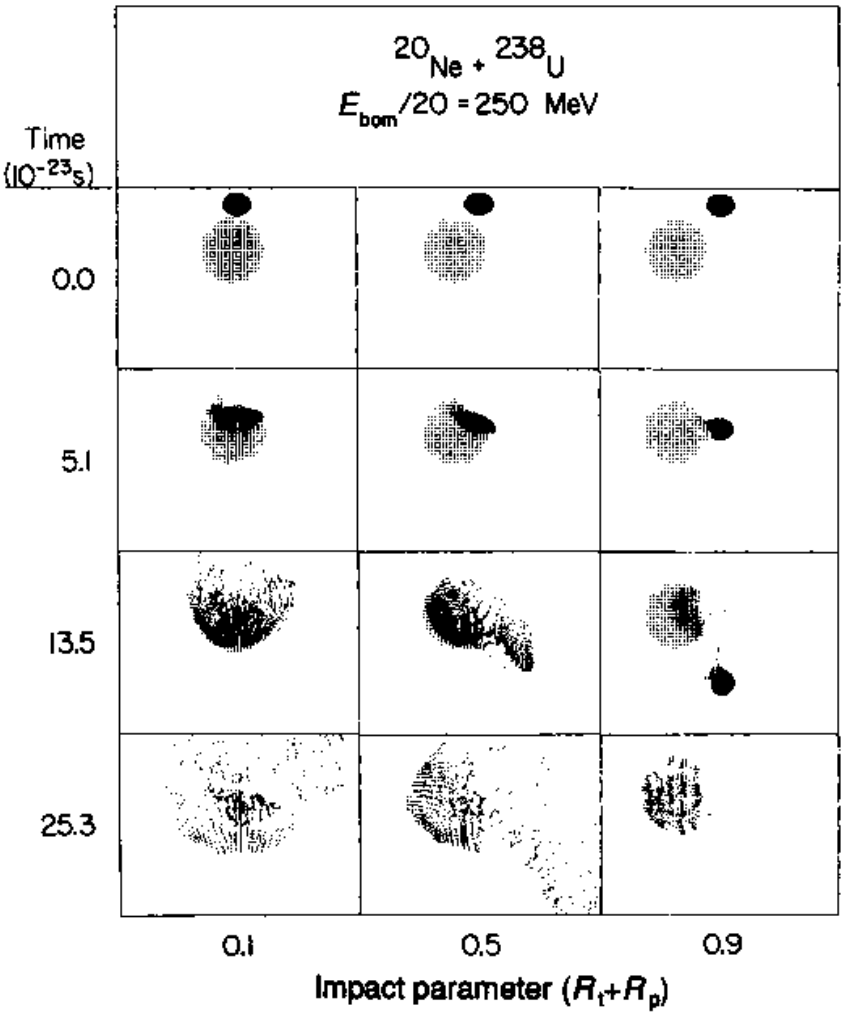

Figure 5.3: continued

Fig. 5.4 shows the results of a Soviet group which calculated the density increase in a heavy ion collision in the relativistic fluid dynamical model [17].

In these collisions the increase of energy density is larger than the increase of baryon density, due to the compressional and thermal energy. In an ideal gas the compressional energy is not present, thus it is a very *soft* matter. The time dependence of the energy density reachable in a heavy ion collision was calculated by a group at the University of Frankfurt, ref. [18]. It turned out that the large projectile and target mass is more important to reach high energy density for as many nucleons as possible. The increasing beam energy is secondary but it also results in an increase of energy density. Fig. 5.5 illustrates the energy density increase at two beam energies, 5 and 15 GeV/nucleon.

In all these solutions the density increases in relatively sharp fronts of widths of a few Fermi. The reason is that the speed of the incoming projectile and consequently the flow velocity is *supersonic*. The sound speed in (ground state) nuclear matter is

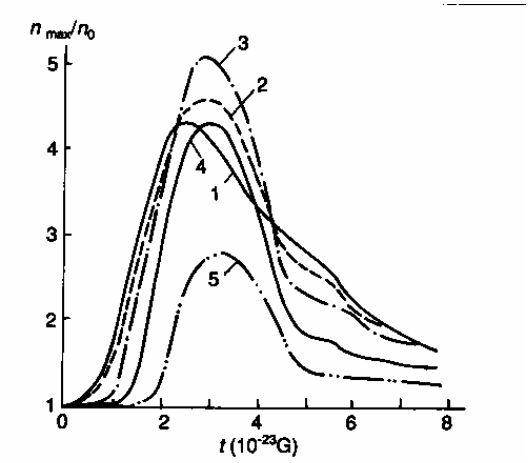

Figure 5.4: The maximum of the nuclear density as a function of time from a numerical calculation for the reaction: 3.6 $GeV/nucl.$ $C + Pb$ at different impact parameters. The parameter of the curves is the impact parameter, denoted by ρ in units of $R_t + R_p$, $b = \rho(R_p + R_t)$. Curve 1: $\rho = 0.1$, Curve 2: $\rho = 0.3$, Curve 3: $\rho = 0.5$, Curve 4: $\rho = 0.7$, Curve 5: $\rho = 0.9$. Reproduced with permission from [17].

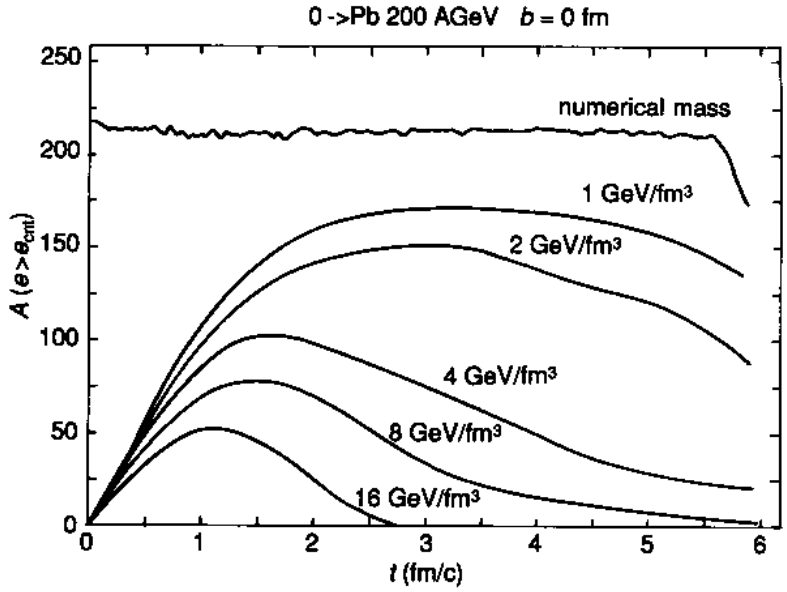

Figure 5.5: The number of nucleons that exceed a given energy density, e_{crit}, at a given time, t, in a heavy ion collision. The energy density of the ground state nuclear matter is $e_0 = E/V = n_0\varepsilon_0(n_0) \approx 0.15GeV/fm^3$ so that $e_{crit} = 2GeV/fm^3$ is already more than ten times larger than that of the normal nuclear matter. A is the number of nucleons that are in the region where $e > e_{crit}$ at different times t. Reproduced by permission of World Scientific Publishing Co. from [19].

about $v_{sound} \approx 0.2c$.

In the Eulerian fluid dynamics the formation of such sharp fronts would rigorously mean that there is no continuous solution to the equations of fluid dynamics at the given boundary condition and discontinuity or discontinuities should develop in the solution. These ("infinitely sharp") discontinuities should then be described by the Rankine–Hugoniot–Taub equations [20].

Physically shock waves do really exist but these are not infinitely sharp. Depending on the dissipative processes (viscosity, heat conductivity, reaction rates, and/or incomplete equilibrium of some other kind) a shock front of finite width will develop and after some initial transients it will propagate stationarily. The final state of the shocked matter is, however, identical with the final state we would obtain in an infinitely sharp shock front, because it is fully determined by the energy, momentum and baryon conservation. Only the internal structure of the front depends on the dissipative non-equilibrium processes [11, 12, 13, 14, 20].

There seems to be a contradiction here, since the numerical codes we mentioned are solving the relativistic Euler equations, and they still yield shock fronts of finite width. This is due to the numerical method which always yields a so called *numerical viscosity* [21]. This is unavoidable because all numerical codes have finite spatial resolution. The final state is, however, correct and only the internal structure (and width) of the front depends on the numerical method.

5.3.3 Conclusions

1 Final states of compression fronts can be studied in a simple way, by means of the Taub equations. This final state in an ideal situation depends only on the Equation of State of the nuclear matter. These compression phenomena include shocks, detonations, deflagrations, etc. Their details will be discussed later during this course.

2 In realistic descriptions dissipation should be studied in two ways:

(2a) If deviations from equilibrium are small we may use an "expansion" around $f^{eq.}$. This is the Chapman–Enskog expansion, which leads to the *Navier–Stokes* equations of fluid dynamics in first order.

(2b) If deviations from equilibrium are large, other approximations are necessary to solve the physical problem like: Multi component fluid dynamics, Cascade models, Mean field theories with cascading particles like, Vlasov–Uehling–Uhlenbeck (VUU), Boltzmann–Uehling–Uhlenbeck (BUU), Landau–Vlasov (LV) or Molecular Dynamical models.

3 In perfect relativistic fluid dynamics there is **no** entropy increase, the flow is adiabatic. In these models entropy could be generated in discontinuities (shock fronts) only.

5.4 Numerical methods

To solve the equations of numerical fluid dynamics there are two basic approaches, the Eulerian and the Lagrangian solution methods. In the Eulerian method we fix our computational reference frame (or computational grid) in the space some way and the fluid flows across these grid cells. This method is frequently used if flow around some known object is studied, like flow around a ship or flow in a pipeline, or in a channel. It is also very practical for incompressible or just weakly compressible fluids.

In the Lagrangian method the reference frame is fixed to the fluid itself, and the fluid does not flow in or out of the cells. In a flow these cells, however, change their shape and position, and even their volume if the fluid is compressible. This method is preferred if there are big changes in compression, if there are no fixed objects in the flow, etc. If, however, the flow is three dimensional, with large shears, or if the flow is getting close to turbulent, this method cannot be used because the neighbors of a cell are not the same during the flow.

In relativistic heavy ion physics two solution methods are used for large scale calculations the Particle in Cell method, and the Flux Corrected Transport method. Here we demonstrate briefly these two methods based on a review of Maruhn [22].

5.4.1 The Particle in Cell (PIC) method

The PIC method developed at Los Alamos by Amsden and Harlow [23, 24] is a very fast and efficient algorithm with some necessary drawbacks in accuracy. The formulation is Eulerian, but with a Lagrangian admixture via the inclusion of numerical marker particles that flow through an Eulerian-grid. (These particles are purely fictitious and have nothing to do with nucleons). The fluid quantities N, $\vec{M}$, and E are defined on this space-fixed grid, and the marker particles are there to exchange some of these quantities between neighboring cells. The principal part of the calculation in each time step is divided into two phases:

(i) Updating $\vec{M}$ and E without including transport between neighboring cells, i.e. using

$$\frac{\partial \vec{M}}{\partial t} = -\nabla p, \quad \frac{\partial E}{\partial t} = -\nabla(p\,\vec{v}). \tag{5.9}$$

(ii) The momentum and energy content of each cell are distributed evenly among the marker particles in the cell. Each marker particle is then assigned a velocity by interpolating the velocities of the neighboring grid points to the particle position, and is then moved using that velocity. If it crosses a cell boundary, its momentum and energy content are added to its new cell and subtracted from the old one.

Note the differences from "molecular dynamics" simulation: after each time step the particles "forget" some information such as their previous velocities; also the momentum and energy carried by a particle are not related to its velocity. The precise formulation of the code for relativistic hydrodynamics is given by Harlow, Amsden and Nix [21]. The transport is "quantized" in the method: the number of particles in each cell determines

in which increments mass, energy, and momentum can be exchanged with other cells. This is especially constraining in the final stages of the reaction when densities get quite low.

5.4.2 The Flux Corrected Transport algorithm (FCT)

This algorithm, developed originally by Boris and Book [25, 26, 27], is applicable to any one-dimensional conservation equation of the type

$$\frac{\partial n}{\partial t} + \frac{\partial (n \cdot v)}{\partial x} = S \ . \tag{5.10}$$

All the equations of motion of hydrodynamics can be written this way. Three dimensional motion can be incorporated by moving alternately along the three axes ("time step splitting"). We will discuss the algorithm in the SHASTA -version (one variant of this, phoenical SHASTA [26] is the one actually used in the nuclear collision calculations). The transport is derived by moving the density, n, according to the flow velocity in a Lagrangian way, and then reinterpolating the result onto the space-fixed Eulerian grid. This leads to the equations for the density n after the motion:

$$\bar{n}_j = \frac{1}{2} Q_j^{+2} (n_{j+1} - n_j) + \frac{1}{2} Q_j^{-2} (n_{j-1} - n_j) + + (Q_j^+ + Q_j^-) n_j + \Delta t \ S_j, \tag{5.11}$$

with

$$Q_j^+ = \epsilon_j^- / (\epsilon_{j+1}^+ - \epsilon_j^-), \qquad Q_j^- = 1 - Q_{j-1}^+, \tag{5.12}$$

and

$$\epsilon_j^\pm = \frac{1}{2} \pm v_j \Delta t / \Delta x. \tag{5.13}$$

What important is that these finite difference equations contain a strong diffusion, which is most easily seen for the simple case $v = S = 0$:

$$\bar{n}_j = n_j + \frac{1}{8} (n_{j+1} - 2n_j + n_{j-1}). \tag{5.14}$$

On the one hand, this diffusion is disastrous for numerical accuracy, since it smears out all structures rapidly, but on the other hand it prevents instability near shock fronts. The basic idea of the FCT is to remove the diffusion only at those points where it can be done without danger. In the simplest approximation one may correct approximately with an anti-diffusion step

$$\tilde{n}_j = \bar{n}_j - \frac{1}{8} (\bar{n}_{j+1} - 2\bar{n}_j + \bar{n}_{j-1}). \tag{5.15}$$

but cut off the correction wherever this creates new extrema in the profile or enhances existing ones. Note that physical extrema can still be created in the first diffusive step, but cannot be further enhanced by the anti-diffusion. The cutoff is formulated in a relatively complicated minimum-maximum formula [25]. This numerical method has the advantage of being relatively straightforward, explicit, and easy to use in several dimensions while allowing a good representation of shock fronts.

5.5 Simple analytic solutions—Shock waves

In the forthcoming sections we will present some simple solutions of the Fluid Dynamics (FD) relevant to heavy ion collisions. Most of these are one dimensional and analytically calculable. They try to describe some characteristic features of the collision. Some basic solutions important for us are: Shock, detonation and deflagration waves, Bjorken's fluid dynamical model, approximate spherical expansion model, Landau's fluid dynamical model etc.

In central and nearly central relativistic heavy ion collisions the density profile along the beam axis is shown schematically in Fig. 5.6

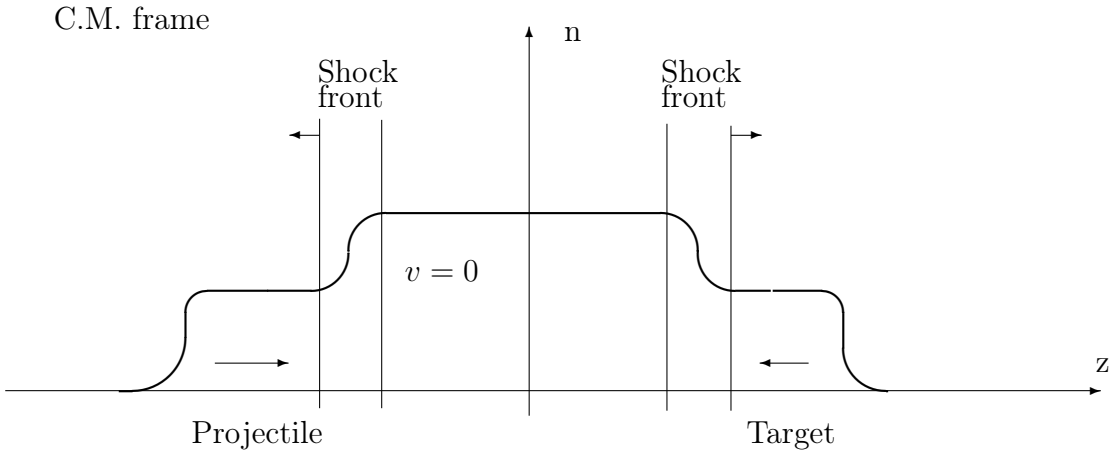

Figure 5.6: Schematic density profile of two colliding nuclei along the central beam axis, z. In supersonic impact the density increase happens in shock fronts. The matter ia at rest in the middle

The shock can be approximated by a one dimensional problem shown in Fig. 5.7. In this figure the local sound velocity is denoted by v_s. The same shock front can be viewed from the front's reference frame, i.e. from the frame where the front is at rest and the matter flows across. Fig. 5.8

If the wave-shape is stationary in the constant volume , V_w, which is moving with the front, the energy, particle number and momentum are constant in the volume, so the incoming and outgoing $\mathcal{N}, \mathcal{E}, \vec{\mathcal{M}}$ should be equal. Let us denote the two sides by "1" and "2", and the difference of a quantity, Q, by $[Q] = Q_2 - Q_1$ (e.g. $[v] = v_2 - v_1$ in the frame where the front is at rest!)

If the front is infinitely sharp (Eulerian FD) we have to consider a sharp surface where the flow variables are discontinuous. The surface of this discontinuity has a unit normal vector, Λ^μ, in the space-time. It can be space-like or time-like:

$$\Lambda^\mu \Lambda_\mu = \begin{cases} +1 & : \ time-like \ \ surface \\ -1 & : \ space-like \ \ surface \end{cases} . \tag{5.16}$$

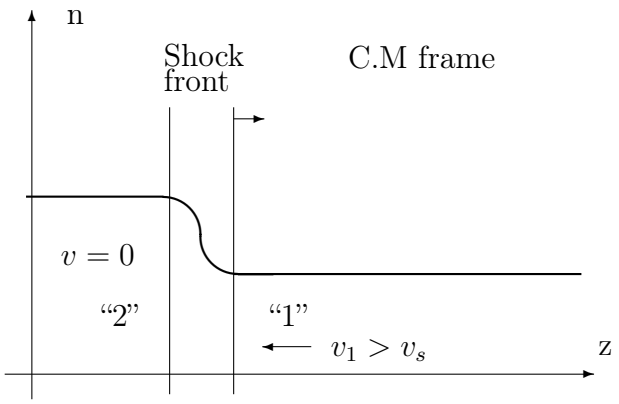

Figure 5.7: One of the shock fronts presented in the previous Figure in the c.m. frame

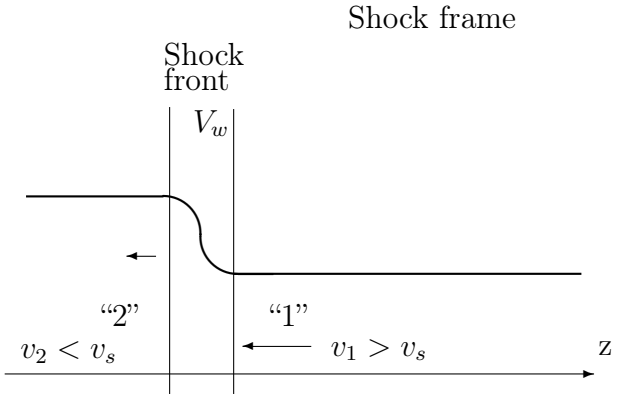

Figure 5.8: The same shock front presented in the previous Figure but in the frame of the shock front. In this frame the shock front is kept at the same location, matter is flowing in and out but with different velocities

Orthogonally to the front the energy and momentum flow should be identical on the two sides:

$$[T^{\mu\nu}\Lambda_\nu] = 0, \tag{5.17}$$

and the particle number should also be conserved:

$$[N^\mu \Lambda_\mu] = 0. \tag{5.18}$$

Eqs. (5.17) and (5.18) are the relativistic Rankine–Hugoniot equations, first written down by A. Taub (but only for space-like surfaces of discontinuity). The shock front propagates (usually) with $v_{shock} < 1$, i.e. the points of the front are in causal connection. This, however, is not necessary, $v_{shock} > 1$ is possible, because the discontinuity does not move with the matter. Space-like fronts can be transformed into their local rest frame (where the front stands), and the matter flows across. Time-like discontinuities can be transformed into local rest frame where the matter at a time t goes over a sudden transition everywhere (e.g. phase transition). This can be caused by the initial conditions, only, and not by the effect of neighboring fluid elements. An example is very slow homogeneous compression or heating. The temperature may exceed a critical value at the same time everywhere in the container and the phase transition may take place simultaneously. See Figs. 5.9,5.10.

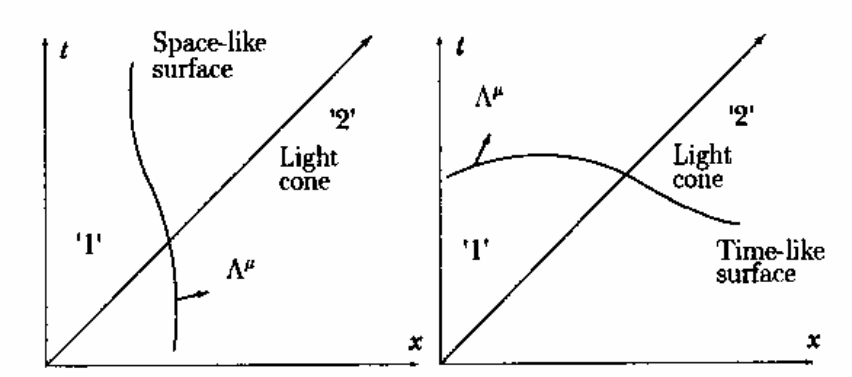

Figure 5.9: Space-like (a) and time-like (b) surfaces of discontinuity

5.5.1 Taub adiabat for finite particle densities

One can eliminate the velocity from eqs.(5.17)-(5.18) and end up with a scalar equation connecting the thermodynamical quantities on the two sides of the shock. The resulting equation is called the *shock or detonation adiabat*.

Let us use Eckart's definition where $N^\mu = nu^\mu$. Outside the shock front we have stationary flow with no dissipation or heat conduction, thus Landau's and Eckart's definitions are equivalent. If, however, there is no conserved particle number, this derivation we present here is not applicable. Still, the Taub adiabat can be derived in a similar fashion as it is shown in refs. [28, 29].

Let us define the particle current across the surface:

$$j \equiv N^\mu \Lambda_\mu. \tag{5.19}$$

This j is an invariant scalar, and according to eq. (5.18) it has the same value on both sides of the shock! j can also be written as $j \equiv nu^\mu \Lambda_\mu$ because outside the front there is no dissipation. In the LR of the front

$$\Lambda_{\mu\ LR} = \begin{cases} (1,\vec{0}) & : \ time-like \ \ surface \\ (0,\vec{e}) & : \ space-like \ \ surface \end{cases}, \tag{5.20}$$

where $\vec{e}$ is a unit 3-vector. Using $u^\mu = (\gamma, \gamma\vec{v})$ we get the current as

$$j_{LR} = \begin{cases} n\gamma & : \ time-like \ \ surface \\ n\gamma(\vec{v}\vec{e}) = n\gamma v_\perp & : \ space-like \ \ surface \end{cases}, \tag{5.21}$$

where $v_\perp$ is the component of velocity normal to the front. Since j is invariant scalar $j = j_{LR}$. Thus, eq. (5.18) can be written as

$$[j] = 0, \tag{5.22}$$

i.e. j is constant across the front!

Eq. (5.17) is a 4-vector equation. To end up with the shock adiabat which is an equation connecting thermodynamical (invariant scalar) quantities, we need two scalar equations projected out of eq.(5.17). So we will have two projections:

(i) Parallel projection to the surface

(ii) Orthogonal projection to the surface

Parallel projection. Let us express the component of the conserved energy-momentum and baryon current, orthogonal to the surface, (parallel to its normal):

$$[T^{\mu\nu}\Lambda_\nu] = 0 \quad \rightsquigarrow [T^{\mu\nu}\Lambda_\nu\Lambda_\mu] = 0$$

$$\rightsquigarrow [wu^\mu u^\nu \Lambda_\mu\Lambda_\nu - p\Lambda^\mu\Lambda_\mu] = 0.$$

Using eq. (5.19): $j = nu^\mu\Lambda_\mu$, ($\rightsquigarrow$ $u^\mu\Lambda_\mu = \frac{j}{n}$), and inserting this into the equation above

$$\left[\frac{w}{n^2}j^2 - P\ \Lambda^\mu\Lambda_\mu\right] = 0,$$

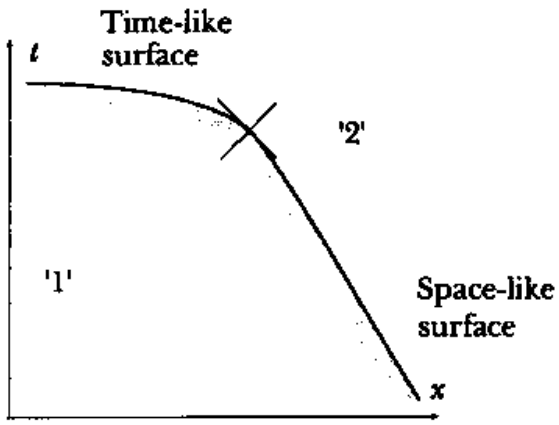

Figure 5.10: Smooth change from spacelike to timelike detonation

$$\left[\frac{w}{n^2}\right] j^2 - [P]\,(\Lambda^\mu \Lambda_\mu) = 0.$$

This leads then to the equation of the *Rayleigh-line*:

$$j^2 = \frac{[P](\Lambda^\mu \Lambda_\mu)}{[X]}, \tag{5.23}$$

where $X \equiv \frac{w}{n^2}$, is the *generalized specific volume*. In the non-relativistic limit $X \longrightarrow m_0 V_{spec.}$. The $[P, X]$ plane corresponds to the $[P, V]$ plane in the non-relativistic limit. The equation of the Rayleigh line is a straight line on the $[P, X]$ plane. It gives the locus of the possible final state coordinates, P_2's and X_2's, if the initial state "1" is given. The slope of the Rayleigh line is given by the current across the front j. In heavy ion reactions j usually increases if the beam energy increases.

Orthogonal projection. Form the orthogonal projection of the 4-vector $T^{\mu\nu}\Lambda_\nu$ with the projector

$$\Delta^{\mu\nu}_{\Lambda} = g^{\mu\nu} - \frac{\Lambda^\mu \Lambda^\nu}{(\Lambda^\mu \Lambda_\mu)}$$

we get a 4-vector tangent to the plane: $G^\tau \equiv T_{\mu\nu}\Lambda^\mu \Delta^{\nu\tau}$, and then a scalar equation by taking the norm:

$$[G^\tau G_\tau] = \; [T_{\mu\nu}\Lambda^\mu \Delta^{\nu\tau} \;\; T^{\sigma\omega}\Lambda_\sigma \Delta_{\omega\tau}] = 0.$$

Since

$$G^\mu = (w u_\tau u_\nu \Lambda^\nu - P\Lambda_\tau)\left(g^{\tau\mu} - \frac{\Lambda^\tau \Lambda^\mu}{(\Lambda^\sigma \Lambda_\sigma)}\right) =$$

$$= w(u_\nu \Lambda^\nu)u^\mu - w(u_\tau \Lambda^\tau)(u_\nu \Lambda^\nu)\frac{\Lambda^\mu}{(\Lambda_\sigma \Lambda^\sigma)} - P\Lambda^\mu + P\frac{(\Lambda_\tau \Lambda^\tau)}{(\Lambda_\sigma \Lambda^\sigma)}\Lambda^\mu =$$

$$= \frac{w}{n} j u^\mu - \frac{w}{n^2} j^2 \frac{\Lambda^\mu}{(\Lambda_\sigma \Lambda^\sigma)}.$$

Thus the scalar equation $[G^\mu G_\mu] = 0$ can now be calculated. One of the cross terms and the last term cancel each other, so

$$\left[\frac{w^2}{n^2} j^2 u^\mu u_\mu - \frac{w^2}{n^4} j^4 \frac{\Lambda^\mu \Lambda_\mu}{(\Lambda_\sigma \Lambda^\sigma)^2}\right] = 0, \ \rightsquigarrow$$

$$\left[\frac{w^2}{n^2}\right] - \left[X^2\right] j^2 (\Lambda^\mu \Lambda_\mu) = 0.$$

This leads to the equation

$$j^2 = \frac{[wX]}{[X^2](\Lambda^\mu \Lambda_\mu)}. \tag{5.24}$$

Comparing eqs. (5.23) and (5.24)

$$\frac{[P](\Lambda^\mu \Lambda_\mu)}{[X]} = \frac{[wX]}{[X^2](\Lambda^\mu \Lambda_\mu)} \quad \rightsquigarrow \quad \frac{[P](\Lambda^\mu \Lambda_\mu)^2}{[X]} = \frac{[wX]}{[X](X_2 + X_1)},$$

which leads to the equation of *Taub adiabat*, shock adiabat or relativistic Rankine–Hugoniot adiabat:

$$[P] = \frac{[wX]}{(X_2 + X_1)}. \tag{5.25}$$

This is an equation defining a curve in the $[P, X]$ plane if an EOS is given. It depends on the EOS and on the initial state "1". The locus of the possible final state P_2's and X_2's are then given by the Taub adiabat. Thus the shock adiabat is a curve in the $[P, X]$ plane, like the normal (Poisson) adiabat. Fig. 5.11.

The difference is that the shock adiabat depends both on the equation of state of the matter on the side "2" and on the initial state, "1", parameters. If the initial "1" and final "2" states have the same equation of state, we have a normal shock, and the shock adiabat goes through the initial point "1" as well. At this point the Poisson adiabat and the shock adiabat are parallel (see ref. [30]). Consequently,

$$-\left.\frac{\partial P}{\partial X}\right|_{\text{"1"}} = (n_1 \gamma_s v_s)^2,$$

because the "infinitely weak" shock wave and the sound wave are identical. The weakest shock wave propagates with the speed of sound, $u_s = \gamma_s v_s$,Fig. 5.12. The "strength" of the shock is characterized by j.

If the current j, or the beam energy, is given, it selects (usually) one final state "2" from the shock adiabat.

The relative speed of matter on the two sides of the front with respect to each other is

$$v_{12} = \frac{v_1 - v_2}{1 - v_1 v_2 / c^2} = \sqrt{\frac{(P_2 - P_1)(e_2 - e_1)}{(e_1 + P_2)(e_2 + P_1)}}.$$

In heavy ion reactions of type **A**+**A** the center of mass system beam energy is $E_{c.m.} = m(\gamma_{12} - 1)$. In heavy ion collisions the initial state, "1", of the shock represents the ground state of nuclear matter. With a given equation of state eq. (5.25) can be solved. A solution is illustrated in Fig. 5.13 (from [31]).

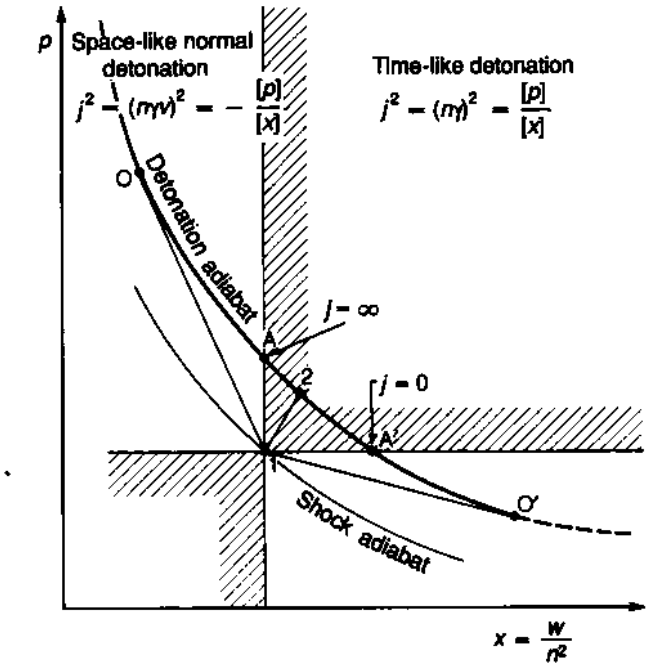

Figure 5.11: Shock and Detonation adiabat in the [P,X] plane. Reproduced with permission from [56].

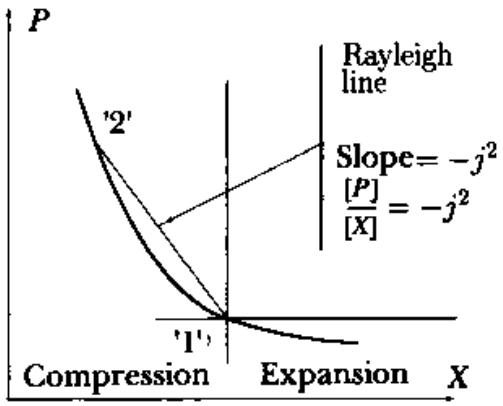

Figure 5.12: The slope of the chord and the current across the shock

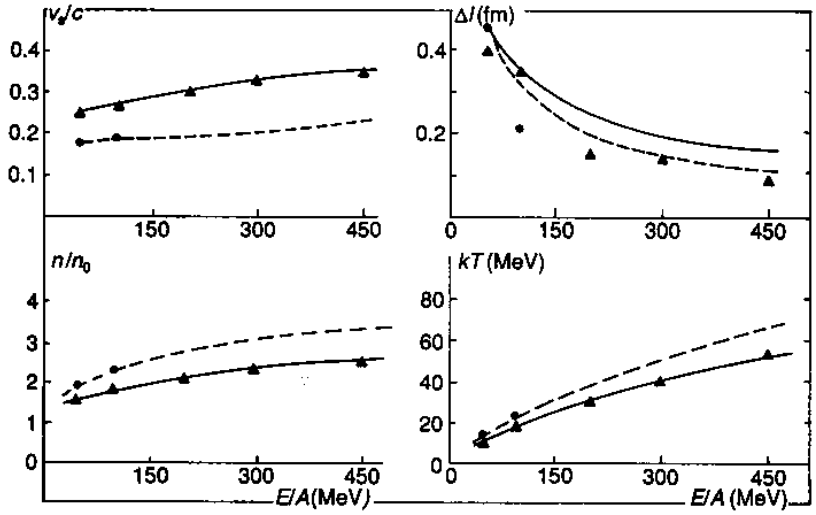

Figure 5.13: Shock velocity, v_S, compression, n/n_0, temperature of the shocked matter, kT, and the width of the front, Δl, calculated analytically with two different Equations of state: stiff — full lines, soft — dashed lines. Points are taken from a 1-dimensional numerical, viscous Relativistic Fluid Dynamical calculation. Reproduced with permission from [31].

5.5.2 Relativistic detonations

These phenomena are also called: Deflagration, Slow combustion, or Condensation waves.

The equation of state before and after the front may be different due to some chemical reaction, rearrangement, structural change, phase transition etc. In such cases the Taub adiabat does not go through the initial point "1" in the $[P, X]$ plane. We have two possibilities in this case (Fig. 5.14):

(i) if exotherm change: it goes above "1"

(ii) if endotherm change: it goes below "1"

Minimum energy to reach a new phase: If we have an exotherm reaction and we want to reach the final state, "2", on a Taub adiabat from the initial state, "1" we can usually do it by compression (X decreases, $X_2 < X_1$) or in expansion (X increases, $X_2 > X_1$). These two cases are called detonation and deflagration, respectively. Deflagrations are also called slow combustion (mainly in the Russian literature).

The least steep chord corresponding to a detonation from state "1" is tangent to the Taub adiabat. This is a Rayleigh-line touching the Taub adiabat at point "CJ". "CJ" is called the *Chapman–Jouguet point*, Fig. 5.15. The slope of this Rayleigh line is:

$$j^2_{min} = -\frac{P_2 - P_1}{X_2 - X_1} = (n_{CJ}\ \gamma_{CJs}\ v_{CJs})^2$$

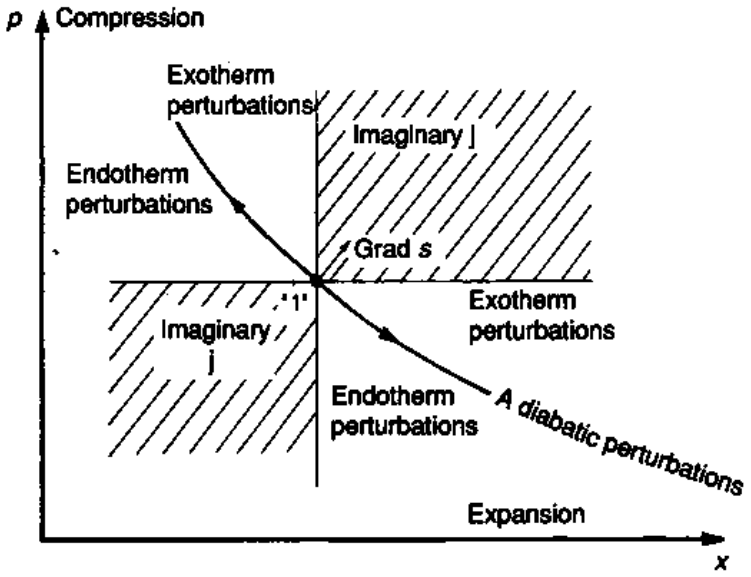

Figure 5.14: Exotherm and endotherm discontinuities. If only space-like discontinuities are considered the current, j, would be imaginary in the hatched areas. Reproduced by permission of the American Physical Society from [32].

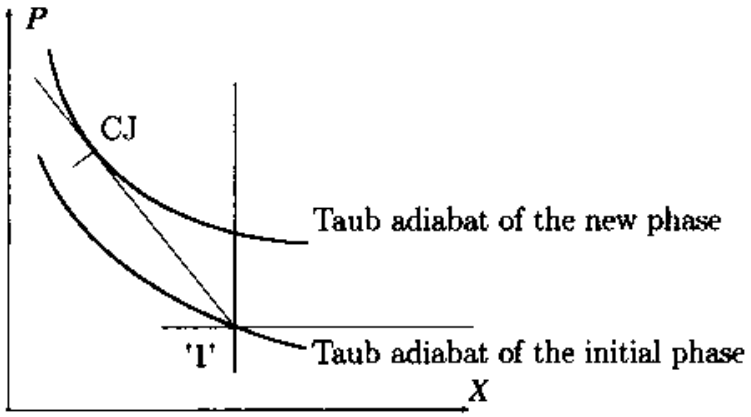

Figure 5.15: Minimum energy detonation

In a weaker shock the new phase is never reached.

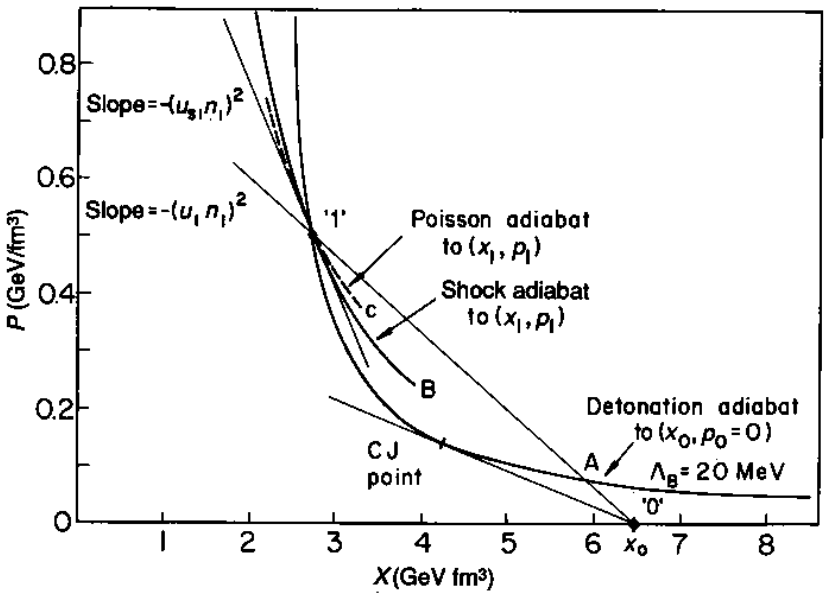

Figure 5.16: Detonation adiabat for QGP EOS. Slopes and sound speeds. Instead of "1" and "2" here the initial state is denoted by "0" and the final state by "1" ! Reproduced by permission of the American Physical Society from [32].

The final states cannot always be reached in a stable detonation front. The study of stability of shock fronts is quite involved. We can see the discussion of mechanical stability of the fronts in the textbook of L. D. Landau and E. M. Lifshitz [30], for the non-relativistic case. The stability of fast detonations dominated by radiation is even more difficult. This is complicated further by relativistic detonations, where discontinuities across timelike surfaces become possible.

In the stable region of the detonation adiabat the velocity of final matter leaving the front, v_2, should be smaller than the local sound velocity, v_{2s}, in that shocked matter $v_2 < v_{2s}$. As we can see in Fig. 5.16 at the final point "1" the Poisson adiabat is steeper than the Rayleigh line. All the points above the Chapman–Jouguet point satisfy this relation, thus these points represent mechanically stable final states. In the final state (at point "1" in Fig. 5.16) the local weak shock adiabat (corresponding to point "1") and the Poisson adiabat are parallel. Both having a slope related to the sound velocity as: $-(u_{1s}n_1)^2$.

Let us list systematically the different possibilities of discontinuities by increasing the current j across the surface of the discontinuity. Fig. 5.17 We discussed before that a minimum current is necessary to have a shock or detonation front. In normal shocks the speed of incoming matter should exceed the speed of sound. In detonations it should exceed the speed of sound at the CJ point.

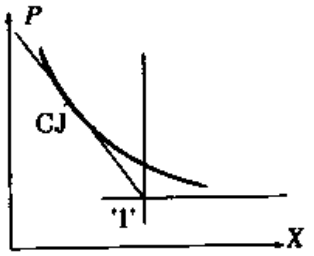

Detonation with j_{min}. This is the smallest current that leads to a detonation. The final state is a CJ point: $j = n_{CJ} u_{CJs}$.

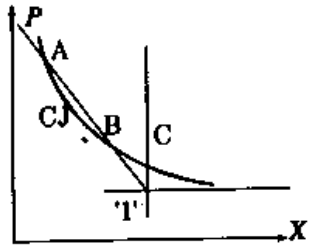

Detonation with $j > j_{min}$. There are two solutions: A and B; A is stable, at B the outgoing matter propagates faster than the local sound velocity, so the shock is unstable. However, if strong heat transfer is present due to radiation, final states in the section CJ-C are also realizable. This can be realized in nuclear bombs, rocket engines and in heavy ion collisions.

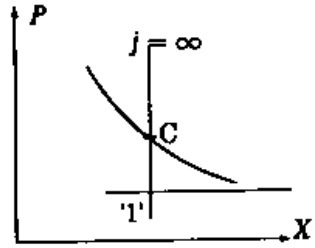

At point C the front propagates with the velocity of light: $j \to \infty$. This is the absolute boundary of propagating shocks due to causality.

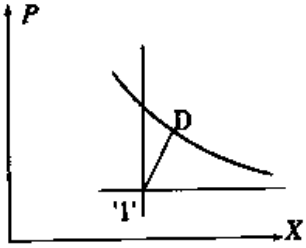

Time-like detonations like '1' → D, can only be caused by the special initial conditions. Otherwise the points on the front are not in causal connection to each other.

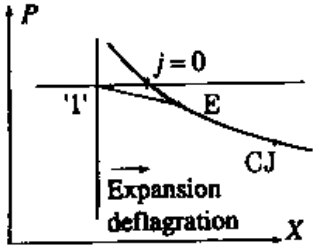

In slow combustion or deflagrations both v_1 and v_2 are subsonic. Thus the stable final point 'E' should lie between the Chapman–Jouguet point and the crossing by the $j = 0$ line. If the reaction rate does not limit the current across the front, the deflagration will propagate with sound velocity with respect to the matter behind the front, '2'. This speed maximizes the entropy production. The final state is then CJ.

Figure 5.17: Detonations with different currents across the front

5.5.3 Detonations to QGP

In RHIC the phase transition to QCD plasma is endotherm, but the transition back into the nuclear-matter in the expansion is exotherm. This goes over in a deflagration or slow combustion, which is an extremely popular subject now. Let us study the Taub adiabat of QCD plasma.

Aside:
Let us first recall some basic formulae about the EOS of ideal Bose and Fermi gases. If we neglect the baryon density, then the pressure and the energy density depends on the temperature T only. This may be a good approximation at high temperatures and low densities. The energy density of an ideal photon gas (ideal massless boson gas) is (c.f. eq. (60.16) in [33])

$$e_\gamma = g_\gamma \frac{\pi^2}{30(\hbar c)^3} T^4, \tag{5.26}$$

where $g_\gamma = 2$ is the degeneracy of photons, (two helicity states exist). The energy density of an ideal fermion gas at high temperatures (like the positron gas in an electron positron equilibrium) when the rest mass is negligible compared to the temperature (c.f. eq. (104.4) in [33]):

$$e^+ = g^+ \frac{7}{4} \frac{\pi^2}{30(\hbar c)^3} T^4, \tag{5.27}$$

where $g^+ = 1$ is the degeneracy of positrons. The electrons have the same energy density. The pressure is one third of the energy density $P = \frac{1}{3}e$.

The equation of state of QCD plasma in zeroth order of the perturbation theory can be given based on the formulae above. More detailed information may be found in the textbook of Kapusta [34]. The plasma contains $2 \times [N_c^2 - 1]$ gluons (bosons), ($N_c = 3$ is the number of colors), and $2 \times N_c N_f$ quarks (fermions), (where N_f is the number of different flavors, $N_f = 2 - 4$). Then e.g. for two flavors and three colors $2 \times [(N_c^2 - 1) + \frac{7}{4} N_c N_f] = 37$, so the pressure of the QGP at vanishing baryon chemical potential is $P_q = \frac{37}{90}\pi^2 T^4/(\hbar c)^3$. One has to note, however, that the QGP exist in the so called perturbative vacuum and not in the physical vacuum. The energy density of the perturbative vacuum is higher, its pressure is lower than that of the physical vacuum according to the MIT bag model. This correction is taken into account via a bag constant $B = \Lambda_B^4/(\hbar c)^3$. A typical value for the bag constant is $B \approx 0.4\text{GeV/fm}^3$, i.e. $\Lambda_B = 235\text{MeV}$ [35]. Then the QGP pressure collecting all ingredients at zeroth order is

$$P_q = \left(\frac{37}{90}\pi^2 T^4 + \frac{1}{9}\mu_B^2 T^2 + \frac{1}{162\pi^2}\mu_B^4 - \Lambda_B^4\right)\frac{1}{(\hbar c)^3}, \tag{5.28}$$

where μ_B is the baryon chemical potential which can be expressed in terms of the quark chemical potential as $\mu_B = 3\mu_q$. Other thermodynamical quantities of the QGP EOS are:

$$e_q = \left(\frac{37}{30}\pi^2 T^4 + \frac{1}{3}\mu_B^2 T^2 + \frac{1}{54\pi^2}\mu_B^4 + \Lambda_B^4\right)\frac{1}{(\hbar c)^3}, \tag{5.29}$$

$$w_q = \left(\frac{74}{45}\pi^2 T^4 + \frac{4}{9}\mu_B^2 T^2 + \frac{2}{81\pi^2}\mu_B^4\right)\frac{1}{(\hbar c)^3}, \tag{5.30}$$

$$n_q = \frac{2}{9}\left(\mu_B T^2 + \frac{1}{9\pi^2}\mu_B^3\right)\frac{1}{(\hbar c)^3}, \tag{5.31}$$

$$s_q = \left(\frac{74}{45}\pi^2 T^3 + \frac{2}{9}\mu_B^2 T\right)\frac{1}{(\hbar c)^3}, \tag{5.32}$$

where n_q is the *baryon number* density in the QGP! Now we observe that the equation of state is rather simple:

$$P_q = \frac{e_q}{3} - \frac{4}{3}B \;=\; \frac{w_q}{4} - B, \tag{5.33}$$

so it follows that $w_q = 4(P_q + B)$. By dropping the index for the final state "2" and assuming that the initial state is the ground state nuclear matter ($P_1 = P_0 = 0$ and $X_0 \approx 6\,\text{GeV fm}^3$, $w_0 = 0.145\,\text{fm}^{-3}(m_N - 8\,\text{MeV}) = 135\,\text{MeV/fm}^3$), the Taub adiabat takes the form:

$$P = \frac{wX - w_0 X_0}{X + X_0}.$$

Here the index "0" is representing our initial state. After straightforward calculation

$$(P + \frac{4}{3}B)(X - \frac{1}{3}X_0) = \frac{1}{3}X_0(w_0 - \frac{4}{3}B). \tag{5.34}$$

This is a hyperbola with its center at $(-\frac{4}{3}B,\ \frac{1}{3}X_0)$ on the [P,X] plane, Fig. 5.18.

Depending on the value of B or Λ_B the parameter of the hyperbola $Q = \frac{1}{3}X_0(w_0 - \frac{4}{3}B)$ can be both positive and negative. The parameter changes sign when $B = \frac{3}{4}w_0$, or in other form, when $\Lambda_B = 167$MeV (or $\Lambda_B = 171$MeV in Fig 5.18 with slightly different parameters).

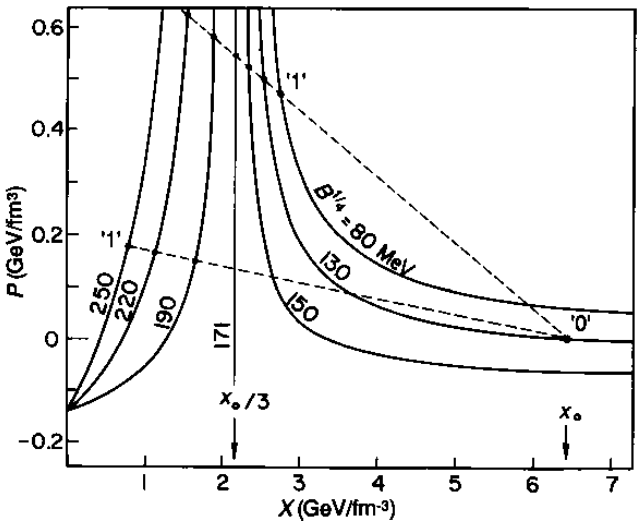

Figure 5.18: Taub adiabats of the QGP initiated from normal ground state nuclear matter depending on the bag constant B or Λ_B. From [32].

If Λ_B is smaller than 127 MeV (or 130 MeV in Fig. 5.18) the reaction is exotherm, otherwise it is endotherm, Fig. 5.18. Usual values range around $\Lambda_B \approx 200$MeV.

It seems that there is no threshold for this bag constant, there is an intersection between the Rayleigh line and the Taub adiabat even at $j = 0$. This would mean that the QGP could be reached in a zero energy detonation front. This does not seem to be reasonable at all.

To any current $j = n_0\gamma_0 v_0 = n_2\gamma_2 v_2$, we can get a solution by using the equation of the Rayleigh line

$$j^2 = -\frac{P-0}{X-X_0}.$$

From here $X = X_0 - P/(j^2)$. Inserting this into the equation of the Taub adiabat (5.34) we get a quadratic equation, which yields the pressure of the final state "2":

$$P_q = \frac{1}{3}\left[(X_0 j^2 - 2B) \pm \sqrt{(2B - X_0 j^2)^2 + 3X_0 j^2(4B - w_0)}\right]. \tag{5.35}$$

This is a seemingly perfect solution for any current j. We can solve the puzzle by calculating all other thermodynamical quantities like the entropy, temperature and baryon density. We will see (in assignment [6.a]) that the solutions have positive temperatures only above a given threshold current, which then gives the absolute threshold energy for QGP formation in a detonation front.

5.5.4 Detonations in baryon free plasma

In the previous derivation of the Taub adiabat and Rayleigh line we assumed that the baryon density is large enough to define a baryon current. If this is not the case we still can use the same formalism as it is shown in refs. [29, 28]. Let us calculate the normal projection of the energy current across the front:

$$[T^{\mu\nu}\Lambda_\mu\Lambda_\nu] = 0.$$

Substituting the expression of $T^{\mu\nu} = wu^\mu u^\nu - Pg^{\mu\nu}$, it follows that:

$$[w(u^\mu\Lambda_\mu)^2] = [P](\Lambda^\mu\Lambda_\mu). \tag{5.36}$$

Similarly the orthogonal projection to Λ^μ can be calculated by using the projector $\Delta^{\mu\nu} = g^{\mu\nu} - \frac{\Lambda^\mu\Lambda^\nu}{(\Lambda^\xi\Lambda_\xi)}$. The resulting projection G^μ is parallel to the surface:

$$G^\mu = \Delta^{\mu\nu}T_{\xi\nu}\Lambda^\xi = w(u^\nu\Lambda_\nu)u^\mu - w(u^\nu\Lambda_\nu)^2\frac{\Lambda^\mu}{(\Lambda^\xi\Lambda_\xi)} - P\Lambda^\mu + P\Lambda^\mu\frac{(\Lambda^\xi\Lambda_\xi)}{(\Lambda^\mu\Lambda_\mu)} =$$

$$= w(u^\nu\Lambda_\nu)u^\mu - w(u^\nu\Lambda_\nu)^2\frac{\Lambda^\mu}{(\Lambda^\nu\Lambda_\nu)}.$$

The length of this vector is an invariant scalar, $(G^\mu G_\mu)$, so instead of $[G^\mu] = 0$, we can use $[G^\mu G_\mu] = 0$, which leads to

$$[\ \ w^2(u^\mu\Lambda_\mu)^2 + w^2(u^\mu\Lambda_\mu)^4\left((\Lambda^\xi\Lambda_\xi) - \frac{2}{(\Lambda^\nu\Lambda_\nu)}\right)\ \ ] = 0\ .$$

Multiplying this with $(\Lambda^\mu\Lambda_\mu)$ we get:

$$[w^2(u^\mu\Lambda_\mu)^2](\Lambda^\nu\Lambda_\nu) = [w^2(u^\mu\Lambda_\mu)^4]\ . \tag{5.37}$$

Let us now introduce the quantity [29]:

$$x \equiv \frac{w(u^\mu\Lambda_\mu)^2}{(w_0(u_0^\mu\Lambda_\mu)^2)},$$

and insert it into eqs. (5.36-5.37).

$$w_0(u_0^\mu\Lambda_\mu)^2[x] = [P](\Lambda^\mu\Lambda_\mu), \tag{5.38}$$

$$w_0(u_0^\mu\Lambda_\mu)^2[wx](\Lambda^\xi\Lambda_\xi) = w_0^2(u_0^\mu\Lambda_\mu)^4[x^2], \tag{5.39}$$

we can express $w_0(u_0^\mu\Lambda_\mu)^2$ from both eqs. (5.38) and (5.39). Equating the two expressions we get:

$$[P]/[x] = [wx]/[x^2].$$

The Λ^μ falls out, so that this is the result both for spacelike and timelike surfaces! This can be cast in the form

$$(P_1 - P_0)(x_0 + x_1) = (w_1x_1 - w_0x_0). \tag{5.40}$$

This is the equation of the shock adiabat. It depends on the initial state and on the EOS of the matter. If plotted on the $[P, x]$ plane the final state "1" should lie on this curve. Since "0" corresponds to the initial state, one can express the equation describing a chord on the $[P, x]$ plane:

$$w_0(u_0^\mu \Lambda_\mu)^2 = (\Lambda^\mu \Lambda_\mu)[P]/[x]. \tag{5.41}$$

This equation contains the information about the spacelike or timelike nature of the surface. The tangent of the chord is positive for timelike surfaces (bulk transitions) and negative for propagating fronts. Eqs. (5.40-5.41) describe two curves on the P, x plane which cross at the initial and final state, thus providing us with the P, x coordinates of the solution we were looking for.

As we have seen earlier if there is a conserved charge and its invariant scalar density is n, the corresponding conserved current across the front is

$$j = nu^\mu \Lambda_\mu, \tag{5.42}$$

which is also an invariant scalar and has the same value j on both sides of the front. In this situation as it is used in earlier works [36, 32, 37, 38, 16, 39, 13, 40, 15], a generalized specific volume X can be introduced: $X = w/n^2$. This is related to x by

$$x = X/X_0$$

Using this variable, eqs. (5.40-5.41) will read as

$$[P](X_1 + X_0) = [wX], \tag{5.43}$$

and

$$j^2 = (\Lambda^\mu \Lambda_\mu)[P]/[X]. \tag{5.44}$$

Eq. (5.43) now contains only thermodynamical quantities of the initial and final states.

5.5.5 Deflagrations from QGP (*)

This is probably the most widely investigated area of discontinuities developing in a fluid-flow involving the Quark-Gluon Plasma. Only one study so far has addressed the expansion of baryon-rich plasma [41], while the big majority of the works dealt with baryon free matter [42, 43, 44, 45, 46, 47, 48, 49, 50].

As we mentioned earlier, the baryon free plasma is expected to occur at ultra-relativistic energies in the mid-rapidity region. It provides an appealing possibility where the theoretical treatment is much simpler. The baryon rich plasma may be formed in the fragmentation regions of transparent ultra-relativistic collisions and at lower energies in the stopping region. In every case there is a possibility that a rarefaction discontinuity or deflagration wave develops during the expansion. This is possible only because of the phase transition in the EOS , otherwise discontinuities do not occur in expansion [30, 51].

Due to a recent development [29] the baryon free plasma can be discussed in the same standard way as the baryon rich plasma in sections 5.5.1-5.5.4. In section 5.5.4

the results of Danielewicz and Ruuskanen are already incorporated, yielding eqs. (5.40) and (5.41). These equations enable us to use the standard discussion of shock waves [30, 51] in terms of adiabats, now on the $[p, X]$ plane.

The shock adiabat (5.40) and the Rayleigh line (5.41) corresponding to a constant enthalpy current $wu^\mu\Lambda_\mu$ or $w_1u_1^2 = w_0u_0^2$ are already defined for the baryon free case. (Here $u_1 = \gamma_1 v_1$ and $u_0 = \gamma_0 v_0$ are quantities measured in the frame of the front.) The Poisson adiabat is somewhat unusual for $n = 0$, since we cannot require the constancy of the specific entropy $\sigma = s/n$. If, however, we have an incoming entropy flow s_0u_0 or $s_0u_0^\mu\Lambda_\mu$, the outgoing entropy flow s_1u_1 or $s_1u_1^\mu\Lambda_\mu$ should be greater or equal in all physically possible processes:

$$s_1u_1^\mu\Lambda_\mu \quad > \quad s_0u_0^\mu\Lambda_\mu. \tag{5.45}$$

We can eliminate the four velocities from this equation by using the definition $x \equiv \frac{w(u^\mu\Lambda_\mu)^2}{w_0(u_0^\mu\Lambda_\mu)^2}$

$$\frac{s_1^2}{w_1}x_1 \;\geq\; \frac{s_0^2}{w_0}x_0. \tag{5.46}$$

In the case of equality, (5.46) is the Poisson adiabat. When $n = 0$, we have $w = Ts$ and so the Poisson adiabat becomes:

$$\frac{s_1}{T_1}x_1 = \frac{s_0}{T_0}x_0. \tag{5.47}$$

For a given equation of state the shock and Poisson adiabats cross each other at the initial point. Shock transitions with $p_1 > p_0$ satisfy the entropy increase law as in the case of $n \neq 0$ compression shocks.

The slope of this Poisson adiabat is related to the sound speed [29] as:

$$wu_{sound}^2 = -x\left(\frac{\partial P}{\partial x}\right)\Big|_{Poisson}. \tag{5.48}$$

It can be shown [29] that at the initial point the Poisson adiabat and the shock adiabat are tangent to each other, similarly to the $n \neq 0$ case.

Using the EOS for the $n = 0$ matter the Taub (shock) and Poisson adiabats can be evaluated for the hadronic, plasma, and mixed phases. The shock adiabat corresponding to the mixed phase is $p = p_{cr.}$, a horizontal line in the $[p, X]$ plane, while the other two phases yield two hyperbolas. The hyperbola corresponding to the plasma state being much steeper than the one corresponding to the hadronic phase. In Fig. 5.19 (from [29]) the shock adiabat of the plasma appears as a vertical line. The following series of figures show the shock adiabats for different initial conditions.

The difficulty in the study of rarefaction fronts lies in the fact that the initial state is not well defined and constant, like in a compression shock originating from normal nuclear matter. The possibilities in the $n \gg 0$ case are even more numerous, that is why the rarefaction studies are constrained mainly to the baryon free plasma case. In a highly excited plasma, $T >> T_{cr.}$ the hadronization via rarefaction discontinuity is not possible, therefore, the plasma cools and expands. (Fig. 5.19).

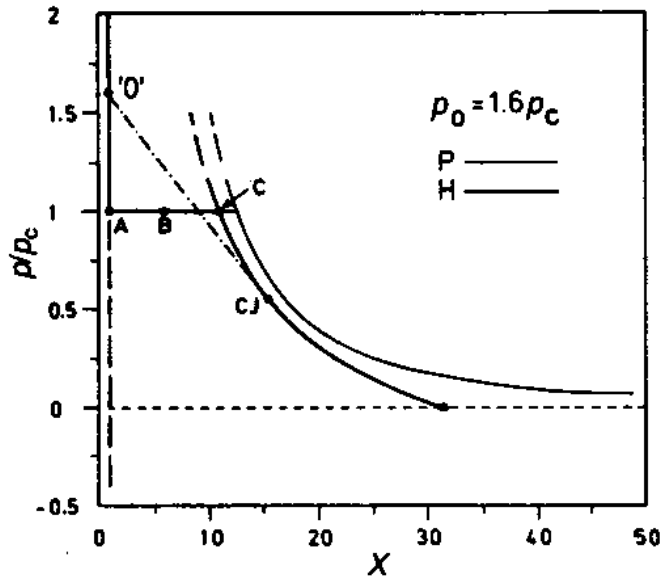

Figure 5.19: Deflagration adiabat (lower thick line) and Poisson adiabat (upper thin line) corresponding to an initial state "0". The OA section of the deflagration adiabat is in the plasma phase, AC is in the mixed phase and below C is in the hadron phase. CJ is the Chapman–Jouguet point. The dashed lines are the continuations of the plasma adiabats representing a supercooled plasma and the continuation of the hadron adiabat representing a superheated hadronic phase. The Poisson adiabat lies everywhere above the shock adiabat. This means that the entropy on the shock adiabat is always lower than the initial entropy. The development of a deflagration front is impossible if $T_0 \gg T_c$ or $p_0 \gg p_c$. Reproduced by permission of the American Physical Society from [29].

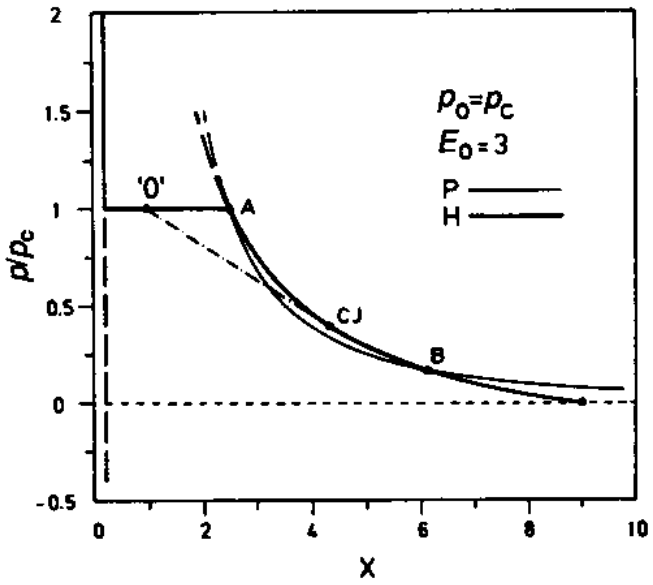

Figure 5.20: The same as the previous Figure with a different initial condition of a smaller initial pressure. The Poisson adiabat (thin line) intersects the shock adiabat at A and B. In the AB section of the shock adiabat the final state has a larger entropy than the initial state at "0". The entropy increase is maximum at CJ. Spontaneously developing rarefaction fronts will propagate with the sound speed, maximizing the entropy increase. The current corresponding to this process can be obtained by using the "0"-CJ chord (dashed-dotted line). If the finite reaction time limits the speed of hadronization the final state will be on the A - CJ section of the shock adiabat. Reproduced by permission of the American Physical Society from [29].

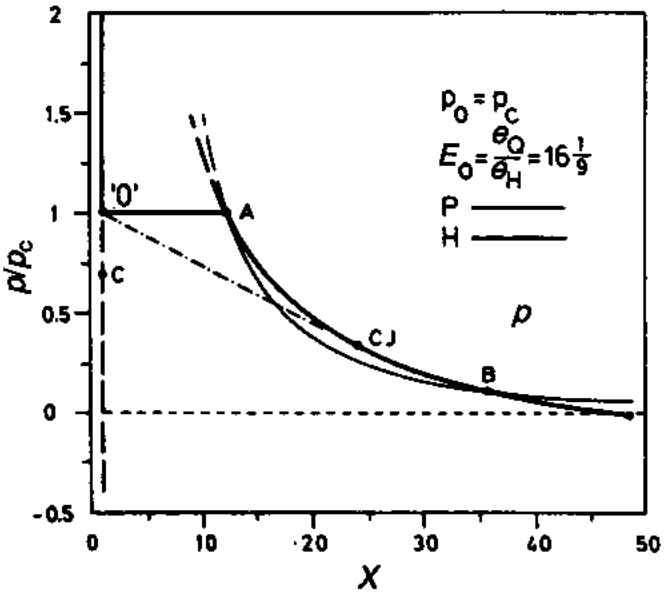

Figure 5.21: The same as the previous figure with an initial state "0" in the mixed phase. Final states on the A-CJ section of the shock adiabat are realizable. The entropy increase is smaller than in the previous case. Reproduced by permission of the American Physical Society from [29].

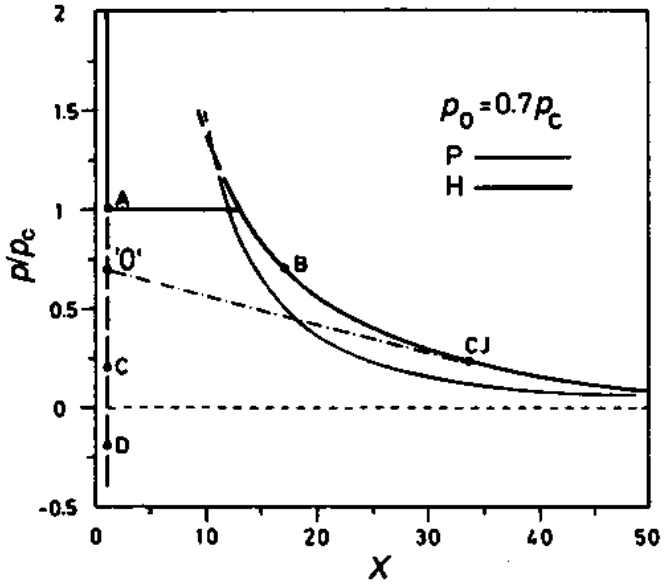

Figure 5.22: The initial state is now in the supercooled (metastable) plasma phase. The entropy increase is bigger than in the previous cases. The maximum of the entropy production is at CJ. Slow deflagrations yield final states laying on the B-CJ section of the adiabat. At B the enthalpy flow across the front vanishes. Reproduced by permission of the American Physical Society from [29].

When the plasma becomes cold enough the rarefaction front may develop, (Fig. 5.20,5.21). The current across the discontinuity is, however, small compared to the expansion speed as numerical fluid dynamical calculations show it [52, 44, 53, 54]. So the matter cools further in the plasma phase, and can reach the supercooled metastable plasma state. Then the timelike deflagration will become possible and the matter can undergo a rapid transition into the hadronic phase, (Fig. 5.22). Although the final states above B are usually considered to be unphysical [55], we have seen in the general derivation (sect. 5.5.4, eq. (5.41)) of the shock equations that final states on the B-E section of the curve can also be realized in timelike deflagrations [56]. In the local rest frame this transition is an instantaneous bulk phase transition; in the laboratory frame, however, it should not happen everywhere at the same time.

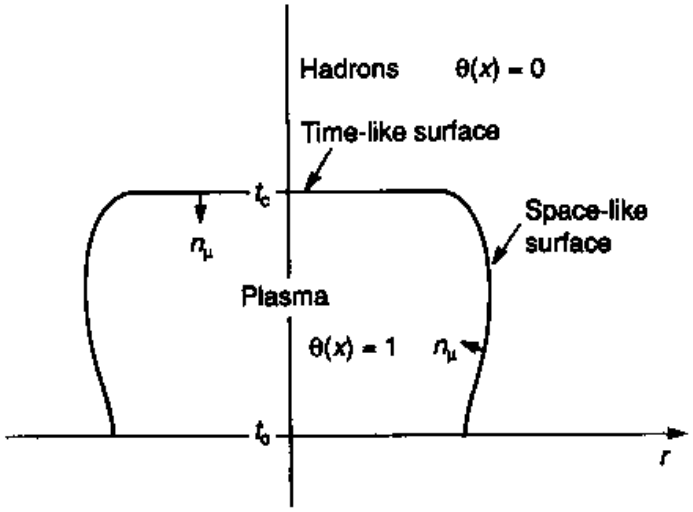

Figure 5.23: Space-time picture of the evolution of QCD-plasma in the mid- rapidity region. The expanding plasma is surrounded by a spacelike and a timelike surface. The plasma temperature monotonically decreases with time according to the calculation. With realistic initial and boundary conditions the time-like surface is not necessarily at $t = const$. Reproduced by permission of the American Physical Society from [52].

The necessity to complete the hadronization process with a timelike deflagration was indicated by the results of ref. [52], (Fig. 5.23 from ref. [52]). Similarly the freeze out transition calculated numerically in ref. [44] ends in a transition across a timelike surface. See also Fig. 1 of ref. [53].

Earlier works did not realize the possibility of time-like deflagrations [47, 49, 43] and this led to the conclusion that the hadronization across the plasma surface is too slow and does not allow for the complete hadronization of the plasma. Consequently it was necessary to assume that inside the plasma, hadronic bubbles will form and expand [43], which lead to observable density and rapidity fluctuations. Since the spontaneous formation of numerous hadronic bubbles in a bulk volume and their percolation can be approximated by an effective timelike surface, [56] these two hadronization processes are modeling essentially the same physical processes.

5.6 Assignment 5

5.a Show that in perfect relativistic fluid dynamics the entropy increase in continuous flow is zero.

5.b Calculate the critical temperature and critical pressure for a phase transition between ideal massless hadronic matter (pion gas) and ideal quark gluon plasma. Both are described by Stefan- Boltzmann EOS:

$$P_\pi = \frac{g_\pi \pi^2}{90} T^4, \quad e_\pi = 3P_\pi, \quad g_\pi = 3,$$

$$P_q = \frac{g_q \pi^2}{90} T^4 - B, \quad e_q = 3P_q + 4B, \quad g_q = 37,$$

where B is the "Bag constant".

At the critical point $P_\pi = P_q = P_{cr}$, and $T_\pi = T_q = T_{cr}$ (These are Gibbs' criteria!).

Plot the $P(e)$ and $P(T)$ functions for the different phases and for the phase mixture.

5.c Calculate the latent heat of this phase transition (per unit volume) in terms of the bag constant B, and of the critical pressure P_{cr}.

5.d Calculate the energy density and pressure for a distribution

$$f(x,p) = \sum_{i=1}^{N} j^{Juttner}(x,p;\mu_i, T_i, V_i^\mu),$$

in terms of parameters μ_i, T_i, V_i^μ. For help see ref. [57].

5.6.1 Solutions to Assignment 5

5.a Solution:

$$T^{\mu\nu}{}_{,\nu} = 0.$$

Multiplying this by u_μ:

$$T^{\mu\nu}{}_{,\nu}\, u_\mu = 0 \quad \rightsquigarrow$$

$$u_\mu (w u^\mu u^\nu - P g^{\mu\nu})_{,\nu} = 0 \quad \rightsquigarrow$$

$$u_\mu w_{,\nu}\, u^\mu u^\nu + u_\mu w u^\mu{}_{,\nu}\, u^\nu + u_\mu w u^\mu u^\nu{}_{,\nu} - u_\mu P_{,\nu}\, g^{\mu\nu} = 0 \quad \rightsquigarrow$$

$$w_{,\nu}\, u^\nu + w u^\nu{}_{,\nu} - u^\nu P_{,\nu} = 0.$$

Aside: From the continuity equation, $(nu^\mu)_{,\mu} = 0$ it follows that $u^\mu n_{,\mu} = -n u^\mu{}_{,\mu}$ and $\rightsquigarrow u^\mu{}_{,\mu} = -(u^\nu n_{,\nu})/n$. Inserting this into the previous equation:

$$u^\nu w_{,\nu} - u^\nu n_{,\nu} \frac{w}{n} - u^\nu P_{,\nu} = 0 \quad \rightsquigarrow$$

$$u^\nu [\ \underbrace{\frac{n}{n} w_{,\nu} - n_{,\nu} \frac{w}{n}}_{n\left(\frac{w}{n}\right)_{,\nu}} - P_{,\nu}\ ] = 0 \quad \rightsquigarrow$$

$$n u^\nu \left[\left(\frac{w}{n}\right)_{,\nu} - \frac{1}{n} P_{,\nu} \right] = 0,$$

and using the relation $\partial_\tau \equiv u^\nu \partial_\nu$

$$n\left[\partial_\tau\left(\frac{w}{n}\right) - \frac{1}{n}\partial_\tau P\right] = 0.$$

Then using the second law of thermodynamics, $dE = TdS - PdV$, in terms of the enthalpy, $W = E+PV$, as $dW = TdS+VdP$, and dividing this equation by N to obtain the specific extensive thermodynamical quantities: $d(\frac{w}{n}) = Td\sigma + \frac{1}{n}dP$, the change of the specific entropy is expressed as:

$$d\sigma = \frac{1}{T}\left[d(\frac{w}{n}) - \frac{1}{n}dP\right],$$

comparing this and the previous equation we obtain that

$$\partial_\tau \sigma = \dot{\sigma} = 0.$$

q.e.d.

5.b Solution:

Let us use the Gibb's criteria, $T_h = T_q = T$ and $P_h = P_q = P$, and let us introduce the ratio of degeneracies, $r = g_q/g_h$. This is $r = 37/3$ if the QGP has 2 flavors and 3 colors, and if the hadronic matter is an ideal bose gas of pions.

The Gibb's criteria leads to the equation:

$$P_{cr.} = \frac{g_\pi \pi^2}{90}T^4 = \frac{g_q \pi^2}{90}T^4 - B,$$

which leads to the critical temperature and pressure:

$$T^4_{cr.} = \frac{90B}{g_\pi(r-1)\pi^2}, \quad P_{cr.} = \frac{B}{(r-1)}.$$

Fig. 5.24.

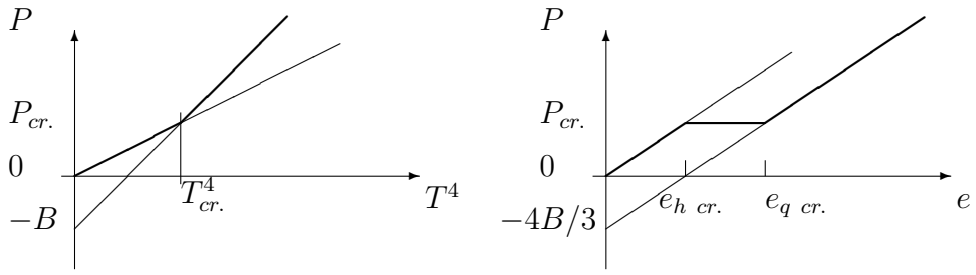

Figure 5.24: Phase transition in baryon free plasma.

5.c Solution: The latent heat is $L = e_{q\ cr.} - e_{h\ cr.} = 3P_{cr.} + 4B - 3P_{cr.} = 4B = 4(r-1)P_{cr.}$. Taking the usual value for B, $B \approx 0.4\text{GeV/fm}^3$, leads to a large latent heat and to $T_{cr.} \approx 169\text{MeV}$, or $P_{cr.} \approx 35\text{MeV/fm}^3$.

5.d Solution:

a., Calculate all quantities in the general (LR) where $u^\mu = (1,0,0,0)$ for the total flow. This is not a rest frame for a single component! In this frame the component "k" has flow velocity $V^\mu_{k(LR)} = (\gamma_k, \gamma_k \vec{v}_k)$, rest density n_{k0} and temperature T_k :

$$f_k^{Juttner} = \frac{n_{k0}}{4\pi g}\left(m_k^2 T_k K_2(\frac{m}{T_k})\right)^{-1} \exp[-(p_\mu u^\mu)/T_k].$$

The four current of this component is $N^\mu_{k(LR)} = n_{k0} V^\mu_{k(LR)}$. The total density is $n = N^\mu u_\mu = \sum_k N^\mu_k u_\mu = \sum_k n_{k0} V^\mu_{k(LR)} u_{\mu(LR)}$. Consequently

$$n = \sum_k n_{k0}\gamma_k \equiv n_k, \quad \text{i.e.}$$
$$n_k \equiv n_{k0}\gamma_k,$$

in other words the kth component contributes $n_{k0}\gamma_k$ to the rest density!

b., Energy density:

$$e = u_\mu u_\nu T^{\mu\nu} = u_\mu u_\nu \sum_k T_k^{\mu\nu} = \sum_k e_k,$$

and this leads to

$$e_k = u^{(LR)}_\mu u^{(LR)}_\nu T^{\mu\nu}_{(LR)} = u^{(LR)}_\mu u^{(LR)}_\nu [(e_{k0} + P_{k0})$$
$$V^\mu_{k(LR)} V^\nu_{k(LR)} - P_{k0} g^{\mu\nu}] = (e_{k0} + P_{k0})\gamma_k^2 - P_{k0}.$$

Here

$$e_{k0} = V^\mu_{k(LR)} V^\nu_{k(LR)} T_{\mu\nu\ k(LR)} =$$
$$4\pi g m_k^4 \exp(\frac{\mu_k}{T_k})\left[3\left(\frac{T_k}{m_k}\right)^2 K_2\left(\frac{m_k}{T_k}\right) + \left(\frac{T_k}{m_k}\right) K_1\left(\frac{m_k}{T_k}\right)\right],$$

and

$$P_{k0} = n_{k0} T_k.$$

As it was calculated before in the solution to assignment 2.c

$$e_k - (e_{k0} + P_{k0})\gamma_k^2 - P_{k0},$$

so that if $\gamma_k \to 1$ then $e_k \to e_{k0}$.

c., Pressure:

$$P_k = -\frac{1}{3}\Delta^{(LR)}_{\mu\nu} T^{\mu\nu}_{k(LR)} = -\frac{1}{3}[g_{\mu\nu} - u^{(LR)}_\mu u^{(LR)}_\nu] \times [(e_{k0} + P_{k0}) V^\mu_{k(LR)} V^\nu_{k(LR)} - P_{k0} g^{\mu\nu}] =$$
$$-[g_{\mu\nu}(e_{k0} + P_{k0}) V^\mu_{k(LR)} V^\nu_{k(LR)} - P_{k0} \underbrace{g^{\mu\nu} g_{\mu\nu}}_{=4}$$
$$-(e_{k0} + P_{k0}) \underbrace{V^\mu_{k(LR)} u^{(LR)}_\mu}_{=\gamma_k} V^\nu_{k(LR)} u^{(LR)}_\nu + P_{k0} \underbrace{V^\mu_{k(LR)} V^\nu_{k(LR)} g_{\mu\nu}}_{=1}]/3 =$$
$$-[(e_{k0} + P_{k0}) V^\mu_{k(LR)} V_{\mu\ k(LR)} - 4P_{k0} - (e_{k0} + P_{k0})\gamma_k^2 + P_{k0}]/3 =$$
$$P_k = \frac{1}{3}[e_{k0}(\gamma_k^2 - 1) + P_{k0}(2 + \gamma_k^2)].$$

If $\gamma_k \to 1$ then $P_k = P_{k0}$. Thus the relative motion contributes to the baryon number density, energy density and pressure as well!

Bibliography

[1] H.Å. Gustafsson, H.H. Gutbrod, B. Kolb, H. Lohner, B. Ludewigt, A.M. Poskanzer, T. Renner, H. Riedesel, H.G. Ritter, A. Warwick, F. Weik and H. Wieman, Phys. Rev. Lett. **52** (1984) 1590.

[2] A.A. Amsden, A.S. Goldhaber, F.H. Harlow and J.R. Nix, Phys. Rev. **C17** (1978) 2080.

[3] L.P. Csernai, I. Lovas, J. Maruhn, A. Rosenhauer, J. Zimányi and W. Greiner, Phys. Rev. **C26** (1982) 149.

[4] W. Busza and A.S. Goldhaber, Phys. Lett. **139B** (1984) 235.

[5] L.P. Csernai and J. Kapusta, Phys. Rev. **D29** (1984) 2664.

[6] L.P. Csernai and J. Kapusta, Phys. Rev. **D31** (1985) 2795.

[7] J. Hüfner and A. Klar, Phys. Lett. **145B** (1984) 167.

[8] R.C. Hwa, Phys. Rev. **D32** (1985) 637.

[9] P. Danielewicz and M. Gyulassy, Phys. Rev. **D31** (1985) 53.

[10] W.A. Hiscock and L. Lindblom, Phys. Rev. **D35** (1987) 3723.

[11] A.A. Amsden, G.F. Bertsch, F.H. Harlow and J.R. Nix, Phys. Rev. Lett. **35** (1975) 905.

[12] A.A. Amsden, F.H. Harlow and J.R. Nix, Phys. Rev. **C15** (1977) 2059.

[13] J.R. Nix, Prog. in Part. and Nucl. Phys. **2** (1979) 237.

[14] H. Stöcker, J. Hofmann, J. Maruhn and W. Greiner, Prog. Part. and Nucl. Phys. **4** (1980) 133.

[15] H. Stöcker and W. Greiner, Phys. Rep. **137** (1986) 277.

[16] R.B. Clare and D. Strottman, Phys. Rep. **141** (1986) 177.

[17] A.S. Roshal and V.N. Russkih, Sov. J. Nucl. Phys. (Jadernaja Fizika) **33** (1981) 1520.

[18] G. Graebner, *et al.*, Proc. Int. Workshop on Gross Properties of Nuclei and Nuclear Excitations XII, Hirschegg, Austria, January 16-21, 1984, (Technische Hochschule Darmstadt, 1984) p. 115.

[19] T. Rentzsch, G. Graebner, J.A. Maruhn, H. Stöcker and W. Greiner, Modern. Phys. Lett. (World Scientific) **A2** (1987) 193.

[20] A.H. Taub, Phys. Rev. **74** (1948) 328.

[21] F.H. Harlow, A.A. Amsden, J.R. Nix, J. Comp. Phys. **20** (1976) 119.

[22] J.A. Maruhn, in "Relativistic Heavy Ion Physics", eds. L.P. Csernai and D.D. Strottman (World Scientific, Singapore 1991) Vol. 5 p. 82.

[23] F.H. Harlow, Proc. Symp. Appl. Math. **15** (1963) 269.

[24] A.A. Amsden, Los Alamos Scientific Laboratory Report, LA - 3466 (1966).

[25] J.P. Boris and D.L. Book, J. Comp. Phys. **11** (1973) 38.

[26] J.P. Boris and D.L. Book, J. Comp. Phys. **18** (1975) 248.

[27] J.P. Boris and D.L. Book, J. Comp. Phys. **20** (1976) 397.

[28] L.P. Csernai and M. Gong, Phys. Rev. **D37** (1988) 3231.

[29] P. Danielewicz and P.V. Ruuskanen, Phys. Rev. **D35** (1987) 344.

[30] L.D. Landau and E.M. Lifshitz: Fluid dynamics (Nauka, Moscow, 1953).

[31] L.P. Csernai, H.W. Barz, B. Lukács and J. Zimányi, Proc. of EPS Top. Conf. on Large Amplitude Collective Nuclear Motions, Keszthely, Hungary (1979) V.2, p. 533.

[32] H.W. Barz, L. P. Csernai, B. Kämpfer and B. Lukács, Phys. Rev. **D32** (1985) 115.

[33] L.D. Landau and E.M. Lifshitz: Statistical Physics (Nauka, Moscow, 1954).

[34] J. Kapusta: Finite Temperature Field Theory (Cambridge University Press, Cambridge 1989).

[35] P. Hasenfratz, R.R. Horgan, J. Kuti and J.M. Richard, Phys. Lett. **94B** (1980) 401, **95B** (1980) 299.

[36] K.S. Thorne, Astrophys. J. **179** (1973) 897.

[37] H.W. Barz, B. Kämpfer, L.P. Csernai and B. Lukács, Phys. Lett. **143B** (1984) 334.

[38] H.W. Barz, B. Kämpfer, B. Lukács and L.P. Csernai, Phys. Rev. **C31** (1985) 268.

[39] B. Kämpfer, H.W. Barz, L. Münchow and B. Lukács, Acta Phys. Pol. **B17** (1986) 685.

[40] H. Stöcker, W. Greiner and W. Scheid, Z. Phys. **A286** (1978) 121.

[41] P.R. Subramanian, H. Stöcker and W. Greiner, Phys. Lett. **B173** (1986) 486.

[42] G. Baym, B.L. Friman, J.P. Blaizot, M. Soyeur and W. Cyz, Nucl. Phys. **A407** (1983) 541.

[43] L. van Hove, Z. Phys. **C21** (1983) 93.

[44] J.P. Blaizot and J.Y. Ollitrault, Nucl. Phys. **A458** (1986) 745.

[45] B.L. Friman, K. Kajantie and P. V. Ruuskanen, University of Helsinki Report HU-TFT-85-21 (1985).

[46] B.L. Friman, Phys. Lett. **B159** (1985) 369.

[47] M. Gyulassy, K. Kajantie, H. Kurki-Suonio and L. McLerran, Nucl. Phys. **B237** (1984) 477.

[48] D. Seibert, Phys. Rev. **D25** (1985) 2812.

[49] B.L. Friman, G. Baym and J.P. Blaizot, Phys. Lett. **132B** (1983) 291.

[50] G. Baym, Nucl. Phys. **A447** (1986) 463c.

[51] Y.B. Zeldovich and Y.P. Raiser: Physics of Shock Waves and High-Temperature Hydrodynamic Phenomena (Nauka, Moscow 1966).

[52] N.K. Glendenning and T. Matsui, Phys. Lett. **141B** (1984) 419.

[53] K. Kajantie, M. Kataja, L. McLerran and V. Ruuskanen, Phys. Rev. **D34** (1986) 811.

[54] K. Kataja, P.V. Ruuskanen, L.D. McLerran and H. von Gersdorff, Phys. Rev. **D34** (1986) 2755.

[55] S. Date, M. Gyulassy and H. Sumiyoshi, Phys. Rev. **D32** (1985) 619.

[56] L.P. Csernai, Sov. JETP **65** (1987) 216; Zh. Eksp. Theor. Fiz. **92** (1987) 379.

[57] A. Rosenhauer, J.A. Maruhn, W. Greiner and L.P. Csernai, Z. Phys. **A326** (1987) 213.

Chapter 6

Simple models

For the compression phase of Relativistic Heavy Ion Collisions in the "stopping" region [1, 2] one can use simple model solutions like:

(i) Shock wave solutions,

(ii) Detonation wave solutions.

In this energy region the expansion is not linear anymore, but spherical or it has a general 3-dimensional distorted shape.

However, in the ultra-relativistic energy region, at $E_{CM} \geq 20 - 30\text{GeV/nucleon}$ the reaction mechanism is expected to be different. From p+p and p+A reactions at these energies one can draw the following conclusions:

(i) The leading baryon is hardly stopped,

(ii) In the rapidity region between the projectile and the target, secondary charged particles (mesons $\pi^+, \pi^-, \pi^0, K^+, K^-$, etc.) are created.

The present theoretical assumptions are based on these p+p and p+A experiments qualitatively shown in Fig. 6.1. At ultra-relativistic energies the mid-rapidity region and the target and projectile rapidity regions are studied separately.

In references [1, 3, 4] the "fragmentation" region is studied, in [5] the "mid-rapidity" region! Refs. [3, 4] present a solution similar to the detonation wave solution with some complications. Basically, the solution is the same as assignment 4a, with source terms in the Rankine–Hugoniot–Taub equation.

6.1 Applicability of simple models

There are several simple models, widely used to describe some aspects of heavy ion collisions. These models have symmetry properties which make them very pleasant to handle but they are not necessarily realistic.

The three most basic collective reaction models are i) the spherical fireball, or different versions of it, ii) the Bjorken model, and iii) the Landau model. In certain sense these are all fluid-dynamical models. All of them are applicable to central

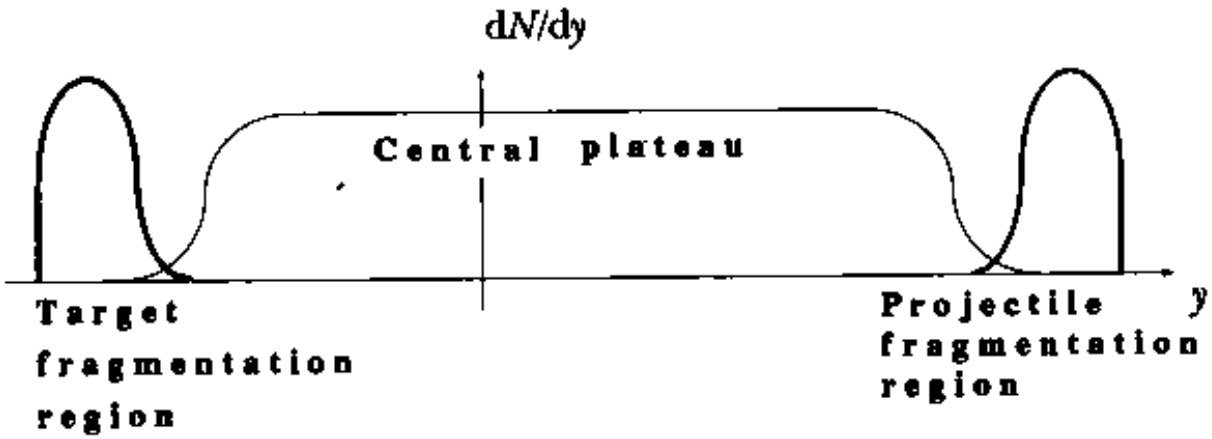

Figure 6.1: Exaggerated plot of observed rapidity distribution of baryons and mesons in ultra-relativistic proton-proton collisions. In reality particles in the fragmentation regions and in the central rapidity region are not separated, their rapidity distributions overlap. Heavy ion collisions are expected to yield similar rapidity distribution at very high energies.

symmetric collisions, since the treatment of spectators is not incorporated in any of the basic versions of these models.

Spherical models: The fireball model assumes spherical symmetry. Although the initial state of a heavy ion collision is never spherically symmetric, at energies in the order of 1 A·GeV the conditions are such that, by the time the maximum density and compression are reached, the system is thermalized and gets close to being spherically symmetric.

Landau model: As the energy increases, around $E_{lab.}$ = 10-100 A·GeV the Lorentz contraction of the projectile and target cannot be disregarded. Even when thermalization is reached rapidly the ratio of the longitudinal thickness versus the diameter of the intermediate object is about 0.05 - 0.1, i.e. close to the aspect ratio of the projectile and target in the c.m. frame, $\gamma^{c.m.}$. Landau's fluid-dynamical model assumes an initial condition as a static homogeneous disk of such an aspect ratio. This model is the most appropriate to apply in this energy range. Although, for simplicity spherical fireball or spherical fluid dynamical models are some times used for characterizing these reactions, one should keep in mind that spherical models are not applicable at these (BNL-AGS and CERN-SPS) energies and quantitative physical conclusions should not be drawn from such comparisons.

Bjorken model: If we increase the energy further to $E_{c.m.}$ = 100 A·GeV or above the expectation is that the Lorentz contracted nuclei will become transparent to each other, in a way that their valence quarks will almost maintain their original rapidities.

At their interpenetration, however, these quanta may exchange some color charge which leads to the creation of a chromo-electric field, similar to the electric field between two condenser plates, where the condenser plates fly apart from each other. The energy density of this field is substantial. Due to the self interaction of the field it is assumed to be confined in the transverse direction to a large extent. Bjorken's model is applicable for such a physical scenario. The model is one dimensional and time dependent. If the transverse expansion of this flux tube is to be studied, or if the behavior around the ends of this object is of interest, the model should be supplemented with the description of these processes separately. This is also done in the literature.

The spherical models and Bjorken's model are 1+1 dimensional, while the Landau model is 2+1 dimensional. If one addresses 3 dimensional effects, like the directed transverse flow in the reaction plane, none of these simple models apply, due to symmetry reasons!

Here we present the spherical models and the Bjorken model in detail, but the Landau model is more involved and it will be discussed only briefly. Landau's fluid dynamical model does not have a simple exact analytic solution, thus we will discuss its physical implications only.

6.2 The Bjorken model

There is a big theoretical interest in the mid-rapidity region, because the EOS is easier if $\mu_B = 0$ and less obscure assumptions are necessary, and because there exist a nice scaling solution for the dynamical problem, the scaling hydrodynamical model of Bjorken [5]. This model has become the basis of many subsequent models [4, 6, 7, 8, 9, 10, 11, 12, 13, 14, 15, 16, 17, 18]. Based on the observation that the rapidity distribution of the charged secondaries is constant in the mid-rapidity region in a p+p reaction one can conclude that the energy density is also constant. Fig. 6.2

If the rapidity distribution of the charged particle multiplicity, $dN_{ch}/dy = \text{const.}$ (≈ 3 at the CERN SPS), this means that it is invariant under Lorentz transformation in the mid-rapidity region. It is reasonable to assume that all other quantities (like $n(y), e(y)$, etc.) also have this symmetry at least at the freeze-out. Thus the density of charged particles, n_{ch}, does depend on the proper time, τ, only because τ is invariant under a Lorentz transformation

$$n_{ch} = n_{ch}(t, z) = n_{ch}(\tau), \tag{6.1}$$

where

$$\tau = t/\gamma = t\sqrt{1 - v^2} = \sqrt{t^2 - z^2}\,, \tag{6.2}$$

if all the particles originate from one point in the space-time, so that their velocity is $v = z/t$ (if the point of origin is the origo of our coordinate system). This point is then the point of impact of the colliding nuclei in the space-time.

We assume that this symmetry is achieved at the time of thermalization and then we look for the solution of Relativistic Fluid Dynamics from that time on [5]. We assume a special boundary condition

$$e = e_0(\tau_0 = 1\text{fm/c}) \approx 1 - 10\text{GeV/fm}^3.$$

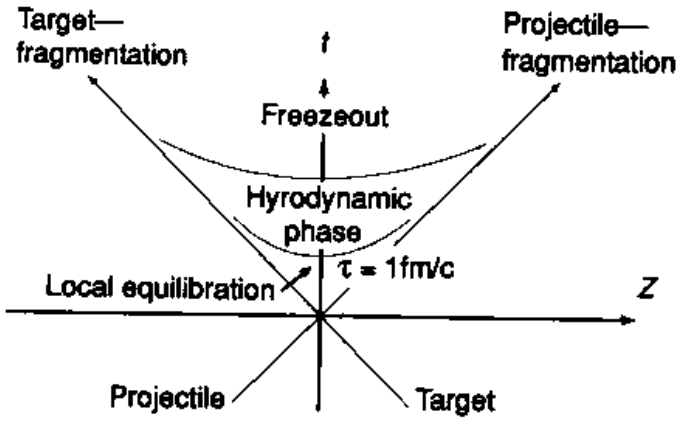

Figure 6.2: Space-time evolution of the mid-rapidity region in the Bjorken-model. The solution is uniform along contours of constant proper time. This ensures that the solution is invariant under Lorentz transformations in the beam direction.

In ref. [5] a simple hydrodynamical model is developed, which is applicable for ultra-relativistic heavy ion collisions under this symmetry. Instead of variables x and t the rapidity y and proper time, τ, coordinates fit the problem better. Let us see how can we estimate the initial energy density at the beginning of the expansion from the observations

$$\left.\frac{dN_{ch}}{dy}\right|_{p+p} = 3 \quad \rightsquigarrow \quad \left.\frac{d < E >}{dy}\right|_{p+p} \approx 1.8\text{GeV},$$

because $dN_{tot}/dy = 3 \times 2 \rightsquigarrow < m_\perp > dN_{tot}/dy = d < E > /dy$, and $< m_\perp > \approx 0.4$GeV.

Due to the Lorentz contraction, the colliding nuclei in their C.M. resemble two flat disks approaching each other. The surface of a disk is A. If it contains N nucleons the average surface per nucleon is $d_0^2 \equiv A/N$, so that in a heavy ion collision $d_0 \approx 0.3 - 1$fm.

If we have a thermalization at $t_0 = 1$fm/c the energy density is:

$$e_0 \approx \frac{1\text{GeV}}{t_0\ d_0^2} \approx 1 - 10\text{GeV/fm}^3.$$

This is the initial condition, i.e. the variables depend on τ but not on the rapidity:

$$e = e(\tau), \quad p = p(\tau), \quad T = T(\tau), \quad \text{etc.}$$

The initial proper time is τ_0, and consequently the initial condition is $e(\tau_0) = e_0$. Let us introduce a four vector $\tilde{x}_\mu = (t, 0, 0, -z)$, [or the same in contravariant coordinates $\tilde{x}^\mu = (t, 0, 0, z)$]. Then, if all particles are at rest in their own LR we can express the velocity field using eq. (6.2) as

$$u^\mu = \frac{1}{\tau}(t, 0, 0, z) = \frac{\tilde{x}^\mu}{\tau} \tag{6.3}$$

$$u_\mu = \frac{1}{\tau}(t, 0, 0, -z) = \frac{\tilde{x}_\mu}{\tau} \tag{6.4}$$

The local velocity is orthogonal to the constant proper time curve everywhere, see Fig. 6.3.

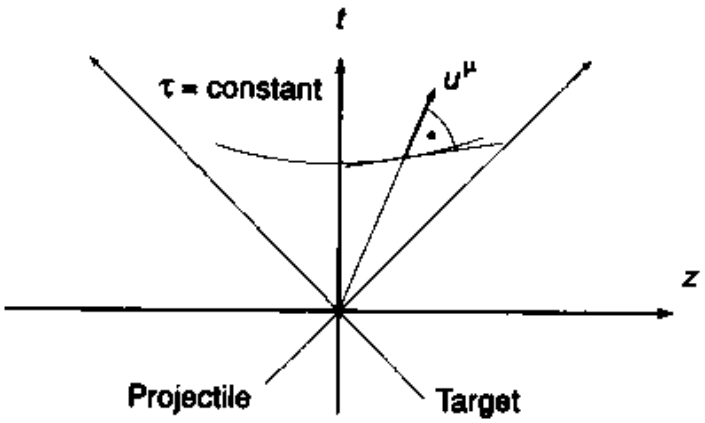

Figure 6.3: The four-velocity vector of the flow in the Bjorken-model is orthogonal to the constant proper time, $\tau = const.$ hyperbolas.

Let us neglect the viscosity and heat conduction and use the equations of perfect fluid dynamics:

$$T^{\mu\nu}{}_{,\nu} = 0, \tag{6.5}$$

where $T^{\mu\nu} = (e+P)u^\mu u^\nu - Pg^{\mu\nu}$. Let us observe that

$$\tau_{,\mu} = \frac{\partial \tau}{\partial x^\mu} = u_\mu \quad \rightsquigarrow \quad \partial\tau = u_\mu \partial x^\mu.$$

We can then rewrite eq. (6.5) as

$$(e+P)_{,\mu}\, u^\mu u^\nu - P_{,\mu}\, g^{\mu\nu} + (e+P)u^\mu{}_{,\mu}\, u^\nu + (e+P)u^\mu u^\nu{}_{,\mu} = 0, \tag{6.6}$$

where the last term vanishes and the others can be rewritten as shown below.

Aside:

$$u^\nu{}_{,\mu} = \left(\frac{\tilde{x}^\nu}{\tau}\right)_{,\mu} = \frac{1}{\tau}\tilde{g}^\nu_\mu - \frac{\tilde{x}^\nu}{\tau^2}\frac{\tilde{x}_\mu}{\tau} = \frac{1}{\tau}(\tilde{g}^\nu_\mu - u^\nu u_\mu),$$

where $\tilde{g}^\nu_\mu = \delta^\nu_\mu$ if $\mu = 0, 3$ else 0. I.e. $\tilde{g}^0_0 = 1$ and $\tilde{g}^z_z = 1$. Consequently:

$$u^\mu{}_{,\mu} = \frac{1}{\tau}(2-1) = \frac{1}{\tau}.$$

Inserting this into eq. (6.6):

$$(e+P)_{,\mu}\, u^\mu u^\nu - P_{,\mu}\, g^{\mu\nu} + (e+P)\frac{1}{\tau}u^\nu + (e+P)\underbrace{\frac{1}{\tau}u^\mu(\tilde{g}^\nu_\mu - u^\nu u_\mu)}_{\frac{1}{\tau}(u^\nu - u^\nu u^\mu u_\mu)} = 0,$$

where we see that the last term vanishes and multiplying the first two terms by u_μ/u_μ leads to

$$\frac{\partial(e+P)}{u_\mu \partial x^\mu} u^\mu u_\mu u^\nu - \frac{\partial P}{u_\mu \partial x^\mu} u_\mu g^{\mu\nu} + (e+P)\frac{1}{\tau}u^\nu = 0.$$

Using the relation $u^\mu u_\mu = +1$ and the definition of τ

$$\frac{\partial(e+P)}{\partial \tau} u^\nu - \frac{\partial P}{\partial \tau} u^\nu + (e+P)\frac{1}{\tau}u^\nu = 0.$$

This should be satisfied for all u^ν's, thus

$$\frac{\partial e}{\partial \tau} = -\frac{e+P}{\tau}. \tag{6.7}$$

This is the basic differential equation of Bjorken's hydrodynamical model. $e(\tau_0) = e_0$ is given as initial condition.

6.2.1 Entropy conservation

We have seen that in perfect fluids $S^\mu{}_{,\mu} = 0$, where $S^\mu = su^\mu$ and s is the entropy density in the proper frame. This equation:

$$\frac{\partial(su^\mu)}{\partial x^\mu} = \frac{\partial s}{\partial x^\mu}u^\mu + s\frac{\partial u^\mu}{\partial x^\mu} = \frac{\partial s}{u_\mu \partial x^\mu}u_\mu u^\mu + s\frac{1}{\tau} = 0,$$

leads to the differential equation

$$\frac{\partial s}{\partial \tau} = -\frac{s}{\tau}. \tag{6.8}$$

The solution of this equation is

$$s(\tau) = s(\tau_0)\frac{\tau_0}{\tau}.$$

Consequently dS/dy =constant. To solve the dynamical equations of the fluid dynamics we need an EOS as was mentioned before, so eq. (6.7) still allows several solutions. For an ideal ultra-relativistic gas the EOS is: $e = 3P$. This reduces eq. (6.7) to $\frac{de}{d\tau} = -\frac{4}{3}\frac{e}{\tau}$, which leads to the solution

$$e(\tau) = e(\tau_0)\left(\frac{\tau}{\tau_0}\right)^{-4/3}.$$

6.2.2 Multiplicity estimate in ultra-relativistic collisions

The "chromo-electric" field between the projectile and target constituents is frequently considered as a flux-tube or as a string of negligible transverse extent. If the field is created by several constituents at the same time, the field strength increases or we can say that the number of strings increases.

We have seen that in an A+A collision a large number of hadron collisions occur. This number is proportional to the surface of the projectile and target nuclei orthogonal

to the beam. Thus the number of strings increases and so, the entropy per unit rapidity increases the same way as well:

$$\left(\frac{dS}{dy}\right)_{A+A} = \frac{r_0^2 A^{2/3}\pi}{d_0^2}\left(\frac{dS}{dy}\right)_{p+p}.$$

Assuming that the pion multiplicity and the entropy are proportional (this is the case for an ideal Bose gas), $N_\pi \sim S$, we can estimate the parameter d_0^2 by comparing the results of p+p collisions and $\alpha + \alpha$ collisions from ISR at 30+30 GeV/nucleon:

$$\frac{(dN_\pi/dy)_{A+A}}{(dN_\pi/dy)_{p+p}} = \left(\frac{2fm}{d_0}\right)^2 A^{2/3}.$$

Inserting the experimental results into this equation we get

$$d_0 \approx 0.7 \text{ fm}.$$

This estimate leads to a multiplicity increase proportional to $A^{2/3}$, but the cross section is somewhat bigger than one layer of nucleons would produce. I.e., not only the first but the subsequent nucleons in a row also contribute to the collision. Later on this problem of subsequent or better to say multiple collisions on a row of nucleons was studied extensively in a study of "Nuclear Stopping Power"(see section 10.5). Bjorken already estimated the multiplicity[5] one could get in a U+U collision, and his estimate was $\frac{dN_\pi}{dy} \approx 800$. This estimate indicates the difficulty of future heavy ion experiments, but as the first CERN measurements indicate, the present measurement techniques can cope with this task.

6.2.3 Inclusion of phase transition in the Bjorken model (*)

One of the most important questions is how to estimate the initial energy density of an expansion from the measurables. If the energy density is high QGP is probably formed in the collision. The energy density can be related to the entropy density if the EOS is known, and the entropy density can be related to the particle multiplicities at the end of the collision. In ref. [19] the assumption of the initial energy density was modified considering the fact that the expansion is not free. The basic idea is that the expansion is very likely to be adiabatic and therefore the initial and final entropy is the same (per unit rapidity). On the other hand the time evolution of the energy density depends on the equation of state. The starting point of the discussion is that the entropy density s and the density of quanta $\tilde{n}$ (not necessarily the density of conserved particles) are related to each other by $s = \xi\tilde{n}$, where ξ is a constant $\xi \approx 4$, and e.g. for quark-gluon plasma $\tilde{n} = n_q + n_{\bar{q}} + n_g$. (Typical ξ values: Bose gas – ξ =3.6, Boltzmann gas – ξ = 4.0, Fermi gas - ξ = 4.2, etc.) It follows then that

$$\frac{dS}{dy} \approx 4\frac{dN}{dy}.$$

This was also the basic assumption in the Landau theory of multiparticle production [20]. Thus

$$\frac{dN}{dy} = \frac{1}{dy}\int d^3x\ \tilde{n} = \frac{1}{dy}\int d^2x(\tau\ dy)\xi^{-1}s = d_0^2\tau s/\xi = d_0^2\tau_0 s_0/\xi.$$

The relation between s_0 and e_0 depends on the EOS of the initial state. Using the EOS for the hadronic matter:

$$s_{h0} = \frac{4}{3}e_{h0}/T_0 = \frac{4}{3}\left(\frac{3}{30}\right)^{1/4} e_{h0}^{3/4},$$

and for QCD-plasma:

$$s_{q0} = \frac{4}{3}(e_{q0} - B)/T_0 = \frac{4}{3}\left(\frac{37}{30}\right)^{1/4} (e_{q0} - B)^{3/4}.$$

This leads us to the conclusion that

$$e_0 \propto \left(\frac{4}{\tau_0\ d_0^2}\frac{dN}{dy}\right)^{4/3},$$

somewhat larger than the original estimate of Bjorken for e_0 [5].

If our EOS includes a phase transition the expansion is different from the one presented earlier, at the discussion of the Bjorken model. Inserting the EOS of the QGP into eq. (6.7) we get another solution

$$e(\tau) = B + [e(\tau_0) - B]\left(\frac{\tau}{\tau_0}\right)^{-4/3}. \tag{6.9}$$

Thus if we start the expansion from QGP, this is the solution we follow initially. There are several possibilities if we have a phase transition: i) we can assume that the expansion is still adiabatic, i.e. no dissipation will occur due to the transition, ii) we may assume that the expansion is isoergic, i.e. the internal energy remains constant, and no internal energy is converted into the kinetic energy of the expansion so that the matter is coasting during the transition with constant speed, or probably the most realistic assumption is that iii) the QGP supercools to some temperature $T_q < T_{cr.}$, and then it undergoes a time-like deflagration into hadronic matter[21]. To discuss all these scenarios would be quite extended, so let us sketch the procedure for case i) briefly. The expansion starts in the plasma and from eq. (6.8) the temperature decreases as

$$T(\tau) = T(\tau_0)\left(\frac{\tau}{\tau_0}\right)^{-1/3}, \tag{6.10}$$

while the energy follows (6.9). When during the expansion the critical temperature is reached in the QGP phase the formation of hadronic matter begins. For a while we will have a phase mixture, during the existence of the mixture the temperature will

not drop but it stays at the critical $T_{cr.}$. When the matter is converted completely into hadronic phase the expansion continues according to the solution we have seen before:

$$e(\tau) = e(\tau_0) \left(\frac{\tau}{\tau_0}\right)^{-4/3}.$$

The time scale of the expansion is given by eq. (6.8) and by the fact that $s(\tau) = \lambda(\tau) s_{q\ cr.} + [1-\lambda(\tau)] s_{h\ cr.}$, where λ is the volume ratio of QGP in the expanding matter (it is 1 initially and 0 at the end of the transition):

$$\lambda(\tau) = \frac{37}{34}\left[\frac{T(\tau_0)}{T_{cr.}}\right]^3 \left(\frac{\tau_0}{\tau}\right) - \frac{3}{34}. \tag{6.11}$$

The phase transition begins at $\tau_1 = [T(\tau_0)/T_{cr.}]^3\ \tau_0$, and it ends ($\lambda = 0$) at $\tau_2 = \frac{37}{3}\tau_1$. If $T_0 = T(\tau_0) = 200$MeV, $T_{cr.} = 169$MeV (i.e. $\Lambda_B = 235$MeV, or $B = 0.397$GeV/fm^3) and $\tau_0 = 1$fm/c the characteristic times are: $\tau_1 = 1.66$fm/c and $\tau_2 = 20.4$fm/c.

The relation between the initial energy density and entropy density is different if we start from different phases. If we start from QGP

$$s = \frac{4}{3}\left(\frac{37}{30}\right)^{1/4} (e_{q0} - B)^{3/4},$$

if we start from the mixed phase

$$s = [e_{m0} - \frac{1}{3} e_h(T_{cr.})]/T_{cr.},$$

and if we start from the hadronic phase

$$s = \frac{4}{3}\left(\frac{3}{30}\right)^{1/4} e_{h0}^{3/4}.$$

In [19] the initial energy density was calculated for two different EOS-s, (1) and (2), describing phase mixture between the quark and hadronic phases with bag constants B=0.74(1), 0.05(2) GeV/fm^3. The resulting relation between the initial energy density at τ_0=1fm/c and the pseudo rapidity density of the emitted particles is plotted in Fig. 6.4 (from [19]): curves (1) and (2) assuming the adiabatic scenario i). The points above the black dot on the dashed lines, (1) and (2), correspond to QGP initial states, below the dots to mixed phase initial states. The full line corresponds to the isoergic expansion scenario ii), which involves entropy increase during the expansion, thus the initial entropy and energy densities are smaller.

If one wants to develop a complete model one has to consider the transverse expansion during the same time when the Bjorken type of longitudinal expansion is happening. Furthermore, one has to take into account that the string is not infinitely long and at the end of the expanding string important physical processes may be present as well. This complicated task can be approached numerically. The first numerical solutions (ref. [22]) included source terms in the fluid dynamical equation in order to simulate the fact

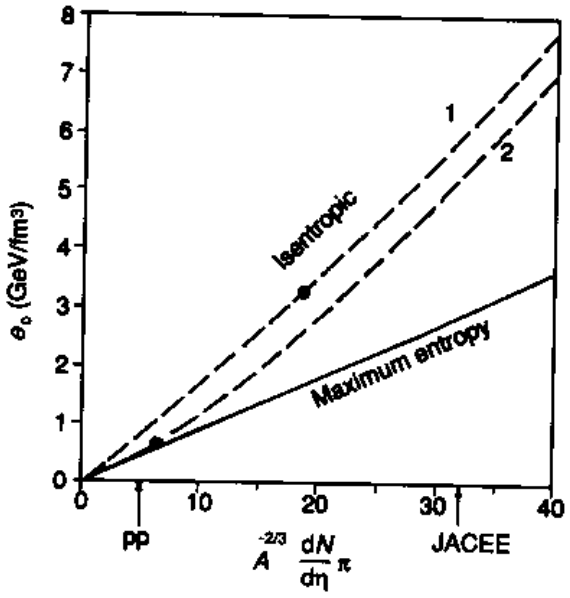

Figure 6.4: Dependence of initial energy density on $dN/d\eta$ at τ_0=1fm/c calculated in the framework of the Bjorken fluid dynamical picture. The transverse area is taken to be $d_0^2 = A^{2/3} r_0^2 \pi$, (with r_0=1.18fm). Multiplicities observed in cosmic ray events suggest that an initial energy density of 3-6 GeV/fm^3 can be reached in heavy ion reactions. Reproduced with permission from [19].

that the constituents of the matter are not immediately thermalized after the collision. If we consider one nucleon nucleon collision from the many present in a nucleus nucleus collision, the constituents (quarks and gluons) of these two nucleons thermalize only after some proper time, τ_0, has passed! The estimate for this time is $\tau_0 \approx 1$fm/c. Thus the energy and momentum contribution of one nucleon nucleon collision will be added to the fluid flow τ_0 proper time after the collision only. The locus of the points having a proper time distance from the point of the collision (event) in space-time lies on a hyperbola. Fig. 6.5 from [22].

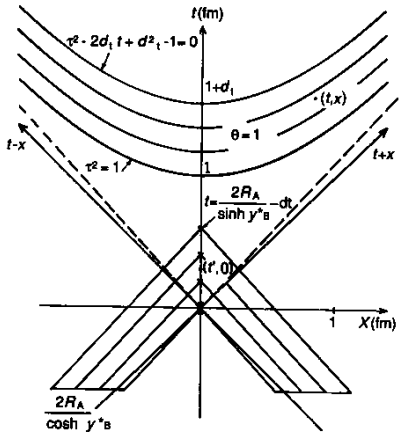

Figure 6.5: Space-time picture of 4-4 nucleons colliding on each other. The contribution to the subsequent flow starts at different proper time hyperbolas. Reproduced by permission of Elsevier Science Publishing from [22].

In the fluid dynamical equations these subsequent contributions can be represented by source terms [10, 22]. Thus the equations solved in this numerical study were:

$$T^{\mu\nu}{}_{,\mu} = \Sigma^{\nu}, \tag{6.12}$$

and

$$N^{\mu}_{B,\mu} = \sigma_B. \tag{6.13}$$

The source terms were based on the observations extracted from p+p collisions:

$$\Sigma^{\nu}_{p+p} = \Sigma_{i=N,\pi,K,\ldots} m_i \ \rho_i(y) \ x^{\nu}\delta(\tau - \tau_0),$$

where $\rho_i(y)$ is the observed rapidity distribution of different particle types, i, in a p+p collision. The source term of the baryon continuity equation was assumed to be

$$\sigma_B = \rho_B(y)\delta(\tau - \tau_0).$$

These source terms were implemented in the model for A+A collisions where

$$\Sigma^{\mu} = \sum_{i=coll.} \sum_{c=\pi,N} \frac{< m_T >}{d_0^2} \frac{dN_c(y)}{dy} v_i^{\mu} 2\delta(\Delta\tau_i^2 - \tau_0^2) = e_c v_i^{\mu} 2\delta(\Delta\tau_i - \tau_0). \tag{6.14}$$

Here v_i^μ is the 4-velocity of the deposited quanta, $v_i^\mu = \frac{(x-x_i)^\mu}{\tau}$, which originates from the nucleon nucleon collision at (t_i, z_i) , and at the same time v_i^μ is the normal unit vector of the proper time hyperbola:

$$(t - t_i)^2 - (z - z_i)^2 = \tau_0^2. \tag{6.15}$$

$\Delta\tau_i$ is the proper time difference between the space time point of a collision (t_i, z_i) and another space time point (t, z):

$$\Delta\tau_i^2 = (t - t_i)^2 - (z - z_i)^2.$$

In order to model a heavy ion collision of a given energy in ref. [10, 22], the function $dN_c(y)/dy$ had to have a smooth cut off at the target and projectile rapidities.

In pp and pA experiments, the net baryon charge is observed around the original target and projectile rapidities. It is convenient to introduce a similar source term for the baryons in the continuity equation:

$$\sigma_B = \sum_{i=coll.} \frac{1}{d_0^2} \frac{dN_B(y)}{dy} 2\delta(\Delta\tau_i^2 - \tau_0^2),$$

and $dN_B(y)/dy$ is chosen to be a smooth function simulating the final baryon rapidity distribution. In this way the baryon charge is not conserved in the calculation and in fact, initially the baryons are not present, nor is the energy carried by them.

Eqs. (6.12) and (6.13) were solved numerically [22, 23, 24] and a gradual increase of the energy density was obtained until the energy of the last nucleon-nucleon collision added its contribution to the flow. At this moment in a U + U collision with beam rapidity y=3.4, the maximum energy density reached was e=5.8 GeV/fm^3 in the center. In the target rapidity region, however, the energy density remained below 1GeV/fm^3, which is much less than previous estimates [1, 25, 26], Fig. 6.6, from [22].

6.2.4 Baryon recoil in the Bjorken model (*)

To overcome the baryon conservation problem above, a model was formulated to include nuclear recoil in a way which guarantees the conservation of baryon flux at all times [4]. This could be accomplished by treating recoil as arising from acceleration in an effective external field $F^{\mu\nu}$. The physical picture behind the model stems from the chromoelectric flux tube or string models [27, 28]. We assume that the interaction between the projectile and target nucleons leads to the formation of multiple incoherent color flux tubes. In effect the projectile and target parton clouds are "charged" up to color non-singlet states due to multiple gluon exchange. The covariant constant color electric field in each flux tube gives rise to a field energy per unit length or effective string tension σ^*. For pp collisions we expect $\sigma^* = 1$ GeV/fm^3. For A+A collisions, a random walk in color space may lead to much larger effective string tensions. Through pair production the color fields are eventually neutralized, thus, in the final state leading to pions distributed approximately uniformly in rapidity. However, the string tension also acts to accelerate the partons in the target fragmentation region and to slow down

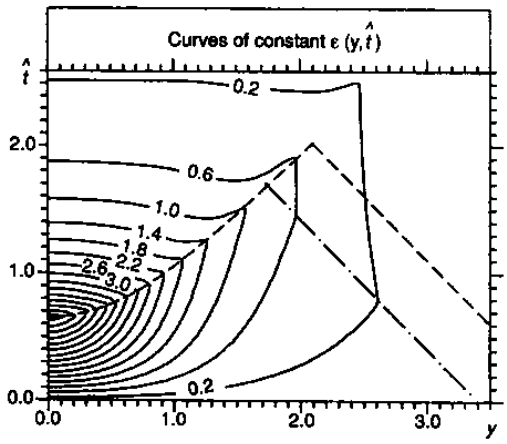

Figure 6.6: Contour lines of energy density in the rapidity y, proper time variable $\hat{t} = \ln(\tau/\tau_0)$ plane for an U + U collision. Reproduced by permission of Elsevier Science Publishing from [22].

the partons in the projectile fragmentation region. This is the main mechanism for baryon recoil. It can be described by modifying Eqs.(6.12-6.14) such that

$$T^{\mu\nu}{}_{,\nu} = \Sigma^{\mu}_{\pi} + F^{\mu\nu} N_{\nu}, \tag{6.16}$$

$$N^{\mu}{}_{,\mu} = 0, \tag{6.17}$$

where the source term Σ^{μ}_{π} is due to pions alone, and where $F^{\mu\nu}$ is parametrized as

$$F^{\mu\nu} = \begin{pmatrix} 0 & -\sigma^* \\ \sigma^* & 0 \end{pmatrix}. \tag{6.18}$$

These equations have the advantage of incorporating longitudinal growth as well as exact baryon flux conservation. The price paid is the introduction of an effective external field. In principle the rate of change of four momentum flux, Σ^{μ}, due to the conversion of field energy density into secondary particles, must be calculated consistently from the color neutralization equations [27, 28].

In the absence of the source term, Σ^{μ}, the fluid compression is due entirely to recoil in the external field. In the "dust" limit, where the internal pressure is neglected in comparison to the energy density, to calculate the recoil compression is particularly simple. The "dust" equation of state ($p = 0$) allows us to write

$$T^{\mu\nu} = m^* n u^{\mu} u^{\nu}. \tag{6.19}$$

Since $m^*{}_{,\mu} = 0$, and $(nu^{\mu})_{,\mu} = 0$, we obtain that

$$\partial_{\tau} u^{\mu} = \frac{1}{m^*} F^{\mu\nu} u_{\nu}. \tag{6.20}$$

In the target frame, the external field is assumed to be turned on as the Lorentz contracted projectile nucleus passes by. For $t < z$, we thus assume that $F^{\mu\nu} = 0$.

For $t > z$ we parametrize $F^{\mu\nu}$ by Eq. (6.18). The solution of (6.20) for the fluid flow rapidity as a function of the fluid proper time is then

$$y(\tau) - y(\tau_0) = (\tau - \tau_0)/\tau^*, \tag{6.21}$$

where $\tau^* \equiv m^*/\sigma^*$. The fluid flow velocity is then $u^\mu(\tau) = (\cosh(y(\tau)), \sinh(y(\tau)))$. Thus, a fluid element initially at (t_j, z_j) with velocity $u^\mu(0) = (\cosh(y_0), \sinh(y_0))$ moves in absence of a source, Σ^μ_π, along the hyperbola:

$$(z - z_j + \tau^* u^1(0))^2 - (t - t_j + \tau^* u^0(0))^2 = (\tau^*)^2. \tag{6.22}$$

Note that the light cone variable, $x^- = t - z$, for the trajectory of the fluid cell is bounded between $x^-(0) < x^- < x^-(0) + \tau^* e^{-y_0}$. For our problem the boundary condition is $y = 0$ on the forward light cone, i.e., $x^-(0) = 0$.

The acceleration ceases in this model when the field is neutralized by pair production. However, the energy stored in the field must also be accounted for. Physically, the neutralization process is the mechanism by which the energy stored in the field is converted into energy in the matter fields. The source term, Σ^μ_π, is included in (6.16) to take into account this additional source of energy and momentum in the matter fields. We assume that each struck nucleon contributes to an independent string that neutralizes along a proper time curve characterized by τ. We thus parametrize the i-th source function by eq. (6.14), except the baryon contribution, because these are always present in this model. The energy density of the matter produced along the neutralization hyperbola must be proportional to the effective string tension, σ^*, since both are proportional to the initial field energy density.

Trying to use the results of recent stopping power studies [29, 2, 30], in a similar analysis it turns out that the space-time structure of the energy deposition is very important. The interplay between the baryon recoil and the energy deposition from the neutralization of different chromoelectric flux tubes leads to much higher energy densities in the fragmentation region than it was expected before. The sudden energy-momentum deposition on a hypersurface, leads to a discontinuity of the flow pattern.

In two-dimensional space-time the surface of neutralization is described by Eq. (6.15). The normal four-vector to this surface is v_i^μ , at a space-time point x^μ. This is a time-like surface because $v^\mu v_\mu = +1$. We can use the formalism of time-like discontinuities for this problem. The discontinuity here, however, is caused by the source term Σ^μ_π, thus our conservation equations across the surface of discontinuity are:

$$[n u^\mu v_{i\mu}] = 0, \tag{6.23}$$

$$[T^{\mu\nu}, v_{i\nu}] = \frac{1}{d_0^2} \int_{\delta V} d^4x \Sigma^\mu_\pi = e_\pi v_i^\mu. \tag{6.24}$$

We can now introduce an invariant (time-like) baryon current [31] across the i-th surface of discontinuity:

$$j_i = n u^\mu v_{i\mu}. \tag{6.25}$$

According to eq. (6.23) j_i is the same on both sides of the discontinuity. Making the orthogonal projection of eq. (6.24) to the surface and using the definition of j_i we obtain

that

$$j^2 = ([P] + e_\pi)/[X], \tag{6.26}$$

where $X = (e + P)/n^2$ is the generalized specific volume. Eq. (6.26) differs from the similar equation for standard shock waves in the sign, because of the time-like discontinuity, and also in the additive term which arises from the energy-momentum source term (6.24). The parallel projection of eq. (6.24) leads to $j^2 = [(e + P)X]/[X^2]$. Eliminating j_i from the above equations, yields the usual Taub adiabat except that the source now contributes as an additive term to the pressure difference

$$([P] + e_\pi)(X_1 + X_0) = [(e + P)X]. \tag{6.27}$$

Thus we derived two invariant scalar equations (6.26-6.27) from the basic relations (6.23-6.24). The velocity four vectors appear explicitly only in the definition of the invariant baryon current j_i .

Now we can form a model describing the space-time development of the fragmentation region in an ultra-relativistic nuclear reaction. The highly Lorentz contracted projectile sweeps through the target. It meets first the first nucleon in the row, and a chromoelectric flux-tube is formed. This will pull that nucleon forward until its neutralization, τ_0 proper time later. The second and subsequent nucleons in the row will also be passed by the projectile. During that time, however, these will be pulled by the chromoelectric field the projectile forms when passing them. (Fig. 6.7) The field created at contact with a previous nucleon will not result in extra recoil of the nucleons sitting deeper inside the target. Thus, the nucleon recoil is uniform initially.

When the first chromoelectric tube neutralizes it distributes its energy and momentum over the whole target on a 3-dimensional hypersurface, which is represented by Eq. (6.15) in our 1+1 dimensional model. Previous to this moment the momentum of the field and of the recoiling target nucleons was different. At the neutralization these two components thermalize and the matter will obtain a uniform momentum and its energy will change. Our task is now first to find the space-time points where the neutralization surface reaches each target nucleon in the row. For the i-th neutralization surface and for the j-th nucleon in the row we should solve the system of Eqs. (6.15) and (6.22). In the absence of intermediate sources the intersection is at τ_c where

$$\tau_c/\tau^* = \cosh^{-1}\left(1 + \tau_0^2\right) / \left(2\tau^{*2}\right). \tag{6.28}$$

The recoil rapidity at this point is $y_r = \tau_c/\tau^*$. At this point (t_k, z_k) we know the recoil velocity of each baryon u^μ, the density n, and the effective mass m^*. Using Eqs. (6.23,6.26,6.28) we can determine the values of these quantities after crossing the discontinuity. Then we propagate the target baryons according to Eq. (6.22) until they reach the next neutralization surface, and so on.

According to the above scenario the complete fluid dynamical problem was solved on a grid specifically suited to the description of the fragmentation region [4]. The results indicate that the energy density inside the target increases approximately linearly with the target depth. The deposited energy increases with increasing projectile mass. For a thicker projectile the field strength is greater and this leads to larger recoil rapidities

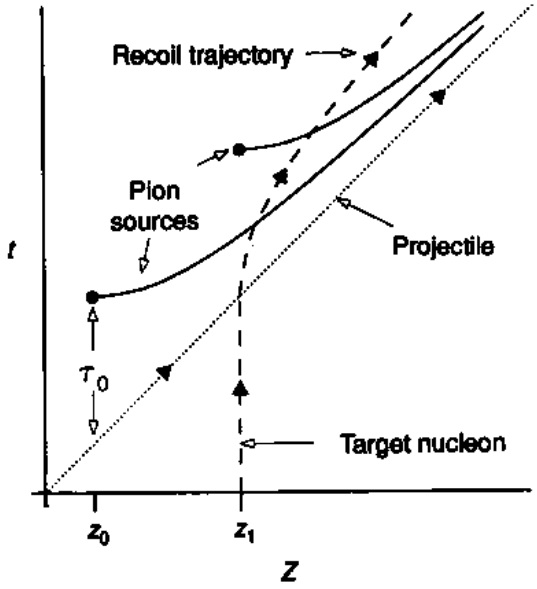

Figure 6.7: Space-time picture of the recoil and color neutralization. As a result of interactions between projectile and target at depth z_0 and z_1, two incoherent strings neutralize along hyperbolas indicated. The fluid cell initially at depth z_1 follows the dashed world line. Reproduced by permission of Elsevier Science Publishing from [4].

[29, 32, 2, 33]: $\Delta y = \Delta y(\nu_p)$, where ν_p is the average number of wounded nucleons in the projectile per inelastic collision (eg. in p+A). Since the empirical rapidity shift Δy is the recoil rapidity, Eq. (6.28) is used to set the parameter τ^* characterizing the field strength. The resulting energy density and the divergence of the flow $u^\mu{}_{,\mu}$, is plotted for a fluid element initially at 6.9 fm depth in the target in Fig. 6.8. The flow divergence characterizes the compression, because from the continuity equation: $(nu^\mu)_{,\mu} = 0$ it follows that $\dot{n}/n = -u^\mu{}_{,\mu}$. The dashed line is the result of the model without baryon recoil [22], with $\nu_p = 6$. The small energy density obtained in [22] is due to the lack of recoil.

6.3 Spherical expansion

Up to now linear 1-dimensional solutions were discussed. Another type of simple solutions are spherical 1-dimensional solutions which are applicable for central relativistic heavy ion collisions at late expansion stage.

Initial condition. Initial conditions for such an expansion are the following (these are idealized simplifying assumptions):

(i) The sphere is at rest in the C.M. system,

(ii) Uniform density, pressure, temperature, etc. distribution,

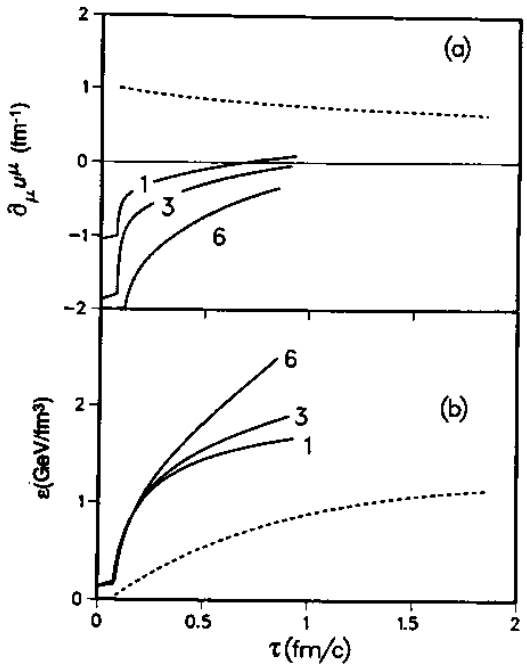

Figure 6.8: *The divergence of the flow (a) and the energy density (b) as a function of proper time for a fluid element in the target at* $z_0 = 6.9fm$. ν_p *is the projectile thickness in units of mean free path. Reproduced by permission of Elsevier Science Publishing from [4].*

(iii) $v_r(t=0)=0$, i.e. there is no radial flow initially.

For a given reaction at a well defined C.M. energy there is one free initial parameter in such a parametrization either the density, $n(t=0)$, or the temperature (or some other thermodynamical quantity). If one of these is given the others can be calculated from energy conservation if the beam energy and the EOS are known.

Final break-up condition. There is on more (free) parameter in the solution, because the validity of the fluid-dynamical approach has to break down at some late stage in the collision when the particles do not interact strong enough to maintain local equilibrium. Usually the break-up density, n_{BU} is chosen as, $n_{BU} \approx 0.1 - 0.7\ n_0$. *This determines, or at least strongly influences the observables!* We will discuss three simple models for spherical t expansion: The Fireball model, the Blast-Wave model, and an approximate time dependent solution.

6.3.1 Fireball model

This model was the first attempt [34, 35] to describe the measured cross sections of a heavy ion collision in a collective thermal model. Strictly speaking collective flow is not included in this model. The matter is assumed to be *globally* thermalized by the end of the reaction, and the cross section is determined from the thermal momentum distributions of the particles present in this final heat-bath.

At this stage it is *assumed* that $n = n_{BU}$, and that there is no flow. Then cross sections are easily calculated because from the energy conservation and the EOS, $e(n,T)$, the temperature of the system, T_{BU}, can be determined:

$$\epsilon_{inc.}^{c.m.} = \frac{e(n_{BU}, T_{BU})}{n_{BU}},$$

where $\varepsilon_{inc.}^{c.m.}$ is the c.m. energy per particle for the incoming beam. Thus T_{BU} can be calculated if we assume n_{BU}, or vice versa.

When this model was used first, it was assumed that the temperature is high and the density is low enough so that the matter is close to an ideal gas at break-up. So, the momentum distribution of the nucleons, $f(\vec{p})$, is known, and can be measured by the detectors. Thus the researchers assumed that T_{BU} was directly measured by the energy spectra, since

$$f \propto e^{-\varepsilon/T_{BU}}\ .$$

It turned out, however, that this was wrong or at least largely oversimplified because:

(i)) No collective flow was assumed,

(ii) Ideal gas EOS was assumed.

This showed up in form of "experimental" problems, such as:

(i) Pion and proton "temperatures" were different,

(ii) The "entropy" did not go to 0 when $E_{beam} \rightarrow\ 0$,

(iii) Transverse flow was observed in noncentral collisions.

This simple model was, nevertheless, very powerful and many basic facts were interpreted correctly by the model. Even nowadays the "temperature" extracted from the data in this simple fashion is frequently used. It is called slope temperature, slope parameter or effective temperature, indicating the fact that the c.m. energy spectrum of particles on a logarithmic plot is frequently a linearly decreasing curve or very close to it.

6.3.2 Blast-wave model

The thermalization can be reached at high densities (i.e. much before the break-up), then a collective and (almost) adiabatic expansion follows. This lasts until the matter becomes dilute enough. The resulting final break-up state thus has a collective expansion, or radial flow and the superposed thermal motion. This idea was considered by Siemens, Rasmussen and Kapusta, and the cross sections were evaluated in the presence of a spherical flow [36, 37]. In this model it was assumed that the spherical flow had one constant radial flow velocity, u_r.

Later in ref. [38] this strong assumption was relaxed and the radial expansion was calculated numerically in a 1-dimensional spherically symmetric relativistic fluid dynamical model. The viscosity of nuclear matter was also taken into account, but during the expansion it did not cause strong changes in the flow. The initial state of the expansion was a uniform sphere, where the temperature, T_0, and the density, n_0, were taken from the relativistic Rankine–Hugoniot relations (discussed in section 5.4). Fig. 6.9-6.10 from [38].

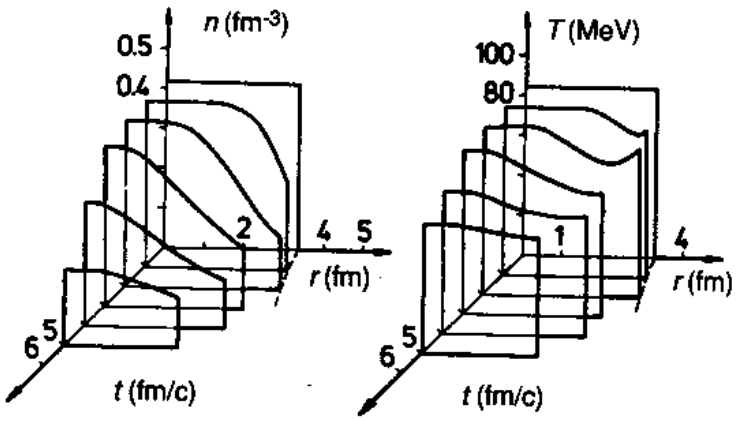

Figure 6.9: Time dependence of density and temperature profiles calculated in a relativistic, viscous, spherical fluid dynamical model for the reaction $Ar + KCl$ at 800 MeV/nucleon projectile energy. The break-up is gradual in this model, it happens layer by layer. Reproduced by permission of Springer-Verlag from [38].

At the initial state of the expansion some part of the energy is in the form of compressional energy. The break-up temperature, T_{BU}, is smaller than the initial temperature, T_0 , because the expansion is close to adiabatic, the matter cools nearly adiabatically and the energy is converted into the energy of the collective flow (see Fig. 6.10). For the same reaction the fireball model temperature T_{FB} is higher than T_0, because ideal gas EOS is assumed and there is no compressional energy in the initial (and in the Fireball model final) state.

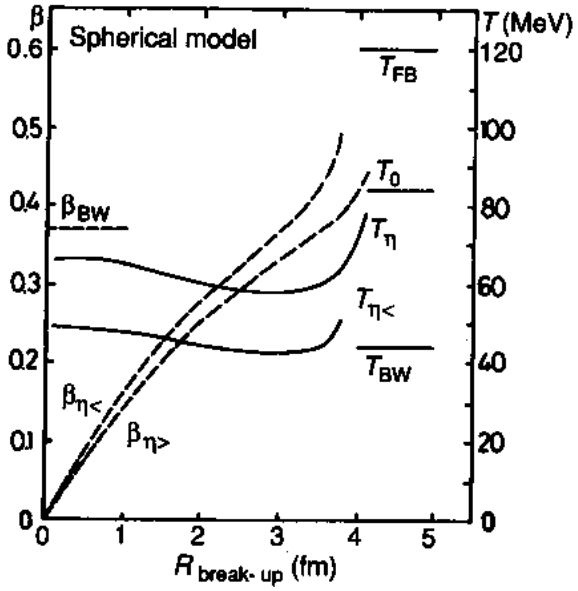

Figure 6.10: Dependence of the break-up velocity, β, (dashed curves) and of the break up temperature, T, (full curves) on the break up radius in the same spherical fluid dynamical model. The subscripts $\eta_<$ and $\eta_>$ belong to constant viscosity, 6 $MeV/(fm^2\ c)$, and to temperature dependent viscosity, $[6 + 2(T/MeV)^{1/2}]\ MeV/(fm^2\ c)$, respectively. T_{BW} and β_{BW} correspond to the Blast-Wave model parameters, T_0 is the initial temperature and T_{FB} is the temperature of the Fireball model. The temperature of the Blast-Wave model, T_{BW} is close to the numerically obtained break up temperatures, $T_{BU}(t)$. Reproduced by permission of Springer-Verlag from [38].

Basic assumptions of the Blast Wave model

At the break-up

- the radial flow velocity is constant (free parameter),
- the local temperature, T, is constant (not a free parameter because of energy conservation).

Now part of the energy is in form of kinetic energy of the collective flow. Thus the observed particle velocities have two components:

- thermal random velocity, parametrized by T_{BU} (same for all particles) and
- collective flow velocity, v, or β_{flow} (same for all particles).

These basic assumptions are of course debatable and can be relaxed if necessary. For example it is easily possible that secondary created, weakly interacting particles (having smaller than the average cross section) leave the system before the general break-up. In this case these particles represent an earlier stage of expansion with higher temperature and smaller expansion velocity. In the original Blast Wave model this possibility was, however, not considered.

Due to the basic assumptions if we have particles of different masses, like $m_\pi \ll m_p$, then the flow energies such that,

$$E_p^{flow} \gg E_\pi^{flow} \ ,$$

while the thermal energies are equal, $E^{therm} = \frac{3}{2}T_{BU}$. At the same time the flow velocities are equal, but the random thermal velocities of the lighter particles are larger.

As a consequence this model explains one basic feature of the observations. The energy spectra of pions decrease steeper than of proton spectra, Fig. 6.11 (from [36]).

6.3.3 An approximate spherical solution

An approximate solution for adiabatic (or dissipative) expansion of a sphere of radius R is frequently used in the literature [39, 40]. This model is an alternate to the scaling spherical expansion model presented in section 6.4.2. It is based on simple assumptions like the models above:

- all thermodynamical quantities are uniform during the expansion, $P(r,t) = P(t),\ T(r,t) = T(t),\ n(r,t) = n(t)$, etc.,
- the 4-velocity is linearly increasing with the radius $\vec{u}_r(\vec{r},t) = \gamma_r \vec{v}_r = \frac{\dot{R}(t)}{R(t)}\vec{r}$.

As we have seen at the beginning of sect. 6.3.2, these assumptions are acceptable according to detailed numerical solutions [38].

Now, we can get the time dependence of parameters from the energy conservation, i.e. that the total energy of the expanding system stays the same, and from a further condition. The simplest additional assumption is to assume adiabatic expansion. In

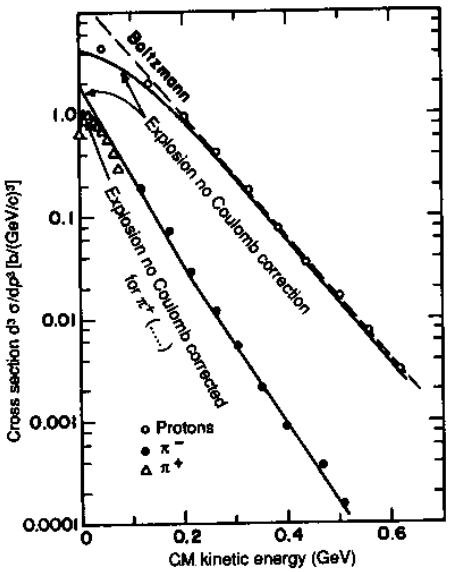

Figure 6.11: Inclusive cross sections, $d^3\sigma/dp^3$, at $\Theta = 90^0$ in the c.m. for the $^{20}Ne + NaF$ reaction at 800 MeV/nucleon laboratory beam energy. Open circles are protons, closed circles are π^-'s. Solid lines are the results of the Blast Wave model: the free parameter the flow velocity is chosen as $\beta_{flow} = 0.373$, then the resulting temperature is $T = 44$ MeV. The number of charged pions is 9.4% of the protons. Reproduced with permission from [36].

this case all of the internal energy of the dense compressed system will be converted into the collective energy of the flow, and the entropy per particle (baryon) remains constant. It is also possible that dissipative processes, like viscosity, heat conductivity or delayed first order phase transition, lead to entropy increase. In the most dissipative case the energy of the flow does not increase during the expansion, the matter is coasting and the entropy increases. The initially developed collective flow energy, if any, is maintained during the expansion. Without such initial collective expansion energy such maximum dissipation expansion is not possible. For adiabatic expansion ($\sigma = const.$) the estimated process of expansion goes as follows. The energy density

$$T^{00}(r) = [e(\sigma, n) + P(\sigma, n)]\gamma^2(r) - P(\sigma, n) \tag{6.29}$$

depends on the radius r. The total energy of the system is then

$$V[(e + P) < \gamma^2 > -P] = E^{tot}_{init.} \ , \tag{6.30}$$

where $< \gamma^2 >$ is the volume average, because the other quantities are assumed to be independent of r. We can calculate the volume average

$$< \gamma^2 >= \frac{4\pi \int_0^R \frac{1}{1-v^2} r^2 dr}{4\pi R^3/3}. \tag{6.31}$$

Using the assumed linear velocity profile it follows that $v^2 = x^2/(1 + x^2)$ where $x = r\ \dot{R}/R$. Inserting this into the expression above

$$< \gamma^2 >= \left[4\pi \frac{R^3}{\dot{R}^3} \int_0^{\dot{R}} (1 + x^2)x^2 dx \right] /(4\pi R^3/3) = \frac{3}{\dot{R}^3} \int_0^{\dot{R}} (1 + x^2)x^2 dx = 1 + \frac{3}{5}\dot{R}^2. \tag{6.32}$$

Inserting (6.32) into (6.30) we get an equation for the radius

$$\dot{R} = \sqrt{\frac{\frac{5}{3}\left(\frac{R^3_{in}}{R^3} e_{in} - e\right)}{e + P}} \ , \tag{6.33}$$

where e and P depend on the density $n(t) = \frac{3A_{tot}}{4\pi R^3}$ only since σ is constant. This equation gives us a simple estimate of the time-scale of the radial expansion. If the break-up density is reached the thermal contact between the particles is lost and we can calculate single particle cross sections (see the next sections) or e.g. two pion correlations [41].

The calculation for the most dissipative, isoergic ($\varepsilon = e/n = \text{const.}$) expansion can be done similarly. Such an expansion should be preceded by an adiabatic or close to adiabatic expansion[40], so that $e_{in}R^3_{in} \neq e(t)R^3(t)$, otherwise the system would not expand. Unlike in the scaling spherical expansion model (see section 6.4.2) the expansion velocity of the surface is not constant in this model.

6.4 The Landau model

At $E_{lab.}$ = 10-100 A·GeV the Lorentz contraction of the projectile and target in the c.m. frame, is $\gamma^{c.m.}$. Landau's fluid-dynamical model [20, 42] assumes an initial condition as a static homogeneous disk of such an aspect ratio. Since this disk is rather flat and orthogonal to the beam direction the pressure gradient is the largest in the beam direction.

6.4.1 Physical assumptions

Because of the strong interactions, relevant relaxation times are very short and the created pre-hadronic matter can be thought of as being in local statistical equilibrium. Phrased another way, mean free paths of the quanta involved are assumed to be much smaller than the characteristic lengths. Thus the system can be treated as a classical fluid whose collective motions are governed by the laws of relativistic hydrodynamics.

The special features of the model - dynamics (apart from the equation of state) are embodied in the initial and final (break-up) boundary conditions on the hydrodynamic equations. The initial condition on the equations is to specify the initial temperature distribution of the fluid. We assume baryon free matter for simplicity, thus we must make certain assumptions about the initial size of the system, and determine the initial temperature distribution from the center-of-mass energy via some knowledge of the relevant dynamics.

Because of the large pressure the system expands and cools. At the first stage the expansion then can be approximated as a linear expansion in the beam direction. Only when the system expanded in the beam direction to a size comparable or larger than its transverse diameter will the transverse expansion be also considered. In this second phase the expansion is already 2+1 dimensional. This separation of the expansion to two stages is of course somewhat artificial, and it is done for the sake of developing an approximate method of solution. [43, 44] This approximate analytic solution, however, is valid only for a restricted lass of EOS's with small sound speeds [45]. Both the linear and the spherical expansion can be handled similarly to the case presented at the solution of the Bjorken model earlier.

Originally the model was developed for $p + p$ collisions, but it is well applicable to heavy ion collisions as well. In this case there is a natural choice of initial condition, the Lorentz-contracted disk of matter comprising the protons or heavy ions in the c.m. frame. Thus it is expected that the initial volume, V_0, is not very different from $V_0 = V_{rest.}/\gamma^{c.m.}$, where $\gamma^{c.m.}$ is the Lorentz gamma factor in the center of mass frame.

If the system undergoes a large expansion, then it is irrelevant how the initial energy is distributed over V_0, and it is sufficient to assume that the initial energy density is just constant over V_0, i.e.,

$$e_0 = \frac{E_{c.m.}}{V_0}. \tag{6.34}$$

The matter is at rest initially in this highly Lorentz contracted disk, which is orthogonal to the beam direction. The expansion will be initially much stronger in the beam direction, because the pressure gradients are much larger.

6.4.2 Quasi-analytic solution

Let us introduce the rapidity coordinate in the beam ($z-$) direction, $\alpha(z,t)$

$$\alpha \equiv \frac{1}{2}\ln\left(\frac{t+z}{t-z}\right) \tag{6.35}$$

and the proper time coordinate, $\tau \equiv \sqrt{t^2-z^2}$. We can introduce a parameter, β, to characterize the proper time with respect to the initial size of the system

$$\beta \equiv \ln\left(\frac{\tau}{r_0}\right), \tag{6.36}$$

where r_0 is a parameter characterizing the Lorentz contracted initial disk, $r_0 \approx d/\gamma^{c.m.}$, and d is the diameter of the colliding object. For protons $d \approx m_\pi^{-1}$. Furthermore, we can introduce the rapidity of the flow, η, and the rapidity of the particles emitted, y. These latter two are not the same, even at the end of the collision, because of the random thermal motion of the particles in a fluid element. The flow rapidity in terms of the flow velocity is

$$\eta \equiv \mathrm{arth}v_\parallel = \mathrm{arth}v_z \tag{6.37}$$

If we have a scaling solution, as in the case of the Bjorken model, the flow rapidity and the coordinate rapidity are equal, $\alpha = \eta$, which means that the flow velocity satisfies the equation

$$v_z = z/t. \tag{6.38}$$

This parametrization is also possible for a scaling *spherical* solution, where we just replace the coordinate z, with the radial coordinate r. In this case the scaling solution implies that $v_r = r/t$ and the radial coordinate rapidity α_r will be equal with the radial flow rapidity η_r. In one-dimensional scaling solutions the introduction of these radial coordinates is possible. In both of these scaling cases the fluid dynamical equations reduce to [45]

$$\partial_\beta \ln T + \lambda c_0^2 = 0, \qquad \partial_\alpha \ln T = 0, \tag{6.39}$$

or

$$\frac{\partial e}{\partial \tau} = -\lambda\frac{(e+P)}{\tau}, \tag{6.40}$$

where

$$\lambda = \begin{cases} 1, & \mathrm{linear\ one-dimensional\ expansion} \\ 3, & \mathrm{spherical\ expansion} \end{cases}$$

and c_0 is the sound speed of the EOS, $dP/de = c_0^2$. The second equation in (6.39) expresses the assumption that the thermodynamical quantities, i.e. T, are independent of the coordinate rapidity. For simplicity we assume that the sound speed is constant, $dP/de = c_0^2 =$ constant and $e \sim T^{1+1/c_0^2}$. Then eqs. (6.39) yield the solution

$$\begin{aligned} \frac{T}{T_0} &= \left(\frac{\tau}{r_0}\right)^{-\lambda c_0^2}, \\ \frac{e}{e_0} &= \left(\frac{\tau}{r_0}\right)^{-\lambda(1+c_0^2)}, \end{aligned} \tag{6.41}$$

where T_0 and e_0 are the initial temperature and energy density. This result is formally the generalization of the result obtained at the introduction of the Bjorken model above.

For a three-dimensional solution eq. (6.38) is never valid, although as we will see, when the beam energy increases the solution will approach the scaling solution even if we assume the initial conditions of the Landau model!

In Landau's approximate three dimensional solution the first stage of the expansion is approximated as a linear expansion in the beam direction. When the system expanded in the beam direction to a size comparable or larger than its transverse diameter the transverse expansion is also considered.

When the energy density reduces to that of the freeze-out (or break-up) density, $e_{bu} \approx e_\pi \approx 1$ GeV/fm^3, then the number of particles becomes a well-defined quantity. We then say that the fluid "breaks up" into quasi-free final particles. We can make this criterion more specific for a given equation of state. The break-up criterion defines a space-time surface, σ, which is an isotherm, $T(\vec{r}, t) = T_{bu}$. Along this surface N_π is well defined, and we can determine the distribution of energy and number of particles as a function of the collective velocities.

If we neglect the random thermal velocity, the distribution of particle rapidities, y, at break up will follow the flow rapidity, η, distribution [45]:

$$\frac{dN}{d\eta} \approx \pi d^2 n_{bu} \left(\frac{e_0}{e_{bu}}\right)^{1/(1+c_0^2)} \times r_0 \ \exp\left(\frac{-\eta^2}{2|L|}\right), \tag{6.42}$$

where

$$L = \frac{2c_0^2}{1-c_0^4} \ln\left(\frac{e_0}{e_{bu}}\right),$$

and n_{bu} is the break up density of particles.

6.4.3 Numerical solution

Cooper *et al.,* provided a numerical solution of the model,[45] which is generally applicable. As it is illustrated in Fig. 6.12, the flow pattern in the middle of the system is similar to the flow pattern of the Bjorken model, if the initial energy density or temperature are high.

In the one-dimensional case an exact solution is known for the expansion of the fluid into vacuum [45]. The motion of the leading edge is a progressive wave, in which η and T are related by

$$\ln(T/T_0) = -c_0\eta. \tag{6.43}$$

In the three-dimensional case no such analytic solution is known. However, it is easy to show that for a very short time after the beginning of the spherical expansion this behavior still holds.

Thus the boundary conditions can be chosen somewhat arbitrarily so that no discontinuity appears in the temperature distribution after the beginning of the expansion. The initial conditions at $t = 0$ are set as

$$T(z, 0) = T_0, \quad \eta = 0, \quad \text{for} \quad 0 < z < r_0 - \epsilon \quad \text{and} \tag{6.44}$$

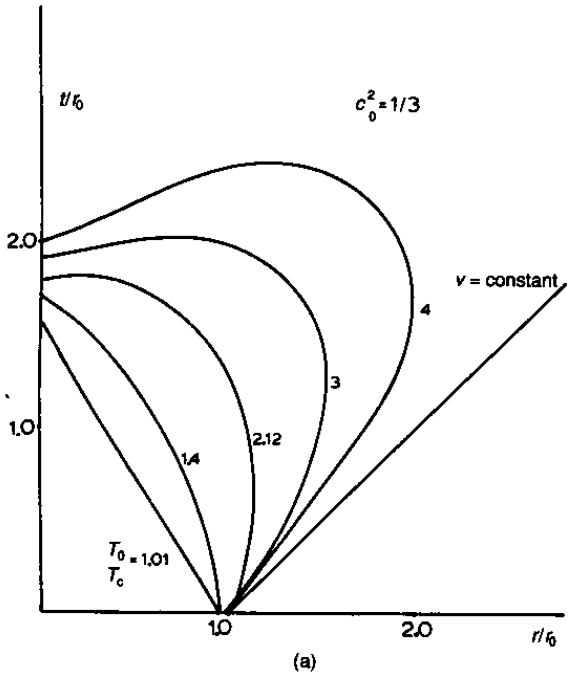

Figure 6.12: The isotherms of the flow at the break up when the temperature reaches $T_{bu}(= T_c$ in the figure). The ratio of the initial temperature, T_0, to the final temperature, T_{bu}, is the parameter of the contours. The solution depends on the sound speed, c_0, and on the initial thickness of the disk, r_0. As the initial temperature increases the solution at break up approaches the Bjorken model solution, particularly for a soft EOS like $c_0^2 = 1/6$. Reproduced with permission from [45].

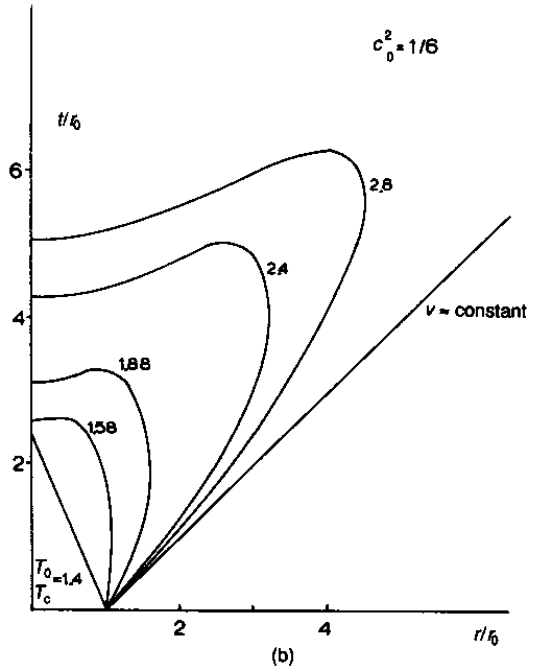

Figure 6.12: continued

$$T(z,0) = T_0\ (r_0 - z)/\epsilon, \quad \eta = -\frac{1}{c_0}\ln\left(\frac{T}{T_0}\right), \quad \text{for} \quad r_0 - \epsilon < z < r_0\ , \tag{6.45}$$

where $\epsilon \ll r_0$. The results are insensitive to the choice of ϵ as long as $\epsilon < 0.2 r_0$.

The three-dimensional expansion has qualitative features similar to those of the linear one-dimensional problem:

During an initial period from $t = 0$ to $t = r_0/c_0$ the initial disturbance at the edge propagates inward and sets the fluid in motion. At the same time the edge of the fluid moves outward at a speed $v \approx 1$. In the region of the leading edge the isotherms are space-like, propagate as usual discontinuities and begin as straight lines.

For $t > r_0/c_0$ the whole fluid is in motion, and because of the three - dimensional nature of the expansion it cools very rapidly. By the time the initial sphere has expanded to a few times its original size, the fluid is completely cool, and the final particles have "evaporated" from it. The critical isotherm becomes time-like after some time $t > r_0/c_0$, and for very high initial temperatures starts looking like a hyperbola. This is similar to the behavior of the fluid in the central region of the one-dimensional Bjorken problem. However, in the one-dimensional problem the expansion takes much longer, and the isotherm in the central region is closer to a hyperbola whose asymptote is the light cone.

The expansion lasts until a freeze out, when the mean free path becomes comparable to the size of the system. We can display the critical isotherm $T(z,t) = T_{bu} = m_\pi$ for $c_0^2 = 1/3$ and for various T_0 values in Fig. 6.12(a). Notice that for $T_0 < 2m_\pi$, there is no hint of the isotherm looking like $\tau =$constant. For $T_0 = 4m_\pi$, we see the beginnings of such behavior. However, even at $T_0 = 4m_\pi$, the outer edge of the isotherm is far from a

hyperboloid, and that is where most of the entropy lies.

For $c_0^2 = 1/6$ the cooling is slower [see Fig. 6.12(b)] and for $T_0/T_{bu} = 3.8$ and $z < 3r_0$ the isotherm is almost a hyperbola. Thus for small c_0^2 cooling is slow enough so that scaling will eventually set in.

Finally one should mention that at energies 15 and 60 A·GeV, for symmetric central heavy ion collisions full scale numerical three - dimensional relativistic fluid dynamical models reproduce the prediction of the Landau model regarding the final rapidity distribution of pions, to a good accuracy[46]. This is even more interesting than one would think first, because the initial condition in this model calculation is the one preceding the impact, i.e. two Lorentz contracted heavy ions approaching each other. This indicates that the fine details of the initial condition are irrelevant by the end of the collision if sufficient room for equilibration and thermalization is left during the collision.

6.5 Assignment 6

6.a Calculate the temperature of the QCD plasma generated in a detonation front from normal nuclear matter (for help see ref. [3] and determine the threshold beam energy for QCD plasma creation considering that $T > 0$ is required!

6.b Solve the Taub adiabat for an ultra-relativistic ideal gas with the EOS

$$P = \frac{e}{3},$$

and determine the density increase, $\frac{n}{n_0}$ as a function of $\gamma_{beam}^{(CM)}$, for a given $\gamma_{beam}^{(CM)}$ of the incoming beam, if $\gamma_{beam}^{(CM)} \gg 1$. The initial state is normal nuclear matter of $n_0, e = n_0 m_N, P_0 = 0$.

6.c Solve the Taub adiabat and the Rayleigh line equations for the relativistic ideal gas in the low temperature limit having the EOS:

$$e = n(m_N + \frac{3}{2}T),$$

and show that $\frac{n}{n_0} \to \infty$ if the beam energy increases. The initial state is normal nuclear matter.

6.d Show that

$$\frac{dS}{dy} = \text{constant},$$

for the solution of the Bjorken hydrodynamical model.

6.5.1 Solutions to Assignment 6

6.a QCD plasma cannot be reached in a zero energy or $j = 0$ detonation front because the temperature of the final state should be positive [3]. From the EOS of QGP with $N_{color} = 3$ and $N_{flavor} = 2$, eqs.(5.29-5.32), the temperature is

$$T^2 = \frac{9n_B(\hbar c)^3}{2\mu_B} - \frac{\mu_B^2}{9\pi^2}. \tag{6.46}$$

One can cast this in the form

$$\frac{9\pi^2 T^2}{\mu_B^2} = \frac{81\pi^2 n_B}{2\mu_B^3} - 1.$$

Since $T > 0$ and $\mu_B > 0$ the positivity of the temperature leads to the requirement that the dimensionless quantity

$$z \equiv \left[\frac{2\mu_B^3}{81\pi^2 n_B(\hbar c)^3}\right]^{1/3} < 1. \tag{6.47}$$

Using eq. (6.46) we can express the enthalpy density $w = e + P$ as a function of μ_B and n_B:

$$w = \frac{74}{45}\pi^2\left(\frac{9n_B}{2\mu_B} - \frac{\mu_B^2}{9\pi^2}\right)^2 + \frac{4}{9}\mu_B^2\left(\frac{9n_B}{2\mu_B} - \frac{\mu_B^2}{9\pi^2}\right) + \frac{2}{81\pi^2}\mu_B^4.$$

Multiplying this by $\frac{2\cdot 5\cdot\mu_B^2}{9n_B^2\pi^2} = \frac{9\cdot 5}{2\pi^2}\left[\frac{2\mu_B}{9n_B}\right]^2$ we obtain

$$w\frac{2\cdot 5\cdot\mu_B^2}{9n_B^2\pi^2} = \frac{37}{9\cdot 5}2\pi^2\left[\frac{9\cdot 5}{2\pi^2}\left(1 - \frac{2\mu_B^3}{81\pi^2 n_B}\right)^2\right] +$$

$$\frac{2\cdot 2}{9}\frac{9\cdot 5}{2\pi^2}\frac{2\mu_B^3}{9n_B}\left(1 - \frac{2\mu_B^3}{81\pi^2 n_B}\right) + \frac{9\cdot 5\cdot 2}{9\cdot 9}\frac{2\mu_B^6}{81\pi^4 n_B^2}.$$

Inserting z, eq. (6.47), into this equation we get

$$Az^2 - 37 - 16z^3 + 8z^6 = 0, \tag{6.48}$$

where $A = \frac{15w(2/3)^{1/3}}{n_B^{4/3}\pi^{2/3}(\hbar c)}$. Eq. (6.48) has a physical root in $z\epsilon[0,1]$ only if $A > 45$. Let us plot the $f(z) = 8z^6 - 16z^3 + Az^2 - 37$ function, Fig. 6.13.

If $A = 45$ the only non-negative root is at $z = 1$ which implies $T = 0$. Using the expression of A and the requirement $A > 45$ we get a relation between w and X or P and X. From $A^3 \geq 45^3$ it follows that

$$w \geq \frac{81\pi^2(\hbar c)^3}{2X^2},$$

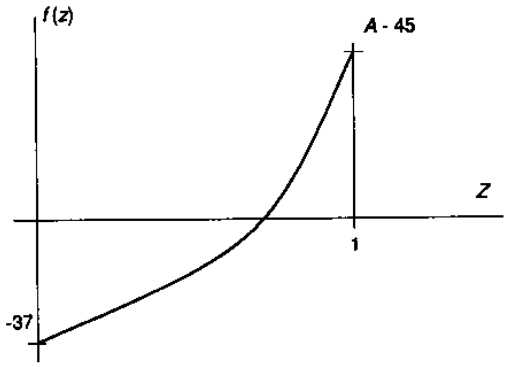

Figure 6.13: The $f(z)$ function

or

$$P \geq \frac{81\pi^2(\hbar c)^3}{8X^2} - B \tag{6.49}$$

Eq. (6.49) gives the lower limit of the detonation adiabat where $T = 0$. Eqs. (6.49,5.34) lead to a 3rd order equation in X, which can be solved analytically. (Formula of Cardano.) If we have the solution X_2 for a given Bag constant the corresponding pressure can be obtained from the EOS. From the pressure and X and from the initial state the corresponding current can be calculated by using the equation of the Rayleigh line.

Thus there exists a minimum current or beam energy to reach $T > 0$ QCD plasma, Fig. 6.14. Using eq. (6.49) with $\Lambda_B = 235MeV$ and $n_0 = 0.16fm^{-3}$, $P_0 = 0$, $X_0 = 6$GeV fm^3, the final state at the threshold $T > 0$ is

$$P = 0.29GeV/fm^3, \tag{6.50}$$

$$X = 1GeVfm^3. \tag{6.51}$$

sing $(n_0\gamma_0 v_0)^2 = j^2 = -\frac{P}{X-X_0} \approx 0.058fm^{-6}$ we can calculate the incoming rapidity in the shock's frame $\sinh(y) = v_0\gamma_0$:

$$y_0 = \text{arsinh}(\frac{\sqrt{0.058}}{n_0}) \approx 1.19.$$

The current is the same in the shocked matter $n_B\gamma v$. In order to get the rapidity we have to calculate the density of the shocked matter at the threshold. Form the pressure and the EOS $w = 4(P + B) = 4(0.29 + 0.4) = 2.76$GeV/fm^3, then using the definition of X the final density is $n_B = 1.66$fm^{-3}. Thus the shocked matter leaves the detonation front with a rapidity

$$y_1 = \text{arsinh}(\frac{\sqrt{0.058}}{n_1}) \approx 0.14.$$

The shocked matter is at rest in the c.m. frame of a central symmetric heavy ion collision. So, the incoming rapidity of the ground state nuclear matter in the c.m.

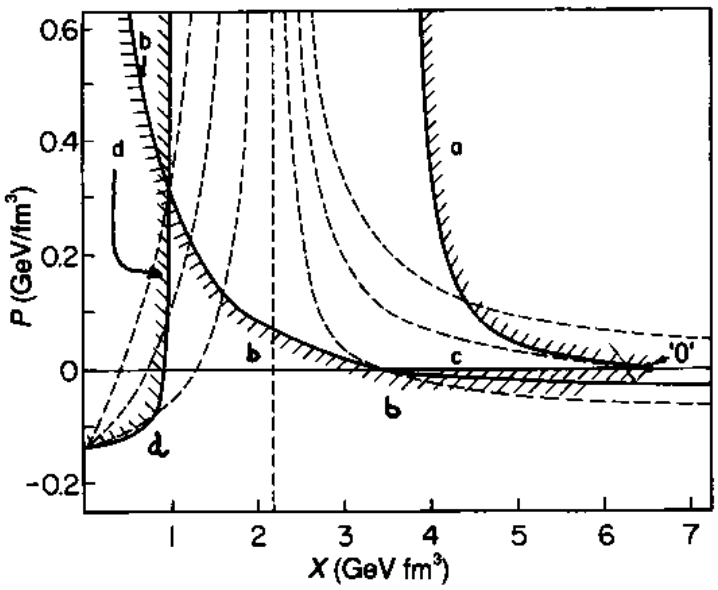

Figure 6.14: Boundaries (hatched) of the physical region in the pressure versus X plane given by the entropy condition (a) shock stability conditions (b) and (c) and by the positivity of the temperature (d). Dashed lines are Taub adiabats. For details see ref. [47].

frame (the same as the c.m. rapidity of the beam) is $y_0^{c.m.} = y_0 - y_1 = 1.05$. In a symmetric heavy ion collision $y_0^{Lab.} = 2y_0^{c.m.} = 2.1$. This yields a threshold energy of $E_{Lab.}^{Min.} = m_0(\gamma_0^{Lab.} - 1) = m_0(\cosh y_0^{Lab.} - 1) \approx 3$ GeV/nucleon. This threshold energy depends somewhat on the parameters and it is also influenced by the fact that we used an ideal Stefan - Boltzmann gas EOS for the QCD plasma which might not be too realistic around the phase transition threshold. Therefore it is reasonable to assume a threshold which is about 50% higher i.e. $E_{Lab.}^{Min.} = 4 - 6$ GeV/nucleon.

The threshold energy could be even higher if the nuclear stopping is not immediate, as it is assumed in the shock description, but there is a substantial interpenetration at the initial phases of the collision. Then the density increase is less and the thermal excitation increases. This process and the finite nuclear size can delay the plasma formation and increase the threshold further.

6.b Since $e_2 = 3P_2 \rightsquigarrow w_2 = 4P_2$ and $X_2 = 4P_2/n^2$, so the Taub adiabat takes the form

$$P_2 = (16P_2^2/n_2^2 - m_0^2)/\left(\frac{4P_2}{n^2} + \frac{m_0}{n_0}\right).$$

This can be cast in the form

$$\frac{12}{9}\left(\frac{3P_2}{n}\right)^2 = m_0^2\left(1 + \frac{n}{3n_0m_0}(\frac{3P_2}{n})\right).$$

Since $3P_2/n = \varepsilon = e/n$ and $\varepsilon \approx m_0\gamma_{c.m.} \gg m_0 \rightsquigarrow$

$$\frac{n}{n_0} = 4\gamma_{c.m.}$$

Note: Unfortunately $\frac{n}{n_0}$ is not measurable. The entropy, however, does not decrease, so it provides information from the hot and dense stage of the collision.

6.c The Taub adiabat is $[P] = [wX]/(X_1 + X_2)$, where

$$p_1 = 0, \quad w_1 = m_0 n_0, \quad X_1 = m_0/n_0,$$

$$p_2 = 0, \quad w_2 = (m_0 + \frac{5}{2}T)n, \quad X_2 = (m_0 + \frac{5}{2}T)/n.$$

Now the Taub adiabat takes the form

$$nT - 0 = \frac{\left(m_0 + \frac{5}{2}T\right)^2 - m_0}{\left(\frac{m_0 + \frac{5}{2}T}{n}\right) - \frac{m_0}{n_0}}$$

After straightforward calculation

$$\frac{n}{n_0} = 4 + \frac{15}{4}\frac{T}{m_0}.$$

Due to energy conservation $\varepsilon_{beam} = \varepsilon_2$ in the c.m. frame, so $m_0 + \frac{3}{2}T = m_0\gamma_{c.m.}$, and so the temperature is $T = \frac{2}{3}m_0(\gamma_{c.m.} - 1)$. Inserting this into the expression of $\frac{n}{n_0}$

$$\frac{n}{n_0} = \frac{3}{2} + \frac{5}{2}\gamma_{c.m.}.$$

In the non-relativistic limit $\gamma_{c.m.} \approx 1 + v^2/2 \approx 1$, so that

$$\frac{n}{n_0} \approx 4.$$

6.d The volume element in the LR frame of the fluid d^3x is

$$d^3x = d^2x_\perp \ \tau \ dy.$$

The entropy contained in interval dy around $u = 0$ is

$$dS = \int s_0 d^3x = \tau s \int d^2x_\perp dy,$$

consequently

$$\frac{d}{d\tau}\left(\frac{dS}{dy}\right) = \frac{d}{d\tau}\left(\tau s \int d^2x_\perp\right) = \left(s + \tau\frac{ds}{d\tau}\right)\int d^2x_\perp = \left(s - \tau\frac{s}{\tau}\right)\int d^2x_\perp = 0.$$

I.e., the entropy per unit rapidity is constant during the "scaling" expansion.

Bibliography

[1] R. Anishetti, P. Koehler and L. McLerran, Phys. Rev. **D22** (1980) 2793.

[2] L.P. Csernai and J. Kapusta, Phys. Rev. **D29** (1984) 2664.

[3] L.P. Csernai, Phys. Rev.**D29** (1984) 1945.

[4] M. Gyulassy and L.P. Csernai, Nucl. Phys. **A460** (1986) 723.

[5] J.D. Bjorken, Phys. Rev. **D27** (1983) 140.

[6] N.K. Glendenning and T. Matsui, Phys. Lett. **141B** (1984) 419.

[7] J.P. Blaizot and J.Y. Ollitrault, Nucl. Phys. **A458** (1986) 745.

[8] J.P. Blaizot and L. McLerran, Phys. Rev. **D34** (1986) 2739.

[9] P. Koch and J. Rafelski, Nucl. Phys. **A444** (1985) 678.

[10] K. Kajantie and L. McLerran, Nucl. Phys. **B214** (1983) 261.

[11] T. Matsui, B. Svetitsky and L. McLerran, Phys. Rev. **D34** (1986) 783.

[12] K. Kajantie, M. Kataja, L. McLerran and V. Ruuskanen, Phys. Rev. **D34** (1986) 811.

[13] K. Kajantie, J. Kapusta, L. McLerran and A. Mekjian, Phys. Rev. **D34** (1986) 2746.

[14] K. Kataja, P.V. Ruuskanen, L.D. McLerran and H. von Gersdorff, Phys. Rev. **D34** (1986) 2755.

[15] H. von Gersdorff, L. Mclerran, M. Kataja and P.V. Ruuskanen, Phys. Rev. **D34** (1986) 794.

[16] B.L. Friman, Phys. Lett. **B159** (1985) 369.

[17] B.L. Friman, K. Kajantie and P. V. Ruuskanen, University of Helsinki Report HU-TFT-85-21 (1985).

[18] B.L. Friman, G. Baym and J.P. Blaizot, Phys. Lett. **132B** (1983) 291.

[19] M. Gyulassy and T. Matsui, Phys. Rev. **D29** (1984) 419.

[20] L.D. Landau, Izv. Akad. Nauk SSSR **17** (1953) 51.

[21] J. Kapusta and A. Mekjian, Phys. Rev. **D33** (1986) 1304.

[22] K. Kajantie, R. Raitio and V. Ruuskanen, Nucl. Phys. **B222** (1983) 152.

[23] M.C. Chu, Phys. Rev. **D34** (1986) 2764.

[24] R. Raitio, Nucl. Phys. **A418** (1984) 539c.

[25] M. Gyulassy, Proc. of Bielefeld Workshop "Quark Matter formation in heavy ion collisions" ed. by M. Jacob and H. Satz, (World Scientific, 1982) p. 81.

[26] L. McLerran, Phys. Rep. **88** (1982) 379.

[27] A. K. Kerman, T. Matsui and B. Svetitsky, Phys. Rev. Lett. **56** (1986) 219.

[28] M. Gyulassy and A. Iwazaki, Phys. Lett. **165B**, 157 (1985).

[29] W. Busza and A.S. Goldhaber, Phys. Lett. **139B** (1984) 235.

[30] S. Date, M. Gyulassy and H. Sumiyoshi, Phys. Rev. **D32** (1985) 619.

[31] L.P. Csernai, Sov. JETP **65** (1987) 216; Zh. Eksp. Theor. Fiz. **92** (1987) 379.

[32] P. Danielewicz and M. Gyulassy, Phys. Rev. **D31** (1985) 53.

[33] L.P. Csernai and J. Kapusta, Phys. Rev. **D31** (1985) 2795.

[34] G.D. Westfall, J. Gosset, P.J. Johansen, A.M. Poskanzer, W.G. Meyers, H.H. Gutbrod, A. Sandoval and R. Stock, Phys. Rev. Lett. **37** (1976) 1202.

[35] J. Gosset, J. Kapusta and G. Westfall, Phys. Rev. **C18** (1978) 844.

[36] P.J. Siemens and J. Rasmussen, Phys. Rev. Lett. **42** (1979) 880.

[37] P.J. Siemens and J.I. Kapusta, Phys. Rev. Lett. **43** (1979) 1486.

[38] L.P. Csernai and H.W. Barz, Z. Phys. **A296** (1980) 173.

[39] T. Biró, H.W. Barz, B. Lukács and J. Zimányi, Phys. Rev. **C27** (1983) 2695.

[40] L.P. Csernai, Phys. Rev. Lett. **54** (1985) 639.

[41] S. Pratt, Phys. Rev. Lett. **53** (1984) 1219.

[42] L.D. Landau and S.Z. Belenkij, Usp. Phys. Nauk **56** (1956) 309, and Nuovo Cimento Suppl. **3** (1956) 15.

[43] G. Milekhin, Zh. Eksp. Teor. Fiz. **35** (1958) 1185; Sov. Phys. - JETP **35** (1959) 829.

[44] G. Milekhin, in Proc. of the Moscow Cosmic Ray Conf., Moscow, 1959, ed. by N.M. Gerasimova and A.I. Nikishov (IUPAP, Moscow 1960) Vol. 1, p. 220.

[45] F. Cooper, G. Frye and E. Schonberg, Phys. Rev. **D11** (1975) 192.

[46] E.F. Staubo, A.K. Holme, L.P. Csernai, M. Gong and D. Strottman, Phys. Lett. **B229** (1989) 351.

[47] H.W. Barz, L. P. Csernai, B. Kämpfer and B. Lukács, Phys. Rev. **D32** (1985) 115.

Chapter 7

Measurables

7.1 The freeze out process

In microscopic models which simulate the collisions like an event generator the evaluation of the measurables is identical to the way it is done in experiments.

In continuum problems, however, there are principal difficulties in evaluating the measurables. This is because when the particles reach the detectors they do not interact already for a long time, so there is a process when the strongly interacting continuum of the matter becomes dilute and its particles become independent. Although this gradual process could be handled in fluid dynamics, by the introduction of source and drain terms, it is very seldom done [1].

The freeze out process is most usually replaced by a sudden freeze out, or sudden break up. At a given instant in the space-time thus the constituents of the continuum will become independent particles. The final interactions and collisions among these particles are then neglected.

There are different levels of possible sophistication if we want to describe this freeze out process and evaluate the measurable quantities. The sudden freeze out is a hypersurface in the space-time. The matter flows according to the rules of fluid dynamics until this surface is reached. This surface, of course, can be defined by using the characteristic quantities of the flow, like density, temperature or pressure.

In the simplest approximation one can just assume that the particles will follow the flow velocities after the break up and evaluate the measurables accordingly (while disregarding the random thermal motion). This procedure was used for the description of heavy ion reactions of BEVALAC in the 1970's. The procedure can be justified only if the break up happens very late when the thermal velocity and energy, as well as the pressure are negligibly small. The break up, particularly in a small system can happen earlier.

The next, and most frequently used step is to consider the thermal velocity distribution at the break up also. Thus the random thermal velocities are added to the collective flow velocities to calculate the measurables. This procedure is based on the Jüttner distribution and in the recent times it was used by Milekhin [2] to calculate measurables in Landau's fluid dynamical model for hadron-hadron collisions. In this

chapter we will introduce this approximation. Although this procedure is already taking into account a major part of the neglected thermal energy it is still not exact.

7.1.1 Formal treatment of the freeze out

In fact the freeze out across a hypersurface is a discontinuity, where the EOS of the matter changes according to our assumption to an ideal gas. Thus the energy - momentum tensor changes discontinuously across this surface. If the flow is not orthogonal to this surface this can lead to a change in the flow. The importance of this difference between the flow direction and the normal to the freeze out surface was first realized by Cooper and Fry [3]. Many most recent theoretical introductions and works are not aware of this problem and ignoring it [4, 5]. The freeze out discontinuity is a time-like surface in most cases, and so the methods introduced in Chapter 5 for the description of time-like detonations and deflagrations should be used [6].

Hence the flow velocity may also be discontinuous when the matter flows across this surface. If the pressure at the breakup is small or if the flow is orthogonal to the freeze out surface the effect is negligible. A qualitative estimate for the importance of this effect is given in ref. [7].

The freeze out surface in the space-time is a three dimensional hyper-surface, S, with normal vector, $d\sigma^\mu$. The surface is not a closed surface, but it crosses the world-lines of all particles. The particles after crossing this surface are considered to be frozen out, i.e. their energies and momenta will not change (except due to final decays or due to final long range Coulomb interaction if these effects are considered). The particles always propagate along time-like paths, thus most of the time (but not always) the freeze out surface they are crossing is a time-like surface with a time-like normal vector, $d\sigma^\mu$.

The invariant number of particles crossing this surface at some point is $dN = N^\mu \, d\sigma_\mu$ and the total number of all the particles crossing this surface is

$$N = \int_S N^\mu \, d\sigma_\mu \ . \tag{7.1}$$

This total number, N, and the total energy and momentum are of course the same at both sides of the freeze out surface. However, the four-current, N_μ, and the energy momentum tensor, $T^{\mu\nu}$, are generally discontinuous! This is easy to see, since after the freeze out we consider an ideal gas of particles where interactions are neglected, with an ideal gas EOS. The matter in the flow is on the other hand described by an EOS where interactions are included, i.e., by another EOS. Unless the EOS is an ideal gas EOS on both sides of the freeze out surface N^μ and $T^{\mu\nu}$ are discontinuous. Therefore to evaluate the measurables we have to use the parameters of the matter after the discontinuity! The proper calculation of N^μ and $T^{\mu\nu}$ after such a discontinuity can be performed if the surface, S, is known and the pre freeze out quantities N_0^μ and $T_0^{\mu\nu}$ are known (see sect. 5.5). In fact the correct determination of the freeze out surface is an involved problem. In most cases this surface is not obtained as the solution of the dynamical problem but it is prescribed directly, or defined by requiring some condition(s) to be satisfied.

If the normal freeze out surface is not identical to the flow velocity the momentum of the matter changes due to the freeze out[7]. Even if the two vectors are identical and just the EOS changes, the parameters of the post freeze out matter, like the temperature, will be different, due to the fact that the energy contained in the interactions before freeze out should be added to the kinetic energy of the particles of the noninteracting ideal gas. This temperature change can be neglected only if the freeze out is chosen so, that all interaction energies are negligibly small already.

Let us now assume that we have determined the post freeze out quantities, N^μ and $T^{\mu\nu}$, from the relations (see sect. 5.5):

$$[N^\mu \ d\sigma_\mu] = 0 \quad \text{and} [T^{\mu\nu} \ d\sigma_\mu] = 0. \tag{7.2}$$

Then for an ideal gas we know that

$$N^\mu = \int \frac{d^3p}{p^0} p^\mu \ f_0(x,p) \ , \tag{7.3}$$

where f_0 is the phase space distribution of the ideal gas including the collective flow (see e.g. sect. 2.4). The total number of particles frozen out can be calculated via eq. (7.1).

The experimental measurables are usually differential quantities (i.e differential cross sections or double differential cross sections) normalized per event (not per unix incoming flux). For example such a differential quantity is

$$\frac{dN}{d^3p}$$

satisfying the normalization

$$N = \int_S \frac{dN}{d^3p} d^3p = \int_S \left(\int \frac{d^3p}{p^0} p^\mu \ f_0(x,p) \right) \ d\sigma_\mu = \int_S n(x) \ u^\mu d\sigma_\mu \ . \tag{7.4}$$

Similarly some component of the overall momentum of emitted particles is frequently measured, like the transverse momentum in the reaction plane p^x

$$p^x_{tot} = \int_S \frac{dN}{d^3p} p^x \ d^3p = \int_S \left(\int \frac{d^3p}{p^0} p^\mu p^x \ f_0(x,p) \right) \ d\sigma_\mu = \int_S T^{\mu x} d\sigma_\mu \ . \tag{7.5}$$

If we are interested in differential quantities we use relations based on eqs. (7.4,7.5), where not all the integrals, d^p are performed. We will see some examples for these in the following sections.

A frequent simplifying assumption is that the normal of the freeze out surface is parallel to the flow, $u^\mu = d\sigma^\mu$. This simplifies eqs. (7.4,7.5), and reduces the complications related to evaluating N^μ and $T^{\mu\nu}$ after the freeze out discontinuity. In such a simplified case only the energy conservation across the break up surface should be taken care of, usually resulting in a somewhat modified freeze out temperature.

In numerical models with a calculational grid of a finite resolution this approximation cannot be done exactly, because the cells are freezing out at discrete times and they have finite sizes. Thus this approximation leads to a ragged surface in a way that in

each freezing out cell the normal of the freeze out surface is parallel to the flow. The surfaces of the neighboring freeze out cells are connected by connecting surfaces which are parallel to the flow so that there is no matter flux across these connecting surfaces. In this situation the integral over the freeze out hypersurface of the cell yields the proper volume of the cell, γV_{cell}. The connecting surfaces parallel to the flow do not contribute to the measurables.

In analytic models or in models where spherical or cylindrical symmetry is assumed the freeze out surface frequently satisfies $u^\mu = d\sigma^\mu$, so that extra assumptions or complications in evaluating the after freeze out quantities do not appear. In the following sections we study a few examples where the $u^\mu = d\sigma^\mu$ approximation is used.

In sections 7.2 and 7.3 we evaluate some of the most common measurable quantities used in the relativistic and ultra-relativistic heavy ion collisions. In sections 7.4 and 7.5 quantities frequently used in intermediate energy reactions are discussed, while measurables directly connected with the collective motion are presented in sections 7.6 and 7.7.

7.2 Baryon measurables

We assume that the local baryon momentum distribution at a space-time point x is a Jüttner distribution $f(x,p)$. This is a reasonable assumption if the flow velocities are relativistic, the temperature is high (e.g., a few hundred MeV), but $T \ll m$. Thus the approximation holds for nucleons and heavy baryons. From the point of view of the measurable quantities it is practical to introduce another parametrization of the flow velocity u^μ also

$$u^\mu = \gamma(1, v_\parallel, \vec{v}_\perp) = \gamma_\perp(\cosh(y_0), \sinh(y_0), \vec{V}_\perp),$$

where y_0 is the rapidity of the fluid cell. It follows from this definition that $v_\parallel = \tanh(y_0)$, $\vec{V}_\perp = \vec{v}_\perp/\sqrt{1-v_\parallel^2}$, and $\gamma_\perp^2 = (1-v_\parallel^2)/(1-v_\parallel^2-v_\perp^2) = 1/(1-V_\perp^2)$. Using the second notation of u^μ above, the $p^\mu u_\mu$ product takes a transparent form:

$$p^\mu u_\mu = \gamma_\perp \left(m_\perp \cosh(y - y_0) - \vec{p}_\perp \vec{V}_\perp \right),$$

where y, $\vec{p}_\perp$ and $m_\perp$ are the rapidity, transverse momentum and transverse mass of a particle of 4-momentum p^μ. Based on ref. [8] we review briefly the different projections:

7.2.1 Rapidity distribution

We can split up the phase space integrals by observing that $d^3p = dp_{||} d^2p_\perp = p^0 dy\, d^2p_\perp$. Thus the contribution of a fluid cell to the final baryon rapidity distribution is:

$$\frac{dN_{cell}}{dy} = \gamma V_{cell} \int \frac{d^3p}{p^0} \frac{d}{dy} \left[p^\mu u_\mu \; f(x,p) \right].$$

Performing the integrals yields

$$\begin{array}{rcl} \frac{dN_{cell}}{dy} & = & \frac{\gamma V_{cell}\ g_N}{(2\pi\hbar)^3}\exp(\frac{\mu}{T})\ 2\pi T m^2\ \sqrt{\frac{2}{\pi}}\ \sqrt{hm}\times \\ & & \sum_{k=0}^{\infty}\ \left(\frac{g^2 m}{2h}\right)^k\ \frac{1}{k!}\left[\left(1-(\frac{g}{h})^2\right)K_{k+\frac{5}{2}}(hm)\ -\ \frac{1}{hm}K_{k+\frac{3}{2}}(hm)\right], \end{array} \tag{7.6}$$

where V_{cell} is the volume of the fluid cell, g_N is the degeneracy of nucleons ($g_N = 4$), $h = \gamma[\cosh(y) - v_{\parallel}\sinh(y)]/T$, and $g = \gamma v_{\perp}/T$. If $mg^2 \ll h$ and $g \ll h$ this expression reduces to

$$\frac{dN_{cell}}{dy} = \frac{\gamma V_{cell}\ g_N}{(2\pi\hbar)^3}\exp(\frac{\mu}{T})\ 2\pi T m^2\ \left[1+\frac{2}{hm}+\frac{2}{(hm)^2}\right]\ exp(-hm).$$

Integrating this over the rapidity y yields the total baryon number in the fluid cell. The final rapidity distribution of the baryon charge is then obtained by summing up the contributions from all the fluid cells:

$$\frac{dN}{dy} = \sum_{cell}\frac{dN_{cell}}{dy}.$$

7.2.2 Transverse Momentum Spectra

Another usual quantity measured experimentally is the transverse momentum distribution. The contribution of a fluid cell to the final baryon transverse momentum distribution is:

$$\frac{dN_{cell}}{p_{\perp}dp_{\perp}} = \gamma V_{cell}\ \int\frac{d^3p}{p^0}\ \frac{d}{p_{\perp}dp_{\perp}}\ \left[p^{\mu}u_{\mu}\ f(x,p)\right].$$

Performing the integrals yields

$$\frac{dN_{cell}}{p_{\perp}dp_{\perp}} = \frac{\gamma V_{cell}\ g_N}{(2\pi\hbar)^3}\exp(\frac{\mu}{T})\ T\left(aK_1(a)I_0(b)\ -\ bK_0(a)I_1(b)\right), \tag{7.7}$$

where $a = \gamma_{\perp}m_{\perp}/T$, and $b = \gamma_{\perp}(\vec{V}_{\perp}\vec{p}_{\perp})/T$.

7.2.3 Collective Sidewards Flow

A sensitive method to detect the collective sidewards flow is the *Transverse Momentum Analysis* [9]. We can evaluate the transverse momentum flow $< p^x/a >$ in relativistic fluid dynamics also. Since we know the reaction plane exactly the majority of the complications are nonexistent in a theoretical calculation. Under the same assumptions that were used above, the contribution of a fluid cell to the transverse momentum projected to the reaction plane (x, z) in the C.M. system is: $p^x_{tot\ cell} = V_{cell}\int d^3p\, p^x f(x,p)$. The yield falling into a unit rapidity interval around y is

$$\frac{dp^x_{cell}}{dy} = V_{cell}\int d^2p_{\perp}\ p^0 p^x f(x,p).$$

This quantity is not an invariant scalar therefore we are not allowed to evaluate it in an arbitrary frame. After a straightforward calculation we can arrive at the result

$$\frac{dp^x_{cell}}{dy} =$$

$$2\pi\ \cosh(y) m^2 C Q V_{cell} \sqrt{\frac{2}{\pi}} \sum_{k=0}^{\infty} \frac{g^{2k+1}}{2^k k!} (\frac{m}{h})^{k+\frac{3}{2}} \left(K_{k+\frac{3}{2}}(hm) + \frac{2(k+2)}{hm} K_{k+\frac{5}{2}}(hm) \right), \tag{7.8}$$

where $Q = \cos(\phi_R)$ is the cosine of the azimuth angle of the fluid cell measured from the reaction plane, the constant C is given in terms of the baryon density and cell temperature as $C = n g_N/[4\pi m^2 T K_2(m/T)] = g_N \exp(\mu/T)/(2\pi\hbar)^3$. The average transverse momentum per nucleon at a given rapidity y is then given by

$$< p^x/a >= \frac{\sum_{cell} dp^x_{cell}/dy}{\sum_{cell} dN_{cell}/dy}.$$

7.2.4 Average Transverse Momentum

We can also calculate the average transverse momentum $< p_\perp/a >$ which is the magnitude of transverse projection of momentum. Similarly to the case of $< p^x/a >$, we may define the rapidity distribution of the transverse momentum in the C.M. frame as $\frac{dp_{\perp cell}}{dy} = V_{cell} \int d^2p_\perp\ p^0 p_\perp f(x,p)$. Thus yields after integrations

$$\frac{dp_{\perp cell}}{dy} =$$

$$2\pi\ \cosh(y) C V_{cell} \sum_{k=0}^{\infty} \frac{g^{2k}}{(2k)!!^2} (2k+3)!! (\frac{m}{h})^{k+2} \left(K_{k+2}(hm) + \frac{hm}{2k+3} K_{k+1}(hm) \right). \tag{7.9}$$

Thus the average $p_\perp$ per baryon is

$$< p_\perp/a >= \frac{\sum_{cell} dp_{\perp cell}/dy}{\sum_{cell} dN_{cell}/dy}.$$

7.3 Pion Measurables

If the particles are not heavy the previous assumptions about the applicability of the Jüttner distribution may not hold. This is the case for pions for example, which may reach high multiplicity and thermal equilibrium by the freeze-out time in an ultra-relativistic heavy ion collision. The local pion distribution at a space-time point x is assumed to be a relativistic Bose distribution $f_\pi(x,p)$:

$$f_\pi(x,p) = \frac{g_\pi}{(2\pi\hbar)^3} \frac{1}{exp\left(\frac{p^\mu u_\mu}{T}\right) - 1},$$

where g_π is the degeneracy factor of pions ($g_\pi = 3$). The total pion number can be obtained from the normalization:

$$n_\pi = u_\mu N^\mu_\pi = u_\mu \int \frac{d^3p}{p^0} p^\mu f_\pi(x,p) = \frac{g_\pi}{(2\pi\hbar)^3} \int \frac{d^3p}{p^0} \frac{p^\mu u_\mu}{exp\left(\frac{p^\mu u_\mu}{T}\right) - 1}.$$

Using the power series expansion $[\exp(p^\mu u_\mu/T) - 1]^{-1} = \sum_{k=1}^{\infty} \exp(-k\ p^\mu u_\mu/T)$ we arrive at

$$n_\pi = \frac{4\pi g_\pi m_\pi^2 T}{(2\pi\hbar)^3} \sum_{k=1}^{\infty} \frac{1}{k}\ K_2\left(\frac{km_\pi}{T}\right).$$

In the limit of $m_\pi \to 0$ the modified Bessel function $K_2(\frac{km_\pi}{T}) \to 2(\frac{T}{km_\pi})^2$. Using $\sum_{k=1}^{\infty} k^{-3} = \zeta(3)$, we end up with the well known expression for the *Stefan-Boltzmann* gas:

$$n_\pi = \frac{g_\pi \zeta(3) T^3}{\pi^2 \hbar^3}.$$

This means that we assume a local ideal gas momentum distribution for the emitted pions. The pions are emitted in their own local rest frame (LR), and their number is proportional to this volume and to the temperature. Using the power series expansion we can easily repeat the calculation of the measurables for pions [8]:

Rapidity Distribution:

$$\begin{aligned} \frac{dN_{\pi,cell}}{dy} &= \frac{\gamma V_{cell}\ g_\pi}{(2\pi\hbar)^3}\ 2\pi T m_\pi^2\ \sqrt{\tfrac{2}{\pi}} \sum_{j=1}^{\infty}\ \sqrt{\tfrac{hm_\pi}{j}} \times \\ & \sum_{k=0}^{\infty}\ \left(\frac{j\ g^2 m_\pi}{2h}\right)^k\ \frac{1}{k!}\left[\left(1 - (\tfrac{g}{h})^2\right) K_{k+\frac{5}{2}}(jhm_\pi)\ -\ \tfrac{1}{jhm_\pi} K_{k+\frac{3}{2}}(jhm_\pi)\right]. \end{aligned} \tag{7.10}$$

Transverse Momentum Spectrum

$$\frac{dN_{\pi,cell}}{p_\perp dp_\perp} = \frac{\gamma V_{cell}\ T g_\pi}{(2\pi\hbar)^3} \sum_{j=1}^{\infty} \left(aK_1(ja)I_0(jb)\ -\ bK_0(ja)I_1(jb)\right). \tag{7.11}$$

Collective Sidewards Flow

$$\begin{aligned} \frac{dp^x_{cell,\pi}}{dy} &= 2\pi\ \cosh(y) m_\pi^2 \sqrt{\tfrac{2}{\pi}}\ \tfrac{g_\pi V_{cell}\ \cos(\phi_R)}{(2\pi\hbar)^3} \\ & \sum_{j=1}^{\infty} \sum_{k=0}^{\infty} \tfrac{(jg)^{2k+1}}{2^k k!} (\tfrac{m_\pi}{jh})^{k+\frac{3}{2}} \left(K_{k+\frac{3}{2}}(jhm_\pi) + \tfrac{2(k+2)}{jhm_\pi} K_{k+\frac{5}{2}}(jhm_\pi)\right). \end{aligned} \tag{7.12}$$

Average Transverse Momentum

$$\begin{aligned} \frac{dp_{\perp,cell,\pi}}{dy} &= \tfrac{2\pi\ \cosh(y) V_{cell} g_\pi}{(2\pi\hbar)^3} \\ & \sum_{j=1}^{\infty} \sum_{k=0}^{\infty} \tfrac{(jg)^{2k}}{(2k)!!^2} (2k+3)!! (\tfrac{m_\pi}{jh})^{k+2} \left(K_{k+2}(jhm) + \tfrac{jhm}{2k+3} K_{k+1}(jhm)\right). \end{aligned} \tag{7.13}$$

7.4 Calculation of cross sections

7.4.1 Inclusive and exclusive cross sections

First of all we distinguish inclusive and exclusive reactions. Inclusive reactions include collisions of all impact parameters, while exclusive collisions select a subset of collisions under some more or less well defined criteria. Of course, triggering for inclusive collisions might miss a few events. The triggering of exclusive reactions usually intends to select an impact parameter range, or most frequently the most central collisions.

It is generally assumed that the most central collisions lead to the highest observed particle multiplicities. Also, the number of collisions with impact parameters in the range $[b, b+db]$ is proportional to $2\pi b\ db$. Then the most simple assumption usually is that that a given, $Q\%$, of the highest multiplicity collisions includes collisions of impact parameters in the range, $b = 0 - \sqrt{\frac{Q}{100}} b_{max}$. Of course in reality the cut is not sharp at this impact parameter value, but larger impact parameter collisions might also lead to smaller multiplicities and vice versa due to random fluctuations. The shape of the impact parameter distribution curve corresponding to a given multiplicity range can be calculated approximately in cascade or molecular dynamics models, because these account for random fluctuations [10].

7.4.2 Double and triple differential cross sections

We frequently mention energy spectra, differential, double differential and in high multiplicity heavy ion reactions triple differential cross sections: $d\sigma/\ dE$, $d\sigma/\ d\Theta$, $d^2\sigma/\ dE\ d\Theta$ and $d^3\sigma/\ dE\ d\Theta\ d\phi$ respectively. In low energy nuclear physics the multiplicity of emitted particles is small, the reaction plane could not be identified, so the triple dimensional cross section could not be measured. The cross sections were always averaged over the azimuth.

Since 1984 in relativistic heavy ion collisions the identification of the reaction plane is reliably possible [11], so triple differential cross sections and other even more sensitive projections of the distributions of the emitted particles are measurable. The identification of the reaction plane is based on the sidewards flow or side splash effect, which is a typical collective flow effect first predicted in fluid dynamical models.

Let us see first, based on ref. [12], how do we calculate the cross sections in the fluid dynamical model based on the transformation properties of the local thermal momentum distributions. (An alternative way would be to generate particles randomly according to these distributions and analyze the obtained set of particles, exactly like it is done in experiments[13].)

7.4.3 Boosting thermal distributions

When a fluid element reaches the break-up condition the nucleons in the cell explode into all directions due to their thermal velocities. The thermal distribution of nucleons inside a fluid cell i is described by the relativistic Fermi-distribution (for nucleons

$g_N = 4$):

$$f_i(\vec{p})d^3p = \frac{4}{(2\pi\hbar)^3}\frac{d^3p}{\exp\left[\frac{\sqrt{m^2+p^2}-\mu_{ch,i}}{T_i}\right]+1} , \tag{7.14}$$

where $\mu_{ch,i}$ is the chemical potential of the ith cell taken from the normalization condition

$$n_i = \int d^3p \; f_i(\vec{p}) \; , \tag{7.15}$$

and $\sqrt{m^2+p^2} = p_i^0$ is the energy of the emitted particle in the local rest frame of the cell. In this section we will use the $p^\mu = p^\mu_{LR}$ notation. Since the distribution depends on the energy p^0_{LR} only this dependence is the same what we have seen at the introduction of the Jüttner distribution, i.e. $p^\mu u_\mu \equiv p^0_{LR} = p^0$. The particle momenta in any other than the LR frame will be denoted by P^μ or q^μ_{cm} here. Obviously the total number of particles N_i in a cell of rest volume $V_i^{(LR)}$ is $N_i = V_i^{(LR)} \; n_i$.

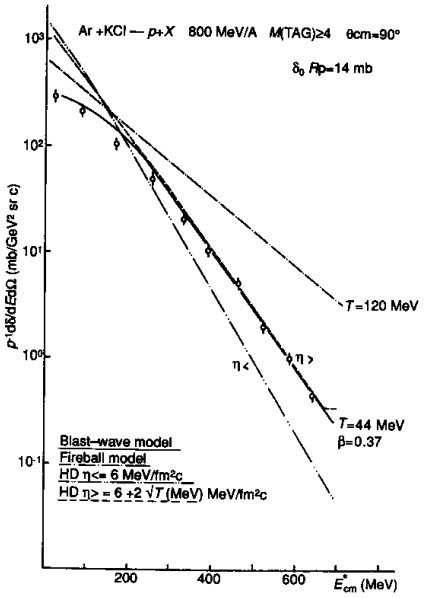

Figure 7.1: Invariant proton cross sections of central Ar + KCl collisions at 800 MeV/nucleon projectile energy ($\Theta_{cm} = 90^0$). Open circles are experimental points. Full (dashed-dotted) curves represent the cross sections obtained in the Blast-Wave (Fireball) models. The presented viscous fluid dynamical model calculations with two different viscosity values yielded the dashed and dashed double dotted results. Reproduced by permission of Springer-Verlag from [12].

For zero temperature matter the distribution is sharply cut off at $p = p_F$, that is $\mu^0_{ch,i} = \sqrt{m^2+p_F^2} = \sqrt{m^2+\hbar^2(\frac{3}{2}\pi^2 n_i)^{2/3}}$. For finite temperature the normalization is more complicated.

To obtain the momentum distribution, $F(P)$, of all nucleons in one definite reference frame the distributions (7.14) should be Lorentz-transformed from LR to this given

frame (for example lab.) by the relative boost velocity, $\beta_i^{flow} = \beta_i$, of the cell i. We can introduce a distribution function, $F(P)$ which is not an invariant scalar but it has the property that it is normalized to $n = n_i$ in the Lab. frame for example:

$$n = N^\mu u_\mu = \int \frac{d^3p}{p^0} \underbrace{p^\mu u_\mu}_{=p^0_{LR}} f(\underbrace{p^\mu u_\mu}_{=p^0_{LR}}) =$$

$$\int d^3P \underbrace{\frac{p^0_{LR}}{P^0} f(p^0_{LR})}_{\equiv F(P)} = \int d^3P \; F(P) \; , \tag{7.16}$$

where $F(P)$ is function of P only since the local rest frame momentum, p^0_{LR}, can be expressed in terms of P and the relative speed of the ith cell: $p^0 = p^0_{LR} = p^\mu u_\mu = P^\mu U^{(i)}_\mu$. Then the distribution function in the lab. frame can be expressed as

$$\frac{dN}{d^3P} = \frac{dN}{P^2 \; dP \; d\Omega} = F_i^{Lab.}(\vec{P}) = \frac{p^0(\vec{P})}{P^0} f_i\left(\vec{p}(\vec{P})\right) \; , \tag{7.17}$$

where $(p^0), (\vec{p})$ and $(P^0), (\vec{P})$ are the four momenta of emitted particles in the cell and lab. systems, respectively. They are connected by the Lorentz- transformation:

$$p^0 = p^0(\vec{P}) = \gamma_i P^0 - \gamma_i(\vec{\beta}_i \vec{P}) \; ,$$

$$\vec{p} = \vec{p}(\vec{P}) = \vec{P} - \frac{\gamma_i(p^0 + P^0)}{1 + \gamma_i}\vec{\beta}_i \; , \tag{7.18}$$

where $\gamma_i = 1/\sqrt{1 - \beta_i^2}$. In the 1-dimensional, longitudinal hydrodynamical model the scalar product $(\vec{\beta}_i \vec{P}) = \beta_i \cos(\Theta)\sqrt{(P^0)^2 - m^2}$, due to the fact that all cells move along the z-axis.

The differential cross section is essentially proportional to $F(P)$, but the quantities frequently measured are the energies and angles of the emitted particles. Thus, one has to perform the necessary coordinate transformations in the momentum space. The volume element is $d^3P = P^2 dP \; d\Omega$, and since $P^0 = \sqrt{P^2 + m^2}$ the differential $dP^0 = \frac{P}{\sqrt{P^2+m^2}} dP = \frac{P}{P^0} dP$. Consequently

$$\left.\frac{d\sigma}{dP^0 \; d\Omega}\right|_{cell \; i} = P^0\sqrt{(P^0)^2 - m^2} \; \frac{d\sigma}{d^3P} \; = P^0\sqrt{(P^0)^2 - m^2} \; \sigma_0 F(\vec{P}) \; , \tag{7.19}$$

where σ_0 is a constant of dimension fm^2 (see later). Thus from (7.17) and (7.18) we obtain the double differential cross section of primary charged particles, $(p+2d+2\alpha+...)$ as

$$\frac{d^2\sigma_{prim}}{dP^0 \; d\Omega} = \frac{Z_T + Z_P}{A_T + A_P} \sum_i \frac{4V_i^{(LR)}\sigma_0}{(2\pi\hbar)^3} \; \frac{p_i^0(\vec{P})\sqrt{(P^0)^2 - m^2}}{\exp\left[\frac{p_i^0(\vec{P}) - \mu_{ch,i}}{T_i}\right] + 1} \; , \tag{7.20}$$

where $V_i^{(LR)}$ is the volume of the i-th cell in the cell's frame, σ_0 is the target area for exclusive selected central collisions, $\sigma_0 = 4\pi b^2_{select}$, and $p_i^0(\vec{P})$ is the particle energy

in the ith cell's frame, but expressed in terms of the lab. frame quantities: $p_i^0 = \gamma_i \left[P^0 - \beta_i \cos(\Theta)\sqrt{(P^0)^2 - m^2}\right]$. For the general case when the fluid model is three dimensional the distribution (7.20) is valid by using $p_i^0 = \gamma_i \left[P^0 - (\vec{\beta}_i \vec{P})\right]$.

7.4.4 Spherical expansion

In case of spherically symmetric expansion the fluid is divided to spherical layers and each layer i has a radial velocity β_i^R. Let us first evaluate the contribution of one spherical layer of thickness Δl. This layer contains many fluid cells. The summation over these fluid cells can be carried out

$$\sum_{i-cells} V_i^{(LR)} \ ... \ \rightarrow R^2 \Delta l \int d\Omega \ ... \ . \tag{7.21}$$

Due to spherical symmetry the cross section will also be spherically symmetric. We can choose one direction, the z-axis, and calculate the P -distribution in this direction. At one fixed polar angle Θ the contribution of all azimuthal angles are the same

$$R^2 \Delta l \int d\Omega \ ... \ = R^2 \Delta l \int d\phi \ d\cos\Theta \ ... \ = R^2 \Delta l \ 2\pi \ \int d\cos\Theta \ ...$$

$$4\pi R^2 \ \Delta l \ \frac{1}{2} \int d\cos\Theta \ ... \ = V_i^{(LR)} \frac{1}{2} \int d\cos\Theta \ ... \tag{7.22}$$

Transforming the Fermi-distributions from a fluid element of the layer to the c.m. of the system, and then integrating over the whole layer the resulting c.m. distribution is:

$$F_i^{c.m.}(\vec{q_{cm}}) \ = \ \frac{4}{(2\pi\hbar)^3} \ \frac{2\pi}{q_{cm}^0 \beta_i^r \gamma_i^r \sqrt{(q_{cm}^0)^2 - m^2}} \int_{p_1^0}^{p_2^0} \frac{p^0 \ dp^0}{\exp\left[\frac{p^0 - \mu_{ch \ i}}{T_i}\right] + 1} \ , \tag{7.23}$$

where

$$p_{1,2}^0 = \gamma_i^r \ \left[q_{cm}^0 \mp \beta_i^r \sqrt{(q_{cm}^0)^2 - m^2}\right] \ .$$

In the relativistic Boltzmann limit (neglecting the term 1 in the denominator in the integral) the integral can be evaluated analytically and the resulting formula of the Blast Wave model [14] can be obtained.

The different layers may have different β_i^r, $\mu_{ch \ i}$ and T_i values at the break-up, so summing up the contributions of the layers and transforming the distribution a second time now to the lab. system we obtain:

$$\frac{d^2\sigma_{prim}^{BW}}{dP^0 \ d\Omega} = \ \frac{Z_T + Z_P}{A_T + A_P} \sum_i \frac{2V_i^{(LR)}\sigma_0}{(2\pi\hbar)^3} \frac{1}{\beta_i^r \gamma_i^r} \sqrt{\frac{(P^0)^2 - m^2}{q_{cm}^0(\vec{P})^2 - m^2}} \int_{p_1^0}^{p_2^0} \frac{p^0 \ dp^0}{\exp\left[\frac{p^0 - \mu_{ch \ i}}{T_i}\right] + 1} \ , \tag{7.24}$$

where $q^0_{cm} = \gamma_L \left[P^0 - \beta_L \cos(\Theta_L) \sqrt{(P^0)^2 - m^2} \right]$, with Θ_L being the emission angle and β_L the velocity of the c.m. system in the lab. To have the inclusive proton cross section the primary one should be multiplied by the ratio R_p of the emitted protons to the total charge $Z_P + Z_T$. The result of this calculation is shown in Fig. 7.1 (from ref. [12]). The so called *invariant* cross section is plotted due to its preferred relativistic transformation properties: $\frac{1}{P} \frac{d\sigma}{dP^0\, d\Omega}$.

Eq. (7.20) is the most general form which can be used for any number of fluid cells and for any flow pattern.

7.5 Results of three dimensional calculations

The early fluid dynamical calculations from Los Alamos did not take into account the random thermal velocities, barely the distribution of the flow velocities of the fluid cells were evaluated. This resulted in sharp peaks in the sidewards direction. This sidewards flow effect was very dominant in the calculation but it was not obviously seen in experiments.

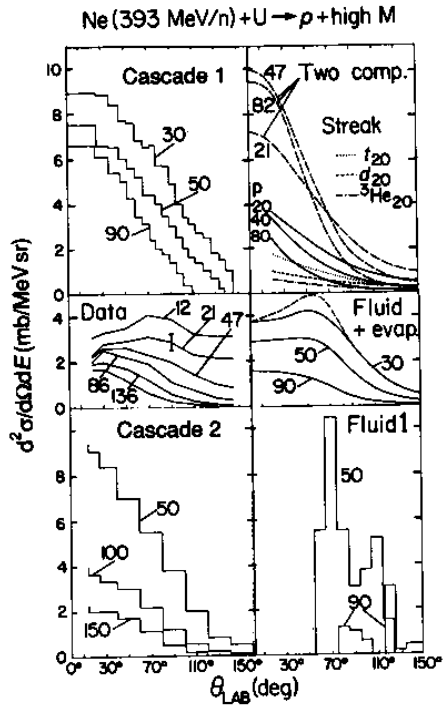

Figure 7.2: The angular dependence of double differential cross sections from experiment and from several theoretical calculations. Reproduced with permission from [15].

Later in Frankfurt the above described thermal distributions were also considered when the cross sections were evaluated, and this contributed to a considerable thermal smearing. In Fig. 7.2 (from ref. [15]) the results of the two calculations are compared

with experimental data and with the results of some Monte-Carlo cascade simulations. Bounce-off or side splash-effects occur only in fluid dynamical scenario. These lead to a peak in the cross section at finite polar angle, $\Theta \approx 30^0 - 60^0$. The reason is in the flow pattern of non-central collisions, Fig. 7.3 (from [16]).

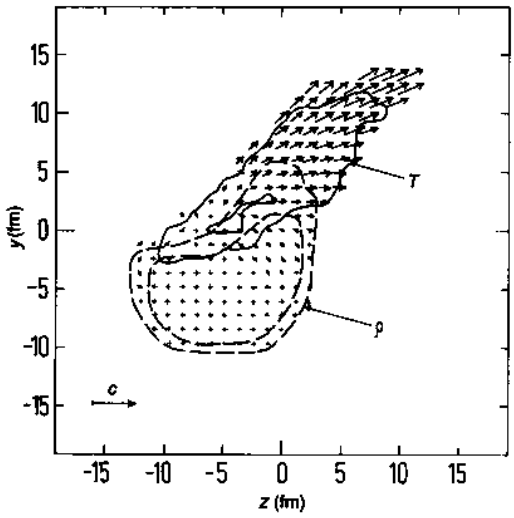

Figure 7.3: Density ($\rho = n$), temperature (T), and velocity (arrows) distributions in a relativistic heavy ion collision (Ne+U 393 MeV/N) in the laboratory system at the breakup moment (t=35 fm/c). The impact parameter of the collision is b=6 fm. The crosses indicate that the flow velocity is $v < 0.1c$. The full contour lines belong to temperatures T=10 and 20 MeV, the dashed ones to nucleon densities ρ =0.05 and 0.1 (1/fm^3). Reproduced with permission from [16].

7.5.1 Fragment emission at the end of the flow

We have discussed already in the chapter on the Equation of State that in an ideal mixture of different isotopes the concentration of all isotopes is determined by the common temperature and the baryon density (Law of mass action). One can have a rough estimate on the fragment production if this picture is used locally at the break-up. Then, in every fluid element the density, n_i, of an isotope, i, in terms of the proton and neutron densities and the temperature is

$$n_i(n_p, n_n, T) = a_i \; n_p^{Z_i} n_n^{N_i} \tag{7.25}$$

where

$$a_i = \lambda_T^{3A_i - 3} \; A_i^{3/2} \; 2^{-A_i} \; (2S_i + 1) \; \exp\left[\frac{E_0^{(i)}}{T}\right],$$

and

$$\lambda_T = \frac{h}{\sqrt{2\pi m_p \, T}}$$

is the thermal de Broglie wave length. The density of a given fragment i of charge Z_i and neutron number N_i ($A_i = N_i + Z_i$) depends on the common temperature T of the mixture, on the proton an neutron densities, and on the physical properties of fragment i, namely on the ground state energy $E_0^{(i)}$ ($E_o^{(i)} = 2.23, 8.49, 7.72$, and 28.3 MeV for i=d, t, ^{3}He, and ^{4}He, respectively) and spins S_i. The unknown parameters n_p, n_n, and T can be obtained from the conservation of local baryon number, charge, and energy:

$$\begin{aligned} n &= A_{cell}/V_{cell} = \sum_i n_i A_i \ , \\ n\frac{Z}{A} &= Z_{cell}/A_{cell} = \sum_i n_i Z_i \ , \\ e &= E_{cell}/V_{cell} = \sum_i n_i (m_i + \frac{3}{2}T) \ , \end{aligned} \tag{7.26}$$

where n is the baryon density in the fluid cell at the break-up moment and E_{cell} is the total internal energy of the fluid cell including binding energy and rest masses ($k_{Boltzmann} = 1$). For simplicity we use nonrelativistic approximations here.

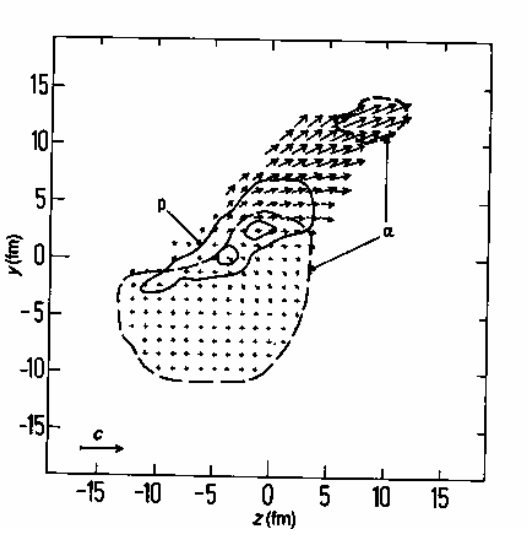

Figure 7.4: Proton (p) and alpha particle (α) density contour lines calculated for the breakup configuration shown in the previous Figure. The protons are formed in the middle of hot regions opposite to alphas which are formed at the sides. The contour lines belong to $n_\alpha = 0.005/fm^3$ and $n_p = 0.003$ and $0.006/fm^3$. Reproduced with permission from [16].

Once the partial densities and the equilibrium temperature are given, the thermal momentum distributions, $f_i^{cell}(\vec{p}, \vec{r})$ in the fluid cell at $\vec{r}$ can be written as

$$f_i^{cell} = \frac{n_i(\vec{r})}{[2\pi m_i T(\vec{r})]^{3/2}} \exp\left[- \frac{p^2}{2m_i T(\vec{r})} \right] \ . \tag{7.27}$$

Since the fluid is moving with the local collective velocity, $\vec{v}(\vec{r})$, these distributions should be transformed to the laboratory system by a Lorentz transformation. If we use a non-relativistic approximation this is barely a shift of the variable. The differential cross section of particle of type i is

$$\frac{d^3\sigma}{dP^3} = \int d^2b\ d^3r\ F_i^{Lab}(\vec{P},\vec{r}). \tag{7.28}$$

Assume that at the break-up not only nucleons, but also light composites exist (p, d, t, ...) in thermal and chemical equilibrium. The consequence is that light and heavy fragments are not formed at the same place, Fig. 7.4 (from [16]).

This typical flow pattern at the break up exhibits itself clearly in the triple differential cross section. Particularly if we plot the contour lines of the cross section in terms of momentum type variables in the reaction plane. We can use the rapidity, y, introduced earlier, and a variable which we can call transverse rapidity, $y_\perp \equiv p_\perp/m$, Fig. 7.5 (from [16]).

Since we have an asymmetric collision the cross section peaks at the rapidity of the heavier target, and there is a secondary peak at the rapidity position of the bounced off projectile. Although the projectile is completely destroyed the peak in the cross section is clearly observable especially for heavier emitted particles like t, ^{3}He, or α. The reason is three-fold:

(i) The temperature is lower at the periphery, i.e. around the deflected projectile rapidity, so mainly heavier particles are formed here,

(ii) The collective flow velocities are larger at the periphery, so the heavier fragments are more deflected from the collective c.m. rapidity,

(iii) The strong anisotropy shows up clearer in heavy fragments because their random thermal velocities are smaller at the same temperature.

The protons are light, their cross sections are smeared out due to large random thermal velocities, and they are originated from central areas of higher temperature. Thus the bounce off effect is less apparent for protons. This isotope effect, or "Fragment flow" (as it was called later) was predicted already in 1983 [16] and it was verified and clearly demonstrated later, around 1987-88 by several experiments.

The observable projectile peak's position may help us to trace down the collective kinematics of the collision. First, at a selected set of exclusive data of nearly the same impact parameter the bounce off, or deflection angle can be see in the cross sections. Due to global momentum conservation the target peak should show up on the other side of the reaction plane, so that the line connecting the target and projectile peaks should go through the nucleus nucleus center of mass. In the rapidity plane the target peak is much closer to this nucleus-nucleus c.m. than the projectile due to the much higher target mass. (In symmetric collision the two peaks would be placed symmetrically around the c.m.)

The deflection angle is close to zero in large impact parameter, so called "grazing" collisions and the deflection increases as the collision becomes more and more central.

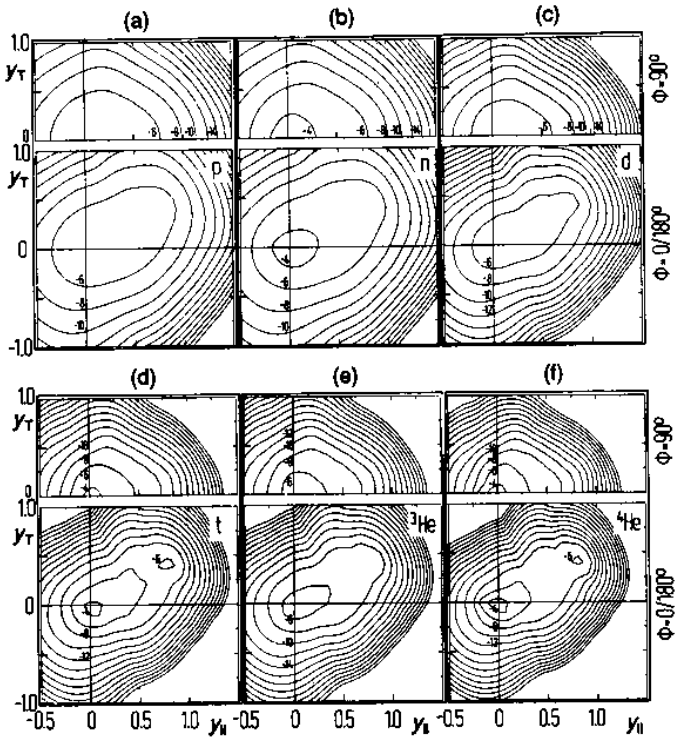

Figure 7.5: Contour plots of invariant triple differential invariant cross sections $(1/p)d^3N/dE\ d\phi\ d\cos\Theta$ for the reaction Ne(393 MeV/N)+ U at the impact parameter b=6 fm in the reaction plane ($\phi = 0^0/180^0$) and in the plane orthogonal to it ($\phi = 90^0$). The contour lines labeled by the parameter q correspond to a value of 10^q /(sr MeV^2). Parts (a), (b), (c), (d), (e), and (f) correspond to p, n, d, t, ^{3}He, and ^{4}He cross sections, respectively. The bounce-off effect is predominantly observable in t, ^{3}He, and ^{4}He spectra. Reproduced with permission from [16].

How large the deflection is at a given impact parameter depends on the stiffness of the nuclear EOS. By now the measurement of this deflection is one of the most sensitive measures of the incompressibility of the nuclear matter.

If the collision would be elastic the distance from the c.m. would be independent on the deflection angle (on the impact parameter), because the collective kinetic energy would be conserved in the collision. However, in reality as the collision becomes more and more central there is more and more thermal excitation, particle creation, etc., so that the collision becomes more and more inelastic. This shows up in the cross section in a way that the peak positions get closer and closer to the c.m. with increasing deflection (particularly the projectile peak). As we can see it in Fig. 7.6 (from [16]) the projectile peak position in collisions of impact parameter, $b = 9,\ 8,\ 7,\ 6,\ \ldots$ fm shows a momentum loss which gradually exceeds 30%.

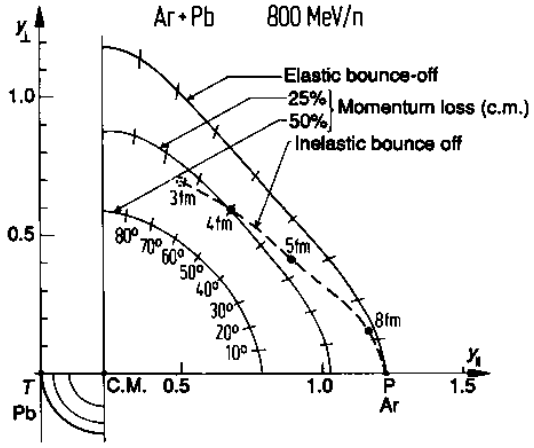

Figure 7.6: The dependence of the c.m. bounce-off deflection angle and inelasticity on the impact parameter b. At impact parameters smaller than 3 fm the second local maximum of the spectrum vanishes, and so, the inelasticity cannot be uniquely determined, but the bounce-off angle is measurable. Reproduced with permission from [16].

7.6 Global flow analysis

It was clear immediately that in relativistic heavy ion collisions the multiparticle correlations carry lots of information. One such dominant correlation is the final *collective flow* pattern.

Although the existence of collective flow, and shock waves was predicted already in 1973-74 by Scheid, Müller and Greiner [17], and by Chapline, Johnson, Teller and Weis [18] independently of each other, it took a long time till some consensus started to develop. Many physicists have debated even in 1982-83 the existence of collective nuclear flow effects in relativistic heavy ion collisions. The double differential cross sections did not provide sufficiently strong evidence to convince all researchers about the

existence of collective sidewards flow. New and new more sophisticated detectors were built and the analysis of data developed rapidly at the same time too. The breakthrough happened in 1984 with the so called Plastic Ball detector in Berkeley. This was a large array of close to 1000 detectors which could detect the simultaneous emission of several hundred emitted particles in one nuclear collision. This made it possible to identify the reaction plane on an event by event basis.

At this time, for the investigation of the possible collective properties several methods were introduced such as the sphericity tensor, energy flow tensor, and thrust analyzes. At the same time the first experimental studies with the plastic ball and with the streamer chamber were in progress. Theoretically it is straightforward to evaluate the real symmetric sphericity matrix in the c.m. frame:

$$M_{\alpha\beta} = \sum_i w_i p_{i\alpha} p_{i\beta} \ , \qquad \alpha = \beta = x, y, z \quad , \tag{7.29}$$

were i runs over all emitted charged particles (up to ^{4}He for the plastic ball experiments), and w_i is a weight factor which may depend on the type of particle i. In case of the "energy flow tensor" analysis $w_i = \frac{1}{2m_i}$. The eigenvalues Q_i and eigenvectors $\vec{e}_1,\ \vec{e}_2,\ \vec{e}_3$, of the tensor can be determined. If we normalize the sum of eigenvalues to unity so that $Q_3 \geq Q_2 \geq Q_1$, we can evaluate the commonly used quantities: sphericity $S = 1.5(Q_1 + Q_2)$, flatness $F = \sqrt{3}(Q_2 - Q_1)/2$, jet angle $\Theta_{c.m.} = \arccos\left([\vec{e}_3]_z/e_3\right)$, and aspect ratios $R_1 = Q_3/Q_1$ and $R_2 = Q_2/Q_1$. The vector $\vec{e}_3$ and the beam axis define the bf experimental reaction plane. After the reaction plane is determined the other important task is to study the distribution of the flow angle Θ (the angle between $\vec{e}_3$ and the beam axis, Fig. 7.7 (from [19]). The distribution of the flow angle in this manner is subject to very little experimental and statistical bias, so this was the first generally convincing evidence for the existence of collective flow.

When the reaction plane is identified the triple differential cross section can be evaluated from the measured data, Fig. 7.8 (from [20, 11]). Due to the asymmetry in the detector acceptance the experimental data are not forward-backward symmetric, but the sideward flow is still clearly observable in the data, especially for the heavier systems. The target peak is missing from the observed triple differential cross sections because of the low energy cut of the detector. The random cascade at this energy does not produce a collective azimuthal anticorrelation between the backward and forward directions.

In cascade and molecular dynamics models the evaluation of global flow parameters is done in the same way as in experiments, since these models create sample events that closely resemble the experimental event sample. The models, however, have direct primary information about the reaction plane. This way one can study the deviation between the principal (theoretical) and experimentally determined reaction plane. The agreement between the two reaction planes gets better with increasing multiplicity, and for high multiplicity events the deviation is in the order of 10 degrees only.

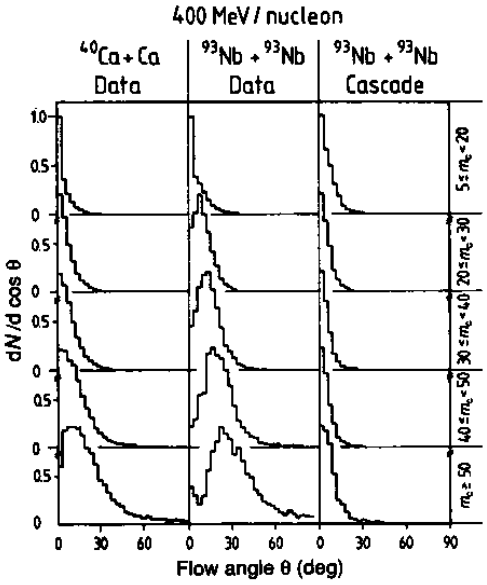

Figure 7.7: The observed and calculated distribution of the flow angle in collisions of different multiplicity. High multiplicity, central, collisions of heavy systems show a clear peak at finite angle, indicating the existence of the sideward flow. The ellipsoid of emitted particles is significantly not aligned with the beam axis. The cascade model does not reproduce this flow effect due to the absence of collective pressure or collective repulsion. Reproduced with permission from [11].

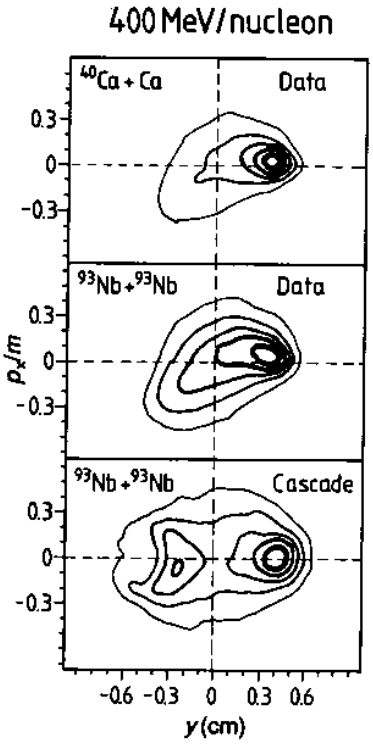

Figure 7.8: Charged particle triple differential cross sections projected to the reaction plane after the reaction plane was identified by the global flow analyzes. The experimental plots show the azimuthal anticorrelation while the cascade model does not. Thus a collective flow effect can be suspected in the data. Reproduced with permission from [11].

7.6.1 Global flow analysis in fluid dynamics

In a fluid dynamical type of model the summations in eq.(7.29) can be replaced by integrals over the continuous particle distributions:

$$M_{\alpha\beta} = \int d^3r \sum_{j-clust} w_j \quad \int d^3P^{c.m.} \; P^{c.m.}_{j\alpha} \; P^{c.m.}_{j\beta} \quad F^{c.m.}_i(\vec{P}^{c.m.}, \vec{r}) \; . \tag{7.30}$$

In a comparison of calculations with the experiments some difficulties arise. The limited sensitivity of the detector in momentum space, and the fact that most detectors do not cover a spherically symmetric region around the c.m. in the momentum space, cause serious problems. The sphericity matrix detected by a given detector is not equal to the one defined by eq. (7.30), but rather is given by

$$\langle M_{\alpha\beta} \rangle_b =$$

$$\frac{1}{2\pi b \; \Delta b^2} \int_{b-min}^{b-max} d^2b \int d^3r \sum_{j-clust} w_j \quad \int_{\mu_{det.}} d^3P^{c.m.} P^{c.m.}_{j\alpha} P^{c.m.}_{j\beta} \quad F^{c.m.}_i(\vec{P}^{c.m.}, \vec{r}) \; . \tag{7.31}$$

where $\mu_{det.}$ is the sensitivity region of the detector in the momentum space.

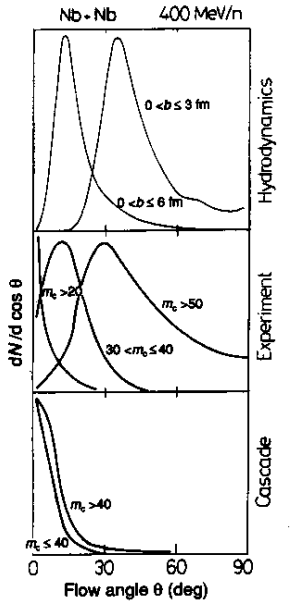

Figure 7.9: Observed and calculated distribution of the flow angle in collisions of different multiplicity. Experimental data are compared to calculations in the hydrodynamical model and in the cascade model. Reproduced with permission from [21].

After having calculated the flow tensor, one can calculate the reaction plane and the "flow angle" in the fluid dynamical model also, Fig. 7.9 (from [19, 22, 23]). The fluid dynamical model reproduces the flow angle distribution as expected. The effect is, however, stronger and sharper in the fluid dynamical model than in the data. This

indicates that the fluctuations are not barely the thermal fluctuations (which were included in the model), but the fluctuations arising from the finite multiplicity are also influencing the data. These fluctuations cannot be reproduced by a continuum model like fluid dynamics.

7.6.2 Decomposition of the global flow tensor

In the nonrelativistic approach there is a transparent way to separate the *thermal* and *collective flow* components in the global flow tensor. The problem is to calculate the energy flow tensor, $M_{\alpha\beta}$ in fluid dynamical approach by assuming Galilei transformation between cell and C.M. systems instead of Lorentz transformation. This approximation gives a nice analytic result and it is very useful also when one has to consider the available computer power for a given task.

Let us recall the definition of the collective flow tensor (7.29):

$$M_{\alpha\beta} = \sum_i w_i \; p_{i\alpha} p_{i\beta} \; , \qquad \alpha = \beta = x, y, z \quad . \tag{7.32}$$

Thus if the particle distribution is described by the function $f_{jH}^{cm}(\vec{p}, \vec{r})$ this leads to

$$M_{\alpha\beta} = \int d^3r \sum_{j-clust=p,d,t,..} w_j \quad \int d^3P^{c.m.} P_{j\alpha}^{c.m.} \; P_{j\beta}^{c.m.} \quad f_{jH}^{c.m.}(\vec{P}^{c.m.}, \vec{r}) \; . \tag{7.33}$$

Although $f_{jH}^{c.m.}(\vec{P}^{c.m.}, \vec{r})$ is known $\int d^3P^{c.m.}$... could be evaluated numerically only. This is an enormous task if you have to do it a few 10000 times (as many times as many fluid cells you have). Since

$$\int d^3r \; \int d^3P^{c.m.} \quad f_{jH}^{c.m.}(\vec{P}^{c.m.}, \vec{r}) \; =$$

$$\sum_{i-cell} N_j^{i-cell} = \sum_{i-cell} \int d^3P^{c.m.} \quad f_{jH}^{c.m.}(\vec{P}^{c.m.}, i-cell) \; , \tag{7.34}$$

we can calculate the contribution of one fluid cell. We assume that the flow and thermal momenta of a particle are additive (Galilei transformation).

$$\vec{P} = \vec{P}_{flow} + \vec{P}_{therm} \; . \tag{7.35}$$

Then the expectation value of the tensor, $M_{\alpha\beta}$, with weights, $w_j = 1$, for one particle species, j, and from one fluid cell, i, is $M_{\alpha\beta}^{j,\; i-cell}$

$$\left\langle M_{\alpha\beta}^{j,i-cell} \right\rangle = N_j^{i-cell} \left\langle P_\alpha P_\beta \right\rangle =$$

$$N_j^{i-cell} \left\{ \langle P_{\alpha,flow} P_{\beta,flow} \rangle + \langle P_{\alpha,therm} P_{\beta,therm} \rangle + \langle P_{\alpha,therm} P_{\beta,flow} \rangle + \langle P_{\alpha,flow} P_{\beta,therm} \rangle \right\} =$$

$$N_j^{i-cell} \left\{ P_{\alpha,flow} P_{\beta,flow} + \langle P_{\alpha,therm} P_{\beta,therm} \rangle + \langle P_{\alpha,therm} \rangle \, P_{\beta,flow} + P_{\alpha,flow} \, \langle P_{\beta,therm} \rangle \right\} \tag{7.36}$$

Since $\vec{P}_{therm}$ follows a symmetric distribution $\langle P_{\alpha,\ therm}\rangle = 0$, so that

$$\left\langle M_{\alpha\beta}^{j,\ i-cell}\right\rangle = N_j^{i-cell}\left\{P_{\alpha,\ flow}P_{\beta,\ flow} + \langle P_{\alpha,\ therm}P_{\beta,\ therm}\rangle\right\} \tag{7.37}$$

Since $f_{jH}^{c.m.}(\vec{P}^{c.m.}, i-cell)$ is a spherically symmetric distribution and $P_{\alpha,\ therm} = (\vec{e}_\alpha \vec{P}_{therm})$ where $\vec{e}_\alpha$ is a unit vector, it follows that

$$\langle P_{\alpha,therm}P_{\beta,therm}\rangle = \left(\vec{e}_\alpha\vec{P}_{therm}\right)\left(\vec{P}_{therm}\vec{e}_\beta\right) = \delta_{\alpha\beta}\left\langle(\vec{e}_\alpha\vec{P}_{therm})^2\right\rangle = \frac{\delta_{\alpha\beta}}{3}\left\langle(P_{therm})^2\right\rangle. \tag{7.38}$$

In the nonrelativistic limit $\varepsilon = \frac{e}{n} = \frac{p^2}{2m}$, thus $< p_{therm}^2 >= 2m_j\varepsilon_{therm}$. In the nonrelativistic Bolzmann limit $\langle P_{therm}^2\rangle = 2m_j(3/2)T = 3m_jT$.

Thus

$$\left\langle M_{\alpha\beta}^{j,\ i-cell}\right\rangle = N_j^{i-cell}\left\{(P_{\alpha,\ flow}^{i-cell}P_{\beta,\ flow}^{i-cell}) + \frac{\delta_{\alpha\beta}}{3}\left\langle P_{therm}^2\right\rangle\right\}. \tag{7.39}$$

The last term does not depend on the cell velocity and it yields a spherical contribution to the flow tensor even after the summation over all fluid cells.

$$\left\langle M_{\alpha\beta}^{j}\right\rangle = \sum_{i-cell} N_j^{i-cell}(P_{\alpha,\ flow}^{i-cell}P_{\beta,\ flow}^{i-cell}) + \frac{\delta_{\alpha\beta}}{3}\sum_{i-cell} N_j^{i-cell}\left\langle P_{therm}^2\right\rangle. \tag{7.40}$$

For the energy flow tensor, $w_j = 1/(2m_j)$, in the Boltzmann limit this yields

$$\left\langle M_{\alpha\beta}^{j}\right\rangle = \frac{1}{2}\left\{\sum_{i-cell} N_j^{i-cell}\left[m_j(v_{\alpha,\ flow}^{i-cell}v_{\beta,\ flow}^{i-cell}) + \delta_{\alpha\beta}T_{i-cell}\right]\right\}. \tag{7.41}$$

One can see in this form of expression that the nonspherical structure of the flow tensor (the non-diagonal part) is exclusively caused by the collective flow velocities, furthermore the heavier particles in a fluid cell contribute to stronger asymmetry!

So in fluid dynamical model the expectation value of the flow tensor, $M_{\alpha\beta}$, can be calculated easily. However, there are fluctuations around this expectation value in a real experiment! This is due to the finite multiplicity of the emitted particles. This finite multiplicity introduces an effective asymmetry in the thermal distribution also, so that in the real life the separation of thermal and collective flow terms is not trivially easy.

This was demonstrated in ref. [24] where instead of realistic hydrodynamics a simple model with 3 thermal particle emitting sources was assumed. These sources were moving with preassigned velocities like 3 large fluid cells (see fig. 7.10).

The impact parameter dependence of the flow angle, $\Theta_f(b)$, and inelasticity are assumed to have simple analytic forms which were extracted from 3 dimensional fluid dynamical calculations. In this simplified model, however, there are only 3 fluid cells!! In this model one could evaluate the flow tensor, its eigenvalues and the corresponding eigenvectors in two ways. First before the simulation of experimental events based on the thermo and fluid dynamical parameters, and then just the same way as in experiments after we have generated randomly emitted particles by an event generator

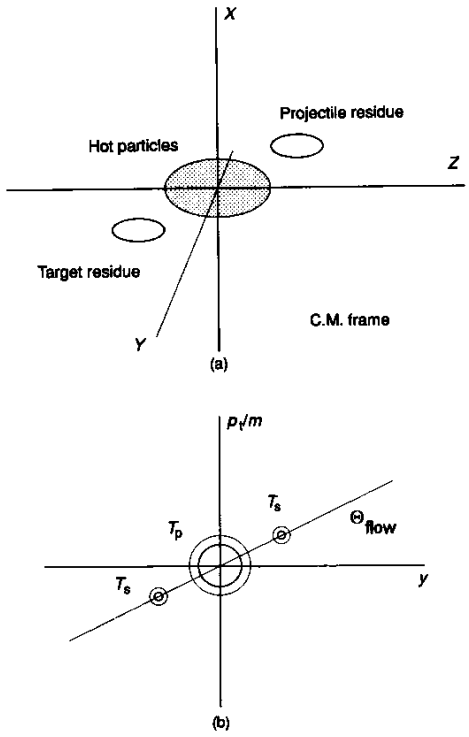

Figure 7.10: Three particle emitting sources simulating the final state of a heavy ion collision, depicted in the configuration and in the momentum space. There is a larger central source at rest in the center of mass frame with higher temperature, representing the hot spectator matter. On the sides there are two colder regions representing the less excited spectator matter with a velocity that has a sidewards pointing component. This sidewards motion (or sidewards flow) is caused by the high central pressure during the intermediate stages of the reaction. Thus the so called "flow angle" is finite due to this collective pressure. In the momentum space it is apparent that the spectators did suffer a highly inelastic collision because the absolute value of their velocities is less than the initial target and projectile velocity in the c.m. frame.

(FREESCO). Theoretical expectation values based on continuum thermo- and fluid dynamics and simulated experimental observables based on generating random events with evaporation of a finite number of particles are compared. Also, fragments are generated randomly according to thermal expectation values. Conservation laws are satisfied. The result of such a comparison is shown in Fig. 7.11 (from [24]).

The impact parameter dependence of the random scattering results are shown in Fig. 7.12 (from [24]).

One can see that the random fluctuations not only scatter around the fluid dynamical expectation, but there is an unmistakable shift: the aspect ratios are shifted from zero to finite values.

Danielewicz and Gyulassy [25] analyzed generally how the random fluctuations shift the expectation value of these observables. They generated random events of multiplicity, M, corresponding to the same fluid dynamical expectation values: $\Theta_{flow} = 0$, and $R_{1/3} \neq 0$. They concluded that the finite multiplicity shifts the observable average of these quantities as indicated in Fig. 7.13 (from [25]).

Thus the observed finite flow angle in itself is not a decisive proof of the existence of a transverse flow!.

Danielewicz and Gyulassy [25] analyzed also how the random fluctuations shift the expectation value of the observable flow angle if the original fluid dynamical expectation is not zero, $\Theta_{flow} \neq 0$. For multiplicity M=40 the observed flow angle was larger for small original angles and smaller when the original fluid dynamical expectation was close to $\Theta_{flow} = 90^o$. The observed flow angle tends to 57^o when the aspect ration tends to one. Fig. 7.14.

These finite multiplicity distortions seemed to make it extremely difficult to identify the transverse flow experimentally. Danielewicz and Gyulassy have succeeded, however, to find a quantity which showed a qualitative sign of the transverse flow. The quantity, which is able to show the real expectation value, is the distribution $dN/d\Theta_{flow}$ itself, i.e. the distribution function of the flow angles in the experimental event sample. While the average arising from this distribution function looses the information about the original flow angle, the distribution shows a peak at a finite Θ_{flow} in the presence of a transverse flow. If there is no inherent transverse flow present the distribution peaks at $\Theta_{flow} = 0$, but it can be a wide distribution yielding a large mean value, Fig. 7.15 (from [25]).

Actually these studies finally led in 1984 to a breakthrough and the experimental group around the "Plastic-Ball" detector system in Berkeley succeeded to identify the collective transverse flow beyond doubt for the first time in history after 10 years of persistent research and scientific debate. This latter method was used for high multiplicity $^{93}Nb + {}^{93}Nb$ reactions at 400 MeV projectile energy. The setup of the detector system is shown in Fig. 7.16.

The detector consisted of 655+160 Plastic Scintillator telescopes (The Plastic Ball) and 60 pairs of scintillator counters plus 36 single counters (The Plastic Wall), with the goal to identify as many emitted particles as possible. Of course the Plastic Ball or any detector has a certain range of sensitivity. The target is in vacuum, so low energy particles cannot penetrate the wall of the vacuum chamber. Thus the target peak cannot be seen on the rapidity distribution measured!! To avoid the inaccuracies

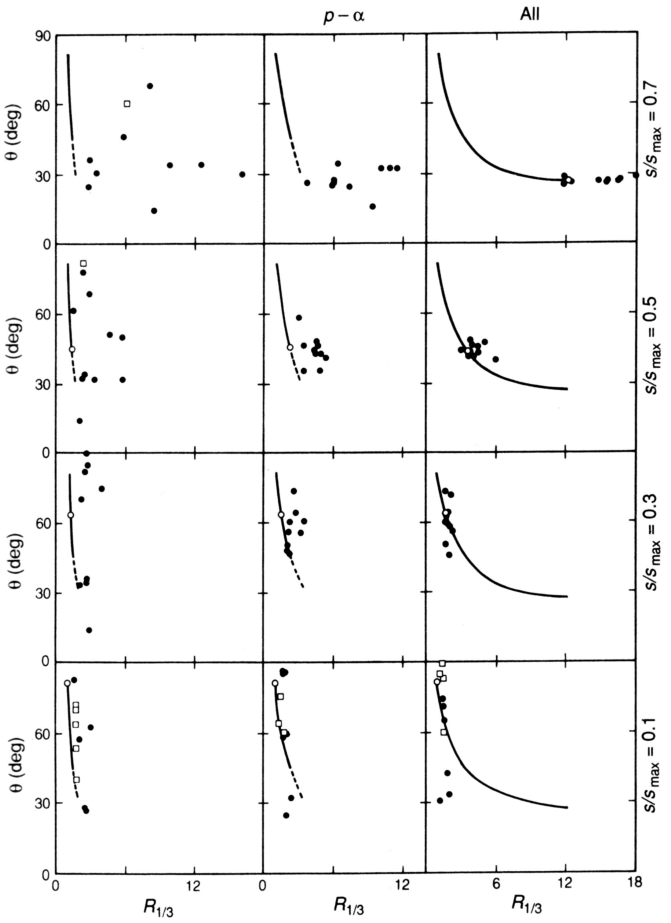

Figure 7.11: Fluid dynamical expectation values (full curves with open circles) and statistically generated events (dots and open squares) yielding flow diagrams: Flow angles versus the aspect ratio of the largest to the smallest eigenvalue of the flow tensor, $R_{1/3}$, for Nb+Nb reaction at 400 MeV/nucleon lab. beam energy. Four different impact parameters, $b = s = 0.1,\ 0.3,\ 0.5,\ 0.7s_{max}$, and 3 different particle species $j = p,\ p - \alpha,\ all$ are shown. At each impact parameter the whole fluid dynamical expectation curve is plotted for all impact parameters, the particular impact parameter of the actual case is indicated by an open circle. This fluid dynamical expectation value depends on the particle species, j. Reproduced by permission of Elsevier Science Publishing from [24].

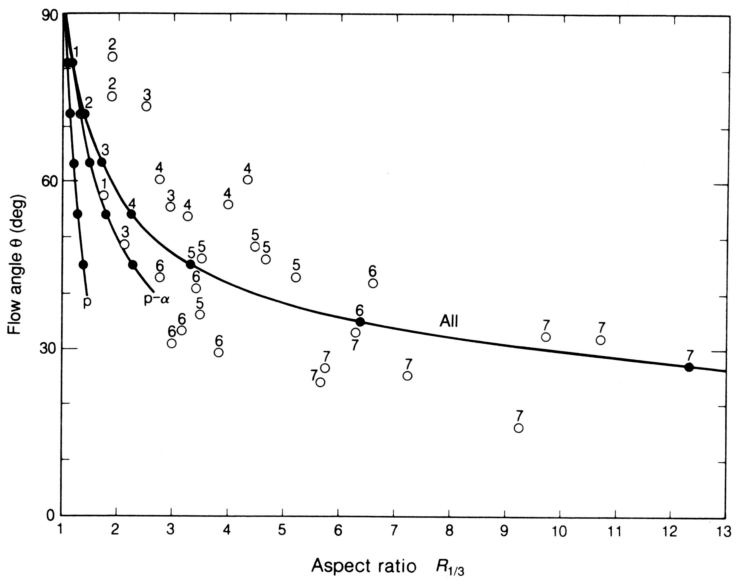

Figure 7.12: Fluid dynamical expectation values (full curves with dots) and statistically generated events (open circles) yielding flow diagrams: Flow angles versus the aspect ratio of the largest to the smallest eigenvalue of the flow tensor, $R_{1/3}$, for Nb+Nb reaction at 400 MeV/nucleon lab. beam energy. The parameters indicate the impact parameter in units of $10s/s_{max}$. The fluid dynamical expectation value depends on the particle species, p, $p-\alpha$, All. Reproduced by permission of Elsevier Science Publishing from [24].

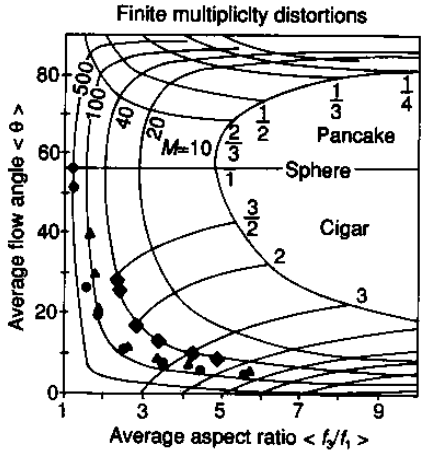

Figure 7.13: Expectation values (full curves) for a given finite multiplicity, M, and statistically generated events (dots and triangles) yielding flow diagrams: Flow angles versus the aspect ratio of the largest to the smallest eigenvalue of the flow tensor, $R_{1/3}$. The original fluid dynamical expectation value did not have any transverse flow in, $\Theta_{flow} = 0$. Reproduced by permission of Elsevier Science Publishing from [25].

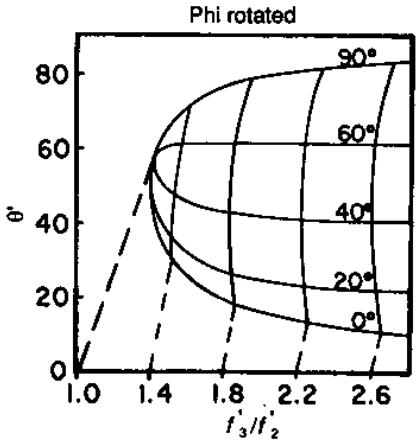

Figure 7.14: Expectation values of the observed flow angle Θ' (full curves) for multiplicity, $M = 40$, of flow diagrams when the original fluid dynamical distribution has the theoretical flow angle indicated by the parameters along the curves. Reproduced by permission of Elsevier Science Publishing from [25].

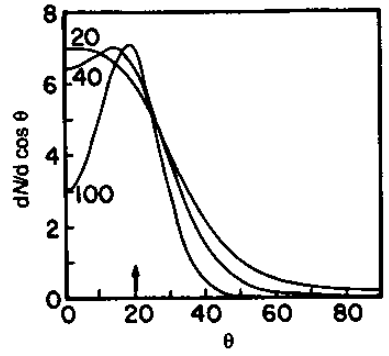

Figure 7.15: Expectation values of the observed flow angle distributions $dN_{event}/d\Theta_{flow}$ (full curves) for multiplicities, $M = 20,\ 40,\ 100$, when the original fluid dynamical flow angle is 20^o. Reproduced by permission of Elsevier Science Publishing from [25].

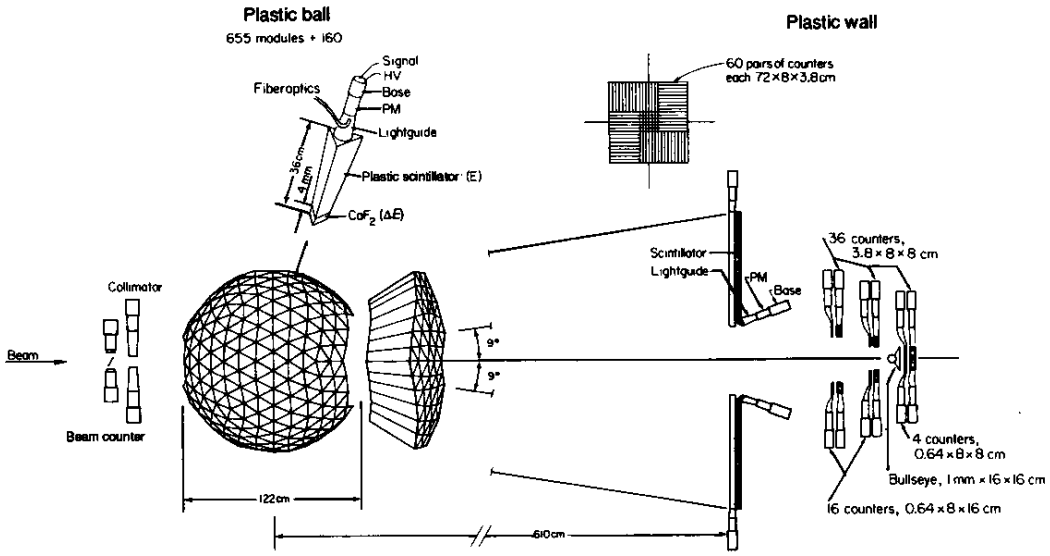

Figure 7.16: The "Plastic-Ball" detector.

the best is to study symmetric A+A collisions. In this case a symmetrization can be performed around the c.m. and the limited sensitivity range of the detector can be circumvented, Fig. 7.17.

The near to 4π detector sensitivity made it possible to perform event by event measurements, which was unheard of in conventional nuclear physics before. The great success of the detector created enormous response in 1984. The achievements were soon got publicity even in the New York Times. The Plastic Ball detector was used later extensively for many quantitative studies of the nuclear Equation of State. Three years later the Plastic Ball detector was transported to the CERN and it was used in the experimental set up of the WA-80 collaboration.

Immediately after the Plastic Ball the collective sidewards flow was detected by the other optical 4π detectors as well: by the streamer chamber and by nuclear emulsions. These latter detectors have a much smaller statistics, much less collisions can be quantitatively analyzed by them, so a mucl more sensitive statistical method was developed originally for streamer chamber by Danielewicz and Odyniecz [9]. This method became widely used and sort of a standard for measuring collective flow. It could even be used for nuclear emulsions, for a sample of few hundred collisions [27]. The method will be introduced in the next section.

7.7 Transverse Flow Analysis

The method we present here was introduced by Danielewicz and Odyniecz [9]. It became a widely used sensitive method to detect the collective transverse flow. It could be used in experiments where the available statistical sample is smaller than in the Plastic Ball:

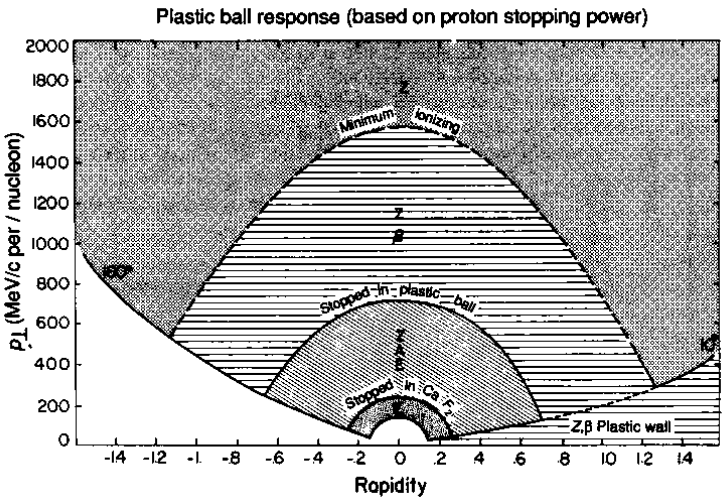

Figure 7.17: The sensitivity range of the "Plastic-Ball" detector in rapidity variables ($u_\perp = p_\perp/m$). From [26].

it was used in streamer chamber experiments and even in emulsion experiments [27].

The method essentially relies on the determination of the reaction plane, and then the transverse momenta of the emitted particles are projected (or rotated) to this reaction plane. The determination of the reaction plane is crucial in an experiment and it is possible only if the multiplicity, M, of the emitted particles is large and the major part of these particles are detected. The method involves two basic ideas: A) to select the rapidity range and rapidity dependent waiting factors in the center of mass system which provide the reaction plane closest to the real reaction plane, and B) to remove trivial and spurious self correlations from the projections.

7.7.1 Determination of the reaction plane (A)

The reaction plane is defined by the transverse vector $\vec{Q}$:

$$\vec{Q} = \sum_{\nu=1}^{M} w_\nu \ \vec{p}_{\perp\nu} \tag{7.42}$$

where the weight factor, w_ν, depends on the rapidity of the emitted particle, ν, so that the central rapidity region, where the particle emission is azimuthally symmetric, is omitted, and the forward and backward rapidity regions get weights with opposite signs. This choice leads to the result that the forward and backward moving particles, —which are azimuthally anticorrelated if there is a collective transverse flow,— will contribute equally to $\vec{Q}$.

$$w_\nu = \begin{cases} +1 & : if y > y_c \\ 0 & : if -y_c < y < y_c \\ -1 & : if y < -y_c \end{cases} . \tag{7.43}$$

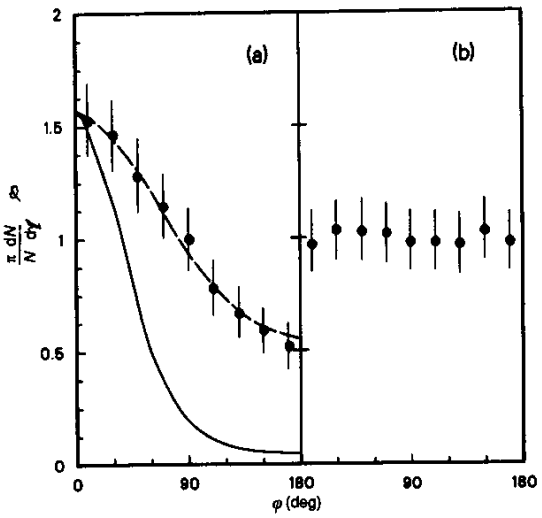

Figure 7.18: The distribution of the azimuthal angle difference, φ, of the two half events (a) from an experimental sample of 1.8 A GeV Ar+KCl reactions measured in a streamer chamber and (b) from artificially created events by mixing up particles from the events of the real sample. Reproduced by permission of Elsevier Science Publishing from [9].

where the cut-off rapidity, y_c, is usually chosen to be $y_c \approx 0.3 y_c^{beam}$. Later this weight factor was modified by other researchers to $w_\nu(y) = Const. \times y$ or to

$$w_\nu(y) = \begin{cases} Cy & : if y > y_c \\ 0 & : if -y_c < y < y_c \\ Cy & : if y < -y_c \end{cases} . \tag{7.44}$$

The constants were determined by trial and error. For this one has to decide if the determined reaction plane is accurate or not. This can be done the following way.

Test of the reaction plane

Let us take one event with multiplicity, M, and separate it randomly into two halves: I and II. Each of them will have multiplicity M/2 (if M was even). We can now evaluate the reaction plane vector in both half events separately, getting $\vec{Q}_I$ and $\vec{Q}_{II}$. The two vectors should not be identical, but they should be close to each other if there was a real physical reaction plane in the underlying physical event. The azimuth angle difference between the two $\vec{Q}$-vectors is then $\Delta\varphi$. Then we should plot the distribution of this $\Delta\varphi$ for the whole experimental sample. If there is a reaction plane and the weighting was lucky we will get a distribution which peaks sharply around $\Delta\varphi = 0$. An example for such a distribution is shown in Fig. 7.18 taken from ref. [9].

The spread of the distribution depends also on the cut, y_c and on the weight factors. These factors and y_c should be chosen to minimize the spread of the distribution.

7.7.2 Self correlations (B)

Let us see what happens if we now project the transverse momenta of each particle on this plane. The plane is defined by

$$\vec{Q} = \sum_{\mu=1}^{M} w_\mu \vec{p}_{\perp\mu}$$

then the projection of a particle's, (ν's), transverse momentum to this plane is

$$p_\nu^{x'} = \vec{p}_{\perp\nu} \frac{\vec{Q}}{|\vec{Q}|}, \tag{7.45}$$

which can be expanded as

$$p_\nu^{x'} = \vec{p}_{\perp\nu} \frac{\sum_{\mu=1}^{M} w_\mu \vec{p}_{\perp\mu}}{|\vec{Q}|} = \frac{w_\nu \vec{p}_{\perp\nu}^{\,2} + \sum_{\mu\neq\nu} w_\mu (\vec{p}_{\perp\nu}\vec{p}_{\perp\mu})}{|\vec{Q}|}. \tag{7.46}$$

If there was no collective correlation

$$\left\langle p_\nu^{x'} \right\rangle |_{y,y+\Delta y} = \frac{1}{<|\vec{Q}|>} \left[w_\nu \left\langle \vec{p}_{\perp\nu}^{\,2} \right\rangle + \left\langle \sum_{\mu\neq\nu} w_\mu (\vec{p}_{\perp\nu}\vec{p}_{\perp\mu}) \right\rangle \right], \tag{7.47}$$

the expectation value in the second term would vanish $< \vec{p}_{\perp\nu}\vec{p}_{\perp\mu} >= 0$ due to symmetry reasons, but the first term would not since $\vec{p}_{\perp\nu}^{\,2} \geq 0$. Thus this definition would yield a finite $< p_\nu^{x'} > |_{y,y+\Delta y}$ even if there are no real collective correlations in the sample. An example for this is shown in Fig. 7.19 where the real sample shows a clear anticorrelation between the forward and backward moving particles (a). But, if we take the emitted particles from all events in the experimental sample and mix them randomly to form an artificial sample where the real physical correlations should be lost, the p^x/a plot still shows a clear azimuthal anticorrelation due to the self correlation effect (b).

We can remove these self correlations by removing the first term in expression (7.47). This can be done if we project each particle's transverse momentum to a reaction plane determined by all other particles:

$$\vec{Q}_\nu = \sum_{\mu\neq\nu} w_\mu \vec{p}_{\perp\mu}. \tag{7.48}$$

Now the projection does not contain the self correlation term

$$p_\nu^{x'} = \frac{1}{<|\vec{Q}|>} \sum_{\mu\neq 1} w_\mu (\vec{p}_{\perp\nu}\vec{p}_{\perp\mu}). \tag{7.49}$$

Thus $p_\nu^{x'}$ is nonzero only if real physical correlations exist.

Fig. 7.20 shows that after removing the self correlation from $\vec{p}_{\perp\nu}\vec{Q}$ the real sample still shows the azimuthal anticorrealtion (a), while the artificial sample shows no effect (b).

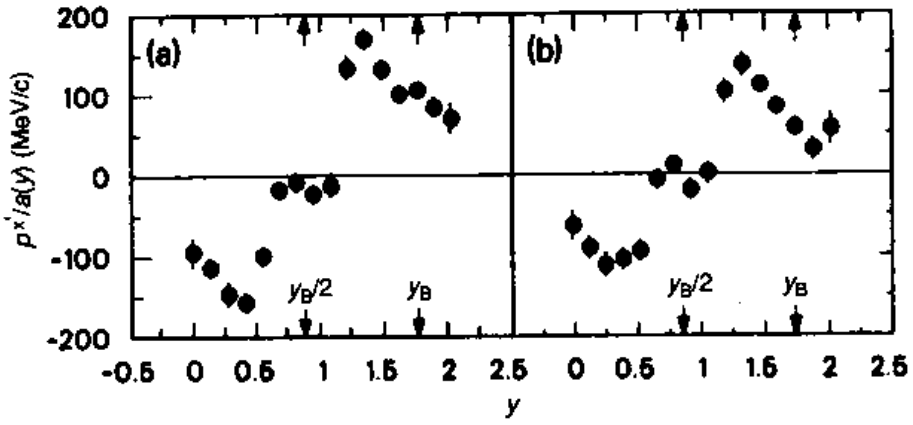

Figure 7.19: Comparison of $p^{x'}/a$ plots of a real physical sample (a) and on a randomized artificial sample (b). Due to the self correlation azimuthal anticorrelation appears between forward and backward moving particles in both cases. Reproduced by permission of Elsevier Science Publishing from [9].

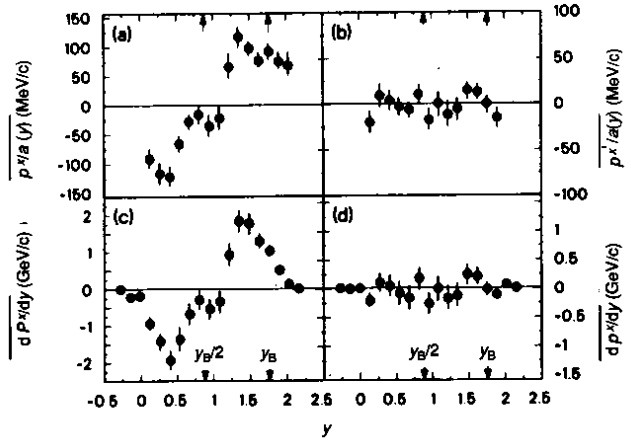

Figure 7.20: Comparison of $p^{x'}/a$ and dP^x/dy plots of a real physical sample (a) and on a randomized artificial sample (b). Due to the removed self correlation azimuthal anticorrelation appears between forward and backward moving particles only for the real physical sample (a). Reproduced by permission of Elsevier Science Publishing from [9].

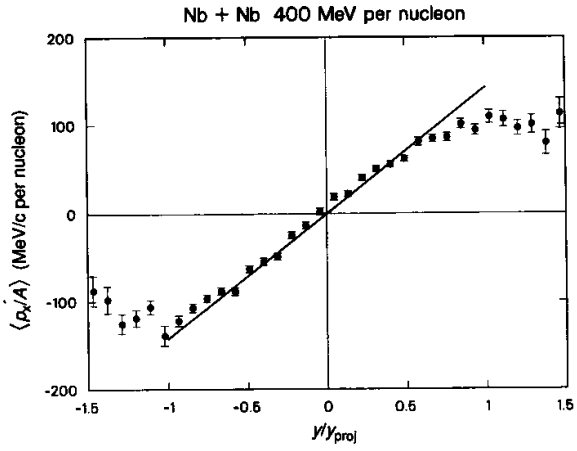

Figure 7.21: Mean transverse momentum per nucleon projected into the reaction plane as a function of the normalized center-of-mass rapidity for 400 MeV per nucleon Nb+Nb in the multiplicity bin, between 50% and 75% of N_p^{max}. The slope of the solid line represents the "flow", F, obtained from fitting the data. Reproduced by permission of Elsevier Science Publishing from [19].

The quantity $p^{x'}/a$ underestimates the transverse momentum because the vector $\vec{Q}_\nu$ fluctuates around the real reaction plane by some azimuthal dispersion angle, $\Delta\varphi$. If we would know this real reaction plane we could estimate the value of p^x projected to the real plane as:

$$< p^{x'} >=< p^x >< \cos\Delta\varphi > .$$

In experiments $\Delta\varphi$ is approximated by the width of the distribution of the azimuthal angle difference between the two reaction planes evaluated from each event in the sample as indicated Figs. 7.18 and 7.18.

A practical definition was introduced by the Plastic Ball team later, the "Flow", F, to measure the transverse momentum transfer:

$$F = \frac{\partial[p^x/a]}{\partial y} \mid_{y=0} .$$

This quantity was subject to less experimental bias then for example the maximum of p^x/a, and it enabled us to compare different reactions and results of different experimental devices to each other, Fig. 7.21.

7.8 Assignment 7

7.a Calculate the double differential cross section by boosting the local Jüttner (relativistic Boltzmann) distribution spherically by a collective flow velocity. (See the Blast-Wave Model of ref. [14].)

7.b Calculate the $p^x(y)$ distribution of nucleons (i.e., the average transverse momentum of particles at rapidity y projected to the reaction plane) if you have 3 thermal

particle emitting sources, described by the non-relativistic Boltzmann distributions. Two of the 3 sources are moving, one forward and one backward in the c.m. frame. These two have opposite transverse flow velocities. The third source is at rest in the c.m. frame. Use Galilei transformation instead of Lorentz transformation.

7.8.1 Solutions to Assignment 7

7.a *Blast wave model* Let us follow the procedure introduced in sect. 7.4. The thermal kinetic energy w of the particle of a given Θ flow polar angle in terms of the observed c.m. variables $\vec{P}, E$ is:

$$w = \gamma(E - \beta^r P \cos\Theta) \ ,$$

where β^r is the radial flow velocity of the expanding spherical layer, and γ is the corresponding gamma factor. Consequently

$$dw = -\gamma\beta^r P \, d\cos Q \ .$$

Now the c.m. momentum distribution can be calculated by summing up the contributions from all flow polar angles

$$f^{cm}(\vec{P}) = \int_0^\pi \frac{w}{E} f^{cell}(\vec{r}) \ 2\pi(-d\cos\Theta) = \\ -\frac{2\pi}{E} \ \frac{1}{\gamma\beta^r \ P} \left(\int_{\gamma(E+\beta^r P)=x_1}^{\gamma(E-\beta^r P)=x_2} w \ f^{cell}(\vec{p}) \ dw \right) \quad (7.50)$$

and by assuming that the cell's momentum distribution in its proper frame a Maxwell–Boltzmann distribution:

$$-\frac{2\pi}{E} \ \frac{1}{\gamma\beta^r\sqrt{E^2-m^2}} \ \frac{4}{(2\pi\hbar)^3} \ \int_{x_1}^{x_2} \frac{x \ dx}{\exp\left[\frac{x-\mu}{T}\right]} = \\ \underbrace{-\frac{2\pi}{E} \ \frac{e^{\frac{\mu}{T}}}{\gamma\beta^r\sqrt{E^2-m^2}} \ \frac{4}{(2\pi\hbar)^3}}_{c} \int_{x_1}^{x_2} \frac{x}{e^{-\frac{x}{T}}} \ dx = \\ -cT^2 \left\{ e^{-x_2/T}(-\frac{x_2}{T} - 1) + e^{-x_1/T}(\frac{x_1}{T} + 1) \right\}$$

Introducing now $\alpha \equiv \gamma\beta^r P/T$ the expression takes the form

$$= c \exp\left(\frac{-\gamma E}{T}\right) \left[\left(\gamma E T + T^2\right) \sinh\alpha - \alpha T^2 \cosh\alpha \right] \ .$$

Thus, finally we get the energy spectrum of the Blast-wave model [14]

$$\frac{dN}{d^3P} = \frac{8\pi e^{\mu/T}}{(2\pi\hbar)^3} \exp\left(\frac{-\gamma E}{T}\right) \left[\left(\gamma + \frac{T}{E}\right) \frac{\sinh\alpha}{\alpha} - \frac{T}{E}\cosh\alpha \right] \ .$$

7.b Let us take a 3 sources: one at c.m. (C) and two symmetrically deflected side (S) sources, with masses A_c, A_s, A_s and temperatures $T_c T_s, T_s$ respectively.

The "s" sources have collective momenta per nucleon: $\vec{p}_s = (p_T, 0, p_L)$ and $-\vec{p}$ where x, z is the reaction plane and z is the beam axis. The transverse momentum projected to the reaction plane can be evaluated by using:

$$< \frac{p^x}{a} >= \frac{\int d^3r \; d^3p \;\; n(r,t) \; f(\vec{p},\vec{r})(\vec{pe}) \mid_{y=y_0}}{A|_{y=y_0}}, \tag{7.51}$$

where $\vec{e}$ is a unit vector in the reaction plane.

Let us assume that we have one central source, c, and two identical side or spectator sources, s. Then the energy and mass conservation in this system yields

$$\begin{aligned} A &= \sum_s A_s = 2A_s + A_c, \\ E_0 &= \left[2A_s \left(\frac{1}{2} m \; u^2(s) + \frac{3}{2} T_s\right) + A_c \frac{3}{2} T_c\right] /A, \end{aligned} \tag{7.52}$$

where

$$\vec{u}(s) = u_\parallel + u_\perp \tag{7.53}$$

Now let us calculate the transverse momentum at $y = y_0$:

$$p^x(y) = N \int d^2p_\perp \; p_x \left[\exp[-\frac{(\vec{p}-\vec{p}_s)^2}{2mT}] + \exp[-\frac{(\vec{p}+\vec{p}_s)^2}{2mT}]\right]\Bigg|_{\text{at } p_\parallel = m_\perp \cosh y_0} \tag{7.54}$$

where N is a normalization constant. The center source does not contribute to p^x because $\vec{p}_c = 0$. Expanding the integrals:

$$p^x(y) = N \left[e^{-\frac{(p_z - p_{sz})^2}{2mT}} \int_{-\infty}^{+\infty} dp_x \; dp_y \; p_x \; e^{-\frac{\left[(p_x - p_{sx})^2 + p_y^2\right]}{2mT}} + \right.$$

$$\left. e^{-\frac{(p_z + p_{sz})^2}{2mT}} \int_{-\infty}^{+\infty} dp_x \; dp_y \; p_x \; e^{-\frac{\left[(p_x + p_{sx})^2 + p_y^2\right]}{2mT}} \right]. \tag{7.55}$$

Performing the integrals:

$$p^x(y) = \frac{A_s}{(2\pi m T_s)^{1/2}} p_{sx} \left[e^{-\frac{(p_z - p_{sz})^2}{2mT_s}} - e^{-\frac{(p_z + p_{sx})^2}{2mT_s}} \right]. \tag{7.56}$$

Here p_z is a function of the rapidity y. Since $y \cong v_z = \frac{1}{m} p_z$ it follows $\rightarrow \; p_z \cong my$. The total number of nucleons $A|_{y=y_0}$ is:

$$A|_{y=y_0} = \frac{A_s}{(2\pi m T_s)^{3/2}} \int d^2p_\perp \left[e^{-\frac{(\vec{p}-\vec{p}_s)}{2mT_s}} + e^{-\frac{(\vec{p}+\vec{p}_s)}{2mT_s}} \right] \; + \; \frac{A_c}{(2\pi m T_c)^{3/2}} \int d^2p_\perp e^{-\frac{\vec{p}^2}{2mT_c}}, \tag{7.57}$$

and after the integration

$$A|_{y=y_0} = \frac{A_s}{(2\pi m T_s)^{3/2}} \left[e^{-\frac{(p_z - p_{sz})^2}{2mT_s}} + e^{-\frac{(p_z + p_{sx})^2}{2mT_s}} \right] + \frac{A_c}{(2\pi m T_c)^{3/2}} e^{-\frac{p_z^2}{2mT_c}}, \quad (7.58)$$

consequently the transverse momentum per nucleon in the three sourcr model is:

$$\frac{p^x(y)}{a} = \frac{\frac{A_s}{(2\pi m T_s)^{1/2}} p_{sx} \left[e^{-\frac{(p_z - p_{sz})^2}{2mT_s}} - e^{-\frac{(p_z + p_{sx})^2}{2mT_s}} \right]}{\frac{A_s}{(2\pi m T_s)^{3/2}} \left[e^{-\frac{(p_z - p_{sz})^2}{2mT_s}} + e^{-\frac{(p_z + p_{sx})^2}{2mT_s}} \right] + \frac{A_c}{(2\pi m T_c)^{3/2}} e^{-\frac{p_z^2}{2mT_c}}}, \quad (7.59)$$

Bibliography

[1] H.W. Barz, L.P. Csernai and W. Greiner, Phys. Rev. **C26** (1982) 740.

[2] G.A. Milekhin, Trudy FIAN **16** (1961) 51.

[3] F. Cooper and G. Frye, Phys. Rev. **D 10** (1974) 186.

[4] J.-P. Blaizot and J.-Y. Ollitraut, in "Quark-Gluon Plasma" ed. by R.C. Hwa (World Scientific, 1990) p. 393.

[5] U. Heinz, K.S. Lee and E. Schnedermann, in "Quark-Gluon Plasm" ed. by R.C. Hwa (World Scientific, 1990) p. 471.

[6] M.I. Gorenstein, Univ. of Frankfurt preprint, UFTP 251/1990.

[7] P. Levai, G. Papp, E. Staubo, A. Holme, D. Strottman and L.P. Csernai, in Proc. of the Int. Workshop on Gross Properties of Nuclei and Nuclear Excitations XVIII, Hirschegg, Austria, Jan. 15-20, 1990 (TH Darmstadt, 1990) p. 90.

[8] E.F. Staubo, A.K. Holme, L.P. Csernai, M. Gong and D. Strottman, Phys. Lett. **B229** (1989) 351.

[9] P. Danielewicz and G. Odyniecz, Phys. Lett. **157B** (1985) 146.

[10] V.D. Toneev and K.K. Gudima, Nucl. Phys. **A400** (1983) 173c.

[11] H.Å. Gustafsson, H.H. Gutbrod, B. Kolb, H. Lohner, B. Ludewigt, A.M. Poskanzer, T. Renner, H. Riedesel, H.G. Ritter, A. Warwick, F. Weik and H. Wieman, Phys. Rev. Lett. **52** (1984) 1590.

[12] L.P. Csernai and H.W. Barz, Z. Phys. **A296** (1980) 173.

[13] P. Danielewicz, Nucl. Phys. **A314** (1979) 465.

[14] P.J. Siemens and J. Rasmussen, Phys. Rev. Lett. **42** (1979) 880.

[15] H. Stöcker, C. Riedel, Y. Yariv, L.P. Csernai, G. Buchwald, G. Graebner, J. Maruhn, W. Greiner, K. Frankel, M. Gyulassy, B. Schürmann, G. Westfall, J.D. Stevenson, J.R. Nix, D. Strottmann, Phys. Rev. Lett. **47** (1981) 1807.

[16] L.P. Csernai, H. Stöcker, P.R. Subramanian, G. Graebner, A. Rosenhauer, G. Buchwald, J.A. Maruhn and W. Greiner, Phys. Rev. **C28** (1983) 2001.

[17] W. Scheid, H. Müller and W. Greiner, Phys. Rev. Lett. **32** (1974) 741.

[18] G.F. Chapline, M.H. Johnson, E. Teller and M.S. Weiss, Phys. Rev. **D8** (1973) 4302.

[19] H.G. Ritter, Nucl. Phys., **A447** (1985) 3c.

[20] H.G. Ritter, et al., Proc. Int. Conf. Balaton, Hungary (1983).

[21] G. Buchwald, G. Graebner, J. Theis, J. Maruhn, W. Greiner, and H. Stöcker, Phys. Rev. Lett. **52** (1984) 1594.

[22] H.H. Gutbrod, H. Lohner, A.M. Poskanzer, T. Renner, H. Riedesel, H.G. Ritter, A. Warwick, F. Weik and H. Wieman, Phys. Lett. **127B** (1983) 317.

[23] R. Stock, *et al.*, Phys. Rev. Lett. **52** (1984) 18.

[24] L.P. Csernai, G. Fai and J. Randrup, Phys. Lett. **140B** (1984) 149.

[25] P. Danielewicz and M. Gyulassy, Phys. Lett. **129B** (1983) 283.

[26] H.G. Ritter, *et al.*, in Proc. of the 6th High Energy Heavy Ion Study, Berkeley, June 28 - July 1, 1983 (LBL-16281, Berkeley 1981) p. 191.

[27] L.P. Csernai, P. Freier, J. Mevissen, H. Nguyen, and L. Waters, Phys. Rev. **C34** (1986) 1270.

Chapter 8

Scaling of the hydrodynamical model

In heavy ion physics scaling is understood in two different ways. At ultra-relativistic energies, scaling solution, or scaling fluid dynamics is frequently mentioned. These refer to the basic assumption of the Bjorken model, i.e., that the observables and thus the dynamics is invariant against a beam directed Lorentz boost. This is, of course only an approximation, which can be applied in the mid rapidity region. This scaling is discussed under the Bjorken model. A related scaling is the Feynman scaling, describing the universality of parton momentum distributions in terms of the Feynman x variable. This is mentioned briefly in the chapter on the search for quark gluon plasma (Chapter 10).

The other meaning of scaling is the way measurable quantities at different target and projectile masses and at different beam energies are compared to each other. These comparisons result in the definition of secondary variables which are invariant under the change of beam energy or the mass of the system. These invariances are of course model dependent and not necessarily exact. If scaling properties of a theoretical approach are confirmed by experiments this indicates that the approach is basically a valid approach. On the other hand it does not exclude other theoretical approaches which yield the same or similar scaling rules. In this chapter we will discuss this latter version of scaling.

8.1 Similarity in classical fluid dynamics

This section is based on ref. [1]. The basic equations for a perfect non-relativistic fluid-dynamical description of a nuclear collision are the continuity equation:

$$\frac{\partial \rho}{\partial t} + \nabla(\rho \mathbf{u}) = 0, \tag{8.1}$$

which relates the mass distribution $\rho(\mathbf{r}, t)$ and the velocity distribution $\mathbf{u}(\mathbf{r}, t)$; the Euler equation:

$$\frac{\partial \mathbf{u}}{\partial t} + (\mathbf{u}\nabla)\mathbf{u} = -\frac{1}{\rho}\nabla P, \tag{8.2}$$

and the equation of state (EOS), which relates, the pressure P to the density p, and the entropy density, $s = S/V$, of the system:

$$P = P(\rho, s) \ . \tag{8.3}$$

For a non-viscous fluid the entropy is constant during the expansion, therefore

$$\nabla P \approx \left(\frac{\partial P}{\partial \rho}\right)_s \nabla\rho = c_s^2 \nabla\rho, \tag{8.4}$$

where c_s is the adiabatic sound velocity. The above equations with the initial conditions on $\mathbf{u}$, ρ, and s, determine the hydrodynamical evolution of the system. In ref. [1] dimensionless, scale-invariant quantities were derived to describe the general properties of a system, and also to compare the hydrodynamical behavior of systems of different masses and energies.

A characteristic mass, m_1, temperature T_1, length l_1, and velocity u_1 can be introduced in a heavy ion collision as:

$$m_1 = mA, \tag{8.5}$$

where m is the nucleon mass and A is the number of nucleons in the system;

$$u_1 = |\mathbf{u}_0| = \left(\frac{2E_0}{m}\right)^{\frac{1}{2}}, \tag{8.6}$$

where E_0 is the initial c.m. energy per nucleon of the projectile; and

$$l_1^3 = \frac{4}{3}\pi r_0^3 \; A, \tag{8.7}$$

which represents the volume of the system.

After introducing the definitions $\mathbf{r} = l_1\tilde{r}$ for the radius, $t = t_1\tilde{t}$ for the time, and $T = T_1\tilde{T}$ for the temperature (where $T_1 = 2/3 \; E_0$), the above characteristic quantities can be utilized to define dimensionless quantities, denoted by a tilde:

$$\rho(\mathbf{r}, t) = \frac{m_1}{l_1^3}\tilde{\rho}(\tilde{r}, \tilde{t}), \tag{8.8}$$

$$\mathbf{u}(\mathbf{r}, t) = u_1\tilde{u}(\tilde{r}, \tilde{t}). \tag{8.9}$$

These characteristic dimensionless hydrodynamical functions are independent of the total mass, A, and energy, E_0, of the system.

Now, since the sound velocity is of the same order as the thermal velocity of the nucleons, $c = u_1\tilde{c}$, with $\tilde{c} \approx 1$, the continuity and Euler's equations can be rewritten in dimensionless form:

$$m_1\left[\frac{\partial\tilde{\rho}}{\partial\tilde{t}} + S\tilde{\nabla}(\tilde{\rho}\tilde{u})\right] = 0, \tag{8.10}$$

$$\frac{\partial\tilde{u}}{\partial\tilde{t}} + S(\tilde{u}\tilde{\nabla})\tilde{u} = -S\tilde{c}^2\frac{\tilde{\nabla}\tilde{\rho}}{\tilde{\rho}}, \tag{8.11}$$

where $S = u_1 t_1/l_1$ is the Strouhal number.

In a small system, such as the one formed in a nuclear collision, the role of viscosity should not be neglected. Assuming that the coefficient of bulk viscosity, ξ, is proportional to the shear viscosity, η, ($\xi = q\eta$, where q is a dimensionless constant) and that the

kinematic viscosity, $\nu = \eta/\rho$, is constant during the expansion, the Navier–Stokes equation can be written (again in dimensionless form) as:

$$\frac{\partial \tilde{u}}{\partial \tilde{t}} + S(\tilde{u}\tilde{\nabla})\tilde{u} = -S\tilde{c}^2\frac{\tilde{\nabla}\tilde{\rho}}{\tilde{\rho}} - \frac{S}{Re}\left[\tilde{\Delta}\tilde{u} + (q+1/3)\tilde{\nabla}(\tilde{\nabla}\tilde{u})\right], \tag{8.12}$$

where Re is the Reynolds number: $Re = l_1 u_1/\nu$. With a proper choice of the time scale, $t_1 = l_1/u_1$, S can be set equal to 1. Then the solutions of the hydrodynamical equations depend on $\tilde{r}$, $\tilde{t}$, and the Reynolds number, Re, only. In this way, the flow patterns of systems of different energies and of different masses are similar if the Reynolds number, $\tilde{r}$ and $\tilde{t}$ are the same.

According to this picture, scale-invariant quantities can be defined, and a deviation from the scale invariance indicates the onset of physical processes which lead to a non-scale-invariant flow in the hydrodynamical description, such as viscosity, a change in the equation of state or in the reaction mechanism.

8.1.1 Application to heavy ion collisions

Let us now assume a non-relativistic perfect flow and study the expansion stage of the reaction. The intermediate most compressed state of the collision should be taken as the initial condition.

Let $\rho(\vec{r}, t)$ be the mass density, in an $A_P + A_T = A$ collision. The normalization is

$$\int \rho(\vec{r}, t)dr = mA. \tag{8.13}$$

In symmetric collisions, in the C.M. system the incoming energy is

$$E_0 = \frac{1}{2}mu_0^2. \tag{8.14}$$

The radii of the nuclei can be characterized by

$$R = R_P = R_T = r_0 A_T^{1/3}. \tag{8.15}$$

Let us repeat the introduction of the characteristic quantities labeled by index "1", and through them dimensionless flow variables labeled by tilde:

$$\begin{aligned} \vec{r} &\equiv l_1\ \tilde{r}, \\ t &\equiv t_1\ \tilde{t}, \\ \rho(\vec{r}, t) &\equiv \frac{m_1}{l_1^3}\ \tilde{\rho}(\tilde{r}, \tilde{t}), \\ u(\vec{r}, t) &\equiv u_1\ \tilde{u}(\tilde{r}, \tilde{t}), \\ T(\vec{r}, t) &\equiv T_1\ \tilde{T}(\tilde{r}, \tilde{t}). \end{aligned} \tag{8.16}$$

Since the kinetic viscosity is $\nu \approx 10^{-1}$fm, and the characteristic time and length are $t_1 \approx 10$fm/c and $l_1 \approx 10$fm for a relativistic heavy ion collision the Reynolds number is

in the order of $Re \approx 10 - 100$. Since the dimensionless break-up time is of the order of unity, $\tilde{t}_{BU} \approx 1$, viscous effects have no time to influence the flow essentially because $\tilde{t}_{BU} \ll Re$. Thus viscosity is not dominating the expansion stage of a relativistic heavy ion collisions. It may, however, cause corrections, like entropy increase of the order of 10 % [2].

Fluid dynamical scaling is only approximate in heavy ion collisions because of the following reasons:

(i) The initial compression stage is not scale invariant since the effect of viscosity is essential in forming the shock profiles.

(ii) Scaling works well if our EOS is similar to an ideal gas. Binding and compressional energy bring in new dimensional constants which violate scaling, especially at low energies (below 100 MeV/nucleon).

(iii) The break-up condition may and may not be formulated in a dimensionless manner. If it includes dimensional constants, like the microscopic cross sections, in an essential way the dimensionless break-up time may not be constant, and this might violate hydrodynamical scaling. However, many break-up descriptions lead to $\tilde{t}_{BU} = const.$

(iv) Physical processes after the break-up may violate scaling, thus preventing the hydrodynamical scaling laws to be seen in the measurables.

Therefore it should be determined experimentally whether scaling is present in the observables or not.

8.2 Scaling properties of cross sections

We will now discuss how to study the fluid dynamical scaling laws in measured cross sections. We have to follow the way we evaluate these cross sections in the fluid dynamical model. We stop the fluid dynamical calculation at some time t_{BU}. We assume that the local momentum distribution is a Maxwell - Boltzmann distribution in each fluid cell at $[t_{BU}, \vec{r}]$. Thus the total momentum distribution in a collision with impact parameter b is

$$F_b(\vec{p}, \vec{r}, t) = n(\vec{r}, t_{BU}, b) f^{MB}[\vec{p} - \vec{p}_{flow}(\vec{r}, t_{BU}, b)], \tag{8.17}$$

where n is the baryon density, $n(\vec{r}, t_{BU}, b) = \rho(\vec{r}, t_{BU}, b)/m$, and $\vec{p}_{flow}(\vec{r}, t_{BU}, b) = m\ \vec{u}(\vec{r}, t_{BU}, b)$. The double differential nucleon inclusive cross section is then

$$\sigma_2 \equiv \frac{d^2\sigma}{dEd\Omega} = \frac{d\sigma}{d^3p} \cdot \frac{d^3p}{dEd\Omega} = \frac{d\sigma}{d^3p} \cdot \frac{p^2 dp d\Omega}{dEd\Omega} = m\sqrt{2mE}\frac{d\sigma}{d^3p}. \tag{8.18}$$

Thus inserting the phase space distribution yielded by the fluid dynamics

$$\sigma_2 = m\sqrt{2mE} \int_0^{b_{max}} d^2b \int d^3r\ F_b(\vec{p}, \vec{r}, t), \tag{8.19}$$

where the total local distribution, F_b, can be factorized to the density, n, and a Maxwell–Boltzmann momentum distribution, f^{MB}, (normalized to unity) which depends on the local temperature and is shifted by the local flow momentum, p_{flow}:

$$\sigma_2 = m\sqrt{2mE}\int_0^{b_{max}} d^2b \int d^3r\ n(\vec{r}, t_{BU}, b)\ f^{MB}(\vec{p} - \vec{p}_{flow}(\vec{r}, t_{BU}, b)). \tag{8.20}$$

We can now introduce the dimensionless variables

$$\begin{aligned} b_{max} &= l_1 \tilde{b}_{max}, \\ \vec{r} &= l_1 \tilde{r}, \\ n &= \frac{A}{l_1^3}\tilde{\rho}(\tilde{r}, \tilde{t}; \tilde{b}, Re). \end{aligned} \tag{8.21}$$

So far we did not introduce the scaling decomposition of the momentum p. We can use the usual procedure

$$\begin{aligned} \vec{p} &= p_1 \tilde{p}, \\ f &= \frac{1}{p_1^3}\ \tilde{f}(\tilde{p} - \tilde{p}_{flow}). \end{aligned} \tag{8.22}$$

The parameter p_1 should be fixed by the typical momentum:

$$p_1 = \sqrt{2mE_0}.$$

Thus the double differential cross section can be written as:

$$\sigma_2 = m\sqrt{2mE}\ l_1^2 A \frac{1}{p_1^3}\int_0^{\tilde{b}_{max}} d^2\tilde{b} \int d^3\tilde{r}\ \tilde{\rho}(\tilde{r}, \tilde{b})\ \tilde{f}(\tilde{p} - \tilde{p}_{flow}), \tag{8.23}$$

where we have separated the dimensional and dimensionless factors. Assume that $b_{max} = \alpha 2r_0\left(\frac{A}{2}\right)^{1/3} = l_1\tilde{b}_{max}$, where α is a constant defining the cut in the impact parameters selected. Using the definition of l_1 we obtain

$$\tilde{b}_{max} = \alpha(3/\pi)^{1/3}.$$

We can now define a dimensionless cross section as

$$\tilde{g}(\tilde{p}, Re) \equiv \frac{\sqrt[3]{2}}{\tilde{b}_{max}^2}\ \int_0^{\tilde{b}_{max}} d^2\tilde{b} \int d^3\tilde{r}\tilde{\rho}(\tilde{r}, \tilde{b}) f(|\tilde{p} - \tilde{p}_f). \tag{8.24}$$

This expression contains only dimensionless quantities, which are invariant under the change of energy or mass of the system. The cross section can be expressed in terms of this quantity as

$$\sigma_2 = \frac{A^{5/3}}{E_0} r_0^2 \alpha^2 \sqrt{X} \cdot \tilde{g}(\tilde{p}, Re)\ , \tag{8.25}$$

where $X \equiv E/E_0$. The double differential cross section, σ_2, is usually measured in terms of E and Θ. The quantity Θ is dimensionless and scale invariant, but E can be replaced

by X to get a dimensionless variable. Thus we can introduce another dimensionless cross section

$$\tilde{G}(X, \Theta, Re) \equiv \alpha^2 \sqrt{X}\ \tilde{g}(\tilde{p}, Re). \tag{8.26}$$

Here α characterizes the multiplicity selection. If $\alpha = 1$ this means $b_{max} = 2R$, i.e. all collisions are taken into account, the cross section is inclusive. If $\alpha < 1$, this choice corresponds to a selection of central events (e.g. $\alpha = \frac{1}{2}$ corresponds approximately to 25% of all events with the highest multiplicity). The double differential cross section in terms of $\tilde{G}$ is

$$\sigma_2 = \frac{A^{5/3}}{E_0} r_0^2 \cdot \tilde{G}(X, \Theta, Re)\ . \tag{8.27}$$

Thus if we measure a cross section at a given energy and mass with a well defined impact parameter selection we can separate the dimensional factors from the double differential cross section to obtain $\tilde{G}$. This dimensionless part $\tilde{G}$ should then be the same for collisions at other energies and masses if the impact parameter selection is the same, and if the hydrodynamical scaling is not violated.

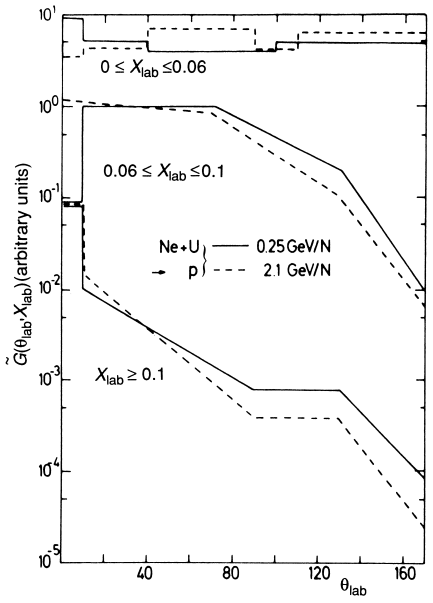

Figure 8.1: Scale invariant double differential cross sections, $\tilde{G}$, taken from 3-dimensional, numerical, perfect, relativistic, fluid dynamical calculations. The break-up was assumed at one third nuclear density. Reproduced by permission of Elsevier Science Publishing from [1].

Results of numerical fluid dynamical calculations show this property clearly. Calculations for 250 $A \cdot MeV$ and 2.1 $A \cdot GeV$ Ne + U collisions in ref. [3] gave similar results in terms of $\tilde{G}$, Fig. 8.1.

If we compare experimental data, similarly strong scaling behavior can be seen, Fig. 8.2 (from [1]). The agreement in the transverse directions indicates that scaling violating factors, like viscosity, do not play dominating role here. The scaling violation

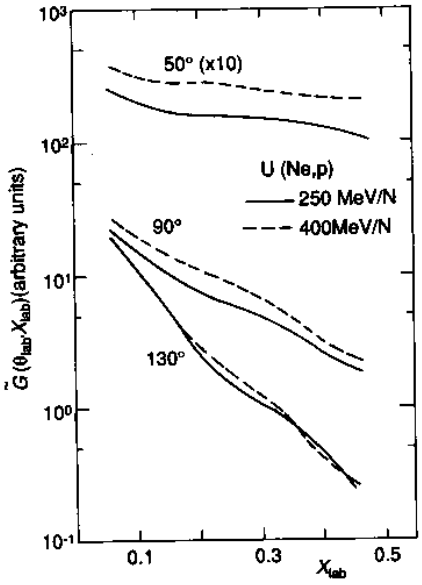

Figure 8.2: Scale invariant double differential cross sections, $\tilde{G}$, taken from two experiments at 250 and 400 A·MeV beam energy. Reproduced by permission of Elsevier Science Publishing from [1].

at forward angles indicates that pre-equilibrium, quasi-elastic scatterings, which are important at this angle, do not follow fluid dynamical scaling laws.

Three sets of experimental data were compared (Fig. 8.3) also by removing the quasi-elastic component from the cross section (using a theoretical model calculation [4]). The 800 MeV cross sections are not affected by the quasi-free scattering, because at this energy the direct scattering is forward-backward peaked, and so it does not influence the 90^0 cross section.

8.3 Scaling properties of the transverse flow

Let us now study the scaling properties of the transverse flow which is a clearly collective fluid dynamical effect in heavy ion collisions. It is expected to occur in the whole energy range discussed in this book. First let us consider the theoretical predictions of the scaling properties of the measurables describing the transverse flow, and then we will see the validity of these predictions in experimental data, as well as the deviations from the scaling behavior and their causes.

8.3.1 Global flow tensor

Let us repeat the definition of the global flow tensor:

$$M_{\alpha\beta} = \sum_{\nu} \frac{1}{2m_\nu} p_\alpha(\nu) p_\beta(\nu), \tag{8.28}$$

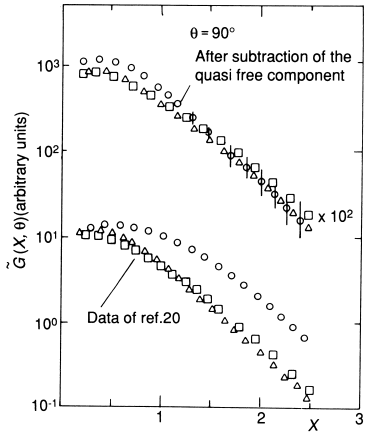

Figure 8.3: Structure functions, $\tilde{G}$, in the C.M. system extracted from experimental proton inclusive data. Circles: 400 A MeV Ne+Ne, triangles: 800 A MeV Ne+Ne, squares: 800 A MeV Ar+Ar. Quasi elastic scattering is removed (top) and maintained (bottom) theoretically. The error bars indicate the uncertainties in the subtraction-procedure of the quasi-free component. Reproduced by permission of Elsevier Science Publishing from [1].

The fluid dynamical expectation value of this quantity is given by

$$\overline{M}_{\alpha\beta} = \int d^3r \; d^3p \; p_\alpha p_\beta \; n(\vec{r}, t_{BU}) f^{MB}[\vec{r}, \vec{p} - \vec{p}_{flow}, T(\vec{r})] \frac{1}{2m}. \tag{8.29}$$

Let us introduce the scaling parameters:

$$p_1 = \sqrt{2mE_0}, \;\; T_1 = \frac{2E_0}{3}, \;\; u_1 = \sqrt{\frac{2E_0}{m}}, \;\; l_1^3 = \frac{4\pi}{3} r_0^3 A, \;\; t_1 = \frac{l_1}{u_1} \;\text{ and }\; f = \frac{1}{p_1^3}\tilde{f}. \tag{8.30}$$

Thus the expectation value of the global flow tensor reduces to:

$$\overline{M}_{\alpha\beta} = \underbrace{\frac{1}{2m} l_1^3 p_1^3 p_1^2 \frac{A}{l_1^3} \frac{1}{p_1^3}}_{AE_0} \underbrace{\int d^3\tilde{r} \; d^3\tilde{p} \; \tilde{p}_\alpha \tilde{p}_\beta \; \tilde{n}(\tilde{r}) \tilde{f}(\tilde{p} - \tilde{p}_f)}_{\tilde{M}_{\alpha\beta}}. \tag{8.31}$$

If we have several fluid cells, and the thermal momentum distribution of the matter in the fluid elements is represented by a Maxwell–Boltzmann distribution, then

$$M_{\alpha\beta} = \frac{1}{2} \sum_{(cell)s=1}^{N} A_s [m \; u_\alpha^{flow}(s) \; u_\beta^{flow}(s) + T(s)\delta_{\alpha\beta}]. \tag{8.32}$$

On the other hand the energy conservation is

$$E_0 = \sum_s E_s = \sum_s \frac{A_s}{A} \left[\frac{m \; u^2(s)}{2} + \frac{3}{2} T(s) \right], \tag{8.33}$$

and we can introduce the partition of thermal and flow energies as

$$\tau_s = \frac{A_s}{A}\frac{3}{2}\frac{T(s)}{E_0}; \quad \lambda_s = \frac{A_s}{A}\frac{1}{2}\frac{m\ u^2(s)}{E_0}. \tag{8.34}$$

Then the energy conservation is:

$$\sum_s \tau_s + \lambda_s = 1\ . \tag{8.35}$$

Thus

$$\tilde{M}_{\alpha\beta} = \sum_s \lambda_s \frac{\tilde{u}_\alpha(s)\tilde{u}_\beta(s)}{\tilde{u}^2(s)} + \tau_s \delta_{\alpha\beta}\frac{1}{3}\ , \tag{8.36}$$

and this leads to:

$$\mathrm{Tr}\,\tilde{M} = \tilde{M}_{\alpha\alpha} = 1. \tag{8.37}$$

The fact that the trace of the dimensionless energy flow tensor is one is a simple consequence of energy conservation.

Experimentally, however, $\tilde{M}_{\alpha\alpha} < 1$, because not all particles are detected. To check the trace of the experimentally measured dimensionless energy flow tensor is a very important test of the experimental acceptance!

8.3.2 Transverse Momentum Analysis

The Blast -Wave model [5] and the Thermal Fireball model [6] do not yield a transverse momentum according to the Danielewicz analysis. The so called "Few Source" model [7] on the other hand does. Let us take a simple example of 3 sources: one in the c.m. (C) and two symmetrically deflected side (S) sources, with masses A_c, A_s, A_s and temperatures T_c, T_s, T_s respectively.

The S-sources have collective momenta per nucleon: $\vec{p}_s = (p^s_\perp, 0, p^s_\parallel)$ and $-\vec{p}_s$ where $[x, z]$ is the reaction plane and z is the beam axis. $p^s_\parallel$ is parallel to the beam, while $p^s_\perp$ is orthogonal and it lies in the reaction plane.

The transverse momentum projected to the reaction plane can be evaluated by using:

$$< \frac{p^x}{a} >= \frac{\int d^3r\ d^3p\ n(r,t)\ f(\vec{p},\vec{r})\ (\vec{p}\ \vec{e}_x)\ |_{y=y_0}}{A|_{y=y_0}}, \tag{8.38}$$

where $\vec{e}_x$ is a transverse unit vector in the reaction plane.

Having one central source and two identical side or spectator sources the energy and mass conservation in this system yields

$$\begin{aligned} A &= \sum_s A_s = 2A_s + A_c, \\ E_0 &= \left[2A_s\left(\frac{1}{2}m\ u^2(s) + \frac{3}{2}T_s\right) + A_c\frac{3}{2}T_c\right]/A, \end{aligned} \tag{8.39}$$

where

$$\vec{u}(s) = u_\parallel + u_\perp \tag{8.40}$$

One can rewrite these conservation laws in scale invariant form by using the scale parameters, $p_1 = \sqrt{2mE_0}$; $T_1 = \frac{2}{3}E_0$,:

$$\begin{aligned} 1 &= 2\tilde{A}_s + \tilde{A}_c, \\ 1 = 2\tilde{A}_s[\tilde{E}_\perp + \tilde{E}_\parallel + \tilde{T}_s] + \tilde{A}_c\tilde{T}_c &= 2\tilde{A}_s[\tilde{p}_\perp^2 + \tilde{p}_\parallel^2 + \tilde{T}_s] + \tilde{A}_c\tilde{T}_c, \end{aligned} \tag{8.41}$$

Now let us calculate the transverse momentum at $y = y_0$:

$$p^x(y) = N \int d^2p_\perp \; p_\perp^s \left\{ \exp\left[-\frac{(\vec{p}-\vec{p}_s)^2}{2mT}\right] + \exp\left[-\frac{(\vec{p}+\vec{p}_s)^2}{2mT}\right] \right\}\Big|_{\text{at } p_\parallel = m_\perp \cosh y_0} \tag{8.42}$$

where N is a normalization constant. The center source does not contribute to p^x because $\vec{p}_c = 0$. Performing the integrals yields (see the solution of Assignment 7b):

$$p^x(y) = \frac{A_s}{(2\pi m T_s)^{1/2}} p_{sx} \left[e^{-\frac{(p_z - p_\parallel^s)^2}{2mT_s}} - e^{-\frac{(p_z + p_\parallel^s)^2}{2mT_s}} \right]. \tag{8.43}$$

Here p_z is a function of the rapidity y. Since $y \cong v_z = \frac{1}{m}p_z$ it follows that $p_z \cong my$. The total number of nucleons $A|_{y=y_0}$ is:

$$A|_{y=y_0} = \frac{A_s}{(2\pi m T_s)^{3/2}} \left[e^{-\frac{(p_z - p_\parallel^s)^2}{2mT_s}} + e^{-\frac{(p_z + p_\parallel^s)^2}{2mT_s}} \right] + \frac{A_c}{(2\pi m T_c)^{3/2}} e^{-\frac{p_z^2}{2mT_c}}, \tag{8.44}$$

consequently:

$$\frac{p^x(y)}{a} = \frac{2\pi m T_s p_\perp^s \left[e^{-\frac{(p_z - p_\parallel^s)^2}{2mT_s}} - e^{-\frac{(p_z + p_\parallel^s)^2}{2mT_s}} \right]}{\left[e^{-\frac{(p_z - p_\parallel^s)^2}{2mT_s}} + e^{-\frac{(p_z + p_\parallel^s)^2}{2mT_s}} \right] + \frac{A_c}{A-s}\left(\frac{T_s}{T_c}\right)^{3/2} e^{-\frac{p_z^2}{2mT_c}}}, \tag{8.45}$$

Here $p_z = p_z(y) = my$. We will see the scaling behavior of the transverse flow in the framework of the three source model in the next sections.

8.3.3 Fragment flow and scaling

Let us consider the Few Source model. If we have composite fragments emitted at the break up, their momenta are $\vec{p}_\kappa = \vec{p}A_\kappa$, where $\vec{p}$ is the momentum per nucleon and A_κ is the fragment mass.

The transverse momentum per nucleon projected to the reaction plane, determined by the beam axis, and the unit vector $\vec{e}_x$ in the direction of the reaction plane, can be calculated in a fluid dynamical model separately for each type of fragment κ as

$$\left\langle \frac{p^x}{a} \right\rangle_\kappa = \frac{1}{A_\kappa N_\kappa(y, \Delta y)} \int F_\kappa(\vec{p},\ \vec{r})(\vec{p}\ \vec{e}_x)\ d^3r\ d^3p\,\big|_{y<y(p)<y+\Delta y'}\ , \tag{8.46}$$

where the momentum integral is restricted to a given rapidity bin and $A_\kappa N_\kappa(y, \Delta y)$ is the number of nucleons emitted into this bin within fragments of type κ, so that

$A = \sum_\kappa A_\kappa N_\kappa$. The distribution $F_\kappa(\vec{p},\ \vec{r})$ is normalized to $A_\kappa N_\kappa$. Introducing scale invariant variables eq. (8.30) reduces to

$$\tilde{p}^x_\kappa(\tilde{y}) = \frac{\left\langle \frac{p^x}{a} \right\rangle_\kappa}{p_1} = \tilde{N}^{-1}_\kappa(\tilde{y}) \int \tilde{F}_\kappa(\tilde{p},\tilde{r})(\tilde{p}\tilde{e}_x) d^3\tilde{r} d^3\tilde{p}\,\big|_{\tilde{y}<\tilde{y}(\tilde{p})<\tilde{y}+\Delta\tilde{y}'}\ , \tag{8.47}$$

where the range of the momentum integral should be given in terms of the c.m. beam rapidity and $\tilde{y} = y/y_1 = \frac{y}{y^{proj}_{CM}}$ (since we are confining the problem to the non-relativistic regime, $y^{proj}_{CM} = u_1$). Here $\tilde{F}_\kappa(\tilde{p},\tilde{r}) = \frac{p_1^3 F_\kappa}{A}$, is normalized to $\tilde{N}_\kappa = \frac{N_\kappa A_\kappa}{A}$, i.e. $\sum_\kappa \tilde{N}_\kappa = 1$.

The total scale invariant transverse momentum is then given by the average

$$\tilde{p}^x(\tilde{y}) = \frac{\sum_\kappa N_\kappa A_\kappa \tilde{p}^x_\kappa(\tilde{y})}{\sum_\kappa N_\kappa A_\kappa}\ . \tag{8.48}$$

The scaling with beam energy is not expected to be perfect due to the same reasons that were mentioned before.

8.3.4 Fragment flow - mass dependence (*)

Since there can be different fragments, κ, emitted from each source, $q = c, s_1, s_2$, the normalization is given by:

$$\tilde{A}_q = \sum_\kappa \tilde{A}_{\kappa q} = \sum_\kappa N_{\kappa q} A_\kappa / A \quad \text{and} \quad \sum_{\kappa \mathrm{q}} \tilde{\mathrm{A}}_{\kappa \mathrm{q}} = 1\ . \tag{8.49}$$

Here $\tilde{A}_{\kappa q}$ is the fraction of nucleon number in source q within fragments of type κ. Thus the energy conservation can be expressed by:

$$\sum_\kappa \left[2\tilde{A}_{\kappa s} \left((\tilde{p}^s_\perp)^2 + (\tilde{p}^s_\parallel)^2 + \frac{\tilde{T}_s}{A_\kappa} \right) + \frac{\tilde{A}_{\kappa c}\tilde{T}_c}{A_\kappa} \right] = 1 \tag{8.50}$$

If the dimensionless source momentum vector of a given source is $\tilde{p}_q$ the momentum distribution $\tilde{F}_\kappa(\tilde{p},\tilde{r})d^3\tilde{r}$ is represented by a sum over the sources:

$$\int \tilde{F}_\kappa(\tilde{p},\tilde{r}) d^3\tilde{r} = \sum_q \tilde{F}_{\kappa q}(\tilde{p}). \tag{8.51}$$

Let us assume that each source has a local thermal motion, described by a Maxwell–Boltzmann distribution,

$$\tilde{F}_{\kappa q}(\tilde{p}) = \tilde{A}_{\kappa q} \left(\frac{3A_\kappa}{2\pi\tilde{T}_q} \right)^{3/2} \exp\left[-\frac{3A_\kappa(\tilde{p}-\tilde{p}_q)^2}{2\tilde{T}_q} \right], \tag{8.52}$$

normalized to $\tilde{A}_{\kappa q}$.

Now the integral (8.47) can be calculated explicitly. The central source, C, will not contribute to the integral due to symmetry reasons. Nevertheless, it contributes to the normalization constant $\tilde{N}_\kappa(\tilde{y})$:

$$\tilde{p}_t(\tilde{y}) = \tilde{p}^x_\kappa(\tilde{y}) = Const. \left(\frac{\tilde{A}_{\kappa s}}{\sqrt{\tilde{T}_s}}\right) \tilde{N}_\kappa(\tilde{y})^{-1} \tilde{p}^s_\perp$$
$$\left\{ \exp\left[-\frac{3A_\kappa(\tilde{y}-\tilde{p}^s_\parallel)^2}{2\tilde{T}_s}\right] - \exp\left[-\frac{3A_\kappa(\tilde{y}+\tilde{p}^s_\parallel)^2}{2\tilde{T}_s}\right]\right\}. \tag{8.53}$$

where

$$\tilde{N}_\kappa(\tilde{y}) = Const. \left[\left(\frac{\tilde{A}_{\kappa s}}{\sqrt{\tilde{T}_s}}\right)\left\{\exp\left[-\frac{3A_\kappa(\tilde{y}-\tilde{p}^s_\parallel)^2}{2\tilde{T}_s}\right] + \exp\left[-\frac{3A_\kappa(\tilde{y}+\tilde{p}^s_\parallel)^2}{2\tilde{T}_s}\right]\right\} + \left(\frac{\tilde{A}_{\kappa c}}{\sqrt{\tilde{T}_c}}\right) \exp\left(\frac{-3A_\kappa \tilde{y}^2}{2\tilde{T}_c}\right)\right]. \tag{8.54}$$

After a straightforward calculation we obtain that

$$\tilde{p}_t(\tilde{y}) = \tilde{p}^x_\kappa(\tilde{y}) = \tilde{p}^s_\perp \sinh\left(\frac{3\tilde{y}A_\kappa \tilde{p}^s_\parallel}{\tilde{T}_s}\right) /$$
$$\left[\cosh\left(\frac{3\tilde{y}A_\kappa \tilde{p}^s_\parallel}{\tilde{T}_s}\right) + 1/2\left(\frac{A_{\kappa c}}{A_{\kappa s}}\right)\sqrt{\frac{\tilde{T}_s}{\tilde{T}_c}} \exp\left(3\tilde{A}_\kappa \frac{\tilde{y}^2\left(\tilde{T}_c - \tilde{T}_s\right) + (\tilde{p}^s_\parallel)^2 \tilde{T}_c}{2\tilde{T}_c\tilde{T}_s}\right)\right]. \tag{8.55}$$

This expression reproduces qualitatively the basic features of the observed transverse momenta. The transverse momentum, $\tilde{p}_t(\tilde{y}) = \tilde{p}^x_\kappa(\tilde{y})$, as a function of the rapidity crosses the axis at the c.m. rapidity with a tangent of

$$\tilde{F}_\kappa = \frac{\partial \tilde{p}^x_\kappa}{\partial \tilde{y}} \mid_{\tilde{y}=0} = \frac{3A_\kappa \tilde{p}^s_\perp \tilde{p}^s_\parallel}{\tilde{T}_s\left[1 + 1/2\left(\frac{A_{\kappa c}}{A_{\kappa s}}\right)\sqrt{\frac{\tilde{T}_s}{\tilde{T}_c}} \exp\left(\frac{3A_\kappa(\tilde{p}^s_\parallel)^2}{2\tilde{T}_s}\right)\right]}, \tag{8.56}$$

which increases with increasing transverse momentum and decreases with increasing dissipation (increasing T_s).

The collective transverse momentum $\tilde{p}^x_\kappa$ increases with the fragment mass A_κ as well as $\tilde{F}$ does. The dependence is, however, not trivial because of the denominator. The factor $\left(\frac{A_{\kappa c}}{A_{\kappa s}}\right)$ is not necessarily the same for all κ , and if we, as usual, assume that $\tilde{T}_c > \tilde{T}_s$ then $\left(\frac{A_{\kappa c}}{A_{\kappa s}}\right)$ decreases with increasing A_κ enhancing the transverse momentum further. The $\tilde{p}^s_\parallel$ dependence is not trivial either. To show the behavior of the model we can use a parametrization [7] of the three source model based on detailed fluid dynamical calculations [9, 10]. This parametrization for each impact parameter defines the mass partition among the C- and S-sources, (just as in the standard firestreak model). It also redistributes the remainder of the collective kinetic energy among the sources. The thermal energy due to dissipation is also divided up among all three sources. This parametrization can be described by the equations [7]:

$$\Theta_{cm}(b) = z_0(1 - b/b_{max})\pi/2 \tag{8.57}$$

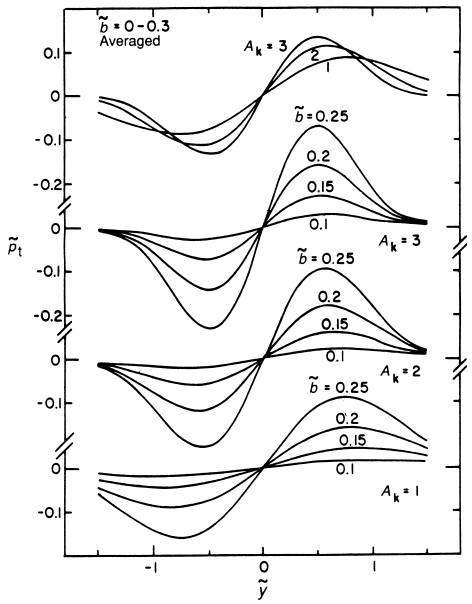

Figure 8.4: Scale invariant transverse momentum distribution calculated in the Few Source (FS) model for different impact parameters $\tilde{b} = 0.05 - 0.25$ and averaged over impact parameters in the range of $\tilde{b} = 0 - 0.3$. The $\tilde{p}_t = \tilde{p}^x_\kappa(\tilde{y}) =$ distribution is different for different fragment masses A_κ. Reproduced by permission of Elsevier Science Publishing from [8].

and $|\vec{p}_s| = p_1 \left[1 - (1 - b/b_{max})^2 y_0\right]$ where z_0 is a parameter governing the transverse momentum transfer and y_0 is responsible for the dissipation. A third parameter x_0 governs the partition of thermal energy among the sources. If Q_h is the fraction of heat energy in the system $Q_h = \sum_\kappa \frac{\tilde{A}_{\kappa q}\tilde{T}_q}{A_\kappa}$ then $x = x_0 \left(1 - \frac{b}{b_{max}}\right)^2$ gives the fraction of thermal energy per nucleon contained in the sources S_1 and S_2 : $x = \frac{\tilde{T}_s}{A_\kappa Q_h}$. Thus the temperature of the sources are $\tilde{T}_s = xQ_hA_\kappa$ and $\tilde{T}_c = \frac{Q_h - 2\tilde{T}_s\tilde{N}_s}{\tilde{N}_c}$, where $\tilde{N}_q$ is the number of fragments in the source q. If composite fragments are present $\tilde{N}_q < \tilde{A}_q$, and we assumed that $\tilde{N}_q = \tilde{A}_q/3$ in the following test (neglecting the possible differences between the C- and S- sources). This also implies that $\left(\frac{A_{\kappa c}}{A_{\kappa s}}\right) = \left(\frac{A_c}{A_s}\right)$ is assumed. Here we use the same values for the model parameters as in ref. [7] ($z_0 = 1, y_0 = 0.6, x_0 = 0.3$).

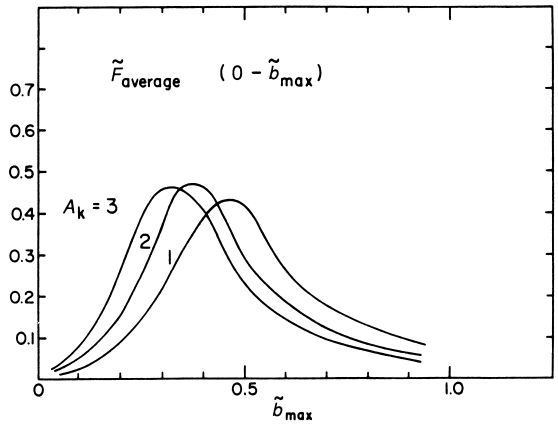

Figure 8.5: Impact parameter averaged scale invariant flow $\tilde{F}$ calculated in the Few Source model (FS) for different maximum impact parameters and for different emitted fragment masses A_κ Reproduced by permission of Elsevier Science Publishing from [8].

In Fig. 8.4 the impact parameter dependence of the calculated scale invariant transverse momentum distribution is shown together with the impact parameter averaged result. The transverse momentum increases with impact parameter (for small impact parameters $\tilde{b} < 0.4$ and it also increases with the fragment mass A_κ for small rapidities. At high rapidities the heavy fragments show less transverse momentum. The Few Source model is not appropriate to describe peripherical collisions $\tilde{b} > 0.7$ similarly to the fluid dynamical model.

The two basic features we should concentrate on are the maximum of the transverse momentum and the tangent of $\tilde{p}_t(\tilde{y})$ at the c.m., eq. (8.56). The latter quantity was also used in ref. [11] to compare different colliding systems, and it was called "Flow" or F. The corresponding scale invariant quantity $\tilde{F}$ is obtained dividing F by the C.M. beam momentum. This quantity averaged over the impact parameter range $0 - \tilde{b}_{max}$, denoted by $\tilde{F}_{av}$, is plotted in Fig. 8.5 versus the maximum impact parameter as it is calculated in the Few Source model. Selecting more central collisions (decreasing b_{max}) leads to an increase of $\tilde{F}_{av}$ until we reach a critical $\tilde{b}^{crit}_{max}$, where $\tilde{F}_{av}$ reaches its maximum. Further

decrease of the maximum impact parameter leads to a rapid decrease of the flow. The value of the critical $\tilde{b}_{max}^{crit}$ decreases with increasing fragment mass A_κ, $\tilde{b}_{max}^{crit} \approx 0.3 - 0.5$.

8.4 Scaling violations

The assumptions we made at the beginning of this chapter do not always hold. We made two major assumptions: i) on the scaling of the speed of sound, which is related to the EOS, and ii) on the smallness of the viscous effects.

Let us start with perfect-fluid hydrodynamics, and let us call $\Phi(\vec{r}, t)$ any field entering these equations ($\Phi = \rho, \vec{u}$, or T). If $\Phi(\vec{r}, t)$ is a solution, then $\Phi(\vec{r}\alpha, t\alpha)$ is also a solution, provided of course that the initial and final (break-up) conditions are scaled in the same way. This is of course realized if one studies a restricted set of systems, e.g. at the same incident energy and at the same impact parameter over radius ratio. Thus every dimensionless quantity is a function of the Strouhal number, S, only. However, if one concentrates on a given impact parameter, another dimensionless geometrical parameter, b/b_{Max}, has to be introduced. Only those collisions yield a similar flow pattern where both the Strouhal number, S, and the parameter, b/b_{Max}, are the same. This could be expressed by requiring the constancy of a dimensionless parameter

$$\Psi = \Psi(S, b/b_{Max}).$$

If the dynamics is closer to viscous fluid dynamics, any dimensionless physical quantity can be expressed as

$$\Psi = \Psi(S,\ Re,\ b/b_{Max}).$$

The usual way to analyze the scaling properties of the collective aspects of nuclear collisions is, thus, to compare e.g. central events only to each other, corresponding to a given per cent of all possible events. This selection is a dimensionless one, thus if the measured quantity is not dependent on viscous effects, for this selected class of events scale invariance still holds. This is the consequence of the fact that the Strouhal number can be fixed to 1 by the appropriate choice of time scale. If the break up time scales according to this time scale the experimental results scale also, and dimensionless quantities, in this case will not show A or $E_0^{c.m.}$ dependence.

If the viscous effects are important such general scale invariance cannot be expected. The constancy of the Reynolds number is also required for scale invariance. This means that not all events with all A and $E_0^{c.m.}$ will be inwariant but only a smaller subset of events, satisfying the relation $Re(A, E_0) = \text{const.}$, will yield scaling flow patterns.

8.4.1 Scaling violation in transverse flow

In ref. [12] , it was shown that the dependence of the transverse flow on the Reynolds number is not negligible. A rough estimate gives (for $b \lesssim b_{Max}/2$)

$$\tan(< \Theta_{flow} >) \approx \frac{1}{3}\left[S\left(1 - \frac{b}{b_{Max}}\right) - \frac{3}{Re}\right]\frac{\bar{\varepsilon}}{\bar{\varepsilon}_z}, \tag{8.58}$$

where $\bar{\varepsilon}$ and $\bar{\varepsilon}_z$ are the average energy and the average energy in the z direction respectively, of the nucleons participating in the flow. Relation (8.58) is compared to experimental data at 400 A·MeV in ref. [13] and it was concluded that $Re \approx 8$ for Nb + Nb, which is very close to the free gas value [14] at this energy. We recall that the viscosity parameter, η, is related to the in medium cross section.

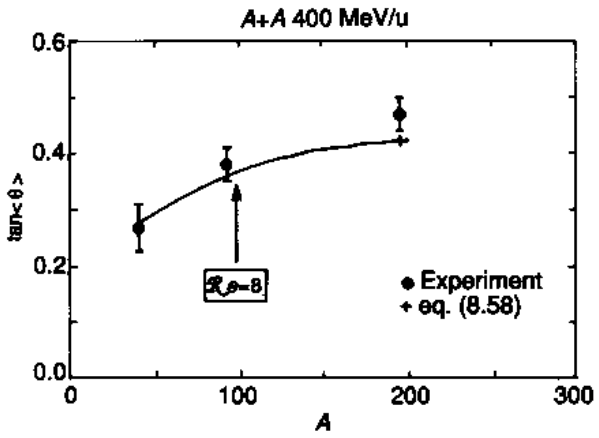

Figure 8.6: Comparison of flow angle dots measured in Ref. [13], with eq. (8.58) (full line), using Reynolds number, $Re = 8$ for Nb+Nb. Reproduced by permission of World Scientific Publishing Co. from [15]

In order to investigate the validity of our scaling as assumption, we first express measured quantities in a scale-invariant way. Following ref. [16], we introduce a scale-invariant transverse momentum per nucleon

$$\tilde{p}^x = p^x / p^{c.m.}_{proj.} \tag{8.59}$$

where p^x is the transverse momentum per nucleon obtained in the experiments and $p^{c.m.}_{proj.}$ is the center of mass momentum of a nucleon in the projectile. In the same way we define the scale-invariant rapidity by

$$\tilde{y} = y^{c.m.} / y^{c.m.}_{proj.}; \tag{8.60}$$

In Fig. 8.6 different experimental data are plotted with the definitions described above. Differences in the results arise from different multiplicity selections (i.e., different impact parameters) and from different types of particles detected.

We use the definition introduced in ref. [8, 16, 17] to characterize the transverse momentum dependence by one quantity: the slope of the rapidity dependence of the transverse momentum near mid-rapidity. This parameter is called "Flow". We denote the corresponding scale-invariant slope by $\tilde{F}$.

A more extensive analysis was done recently [16, 8], not only on the flow properties, but also on other quantities. In Fig. 8.7 we present some of the results of ref. [16]. There is a remarkable resemblance between the dimensionless transverse Flow

$$\tilde{F} = \frac{d\tilde{p}^x}{d\tilde{y}}, \tag{8.61}$$

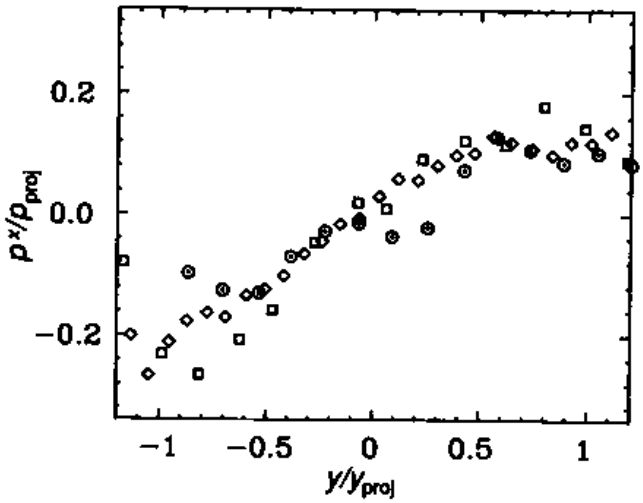

Figure 8.7: Projected transverse flow from three different experiment plotted in dimensionless variables. The curves lie on the top of each other due to approximate scale invariance. Reproduced with permission from [16]

and the value of the Reynolds number calculated with a viscosity coefficient as evaluated in ref. [14]. This strongly suggests that the flow properties are much more sensitive to viscosity than to equation of state.

If we display contour lines of constant $\tilde{F}$ on the same plot, we observe a behavior shown in Fig. 8.8. At medium and high energies the qualitative behavior of the contour lines are similar. The experimental data, however, rise somewhat more sharply than the Reynolds number. This most probably indicates that the viscosity increases faster with energy than $\sqrt{T}$ calculated in ref. [2], because of other inelastic processes, pion emission, etc. The same processes may also lead to a softening of the EOS which will result in smaller transverse flow. Also, at high beam energies a partial transparency is expected to occur which can reduce the transverse flow.

8.4.2 Disappearance of the transverse flow

The most drastic difference between the $Re = \text{const.}$ and $\tilde{F} = \text{const.}$ curves appears at low energies. Below $E^{c.m.}_{nucl.} \approx 60$ - 70 MeV, the scale-invariant transverse flow $\tilde{F}$ drops suddenly with decreasing energy, and below $E^{c.m.}_{nucl.} \approx 10$ - 20 MeV it becomes negative.

A given mean-field potential leads to a well defined EOS (and vice versa) if we assume thermal equilibrium in a given statistics. A sufficiently strong attractive mean field leads to an EOS showing a first order, liquid-gas type, phase transition. Thus, either the EOS or the reaction mechanism should change here drastically. The EOS enters the scaling analysis via the sound speed. Namely, a scale-invariant flow pattern can be obtained only if the pressure satisfies the relation $\nabla p = c_s^2 \nabla \rho$ with a sound

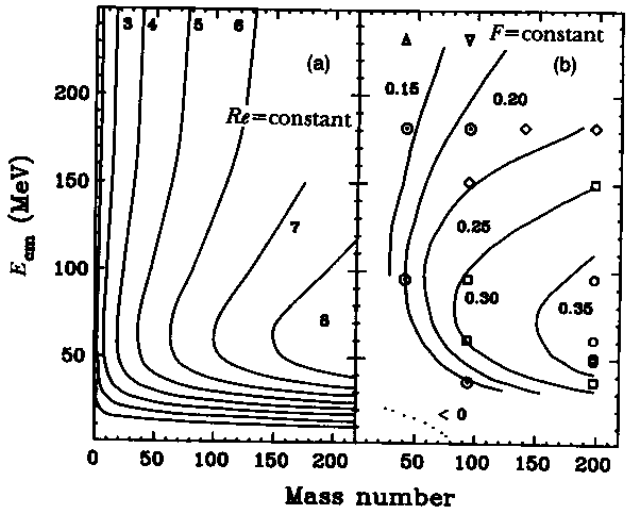

Figure 8.8: Contour plots in the [A.E] plane. Full lines in (a) correspond to constant Reynolds number. Full lines in (b) correspond to constant $\tilde{F}$. The dotted curve indicates the expected behavior of $\tilde{F}$ at low energies. Symbols circles, squares, diamonds, dotted circles, inverted triangles, and triangles correspond to experimentally measured $\tilde{F}$-values of 0.4, 0.325, 0.275, 0.225, 0.175, 0.125, and 0.1 respectively. Reproduced with permission from [16].

speed c_s, which scales with the c.m. energy as

$$c_s = \tilde{c}_s \sqrt{2E^{c.m.}_{nucl.}/m} = \tilde{c}_s \sqrt{2E_0/m}. \tag{8.62}$$

For ideal gas $\tilde{c}_s$ =const. For an EOS with binding energy of 8 MeV and K =250 MeV, the sound speed is $\tilde{c}_s = 0.7 - 0.9$ for $\tilde{n} = 0.3 - 1.0$ and $E_0 = 50 - 240$ MeV (T =35-160 MeV). Below E_0 =40 MeV, the sound speed starts to diverge with decreasing energy: at normal nuclear density, $\tilde{n} = 1$ $c_s \gg 1$, at $\tilde{n} = 0.6$ $c_s = 0.7$ and at $\tilde{n} = 0.3$ $c_s \to 0$. This non-scaling behavior of c_s, at low energies is related to the liquid-gas phase transition of our EOS. Compared with the ideal gas pressure, the phase transition in the EOS leads to a decrease of the pressure and consequently of the transverse flow. In phase equilibrium the pressure is small but always positive. In nonequilibrium phase transition the pressure may even become negative if the matter expands rapidly into the supercooled liquid phase not having sufficient time to establish phase equilibrium. One can also argue that the attractive nuclear interaction overcomes the repulsion caused by the pressure. Such an attractive interaction is out of the scope of the fluid-dynamical scaling studies.

The two effects, the softening of the EOS or the negative pressure caused by the nuclear liquid-gas phase transition, and the predominance of the nuclear attractive mean field (or surface tension), are, of course, the two sides of the same microscopic attractive nucleon-nucleon interaction. Theoretical works in the Boltzmann–Uehling–Uhlenbeck or Vlasov–Uehling–Uhlenbeck approach predict a "negative" deflection angle due to the

nuclear mean field. The same nuclear mean field leads to a fragmentation at a late stage of a collision representing a liquid-gas phase. Recently these effects were also detected and analyzed in detail by Westfall, et al. [18]. The point in energy where the flow vanishes while turning from positive angle flow to negative is shown to be sensitive to the in medium nucleon-nucleon cross section, [19]. i.e. on the viscosity, which determines the scaling violations also.

8.5 Assignment 8

8.a Calculate the nonrelativistic scale invariant cross section in the non-relativistic Blast wave model with local Maxwell–Boltzmann distribution. Assume that at the breakup the ratio of the flow energy to the thermal energy is μ.

8.5.1 Solutions to Assignment 8

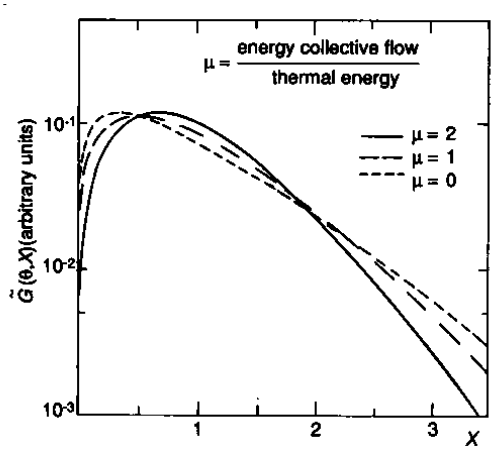

8.a

Figure 8.9: Dimensionless energy (X) distributions calculated in the Blast wave model. Reproduced by permission of Elsevier Science Publishing from [1].

Nonrelativistically $E_{flow} = \frac{p_{flow}^2}{2m}$, $E_{therm} = \frac{3}{2}T$, and the total energy is $E_0 = E_{flow} + E_{therm}$. The thermal distribution is: $f(p) = Const.\ e^{-\frac{p^2}{2mT}}$. Let $\mu = \frac{E_{flow}}{E_{therm}}$. Inserting these parameters into the cross section obtained in the Blast Wave model, and calculating the dimensionless structure function yields:

$$\tilde{G}_{BW}(\Theta, X) = Const.\frac{1+\mu}{\mu^{1/2}} \sinh\left\{3\sqrt{\mu(1+\mu)X}\right\} \exp\left\{-\frac{3}{2}\left[\mu + (1+\mu)X\right]\right\}.$$

The Fireball model result is reproduced for $\mu = 0$. In this case the cross section is $\approx Const.X^{1/2}e^{-\frac{3}{2}X}$. The structure function is plotted in fig. 8.9 for different μ values. At $X < 0.5$ and at $X > 3$ the flow effects are clearly observable.

Bibliography

[1] N. Balázs, B. Schürmann, K. Dietrich and L.P. Csernai, Nucl. Phys. **A424** (1984) 605.

[2] L.P. Csernai and H.W. Barz, Z. Phys. **A296** (1980) 173.

[3] A.A. Amsden, F.H. Harlow and J.R. Nix, Phys. Rev. **C15** (1977) 2059.

[4] B. Schürmann and J. Randrup, Phys. Rev. **C23** (1981) 2766.

[5] P.J. Siemens and J. Rasmussen, Phys. Rev. Lett. **42** (1979) 880.

[6] G.D. Westfall, J. Gosset, P.J. Johansen, A.M. Poskanzer, W.G. Meyers, H.H. Gutbrod, A. Sandoval and R. Stock, Phys. Rev. Lett. **37** (1976) 1202.

[7] L.P. Csernai, G. Fai and J. Randrup, Phys. Lett. **140B** (1984) 149.

[8] A. Bonasera, L.P. Csernai and B. Schürmann, Nucl. Phys. **A476** (1988) 159.

[9] H. Stöcker, L.P. Csernai, G. Graebner, G. Buchwald, H. Kruse, R.Y. Cusson, J.A. Maruhn and W. Greiner, Phys. Rev. **C25** (1982) 1873.

[10] L.P. Csernai, W. Greiner, H. Stöcker, I. Tanihata, S. Nagamiya and J. Knoll, Phys. Rev. **C25** (1982) 2482.

[11] P. Danielewicz and M. Gyulassy, Phys. Rev. **D31** (1985) 53.

[12] J. Cugnon, and D. L'Hote, Nucl. Phys. **A447** (1985) 27c.

[13] H.A. Gustafsson, et al., Phys. Rev. Lett. **52**, 1590 (1984).

[14] P. Danielewicz, Phys. Lett. **146B** (1984) 168.

[15] J. Cugnon, and D. L'Hote, in "Relativistic Heavy Ion Physics", eds. L.P. Csernai and D.D. Strottman (World Scientific, Singapore 1991) Vol. 5 p. 38.

[16] A. Bonasera, L.P. Csernai, Phys. Rev. Lett. **59** (1987) 630.

[17] H.G. Ritter, Nucl. Phys., **A447** (1985) 3c.

[18] G.D. Westfall, *et al.*, Physica Scripta **T32** (1990) 202.

[19] H.-M. Xu, Texas A & M Preprint, (1991), Submitted to Phys. Rev. Lett.

Chapter 9

Direct Solutions of Kinetic Theory

In the study of heavy ion collisions we face a highly dynamical non-equilibrium system. It is not in thermal equilibrium globally and at most of the time not even locally. The solutions we have presented so far were based on perfect fluid dynamics assuming local equilibrium. Usually this approximation is valid only at later stages of heavy ion collisions.

We search for the real physical distribution function of the system for all particles (in principle not only for the single particle distribution function but for the two and more particle distribution functions also). There are different possible approaches to find these non-equilibrium distribution functions like the Chapman–Enskog method or its first order correction the viscous fluid dynamics, two-, three-, or more component fluid dynamics, nuclear cascade models, nuclear cascade models with a mean field like the Boltzmann–Uehling–Uhlenbeck (BUU), Vlasov–Uehling–Uhlenbeck (VUU) or Landau–Vlasov (LV) approaches, molecular dynamics approaches which consider each particle-particle interaction separately, like the Quantum Molecular Dynamics (QMD) approach. There are even more complicated numerical microscopic simulations aimed for higher energy collisions where multiparticle production is dominant. These are different versions of the string or flux tube models like RQMD, QGSM, VENUS, FRITIOF, HIJET, ATTILA, DPM, etc, and parton cascade models.

To present all these models and methods is exceeding the scope of an introductory book. We will discuss only a few of these approaches and give a superficial insight into some of these models, which will enable us just to understand the basic results and constraints of the models.

The Chapman–Enskog method: We may start out from a perfect fluid dynamical solution, which provides us with the local equilibrium phase space distribution, $f^{(0)}(x,p)$. The we search for corrections to this distribution step by step. The first corrected distribution function, $f^{(1)}(x,p)$, is assumed to be only slightly different from the local equilibrium solution, $f^{(1)}(x,p) = f^{(0)}(x,p) + g(x,p)$. This distribution function should satisfy the Boltzmann Transport Equation (BTE), (see Chapter 3)

$$p^\mu \partial_\mu f^{(1)} \equiv D f^{(1)} = C\left[f f_1^{(1)} f_2^{(1)}\right] \ .$$

Since $g \ll f^{(0)}$ and for $f^{(0)}$ the collision integral, $C\left[ff_1^{(0)}f_2^{(0)}\right]$, vanishes, for $f^{(1)}$ the BTE takes the following form

$$Df^{(0)} = C\left[ff_1^{(0)}f_2^{(1)}\right] = C\left[ff_1^{(0)}g_2\right] \ .$$

From this equation we can determine $g(x,p)$. Now we can continue with the next correction, then by inserting it back to the BTE we can evaluate this too [1, 2]. This is schematically the Chapman–Enskog expansion. It is quite useful but the solutions even after many steps of iteration will not deviate essentially or qualitatively from the local equilibrium solution. For example the initial two peaked distribution (see sect. 3.4) in a heavy ion collision cannot be obtained this way.

The importance of this method is that it provides us with the viscous fluid dynamics and the transport coefficients at the same time at the first order step of this expansion. The non-relativistic derivation of viscous fluid dynamics is quite straightforward and it is included in many basic textbooks of statistical physics [1, 3]. The relativistic counterpart (see ref. [2]) is quite involved and exceeds the frame of this introduction.

9.1 Viscous Fluid Dynamics

The viscous fluid dynamics is seldom used in relativistic physics. This is due to the fact that there are still questions around the proper relativistic generalization of viscous fluid dynamics [4]. It was shown that the usual relativistic generalizations of viscous fluid dynamics may lead to unstable solutions. Dissipative effects are, nevertheless, important as many non- relativistic calculations indicate. There exist a few relativistic viscous calculations which can be viewed upon as approximations.

In relativistic dissipative fluid dynamics one adds new terms to the stress-energy-momentum tensor and to the baryon current as follows (see sect. 2.3.1-2) [5, 6]:

$$T^{\mu\nu} = -Pg^{\mu\nu} + (P+e)u^\mu u^\nu + T^{\mu\nu\ (1)}, \tag{9.1}$$

$$N^\mu = nu^\mu + N^{\mu\ (1)}. \tag{9.2}$$

In the absence of dissipation $T^{\mu\nu\ (1)}$ and $N^{\mu\ (1)}$ are both zero, and u^μ is the flow four-velocity of the matter. When dissipation is present one has a choice of defining u^μ to be the velocity of baryon flow or the velocity of energy flow. These are the Eckart and Landau–Lifshitz approaches, respectively. In the Eckart approach $N^{\mu\ (1)}$ is zero by definition. Then $T^{\mu\nu\ (1)}$ is a linear combination of a shear tensor, a projection tensor on the hyperplane normal to u^μ, and a heat flow vector, with coefficients being the shear viscosity η, the bulk viscosity ζ, and heat conductivity λ, respectively. In the Landau–Lifshitz approach $T^{\mu\nu\ (1)}$ does not have the term involving the thermal conductivity; rather, $N^{\mu\ (1)}$ is nonzero and is in fact proportional to λ. These two approaches are completely equivalent and describe the same physics. However, most of the systems we are dealing with have small or no net baryon number, and so the Eckart approach is indeterminate. Thus we must define u^μ to be the velocity of energy flow if the baryon density is negligibly small or vanishes. In these cases the thermal conductivity simply is not defined because there is no net baryon density to define a frame of reference with respect to which energy can be conducted.

9.1.1 Entropy production

Let us use Landau's definition of the flow velocity. It can be shown easily that in the case of perfect relativistic fluids the divergence of the entropy four current vanishes [5] (see Assignment 5.a). If we have both heat conductivity and shear and bulk viscosity, the dissipation in relativistic fluid dynamics is

$$\partial_\iota \left(s u^\iota - \frac{\mu}{T} N^{\iota\ (1)} \right) = -N^{\iota\ (1)} \partial_\iota \left(\frac{\mu}{T} \right) - \frac{1}{T} \Pi^\iota_\nu\ \partial_\iota u^\nu \ , \tag{9.3}$$

where μ is the chemical potential, and $N^{\nu\ (1)} = -\frac{n}{w} I^\nu_q$ is the particle flux density four-vector (with respect to the flow four-velocity) and $\Pi_{\mu\nu}$ is the stress tensor. The particle flux density takes the form

$$N^{\iota\ (1)} = -\frac{n}{w} I^\iota_q = -\frac{\lambda}{c} \left(\frac{nT}{w} \right)^2 \left[\partial^\iota \left(\frac{\mu}{T} \right) - u^\iota u^\nu \partial_\nu \left(\frac{\mu}{T} \right) \right] \ , \tag{9.4}$$

arising from the requirement that the entropy should not decrease [5]. Similarly from the same requirement the stress tensor is

$$\Pi_{\mu\nu} = -\eta \left(\partial_\mu u_\nu + \partial_\nu u_\mu - u_\mu u^\iota \partial_\iota u_\nu - u_\nu u^\iota \partial_\iota u_\mu \right) - (\xi - \frac{2}{3}\eta)(\partial_\iota u^\iota) \left(g_{\mu\nu} - u_\mu u_\nu \right) \ , \tag{9.5}$$

where ξ and η are the coefficients of bulk and shear viscosity.

The equations of dissipative relativistic fluid dynamics form a self consistent set of partial differential equations. These equations are the relativistic generalization of the well known Navier–Stokes equations of fluid dynamics. It can be shown that these equations are of the parabolic type and can lead to the propagation of perturbations faster than the speed of light [7, 8, 4]. This poses a severe limitation on the application of dissipative fluid dynamics to high energy processes. If, however, the flow structure is of a length scale much larger than the mean free path, this precludes propagation velocities faster than the thermal velocities of particles [9]. This is also necessary due to the requirement that dissipative perturbations should be small, compared to other dynamical processes. Consequently, we may use the relativistic theory without any danger, for slow, non-relativistic process, like the droplet formation in relativistic matter [10].

The equations of viscous relativistic fluid dynamics can be formulated in a way similar to the nonrelativistic theory. For the sake of more compact notation we can introduce the operator of derivation orthogonal to the flow

$$\bigtriangledown^\iota \equiv \Delta^{\iota\nu} \partial_\nu = \partial^\iota - u^\iota u^\nu \partial_\nu \ , \tag{9.6}$$

where $\Delta^{\iota\nu} = g^{\iota\nu} - u^\iota u^\nu$ is the projector in the direction orthogonal to the flow. (These have the properties: $\bigtriangledown^0_{(LR)} = 0$, and $\bigtriangledown^i_{(LR)} = -\bigtriangledown_{i\ (LR)} = -\partial_i$, which means that it is purely spatial in the local rest frame (LR) $u^\mu \bigtriangledown_\mu = 0$, and $\Delta^{\mu\nu}_{(LR)} = \Delta_{\mu\nu(LR)} = \mathrm{diag}(0,\text{-}1,\text{-}1,\text{-}1)$ and $\Delta^\mu_{\nu\ (LR)}\ \mathrm{diag}(0,1,1,1)$ and $\Delta^\mu_\mu = 3$, These operators have the following properties: $\Delta^{\mu\nu} u_\nu = 0$, $\Delta^{\mu\nu}\Delta_{\nu\sigma} = \Delta^\mu_\sigma$ and $\bigtriangledown_\mu u^\mu = \partial_\mu u^\mu$. Using these projectors the stress tensor, eq. (9.5), can be written in the form

$$\Pi^{\mu\nu} = -\eta(\bigtriangledown^\mu u^\nu + \bigtriangledown^\nu u^\mu) - \left(\xi - \frac{2}{3}\eta \right) (\bigtriangledown_\iota u^\iota) \Delta^{\mu\nu} \tag{9.7}$$

Using the thermodynamical identity

$$d\left(\frac{\mu}{T}\right) = -\left(\frac{w}{nT^2}\right) dT + \left(\frac{1}{nT}\right) dP \ , \tag{9.8}$$

the particle flux takes the form

$$N^{\iota\ (1)} = \frac{\lambda}{c} n \left(\frac{1}{w}\right) \left[\bigtriangledown^\iota T - \frac{T}{w} \bigtriangledown^\iota P\right] \ , \tag{9.9}$$

where λ is the coefficient of thermal conductivity. $N^{\nu\ (1)}$ tends to zero if the baryon density n tends to zero. Using the thermodynamical identity (9.8) the dissipation given by eq. (9.3) takes the form

$$\partial_\iota \left(s u^\iota - \frac{\mu}{T} N^{\iota\ (1)}\right) = -\frac{\lambda}{c} \left\{ \frac{1}{T^2} \partial_\iota T \bigtriangledown^\iota T + \frac{1}{w^2} \partial_\iota P \bigtriangledown^\iota P - \frac{1}{wT} \left[\partial_\iota T \bigtriangledown^\iota P + \partial_\iota P \bigtriangledown^\iota T\right] \right\} - \frac{1}{T} \Pi^\iota_\nu \ \partial_\iota u^\nu \ . \tag{9.10}$$

For baryon free matter from (9.8) it follows that $(1/T) \bigtriangledown_\iota T = (1/w) \bigtriangledown_\iota p$. Using this for transformations on the right hand side of eq. (9.10), the first term vanishes. I.e., the heat conductivity alone does not lead to dissipation in baryon free matter, and obviously $N^{\mu\ (1)} = -\frac{n}{w} I^\mu_q \to 0$.

Thus, for baryon free matter the equation for the entropy production, (9.10), takes the form

$$\partial_\iota \left(s u^\iota\right) = \frac{1}{T} \eta \frac{1}{2} [\bigtriangledown^\mu u_\nu + \bigtriangledown_\nu u^\mu - \frac{2}{3} \Delta^\mu_\nu (\partial_\sigma u^\sigma)]^2 + \frac{1}{T} \xi (\partial_\sigma u^\sigma)^2 \ , \tag{9.11}$$

so that the dissipation is proportional to η and ξ. Using the relations $\bigtriangledown^\nu = \bigtriangledown_\mu \Delta^{\mu\nu}$ and $\Delta^{\mu\nu} \bigtriangledown_\nu = \bigtriangledown^\mu$, the four divergence of the stress tensor takes the form

$$\bigtriangledown_\mu \Pi^{\mu\nu} = \Delta^\sigma_\mu \partial_\sigma \Pi^{\mu\nu} = -\eta (\bigtriangledown_\mu \bigtriangledown^\mu u^\nu) - \left(\xi + \frac{1}{3}\eta\right) \bigtriangledown_\mu \Delta^{\mu\nu} (\bigtriangledown_\iota u^\iota) \ .$$

In the shearless limit, $\bigtriangledown_\mu \bigtriangledown^\mu u^\nu = \bigtriangledown^\nu (\bigtriangledown_\mu u^\mu)$, this reduces to

$$\bigtriangledown_\mu \Pi^{\mu\nu} = -\left(\xi + \frac{4}{3}\eta\right) \bigtriangledown_\mu \Delta^{\mu\nu} (\bigtriangledown_\iota u^\iota) \quad \propto \quad \partial_\mu \Pi^{\mu\nu} = -\left(\xi + \frac{4}{3}\eta\right) \partial_\mu \Delta^{\mu\nu} (\partial_\iota u^\iota) \ . \tag{9.12}$$

Comparing this to the four divergence of the energy-momentum tensor of a perfect fluid

$$\partial_\mu T^{\mu\nu} = \partial_\mu (e u^\mu u^\nu) + \partial_\mu \Delta^{\mu\nu} P \ , \tag{9.13}$$

we can see that in the equations of motion, in the shearless limit the only change is that the pressure is replaced by

$$P \to P^* = P + \pi \ , \tag{9.14}$$

where the correction to the pressure in the one dimensional case relevant to us, π, is

$$\pi = -\left(\xi + \frac{4}{3}\eta\right) (\partial_\mu u^\mu) \ , \tag{9.15}$$

where the unit of $\xi,\ \eta$ is [MeV fm^{-2} c^{-1}].

The contribution to the stress-energy-momentum tensor due to dissipation is

$$T_{\mu\nu\ (1)} = -\eta \left(\partial_\mu u_\nu + \partial_\nu u_\mu - u_\mu u^\iota \partial_\iota u_\nu - u_\nu u^\iota \partial_\iota u_\mu\right) - (\zeta - \frac{2}{3}\eta)(\partial_\iota u^\iota) \left(g_{\mu\nu} - u_\mu u_\nu\right) \ . \tag{9.16}$$

The coefficients of shear and bulk viscosity must be positive from the requirement that the entropy should not decrease. In fact, the divergence of the entropy current in the absence of baryons is

$$\partial_\mu (s u^\mu) = -\frac{1}{T} T^{\mu\ (1)}_\nu \partial_\mu u^\nu \ , \tag{9.17}$$

from which one can calculate the total entropy change of the system. This equation is a direct consequence of the equations of motion, which are just the usual ones of conservation of energy and momentum, $\partial_\mu T^{\mu\nu} = 0$. In general this description is applicable if the flow three-velocity is small compared to the speed of light. The relativistic treatment is required mainly by the fact that the pressure is comparable to the energy density, and by the absence of a net baryon number to define the motion of the matter.

9.1.2 Shock front profiles

The entropy production can be evaluated in the shearless limit (9.15) following the standard derivation given in sect 127 of ref. [5]. Introducing the notation

$$\dot{a} \equiv u^\mu \partial_\mu a \equiv u^\mu a_{,\mu} \ , \tag{9.18}$$

the entropy production is obtained as [11]:

$$\dot{\sigma} = \left(\xi + \frac{4}{3}\eta\right) \frac{1}{nT} \left(\frac{\dot{n}}{n}\right)^2 = \eta_{\text{eff}} \frac{1}{nT} \left(\frac{\dot{n}}{n}\right)^2 \tag{9.19}$$

This enables us to have a simple estimate for the width or thickness of the compression shock fronts in heavy ion reactions. If the width of the front if L_{sf} the derivatives can be estimated as

$$\dot{\sigma} = \frac{\Delta\sigma}{L_{sf}}, \qquad \dot{n} = \frac{\Delta n}{L_{sf}} \ . \tag{9.20}$$

The values of $\Delta\sigma$ and Δn are fixed by the Rankine–Hugoniot–Taub relations, so these do not depend on the structure or thickness of the front. This way eq. (9.19 yields

$$\frac{\Delta\sigma}{L_{sf}} \sim \bar{\eta}_{eff} \frac{1}{\bar{n}\bar{T}} \frac{\Delta n^2}{L_{sf}^2 \bar{n}^2} \ . \tag{9.21}$$

This indicates that the width of the shock front is proportional to the average effective viscosity in the front

$$L_{sf} \ \sim \ \bar{\eta}_{eff} \ . \tag{9.22}$$

The width of the shock front is an important quantity because the fluid dynamical considerations for the initial stages of the reaction can hold only if the system is considerably larger than the width of the front. Estimates for intermediate energy heavy ion reactions range between $L_{sf} \approx 0.5 - 3$fm.

The value of the viscosity can also be calculated in kinetic theory and for dilute gases it is evaluated in standard textbooks[1, 3]. The viscosity of the quark gluon plasma will be discussed in section 10.4. The viscosity is proportional with $\sqrt{T}$ for dilute gases. Estimates for low energy nuclear matter range between $\eta = 6 - 20$MeV fm^{-2} c^{-1}.

For sub-QGP densities and temperatures the transport coefficients were evaluated by Danielewicz [12], see Fig. 9.1. We see that the viscosity diverges for low temperatures and high densities. This is caused by the Pauli principle which limits the possible collisions.

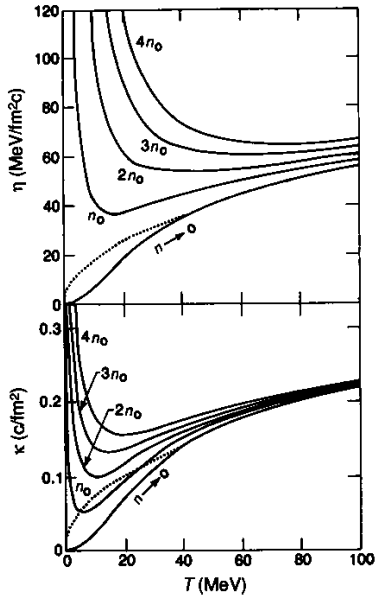

Figure 9.1: The temperature and density dependence of the nuclear matter transport coefficients. The dotted lines denote the Chapman–Enskog results with the effective cross section $\sigma = 30$mb. Reproduced by permission of Elsevier Science Publishing from [12].

This would result in a wide shock front in low energy reactions and therefore the fluid dynamical approach is not valid in this domain. The shock front is sufficiently sharp already at around 400 A MeV beam energy and above (see Fig. 9.2).

Although large scale numerical calculations are mostly in the perfect fluid approach, they yield shock waves with similar thickness. This is due to the so called numerical viscosity in these models.

We have seen the important effects of viscosity on fluid dynamical scaling in Chapter 8. These viscous effects are apparent in the observed transverse flow. The theoretical values for the viscosity were taken from the calculation shown in Fig. 9.1 for the analysis of scaling violation presented in Chapter 8. The good agreement between theory and experiment indicates that heavy ion reactions are able to provide accurate information both on the EOS and on the transport properties of the dense and hot nuclear matter.

9.2 Multi Component Fluid Dynamics

The initial distribution of nucleons in an energetic heavy ion collision is far from a thermal equilibrium distribution. The nucleon distribution is close to the ideal Fermi gas momentum distribution both in the target and the projectile, and these two distributions are separated from each other by the beam momentum, which is much larger than the Fermi momentum at relativistic energies (see sect. 3.4)

The basic idea behind the multi-fluid models is to start with two initially independent

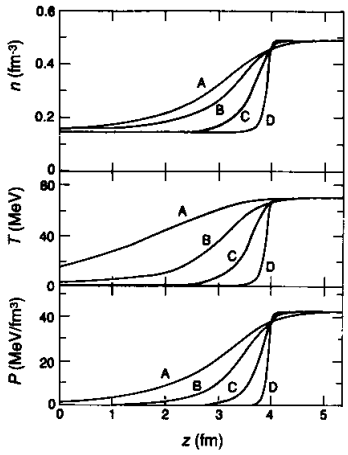

Figure 9.2: Shock front profiles. Rest frame density, n, temperature, T, and pressure, P, as a function of the distance, z, in the shock-wave frame. The shock wave corresponds to $E_{Lab} = 400$A MeV. Curves A and B are calculated using coefficients from Fig. 9.1, curves C with $\eta = 18.6\ (1 + T/20)^{1/2}$ MeV/fm^{2}c and curves D with $\eta = 6$ MeV/fm^{2}c. Curve A includes the effect of heat conductivity also the others do not. Reproduced by permission of Elsevier Science Publishing from [12]

fluid components. These then interact with each other during the heavy ion collision, and either get modified or populate other fluid components like the central thermalized nucleon fluid. It is also possible to consider different particle species as fluid components. Two fluid dynamics for example is a standard theory to describe electron - ion plasma.

There is a large number of such approaches in the literature. [13, 14, 15, 16, 17] We can start out from the BTE again, particularly from the form introduced in sect. 3.5 for mixtures. If the components are identical particles, like nucleons, then the total nucleon phase space distribution is given by

$$f(x,p) = \sum_{k=1}^{N_{comp}} f_k(x,p_k) \ .$$

Each component is then described by a separate BTE

$$D\ f_k = \sum_j C_{kj}\,[f f_k f_j] \ .$$

The sum of these equations returns the full BTE. One can get the conservation laws for each component as in sect. 3.6 and a set of fluid dynamical equations (sect. 3.9). Of course the collision integrals will not vanish completely now, and the obtained set of fluid dynamical equations will have couplings among them, so called drag terms (arising from the collision integrals).

The drag terms among the fluid components can be evaluated in kinetic theory from the collision integrals. Quite frequently simplifying assumptions are applied which are different in different models.

For example in ref. [14] each collision among two different components result in particles belonging to the third thermalized central component. Thus the fluid dynamical equations have a source term in the continuity equation for the third component and two corresponding loss or drain terms in the first (projectile) and second (target) component. The particles scattering into the third thermal component carry all their energy and momentum with them to the third component. Due to this the target and projectile components will have the same specific energy but the temperature of the third thermal component will increase. This leads to a gradual thermalization and local thermal equilibrium is achieved in roughly 8fm/c after the impact (see Figure 9.3)

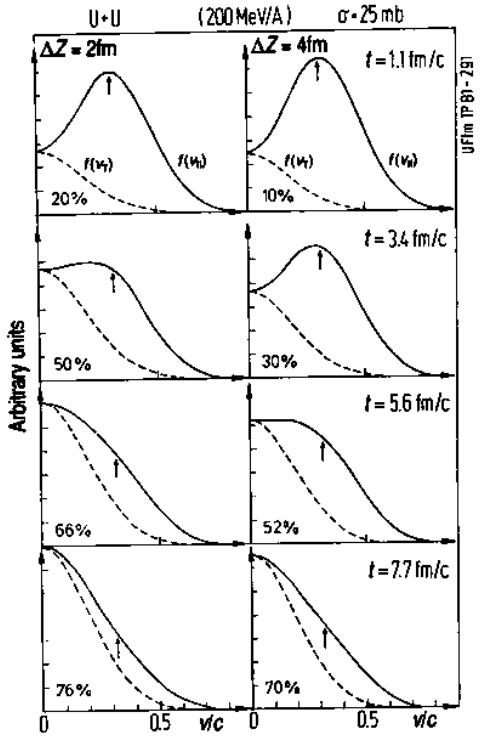

Figure 9.3: The development of the momentum distribution of the central region in the beam direction and in the orthogonal direction. The speed of thermalization is similar to the one obtained in cascade and kinetic models. The arrows indicate the initial target and projectile velocity. The given percent values indicate the degree of thermalization; $< n_3 > / < n >$, in the region Δz around the c.m. Reproduced with permission from [14]

In the multifluid models shock waves also develop and their thickness is of the order of 1-3fm. However, if the nucleon nucleon cross section is reduced to $\sigma = 2mb$, the model becomes transparent, a majority of particles will continue their propagation after the collision in the same direction and only a small third component will develop.

A disadvantage of the multi-component fluid dynamical approach is that the components are not always forming a dilute gas, and consequently the coupled fluid dynamical equations cannot be derived in a rigorous way from the BTE. It is particularly problem-

atic to use more fluid dynamics if we intend to describe a phase transition. The fluid components are generally overlapping in space with different partial flow velocities and other characteristic parameters. It is hard to imagine how can one find a unique well defined description in a more fluid model for a system undergoing a phase transition during the collision. Just imagine one fluid component is in one phase and another component, overlapping with it but flowing in a different direction, is in the other phase or in the mixed phase!

9.3 Solutions on microscopic level

The most straightforward way of solving the Boltzmann Transport Equation is to simulate the particle propagation and collisions on a computer. The numerical Monte-Carlo method for the solution can be performed in many ways. The most frequent is, however, to represent each particle numerically. This makes it easy and straightforward to implement the collision term, cross sections, etc. in the numerical model.

One such simulation gives of course a very fluctuating single particle distribution function, $f(x, p)$, but it is not problematic nowadays to calculate a large number of simulations for the same collision and the average of this ensemble of simulated events will provide already a smooth distribution. Most frequently a statistical ensemble of 1000 to 10,000 events is realized. In most cases the statistical accuracy of the experiments can also be reached by numerical simulations. (The exceptions are exotic particles with a multiplicity of 10^{-4} or 10^{-5} per collision: to reproduce their cross sections with satisfactory accuracy is quite expensive numerically.)

The most important advantage of these microscopic models that they produce a physical event closely similar to the experimental events. The final set of emerging particles in a numerical simulation can be analyzed exactly the same way as it is done in experiments. All measurables can be evaluated in a straightforward way. The numerical codes doing such experimental evaluation are frequently the same and they are used both for measured particle data as well as for simulated data.

Obviously these microscopic models are the most frequent and most popular in the study of heavy ions. They provide immediate explanation to many measured effects based on microscopic assumptions only. Although the realization of all possible microscopic processes may be quite extensive the task is quite straightforward and can be performed safely. These codes are not facing problems with numerical instabilities, etc. unlike many of the numerical fluid dynamical models.

To provide a deeper macroscopic insight into the reaction mechanism and into the collective behavior of the matter needs, nevertheless, a quite serious extra effort in these models. Macroscopic parameters, like local baryon density or energy density can be evaluated using coarse graining. The calculation of all thermodynamical quantities, like the local entropy density, is not an easy task any more. Thus to evaluate e.g. the underlying EOS of such a model is possible but usually so difficult that it is hardly ever done.

9.3.1 Intranuclear cascade models

The Intra-Nuclear Cascade (INC) model was originally introduced for high energy (GeV) p+A collisions more than 40 years ago. It followed numerically the path of the incoming proton in the phase space, followed all its collisions with the nucleons of the target. A collision is simulated the following way: if the proton along its path approaches a nucleon closer than some minimum distance, $d = \sigma(\sqrt{s})$, the proton will scatter and the final state will be randomly generated according to the energy, $\sqrt{s}$, dependent cross section. Total energy and momentum should be conserved of course. Then the outgoing particles propagate along straight line trajectories until the next collision.

Inelastic processes like $N + N \rightleftharpoons N + \Delta$ or $\Delta \rightleftharpoons \pi + N$ can be included in a straightforward way.

At low energies the Pauli principle is also taken account usually in the following way. A collision will be *Pauli-blocked* randomly according to the probability $[1 - f(x, p)]$, evaluated at the final state of the outgoing particles.

The Nucleus - Nucleus INC is a superposition of the earlier p+A models. We describe simultaneously the collisions of all projectile (and target) nucleons. We have to set up an initial state: we generate random positions for the nucleons according to the density distribution of the nucleus, and we also generate random momenta according to the Fermi distribution of the nucleus. These momenta are then boosted by the beam velocity in the frame of calculation.

To avoid that the target and projectile nuclei fly apart before their impact the random Fermi momenta are *frozen in* until their first collision, i.e. they propagate only according to the beam velocity. The first collision unfreezes the random Fermi motion.

The proper treatment of secondary collisions is also important in INC models for Nucleus - Nucleus collisions. Two nucleons within the projectile nucleus or the target nucleus are not allowed to collide until their first collision, but if a nucleon has already collided the secondary nucleons are allowed to collide on any nucleon in the system. Earlier INC models did not always allow all collisions, limiting therefore the possibility to achieve thermalization in the model.

It turns out, however, that the INC is not a solution of the BTE in a strict sense, but rather of an other set of kinetic equations. For details see ref. [18] and references therein.

9.3.2 Mean field models: BUU - VUU - BN - LV

The BTE was introduced in Chapter 3 without an external field. In the non-relativistic theory it is usual to include on the left hand side of the BTE the effect of an external force[3]

$$(\partial_t + \vec{v}\nabla_x + \frac{\vec{F}}{m}\nabla_p) f_1(x, p) = C[f_1 f_2] \text{or}$$

$$(\partial_t + \vec{v}\nabla_x - \frac{\nabla_x U}{m}\nabla_p) f_1(x, p) = C[f_1 f_2] \ .$$

The nucleus being a self-bound system of nucleons is kept together by a mean field potential U. Nucleons are then bound in this self-consistent mean field potential, and

they propagate along curved trajectories as determined by the mean field.

The nucleons were artificially kept together initially in the INC model, furthermore, they did not feel the repulsive effect of nearby nucleons even at large nucleon densities. To avoid these problems it is straightforward to introduce an "external" potential.

Although, the mean field potential is calculated in low energy nuclear physics accurately using advanced methods [18] in most calculations the mean field is assumed to be a simple function of local baryon density. The baryon density is calculated from the average density of the whole calculational ensemble. Thus it provides a smooth potential surface responsible for binding and collective repulsion.

The introduction of such a mean field potential solved the problem of keeping the nuclei together before the collision and freezing in the momentum distribution before the collision is not necessary any more. In this model the initial states of nuclei can be dynamically stable nuclear configurations.

The introduction of mean field led to a revolution in the capacity of the microscopic models. For example the cascade models were not able to describe accurately the observed collective transverse flow in heavy ion collisions. The introduction of mean field, which is repulsive at high average baryon densities reproduced the data without any difficulty.

The mean field potential has a certain degree of freedom, for example the potential may be momentum dependent. Considering such a momentum dependence the same transverse flow experiments can be described with a much softer potential.

Contrary to the overwhelming success of these microscopic models with mean field there are some drawbacks of the model which should be mentioned. One is a theoretical problem of separating the nucleon nucleon interaction to a mean field and a cross section part. In a dense matter this is not a trivial task and obviously the nucleon-nucleon cross section must not be the same as in the vacuum. On the solution of this problem see ref. [19] and references therein.

The other problem is related to the fact that due to the ensemble averaging the mean field is smooth and density fluctuations are decreased. This leads to large discrepancies compared to observed nuclear fragment formation. The smooth mean field does not permit the formation of smaller self-bound clusters or nuclear fragments. This was clearly contrary to experiments. Thus these models are manifestly applicable for single particle observables, but phenomena like fragment formation or multifragmentation cannot be calculated in a one particle theory.

9.3.3 Models of Molecular Dynamics

To solve this problem we need to consider N-particle correlations and N-particle distributions explicitly. This is done in the *classical equations of motion* approach or in molecular dynamics approaches or in the so called Quantum Molecular Dynamics (QMD) approach (see refs. [20, 21, 22] and references therein).

Here we have to follow each particle separately and calculate their interactions with all other particles one by one. This is a much larger computational expense than the previous approaches, but it is necessary to maintain the N-particle correlations.

In the purely classical approaches quantum features are missing. The theoretical problem of constructing a nucleon nucleon interaction which reproduces both the scattering and the ground state properties is also a nontrivial problem[19]. The QMD approach is essentially a classical equation of motion approach also, but it includes a few quantum effects like the random scatterings, Pauli blocking of scatterings and stochastic particle decays. These models are quite successful in reproducing multifragmentation experiments, but similarly to the previous microscopic models it requires a considerable extra effort to extract collective macroscopic information from the model applicable for the dense and hot matter.

9.4 Assignment 9

9.a Assume that we have two coexisting phases in a fluid, $i = 1, 2$, described by volume fractions, $\lambda_i = V_i/V_{tot}$, or equivalently by particle number fractions, $\alpha_i = N_i/N_{tot}$, so that $\lambda_i = \alpha_i n/n_i$, where $n_i = N_i/V_i$. Let us assume that the system is thermalized but the Gibbs criteria are not necessarily fulfilled. The energy momentum tensor for the whole system can be given as

$$T^{\mu\nu} = \sum_i \lambda_i T_i^{\mu\nu} \ .$$

Calculate the entropy production as a function of the change of α_i and λ_i.

9.4.1 Solution to Assignment 9

9.a The partial energy-momentum tensors are given by $T_i^{\mu\nu} = w_i u^\mu u^\nu - P_i g^{\mu\nu}$. From

$$T^{\mu\nu}{}_{,\nu}\, u_\mu = 0 \quad \rightsquigarrow$$

we obtain

$$\sum_i u_\mu \left(\lambda_i (w_i u^\mu u^\nu - P_i g^{\mu\nu})\right)_{,\nu} = 0 \quad \rightsquigarrow$$

$$\sum_i (\lambda_i w_i)_{,\nu} \underbrace{u_\mu u^\mu}_{=1} u^\nu + \lambda_i w \underbrace{u_\mu u^\mu{}_{,\nu}}_{=0} u^\nu + \lambda_i w_i \underbrace{u_\mu u^\mu}_{=1} u^\nu{}_{,\nu} - (\lambda_i P_i)_{,\nu} \underbrace{u_\mu g^{\mu\nu}}_{=u^\nu} =$$

$$\sum_i (\lambda_i w_i)_{,\nu}\, u^\nu + \lambda_i w_i u^\nu{}_{,\nu} - u^\nu (\lambda_i P_i)_{,\nu} = 0.$$

From the continuity equation, $(nu^\mu)_{,\mu} = 0$ follows that $u^\mu n_{,\mu} = -n u^\mu{}_{,\mu}$ and $u^\mu{}_{,\mu} = -(u^\nu n_{,\nu})/n$. Inserting this into the previous equation:

$$\sum_i n u^\nu \left[\underbrace{\frac{1}{n}(\lambda_i w_i)_{,\nu} - n_{,\nu} \frac{(\lambda_i w_i)}{n^2}}_{(\lambda_i w_i/n)_{,\nu}} - \frac{1}{n} \underbrace{(\lambda_i P_i)_{,\nu}}_{=(\lambda_i P_{i,\nu} + P_i \lambda_{i,\nu})} \right] = 0 \ .$$

Using the relation between the volume and particle number ratios of the two phases, $\lambda_i = \alpha_i n/n_i$, we arrive at

$$\sum_i n u^\nu \left[(\alpha_i w_i/n_i)_{,\nu} - \frac{\alpha_i}{n_i} P_{i,\nu} - \frac{1}{n} P_i \left(\frac{\alpha_i n}{n_i} \right)_{,\nu} \right] = 0 \ ,$$

and after performing the differentiations we get

$$\sum_i n u^\nu \left[\alpha_{i,\nu} \left(\frac{w_i}{n_i} \right) + \alpha_i \left(\frac{w_i}{n_i} \right)_{,\nu} - \frac{\alpha_i}{n_i} P_{i,\nu} - \frac{1}{n} P_i \left(\frac{\alpha_i n}{n_i} \right)_{,\nu} \right] = 0 \ .$$

Now we make use of the thermodynamical relations $\chi_i = w_i/n_i = \epsilon_i + P_i\nu_i = T_i\sigma_i + \mu_i$, and its differential form $d\chi = Td\sigma + \nu dP$, which leads to $T_i d\sigma_i = d\left(\frac{w_i}{n_i}\right) - \frac{1}{n_i} dP_i$, and using the relation $\dot{} \equiv \partial_\tau \equiv u^\nu \partial_\nu$ we can rewrite the above expression in the form

$$n \sum_i \left[\dot{\alpha}_i (T_i\sigma_i + \mu_i) + \alpha_i T_i \dot{\sigma}_i - \frac{1}{n} P_i \left(\frac{\alpha_i n}{n_i} \right)^{\cdot} \right] = 0.$$

Reorganizing the terms we arrive at

$$n \sum_i \left[T_i (\dot{\alpha}_i \sigma_i + \alpha_i \dot{\sigma}_i) + \dot{\alpha}_i \mu_i - \nu P_i \dot{\lambda}_i \right] = 0.$$

Let us now assume that $T_1 = T_2 = T$, i.e. the thermal equilibrium is established

$$\dot{\sigma} = \left(\sum_i \alpha_i \sigma_i\right)^{\cdot} = \frac{1}{T} \left[-\sum_i \dot{\alpha}_i \mu_i + \nu \sum_i P_i \dot{\lambda}_i \right] = -\frac{1}{T} (\mu_1 - \mu_2) \dot{\alpha}_1 + \frac{\nu}{T} (P_1 - P_2) \dot{\lambda}_1 \ .$$

Thus non-equilibrium phase transition leads to entropy increase!

To solve the complete dynamical problem each of the not satisfied Gibbs criteria should be replaced by a dynamical equation. According to non-equilibrium thermodynamics the generalized currents like $\dot{\alpha}_i$ or $\dot{\lambda}_i$ are driven by generalized thermodynamical forces which act in the direction of restoring the equilibrium:

$$\mu_1 = \mu_2 \rightsquigarrow \dot{\alpha}_1 = -(\alpha - \alpha_{eq}(n, T, P))/\tau_{ch} \ ,$$

$$P_1 = P_2 \rightsquigarrow \dot{\lambda}_1 = -(\lambda - \lambda_{eq}(n, T, P))/\tau_{pr} \ .$$

Consequently the dissipation is determined by the ratio of the time scale characterizing the dynamics of the process, τ_{dyn}, and the phase equilibration times, τ_{ch} and τ_{pr}. An explicit example for such a calculation with explicit evaluations of the time scales is given in refs. [10, 23]

Bibliography

[1] K. Huang: Statistical Mechanics (Wiley, New York, 1963).

[2] S. R. de Groot, W. A. van Leeuwen and Ch. G. van Weert: Relativistic Kinetic Theory (North-Holland, Amsterdam 1980).

[3] F. Reif: Fundamentals of statistical and thermal physics (McGraw-Hill, 1965).

[4] W.A. Hiscock and L. Lindblom, Phys. Rev. **D35** (1987) 3723.

[5] L.D. Landau and E.M. Lifshitz: Fluid dynamics (Nauka, Moscow, 1953).

[6] S. Weinberg, *Gravitation and Cosmology* (Wiley, New York, 1972).

[7] M. Kranys, Nuovo Cim. **50B** (1966) 48.

[8] D.C. Kelly, Amer. J. Phys. **36** (1968) 585.

[9] H.D. Weymann, Amer. J. Phys. **35** (1967) 488.

[10] L.P. Csernai and J.I. Kapusta, Phys. Rev. **D46** (1992) 1379.

[11] L.P. Csernai and H.W. Barz, Z. Phys. **A296** (1980) 173.

[12] P. Danielewicz, Phys. Lett. **146B** (1984) 168.

[13] A.A. Amsden, A.S. Goldhaber, F.H. Harlow and J.R. Nix, Phys. Rev. **C17** (1978) 2080.

[14] L.P. Csernai, I. Lovas, J. Maruhn, A. Rosenhauer, J. Zimányi and W. Greiner, Phys. Rev. **C26** (1982) 149.

[15] H. W. Barz, B. Kämpfer, L. P. Csernai and B. Lukács, Nucl. Phys. **A465** (1987) 743.

[16] A. Rosenhauer, J.A. Maruhn, W. Greiner and L.P. Csernai, Z. Phys. **A326** (1987) 213.

[17] I.N. Mishustin, V.N. Russkikh and L.M. Satarov, in "Relativistic Heavy Ion Physics", eds. L.P. Csernai and D.D. Strottman (World Scientific, Singapore 1991) Vol. 5 p. 180.

[18] D. L'Hote and J. Cugnon in "Relativistic Heavy Ion Physics", eds. L.P. Csernai and D.D. Strottman (World Scientific, Singapore 1991) Vol. 5 p. 38.

[19] W. Botermans and R. Malfliet, in "Relativistic Heavy Ion Physics", eds. L.P. Csernai and D.D. Strottman (World Scientific, Singapore 1991) Vol. 6 p. 596.

[20] J. Aichelin, A. Rosenhauer, G. Peilert, H. Stöcker, and W. Greiner, Phys. Rev. Lett. **58** (1987) 1926.

[21] J. Aichelin and H. Stöcker, Phys. Lett. **176B** (1986) 14.

[22] H. Sorge, M. Berenguer, C. Hartnack, A. von Keitz, R. Mattiello, G. Peilert, H. Stöcker and W. Greiner, in "Relativistic Heavy Ion Physics", eds. L.P. Csernai and D.D. Strottman (World Scientific, Singapore 1991) Vol. 6 p. 642.

[23] L.P. Csernai and J.I. Kapusta, Phys. Rev. Lett. **69** (1992) 737.

Chapter 10

Search for Quark Gluon Plasma

10.1 Introduction

The search for quark-gluon plasma is in progress at present, thus it is not easy to present a final textbook-like assessment of the field. The basic field theory describing hadrons at high energies is the Quantum ChromoDynamics (QCD). Extensive theoretical and experimental effort is necessary, nevertheless, to establish links between QCD and heavy ion experiments. In this brief introduction most generally accepted directions are mentioned. Subsequently some of the important points are discussed in larger detail.

In collisions of two nuclei at ultra-relativistic energies we expect deposition of energy into a space-time region which is much larger and has longer life-time than the fundamental hadronic scale of 1 fm. Thus such collisions provide us with an opportunity to study hot and dense hadronic matter under conditions similar to those which existed in the early universe. The main goals of such investigation are the determination of the properties of the strongly interacting matter at high densities, the determination of the nature of the quark - hadron phase, the verification of the existence of quark gluon plasma in nature and the determination of the parameters of the quark-hadron phase transition which is predicted by lattice QCD calculations and by phenomenological models.

The investigation of the properties of matter at extreme densities provides a link between nuclear and particle physics. It is a natural extension of the study of properties of the nuclear matter, and it is inspired by the dynamics of strong interactions as revealed in particle physics. It provide an experimental tool to study many-body systems at high energies beyond the possibilities of particle physical studies.

To achieve energy densities which are high enough for the deconfinement of quarks and gluons, nuclear beams with energies above 100 A·GeV are needed (for fixed target experiments), although some idealized theoretical calculations give a threshold to the phase transition as low as 10 A·GeV. A first exploratory phase in 1986-1987 at the CERN-SPS and BNL-AGS pursued successfully the aim to demonstrate the feasibility of an experimental study of dense hadronic matter. New results are expected from experiments in 1990-1993.

At the CERN-SPS, lead beams will be available in 1994, upgrading the present

program with Oxygen and Sulphur beams significantly. Gold beams are presently accelerated at BNL - AGS already. The Relativistic Heavy Ion Collider (RHIC) at BNL will increase the available energy. The CERN Large Hadron Collider, (LHC) which is expected to start operation in 1998, will increase the c.m. collision energy by more than a factor of 100, and is expected to lead to energy densities several times higher than those at SPS energies (see Table 2.1). Even with conservative estimates of the energy densities, the gain from the large collision energy at LHC may well be a decisive factor in the observation of deconfinement transition. On the other hand, the SPS provides the best energy range for the study of matter at high baryon density.

10.1.1 Theoretical expectations

At extreme densities we expect a deconfinement transition because the presence of many color charges will screen the confining potential between the members of a given $q\bar{q}$ or qqq system. In the early universe, this transition presumably took place a few tens of microseconds after the big bang. Heavy ion experiments provide the tool to study in the laboratory both the quark-hadron phase transition and the properties of the primordial quark-gluon plasma. On the theoretical side, strong interaction thermodynamics, including the critical behavior at the transition, is described by QCD.

QCD Predictions

The parameters of the transition (energy density, temperature, baryon density, screening length) have been studied in QCD, both by computer simulation of the lattice formulation and in various phenomenological approaches.

In computer simulations of lattice QCD, one tries to calculate the relevant quantities from first principles, without any simplifying physical assumptions. The results give us a reasonably good general understanding of the critical behavior of strongly interacting matter at vanishing baryon number density ($n_B = 0$). This is the first time that basic microscopic dynamics leads directly to *predictions* for equilibrium thermodynamics.

The main predictions from lattice QCD are:

(i) There is an abrupt change from hadronic to QCD regime, which may be interpreted as a phase transition. Whether the transition is first or second order or smooth depends on several model parameters and it is the subject of current research;

(ii) For 2-3 light quark flavors one finds T_c = 150-200 MeV, which corresponds to a critical energy density ε_c = 1-3 GeV/fm^3, necessary to produce QGP;

(iii) The plasma becomes ideal ($\varepsilon \approx 3P$) only for $T/T_c \approx 1.5 - 2$.

Alternative approaches to lattice QCD are given by effective Lagrangian models, bag models and by chiral perturbation theory. These are able to handle baryon rich matter also. Their results agree essentially with those from lattice QCD.

Global Characteristics of the Collision

The crucial features of the collision, such as the highest energy density, the temperature, or the entropy density cannot be measured directly but have to be inferred from experimental observables. The basic quantities for such estimates are the multiplicity density, dN/dy of produced hadrons, the abundances of various particle species and their distribution in phase space (p_t, y).

Some recent significant experimental observations may be summarized as follows:

Energy density: Large multiplicities, of the order of hundreds per unit of rapidity, have been measured. The multiplicity is strongly correlated to the transverse energy, E_T. The shape of the transverse energy distribution versus multiplicity is governed by the geometry of nucleus-nucleus collisions, reflecting the increasing number of "participants" with decreasing impact parameter, b. The corresponding values of energy density, estimated using the Bjorken model, go up to $\varepsilon \approx 2\text{GeV/fm}^3$ at 200 A·GeV with Oxygen and Sulphur beams at SPS.

Baryon density: From p-A collisions at A≈200, we know that in passing through a nuclear target, the projectile proton loses approximately 2 - 2.5 units in rapidity, $\delta y \approx 2 - 2.5$. With this loss, for heavy ions the maximal stopping occurs for $\Delta y \approx 4 - 5$. Model calculations suggest then that the baryon density, n, becomes as large as $n_B/n_0 \approx 10 - 20$ at the point of maximum stopping. A more detailed discussion of nuclear stopping power is given later in this chapter.

Freeze-out volume: Experimentally, the freeze-out size of the system can be determined by particle interferometry, based on the Hanbury-Brown and Twiss effect, originally invented to measure star sizes. If freeze-out takes place when the mean free path, λ, of pions has reached the size of the system, the transverse freeze-out radius, assuming the Bjorken model scenario, becomes $R_F \approx 0.7\text{fm} \times (dN/dy)^\alpha$, where $\alpha = 1/2 - 1/3$. This yields R_F values almost a factor of two larger than the radii of the projectiles. In case of central lead-lead collisions one thus gets the radii ranging from 17 to 31 fm as the beam energy increases from SPS to LHC energies (17 A·GeV to 6300 A·GeV in c.m.).

10.1.2 Experimental facilities

Existing accelerators provide essentially complete coverage in center-of-mass energies from $\sqrt{s} \approx 3$ to 20 A·GeV(see Table 2.1). The maximum attainable energy density is of the order of the critical value, $\varepsilon_c \approx 2$ GeV/fm^3, needed for a phase transition. The region of maximum baryon density at $y_{cm} = 0$ is expected to be in between the top energies of AGS and SPS for the projectiles presently, available. Luminosity and running time are excellent at the AGS and mostly adequate at the SPS, but still marginal for some rare signals (like J/Ψ). However, only light ions could be accelerated up to 1991, which severely restricted the volume and the lifetime of the intermediate states that can be studied at present machines. The global assessment is therefore that

existing accelerators are adequate in the covered energy range, but heavier projectiles are certainly needed.

With the advent of the new heavy ion injectors at Brookhaven (1992) and CERN (1994) and after completion of RHIC (l997), the full spectrum of ion species will be available for experimentation with essentially complete coverage in energy from $\sqrt{s} = 3$ to 200 A·GeV. The maximum energy density will increase by a factor of two at RHIC, the maximum baryon density could be within the range of the SPS (or slightly above), and the luminosity will increase by over one order of magnitude at the SPS. The luminosity at RHIC will be adequate for most signals, however, rare hard processes will be only marginally within reach. Therefore these new facilities constitute a significant improvement in all aspects.

10.2 Quarks and gluons

The theory of quarks and gluons, the quantum chromodynamics (QCD) is the accepted theory of strong interactions. Quarks and gluons are the constituents of hadrons: quarks are spin-$\frac{1}{2}$ fermions, with fractional electric charge and have one of three colors, $N_c = 3$. The color is a new quantum number analog to the electric charge. Gluons are massless spin 1 bosons, similar to photons, but interact among themselves because of their color charges, which can be as many as $N_c^2 - 1 = 8$. Quarks come in different flavors, $u,\ d,\ s,\ c,\ b,\ t$. (See Table 10.1.) Ordinary hadrons, $p,\ n,\ \pi,\ \Delta$, etc., contain u and d quarks only, strange hadrons, Λ, Ω, K, etc. contain strange quarks also, and so on (see Table 10.2). A detailed introduction to QCD can be found in ref. [1] while a detailed introduction to the thermodynamics of high temperature QCD can be found in [2]. In this chapter we use the units $\hbar = c = 1$.

Name	Flavor	Electric charge	Mass≈ [MeV]
up	u	2/3	5
down	d	-1/3	9
strange	s	-1/3	180
charm	c	2/3	1500
bottom	b	-1/3	5000
top	t	2/3	?

Table 10.1: Quark properties

The color gauge group of QCD is SU(3). The generators of the group are G^a, where $a = 1, ..., N_c^2 - 1$, and they satisfy the commutation relation

$$[G^a, G^b] = i\ f^{abc}\ G^c\ , \tag{10.1}$$

with the group structure constants f^{abc}. The generators are conventionally orthogonalized such that

$$\mathrm{Tr}[G^a G^b] = \frac{1}{2}\delta^{ab}\ . \tag{10.2}$$

The generators of the group can be represented by the 3×3 Gell-Mann matrices, λ^a, e.g. $G^a = \frac{1}{2}\lambda^a$. The gluons are described as the quanta of the gauge field A^μ_a with the color index a, $a = 1, ..., N_c^2 - 1$ and space-time index μ. The field strength is

$$F^{\mu\nu}_a = \partial^\mu A^\nu_a - \partial^\nu A^\mu_a - g\ f_{abc} A^\mu_b A^\nu_c\ , \tag{10.3}$$

where g is the strong coupling constant. The gluon field and the field strength are not invariant under an infinitesimal gauge transformation $\alpha_a(\vec{r}, t)$. The gluon fields transform as

$$A^\mu_a \to A^\mu_a + g\ f_{abc} A^\mu_b \alpha_c\ -\ \partial^\mu \alpha_a\ , \tag{10.4}$$

the field strength as

$$F^{\mu\nu}_a \to F^{\mu\nu}_a + g\ f_{abc} F^{\mu\nu}_b \alpha_c\ , \tag{10.5}$$

and the quark fields as

$$\psi_k \to \exp[igG^a\alpha^a]\psi_k. \tag{10.6}$$

Here G^a is an $N_c \times N_c$ representation of the color group, and ψ_k is an N_c-dimensional vector in the color space representing a quark field of flavor k. The field strength square is invariant under gauge transformations, $F^{\mu\nu}_a F^a_{\mu\nu} \to F^{\mu\nu}_a F^a_{\mu\nu}$. The Lagrangian of QCD is

$$\mathcal{L} = \sum_{k=1}^{N_f} \bar{\psi}_k (i\gamma_\mu \partial^\mu - M_k - g\gamma_\mu A^\mu_a G_a)\psi_k - \frac{1}{4} F^{\mu\nu}_a F^a_{\mu\nu}\ , \tag{10.7}$$

where γ_μ's are the Dirac gamma matrices, g is the coupling constant of quarks to gluons, M_k is the mass of quarks of flavor k, and N_f is the number of flavors. If $g = 0$ this Lagrangian describes non-interacting, massive quarks, and $N_c^2 - 1$ non-interacting, massless, free gluons [2].

In the non-interacting case the EOS of the QGP is just given by the bag model EOS, where we assume a combination of a free ideal fermion gas (quarks) and a free ideal boson gas (gluons) with the appropriate degeneracy. A bag constant, $B \cdot g_{\mu\nu}$, is added to the energy momentum tensor to account for the vacuum energy difference between the physical and perturbative vacua.

The EOS can be directly calculated from the microscopic Lagrangian via the Grand Canonical Partition function,

$$Z \equiv Z_{GC} = Z(V, T, \mu_1, \mu_2, ...) = \mathrm{Tr}\left[\exp\left(-(\hat{H} - \mu_i \hat{N}_i)/T\right)\right], \tag{10.8}$$

for $i = 1, 2, ...$ conserved charges. All thermodynamical quantities can be calculated from the thermodynamical potential $\Omega \equiv \ln Z$ as it is described in chapter 4 (on EOS).

The functional integral representation of the partition function for high temperatures is presented comprehensively by Kapusta in ref. [2].

10.3 Lattice QCD

In this section some basic features and recent results of lattice QCD will be presented. The aim is not to give an introduction to the physics of lattice QCD, just to give an

Hadron	Quark content
$\pi^+,\ \rho^+$	$u\bar{d}$
$\pi^-,\ \rho^-$	$d\bar{u}$
$\pi^0,\ \rho^0,\ \omega^0$	$^\dagger\ u\bar{u},\ d\bar{d}$
$\eta^0,\ \omega_1^0,\ \omega_8^0$	$^\dagger\ s\bar{s},\ u\bar{u},\ d\bar{d}$
ϕ^0	$s\bar{s}$
$K^0,\ K^+,\ K^{0*},\ K^{+*}$	$^\dagger\ u\bar{s},\ d\bar{s}$
$\bar{K}^0,\ K^-,\ \bar{K}^{0*},\ K^{-*}$	$^\dagger\ u\bar{s},\ d\bar{s}$
$p,\ \Delta^+$	uud
$n,\ \Delta^0$	udd
Δ^{++}	uuu
Δ^-	ddd
$\Sigma^+,\ \Sigma^{+*}$	uus
$\Sigma^-,\ \Sigma^{-*}$	dds
$\Sigma^0,\ \Sigma^{0*},\ \Lambda^0$	uds
$\Xi^0,\ \Xi^{0*}$	uss
$\Xi^-,\ \Xi^{-*}$	dss
Ω^-	sss

Table 10.2: Quark composition of some hadrons. (†Linear composition of these)

overview which enables the reader to understand the final results of these calculations, and to understand the present possibilities and limitations of this approach. A detailed introduction to lattice QCD can be found for example in the book of Creutz [3].

One has to mention the numerical constraints of the present computations. To be able to perform calculations in the asymptotic scaling regime especially for QCD with dynamical quarks a new generation of computers with performances of at least 10^3 times the present ones are needed. Such projects are in principle realistic and under study. Taking the pure gluon theory as a guide, many of the results obtained up to now in QCD with dynamical quarks may not change very much when we move into the asymptotic scaling regime. It is expected that in 3-4 years we will know the QCD predictions much better, with an accuracy sufficient to discuss the available experiments at that time.

In this approach we want to start from first principles, the Lagrangian of quantum chromodynamics (QCD), and obtain quantitative results on the equation of state and on transport properties of the plasma. There is no analytical method known, which allows this. Therefore one has to perform extensive numerical simulations. Although

this research is in progress there are some interesting developments regarding the finite temperature phase transition, its temperature in physical units and its order. The physical case, two nearly massless and one massive quark, is difficult to simulate. The simulations have mainly been performed with some other number of flavors, N_f. The calculations have mainly been done in the following cases:

Pure gluon theory ($N_f = 0$)

Here one may introduce quarks as external sources, then this approach is called the valence quark (or quenched) approximation. Due to the relatively easier computation this approach has been widely used, because, the action is local.

Four degenerate flavors

When discretizing the action one wants to keep chiral symmetry[1]because the important mechanism governing the phase transition is supposed to be the restoration of the spontaneously broken chiral symmetry. It is, however, not known how to keep the full chiral symmetry in the lattice discretization without a severe multiplication of the number of flavors. The use of so called Susskind or staggered fermions (see below) is a compromise. Part of the chiral symmetry is explicit at the prize of having four degenerate flavors. The flavor symmetry is broken on the lattice, but should be restored in the continuum limit [5, 6, 7].

There exists now an exact algorithm, the hybrid Monte Carlo algorithm [8] by which the computer time does not seem to grow much worse with the lattice volume than the local Metropolis update for the pure gluon theory. At present values of the coupling constant it is, however, about 1000 times slower and, as will be discussed below, it is expected to become relatively even slower as the continuum limit is approached.

$N_f = 2$ or $2 + 1$

This case is nearer to the physical situation. We can use staggered fermions, however, only by assuming that two flavors correspond to taking the square root of the fermion determinant (see below). There is then no fermionic representation on the lattice, and we don't know if we have the symmetry corresponding to the number of flavors. There is also no exact algorithm.

[1]Chiral symmetry is invariance in QCD under the transformation $\psi \rightarrow e^{\bar{\alpha}\bar{\tau}\gamma_5}\psi$, where $\bar{\alpha}$ is a constant 3×3 transformation matrix, $\bar{\tau}$ is the isospin, SU(2), matrix, and γ_5 is a Dirac gamma matrix. A potential or interaction may act in a way that the energy of the transformed state changes. For free particles the quantity $\langle\bar{\psi}\psi\rangle$ can be expressed by the integral $\langle\bar{\psi}\psi\rangle = m \int d^3p \; 1/\sqrt{p^2 + m^2} f_{Fermi}(p)$, which goes to 0 if the mass tends to zero and to non-zero if the mass is finite. This quantity is used to test the chiral phase transition as an order parameter and called the chiral condensate. In QCD it is finite when chiral symmetry is broken and it drops to zero when chiral symmetry is restored. On chiral symmetry see for example ref. [4]

10.3.1 The lattice formalism

On the lattice we simulate equilibrium thermodynamics. There is very little known theoretically about the non-equilibrium properties, which may of course also be relevant to the heavy ion experiments.

The physical temperature, T, and volume, V, are given by

$$\begin{aligned} T &= 1/(N_\tau\ a) = \beta^{-1} \\ V &= (N_\sigma\ a)^3 \end{aligned} \tag{10.9}$$

where a is the lattice spacing. Then $V_{\text{Lattice}} = L^3 = \left(\frac{N_\sigma}{N_\tau} \cdot \frac{\hbar c}{T}\right)^3$, i.e. the physical volume of the calculational cell (forming the basis of the periodic boundary condition) can be expressed by the temperature and the lattice size in space and temperature direction. The parameters which one can vary are: the coupling constant g, the bare quark mass, $m_q\ a$, the lattice size in the temperature-direction, N_τ, in the space- direction, N_σ, and the number of dynamical quark flavors, N_f. Because of asymptotic freedom there should exist a continuum limit when $g \to 0$. In this limit the correlation lengths go to infinity in lattice units, i.e. for fixed physical masses, which are the inverses of the correlation lengths, the lattice spacing, a, goes to zero. Furthermore we want to take the thermodynamical limit $V \to \infty$ at fixed T.

The lattice discretizes the space-time, so that x becomes a discrete variable, describing the lattice site. There are links in the lattice extending from this site to all neighboring sites. A directed link can be characterized by the site of origin and by the direction of the neighbor: x, μ. Four directed links may form a closed loop, a plaquette. The continuum gluon and quark fields, $A_\mu(x)$ and $\psi_k(x)$, are represented by bosonic and fermionic quantities, $U_{x,\mu}$ and $\chi_{x,k}$ respectively. We can associate a matrix, $U_{x,\mu}$, with every link of the lattice

$$U_{x,\mu} = e^{ig\ A^c_\mu G^c\ a}\ , \tag{10.10}$$

where a is the lattice spacing and μ is the direction of the link. A^c_μ is evaluated at the coordinate of the middle of the link. In fact Wilson [9] proposed an action in terms of the lattice, which returns the QCD in continuum limit. The action is a sum over all elementary squares of the lattice

$$S = \sum_{\square} S_{\square}. \tag{10.11}$$

The action on each of these squares or plaquettes is the trace of the product of the group elements surrounding the plaquette. It consists of a gluonic part, S_G, and a fermionic part, S_F.

The functional integral representation of the partition function, thus can be discretized on the lattice by introducing the contributions of plaquettes to these integrals and reducing the functional integrals to discrete sums over all possible discrete configurations.

$$Z_{QCD} = \int \prod_{x,\mu} dU_{x,\mu} \prod_{x,k} d\chi_{x,k} d\bar{\chi}_{x,k} \exp[-S_G(U) - S_F].$$

The contribution of gluons to $\sum S_{\square}$ in terms of the $U_{x,\mu}$ matrices

$$S_G(U) = \frac{6}{g^2} \sum_{\nu>\mu} \left(1 - \frac{1}{3} Re\ (\ \mathrm{Tr}[U_{x,\mu} U_{x+\mu,\nu} U^+_{x+\nu,\mu} U^+_{x,\nu}])\right), \tag{10.12}$$

is the so called Wilson action [2]

The contribution of the fermions is more complicated, see [10] and references therein. The so called *staggered* fermion action is given by

$$S_F = \sum_{k=1}^{K} \bar{\chi}_{x,k} Q_k^{x,y} \chi_{y,k},$$

where $K = N_f^s$ is the number of staggered fermions (in the continuum limit $N_f = 4N_f^s$), χ and $\bar{\chi}$ are so called *Grassmann variables* [2], and $Q_k^{x,y}(U)$ is the *fermion matrix* defined as

$$Q_k^{x,y}(U) = \sum_{\mu=0}^{3} D_{x,y;\mu} + M_k a \delta_{x,y}.$$

The *hopping matrices*, $D_{x,y;\mu}$, have non-zero elements only for $y = x \pm \hat{\mu}$, and they are given by $D_{x,y;\hat{\mu}} = \frac{1}{2}\eta_\mu(x)\left[U_{x,\mu}\delta_{x,y-\hat{\mu}} - U^+_{y,\mu}\delta_{x,y+\hat{\mu}}\right]$, where the phase factors are $\eta_\mu(x) = (-1)^{x_0+x_1+\ldots+x_{\mu-1}}$ for $\mu > 0$ and $\eta_0(x) = 1$ [11].

The other representation of fermions on the lattice is the so called *Wilson fermion* representation, which we will not discuss here.

The contribution of the fermions can be integrated out [2, 10] and so only the quantities $U_{x,\mu}$ remain in the contribution

$$Z_{QCD} = \int \prod_{x,\mu} dU_{x,\mu} e^{-S_G(U)} \left(\prod_{k=1}^{K} \det\left[Q_k(U)\right] \right), \tag{10.13}$$

where the four dimensional lattice has the size $N_\tau \times N_\sigma^3$. The coefficient $6/g^2 \equiv \beta_{Lattice} = 2N_c/g^2$ is frequently used to study the properties of phase transition. By varying $\beta_{Lattice}$ on a fixed lattice a phase transition may be observed.

The observables can be obtained by taking expectation values with respect to the integrand in (10.13).

To characterize the two phases, hadron matter versus quark-gluon plasma, one usually employs order parameters, namely the *Polyakov loop*

$$\langle L \rangle \equiv \langle \mathrm{Tr} \prod_{x_0=1}^{N\tau} U_{(\vec{x},x^0),4} \rangle, \tag{10.14}$$

or the *chiral condensate*

$$\langle \bar{\psi}\psi \rangle = \langle \mathrm{Tr}[D(U) + m_q a]^{-1} \rangle. \tag{10.15}$$

The Polyakov loop, L, is related to the free energy of a static quark, and is an exact deconfinement order parameter for the pure SU(3) gauge theory. The chiral condensate $\langle \bar{\psi}, \psi \rangle$ becomes an exact order parameter for the restoration of chiral symmetry for all N_f when $m_q a \to 0$. Other physical quantities measured are, e.g. the energy density, e, the pressure, P, the entropy density, s, and the Debye screening length, r_D. These can be defined in terms of the U-matrices.

[2] The core gives the contribution of one plaquette, and the summation runs over all plaquettes.

10.3.2 The order of the phase transition

Regarding the order of the finite temperature phase transition there exist universality arguments relating the field theory to simpler three dimensional spin models [12]. The universality of a phase transition means that transitions belonging to the same symmetry class have similar behavior of the critical exponents and the same order. For example an SU(N) theory has a global Z_N symmetry under which the order parameter, e.g. L, transforms non-trivially. A spontaneous breakdown of this symmetry is possible. The dynamics near the transition may be governed by a (local) Z_N theory. Then one has the prediction that e.g. SU(3) in $d = 3 + 1$ dimensions is related to Z_3 in $d = 3$. For this latter theory only first order transitions are known. Thus SU(3) should have a first order transition. This is not a complete proof, however, because, e.g. the hypothesis of locality of the interaction may be violated.

For $N_f > 0$ and $m_q = 0$, there is an effective model of the chiral symmetry restoration. QCD with N_f dynamical flavors in 3+1 dimensions should be related to a $U(N_f) \times SU(N_f)$ σ-model in 3 dimensions. As was discussed by Pisarski and Wilczek some time ago, the transition in thus model is expected to be first order for all $N_f > 2$. [13] Recent numerical calculations suggest mostly first order phase transition also[14], but in some cases a continuous transition is observed also.

Pure gluon matter

The present situation regarding the pure gauge theory ($N_f = 0$) is that most calculations predict a first order phase transition. However, the transition is weak in the sense that the latent heat Δe is small compared to the discontinuity predicted by inserting the Stefan-Boltzmann value e_{SB} for an ideal gluon gas. In fact $\Delta e \approx e_{SB}/4$. Furthermore the string tension σ is small compared to its value at zero temperature, $\sigma(T_c) \approx \sigma(0)$, and the Debye screening length r_D is big compared to its value further above the transition $r_D(T_c) \approx 3r_D(1.2\ T_c)$.

Calculations with dynamical quarks

Because of computer time limitations, it has not been possible so far to study QCD with dynamical quarks in the same detail. Still there have been several investigations of QCD [15, 16, 17]. The general conclusion is that there is a first order transition when $m_q \leq 0.1\ T_c$. This seems to be consistent for all values of N_f. The fact that the transition appears only for small masses indicates that it is connected to the restoration of chiral symmetry. Presently there seems to be no evidence for a first order transition for $N_f = 2$. For $N_f = 3$ the first order nature reappears. The physical case seems to be just on the borderline between a discontinuous and a smooth transition.

Finite baryon chemical potential

So far there are no final results yet from lattice QCD, regarding baryon rich plasma, which would be important for the description of the stopping beam energy domain (the CERN-SPS and BNL-AGS). In an effective potential model of QCD for large baryon

chemical potential a first order phase transition was found. Decreasing the chemical potential led to a change at a tricritical point where the phase transition changed to be of second order [18, 19]. The critical temperature (at $\mu_q = 0$) was around $T_c \approx 110$ MeV in the model, while the tricritical point was around $T_t \approx 81 - 107$ MeV and $\mu_t \approx 73 - 82$ MeV, depending on the model parameters. This indicates that in baryon rich matter a first order phase transition may be expected.

10.3.3 Critical temperature

It is quite important to determine the critical temperature, T_c, in physical units with some precision, because we expect the energy density, e, needed in the experiments to create the quark-gluon plasma to behave like

$$e = \text{const. } T_c^4 \tag{10.16}$$

and thus to be sensitive to T_c. In a finite temperature lattice calculation one obtains primarily a possible phase transition at a particular value of the bare coupling $g = g_c(N_\tau, N_f, m_q a)$. We assume N_σ to be so big that there is little dependence on N_σ. The temperature in physical units can only be obtained by setting the scale by another physical quantity. There exist "computer measurements" of T_c by several research teams (see, for example, refs. [20, 21, 22]). One possibility to set the scale for T_c is by using asymptotic scaling to relate it to N_τ.

According to present numerical estimates for $N_f = 0$ asymptotic scaling may have been reached for $N_\tau \geq 8$. The critical temperature is saturating around 220 ± 40 MeV [20]. Another possibility to extract T_c in physical units is to assume scaling but not necessarily asymptotic scaling. Then one measures e.g. the hadron masses at the critical value of the coupling constant but on a lattice with large time extent, i.e. at temperature zero. One has then a connection between T_c and the hadron masses in lattice units, which can be extrapolated to the continuum case and then the physical T_c can be extracted. The results show that T_c in QCD with four degenerate flavors is only about half as big as in the $N_f = 0$ case, if one assumes the masses to be independent of N_f. A similar tendency of lower T_c was already seen for $N_f = 2$ [20].

10.3.4 The Equation of State

A simple model giving the equation of state is the bag model, introduced already in chapter 4. The bag model is certainly too simple to give a completely correct description of the nonperturbative effects, however, for most parameter choices it predicts a first order phase transition, where the entropy density has a jump from its value for the free pion gas to a free quark-gluon gas.

It turns out that the entropy density is also the easiest quantity to measure on the lattice, because it does not require a subtraction of the $T = 0$ value [20, 23, 15, 24, 22]. For $N_f = 4$ there is a clear discontinuity, the upper value is essentially in agreement with the free gas value. For $N_f = 2$ the phase transition is presumably continuous. but the entropy density goes fairly quickly to its free gas value. For $N_f = 0$ the discontinuity

is only about a quarter of the Stefan-Boltzmann value thus indicating a "weak first order transition".

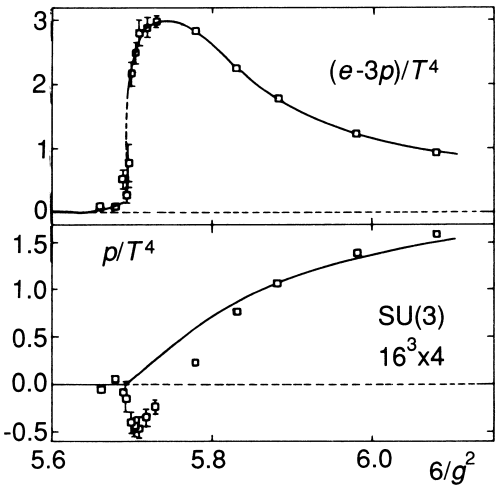

Figure 10.1: The Equation of State as function of the coupling constant g. The pressure p (as p/T^4) and the quantity $(e-3p)/T^4$ is plotted versus $6/g^2$ for $N_f = 0$. From Engels et al., reported in ref. [20]. Reproduced by permission of Elsevier Science Publishers

There are non-perturbative effects, which are clearly seen in some quantities. In Fig. 10.1 the quantity $(e - 3p)/T^4$ for $N_f = 0$ is plotted. It is equal to zero in the free gas limit. In the same figure the pressure is also shown. The data points are from the Columbia University Lattice QCD Group, assuming asymptotic scaling, the full line from Engels, et al. [20], using the same data but defining the pressure by an integral method. Near the transition, the differential method using asymptotic freedom obviously fails. The deviation of the pressure from the free gas value is substantial. For $T = 2T_c$ it is only about 50 % of the free gluon gas value. Clearly the pressure is more sensitive to non-perturbative effects than the entropy density. It must be continuous at the phase transition as discussed by Karsch [25]. The data on pressure and energy density are less precise for $N_f > 0$, still the general picture is the same.

The EOS is a relevant concept for heavy ion collisions only if at some stage of the collision local equilibrium and thermalization do exist. If this is the case already when the maximum baryon charge density and energy density are reached, global collision characteristics are essentially defined by conservation laws for baryon charge, energy and momentum. In such situation the properties of the EOS are largely irrelevant around the transition (1st, 2nd order or smooth) and only the asymptotic properties do matter as it was shown in sect 5.5.

The final hadronization, on the other hand is sensitive to the order of the phase transition. If the transition is 1st order and metastable states exist characteristic phase transition phenomena: supercooling, delayed phase transition, extra entropy production and critical fluctuations become possible.

10.3.5 Screening lengths

One may, in analogy with the screening in an electromagnetic plasma, expect screening in a quark-gluon plasma. This would then lead to disappearance even of "small" resonances like J/ψ or Υ, as was proposed by Matsui and Satz [26]. By resummation of a class of diagrams in perturbation theory one obtains

$$V(r,T) = \frac{\text{const.}}{r^2} e^{-2r/r_D} \ , \tag{10.17}$$

where the potential V is defined on the lattice from the correlation between Polyakov loops

$$\langle L(r)\ L(0)\rangle = \langle L\rangle^2 e^{-\frac{V(r,T)}{T}} \quad \text{and} \quad r_D = \frac{1}{gT\sqrt{1+N_f/6}}. \tag{10.18}$$

This is in analogy with QED where the corresponding Debye screening length can be obtained from classical considerations. In QCD it is uncertain if the thermodynamic limit can be evaluated in perturbation theory, nevertheless, a screening of an effective form

$$V(r,T) = \frac{a}{r^\alpha} e^{-r/r_d} \ , \tag{10.19}$$

is expected, where a, α and r_D are unknown functions of T. Fixing $\alpha = 1$, one obtains values for r_D between 0.1 - 1 [20, 23] Below $r_D \approx 0.3$ the J/ψ should be dissolved. Further studies, extending, the measurements to larger volumes and distances are still needed to clarify the situation.

10.3.6 Summary of present results

Following ref. [20] we can summarize some of the basic results of the ongoing lattice QCD research.

Calculations with dynamical quarks give $T_c < 200$ MeV, if normalized to the hadron masses. If $T_c \approx 150$ MeV in the physical case, the energy density of the quark-gluon plasma just above the phase transition would be only around 1 GeV/fm^3.

For the pure gluon theory, $N_f = 0$, the phase transition is first order, at least for the lattice sizes investigated. For $N_f = 4$ there is also a first order transition for sufficiently small quark masses, thus related to the restoration of chiral symmetry. For $N_f = 2$, however, no discontinuity is observed. The physical case may be a borderline case.

Free gas behavior seems to set in in thermodynamical quantities at least for $T > 2T_c$. For $T < 2T_c$ there may be a modification.

Although the phase transition for $N_f = 0$ is related to deconfinement of static quarks, and for $N_f = 4$ to restoration of chiral symmetry, the properties of the high temperature phase seem to be very similar, in the sense that the quantities e/e_{SB}, s/s_{SB}, r_D and other screening lengths are essentially independent of N_f.

First calculations of the surface tension σ at the phase transition have been performed, still near the strong coupling region. They give $\sigma \approx 0.24 \cdot T_c^3$.

10.4 Surface tension, viscosity and nucleation

If the finite temperature transition is first order there may be supercooling before nucleation occurs. There are indications that large supercooling of the expanding plasma and subsequent rapid deflagration to hadronic matter [27] may be able to explain some recent experimental findings on large strange anti-baryon abundances. As we have seen in the section on shock, detonation and deflagration waves, sect. 5.5, the deflagration may be governed by the nucleation rates in the plasma.

The nucleation rate of baryon free, weakly supercooled, ultra-relativistic QGP was recently estimated in refs. [28, 29]. The rate is governed by the transport coefficients, surface tension, correlation lengths and the EOS. For baryon free matter the heat conductivity is zero. For an ultra-relativistic gas the coefficients of viscosity can be estimated as

$$\eta = \frac{4}{15} a T^4 \tau \quad \text{and} \quad \zeta = 4 a T^4 \tau \left[\frac{1}{3} - \left(\frac{\partial p}{\partial e} \right) \right]^2 , \tag{10.20}$$

where τ is the collision time, and a is the Stefan-Boltzmann constant, defined such that the energy density is $e = aT^4$. Since the square of the sound velocity, $(\partial p/\partial e)$, is close to $\frac{1}{3}$ for ultra-relativistic gases, the bulk viscosity ζ is usually much smaller than the shear viscosity η.

Recently [30] the shear viscosity of quark-gluon plasma was estimated in leading order of QCD. In this case the viscosity is an additive sum of the quark and gluon viscosities, $\eta = \eta_q + \eta_g$. Both components are given in terms of viscous relaxation times for quarks and gluons, τ_q and τ_g. For zero baryon chemical potential

$$\tau_g^{-1} = 4.11 \; T \left(1 + \frac{N_f}{6} \right) \alpha_s^2 \; | \ln \alpha_s | \; , \tag{10.21}$$

where $\alpha_s = g^2/4\pi$ is the QCD fine structure constant. The two terms, 1 and $N_f/6$, come from the contribution of gluon-gluon and gluon-quark scatterings. The viscous relaxation rate for quarks is

$$\tau_q^{-1} \; = \; 0.39 \; \tau_g^{-1} \; . \tag{10.22}$$

Around the critical temperature of 200 MeV, α_s has been estimated to be about 0.23 [2]. The relaxation times at $T = 200$ MeV thus are on the order of 1 fm/c. For QCD with 2 flavors the viscosity is

$$\eta = \frac{1.12 \, T^3}{\alpha_s^2 \ln(1/\alpha_s)} \; . \tag{10.23}$$

The next step is the evaluation of surface tension, σ, in QCD between the two phases. There are calculations for the surface tension using different methods [31, 32]. Conclusive results have only been obtained for $N_f = 0$, and $N_\tau = 2$, i.e. at rather strong coupling. The calculational lattice was divided to two halves, and $\beta_{Lattice}$ was given different values on the two sides of the dividing surface. This resulted in an extra energy, $\Delta E = A \cdot \sigma(\Delta\beta_{lattice})$, compared to the case when no phase difference was present. The energy difference increases with increasing $\Delta\beta_{Lattice}$. The phase transition value of σ

is obtained when $\Delta\beta_{Lattice} \to 0$, so that the dividing surface will be the critical phase transition surface at T_c. The two calculations are in agreement, giving $\sigma = \alpha_0 T_c^3$ where

$$\alpha_0 = 0.24 \pm .06 \quad \text{or} \quad \alpha_0 = 0.22 \pm .05 \tag{10.24}$$

respectively. For $N_\tau = 4$ only an upper limit $\alpha_0 < 1$ has been established. With $T_c \approx 200$MeV the surface tension is $\sigma \approx 50\text{MeV/fm}^2$. This "computer measurement" is certainly a new and interesting application of lattice QCD.

Using these parameters the critical radius, R^*, of a hadronic bubble was estimated to be $R^* \approx 0.5 - 3$ fm for $T \approx 0.8 - 0.97 T_c$ [28], and the transition time due to primary nucleation was in the order of 100 fm/c [29]. The transition is determined then by the interplay between the phase transition dynamics and the global expansion dynamics in a collision. Depending on the mass and energy of the system and the assumed global expansion characteristics the transition may be completed in 5-100 fm/c.

10.5 Nuclear stopping power

Stopping and transparency is a longstanding problem in the description of heavy ion collisions. Different models assume sometimes completely orthogonal viewpoints in this regard.

At the 1 A·GeV energy region the constituents of the nuclear matter are mainly nucleons. At this energy the nucleon mean free path, λ, in heavy nuclei was determined experimentally and turned out to be $\lambda = 2.4 \pm 0.4$fm [33, 34]. According to kinetic theory one needs about $2 - 3\lambda$ for thermalization or interpenetration. Increased density reduces the mean free path proportionally to n_0/n, as well as phase transitions do. Thus the conclusion for the 1 A·GeV region is that ideal one fluid dynamics, which neglects the mean free path, is a rough approximation, viscous or multi-fluid dynamics, as well as different versions of the kinetic models, like VUU, BUU, etc., and molecular dynamics models provide a satisfactory description of the reaction dynamics. (The molecular dynamics models have the leading edge here, due to their ability to describe the final fragmentation[35] more realistically.)

At ultra-relativistic energies the question of stopping is more acute, since the outcome of the experiments is qualitatively influenced by these questions even at the design phase. The results from the 1 A·GeV energy domain cannot be implemented here directly because the basic nucleon nucleon collision mechanism is different: the collision is not a binary collision mostly but associated with multiparticle formation. The reaction products are not distributed isotropically, thus several collisions are needed to reach spherical symmetry. Furthermore the collision is not point like, the produced secondary particles are in a virtual state for some amount of proper time and come to mass shell, as free physical particles, only after. It is still an open question whether the virtual secondaries are able to interact or not in a heavy ion collision.

10.5.1 Proton nucleus collisions

The first question is: can we understand data on nuclear collisions using those for the $p+p$ and the $p+A$ ones? The experimental works[36, 37] studied $p+A$ collisions, at 100 and 200 GeV projectile energy, in order to determine the longitudinal momentum of the leading proton.

There exist a great number of theoretical works [38, 39, 40, 41, 42, 43] where the nuclear stopping power problem is investigated. Different mechanisms of the leading particle deceleration result in the substantial spread in the predicted magnitudes of the nuclear stopping power. This is especially typical for the ultra-relativistic energy region. The models are based on the direct solution of one-dimensional kinetic equations for the leading nucleon momentum distribution. The inelastic NN scattering cross section is parametrized as

$$\frac{1}{\sigma_{NN}}\frac{d\sigma_{NN\to NX}}{dx} = \xi \tag{10.25}$$

where $x = p_z/p_i$, is the ratio of the secondary nucleon longitudinal momentum p_z, and the incident nucleon momentum, p_i (in the lab frame). The quantity ξ is assumed to be independent of p_i[3] and x. This assumption is in good agreement with experimental data on high-energy pp-collisions. For example, as noted in ref. [40], in the region of $E_{Lab.} = 19 - 405$ GeV $\xi_p = \frac{1}{\sigma_{pp}}\frac{d\sigma_{pp\to pX}}{dx}$ varies from 0.43 to 0.55.

The evolution model[35] assumes that the average longitudinal momentum of the leading baryon decreases exponentially with the length of its path, Z, through nuclear matter:

$$\langle p_z(Z)\rangle = p_i \exp[\frac{-Z}{\Lambda_p}], \tag{10.26}$$

where Λ_p is the "momentum degradation length". It is expressed via ξ as

$$\Lambda_p = 2\lambda_N/\xi \ , \tag{10.27}$$

where λ_N is the nucleon mean free path. Eqs. (10.26) and (10.27) are based on the Poisson distribution in the number of leading baryon collisions, ν, with $\langle\nu\rangle = Z/\lambda_N$. For ultra-relativistic energies eq. Eq. (10.26) coincides with the deceleration law used in two fluid dynamics[45]. From a fit to experimental data the value $\Lambda_p = 5.7$fm was extracted in ref. [46].

The evolution or multiple scattering model[35, 39] describes the linear deceleration of a proton in nuclear medium in the $z-$direction. It is assumed that the medium has a thickness of N nucleons in a row. If we introduce the probability distribution, $Q(x)$, that the incident nucleon has momentum fraction x after a collision with one more target nucleon, one can calculate the final x distribution of this nucleon after colliding with N nucleons in a row, $H(x, N)$. If we use the approximate relation, $x \approx p_z/p_i \approx E/E_i \approx \exp[y - y_0]$, valid for ultra-relativistic incident energies outside the narrow region $x \lesssim m_N/p_i$, we can plot the rapidity distribution of the nucleon after penetrating the target:

$$H'(y, N) = H(e^{y-y_i}, N). \tag{10.28}$$

[3] According to the Feynman scaling [44]

$H'(y, N)$ is plotted in Fig. 10.2. We can see that at high values of N, $N = 5,\ 7$ the distribution is peaked by $\Delta y \approx 1.5,\ 2.5$ below the initial proton rapidity, respectively. The spread of the distribution is about twice as large as the deceleration. Considering the fact that $N = 5,\ 7$ represent the diameters of Cu and Pb nuclei, we can conclude that the stopping power is strongly dependent on the size of the nucleus.

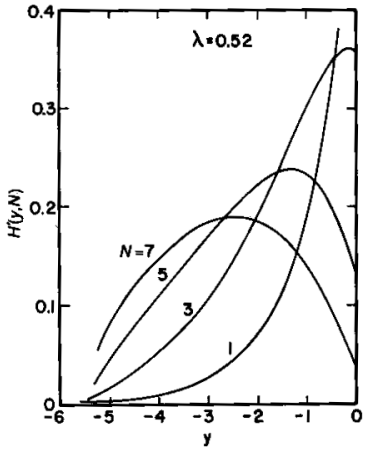

Figure 10.2: Plots of the distribution of nucleon rapidity deceleration, $H'(y, N)$, after the incident nucleon, with rapidity $y_0 = 0$, has collided with N target nucleons in a row. Reproduced with permission from [39].

10.5.2 Heavy ion collisions

The first attempts, before ultra-relativistic experiments were available, estimated stopping in heavy ions based on $p + A$ data. Based on the above estimate two lead nuclei could decelerate each other, so that most nucleons have the c.m. rapidity after the collision, up to collisions with $\Delta y = 5$ or correspondingly up to beam energy $E_{Lab.} = 75$A·GeV. For copper nuclei $\Delta y = 3$ and $E_{Lab.} = 10$A·GeV, respectively. Complete transparency and baryon charge free region at mid rapidity can be expected above $\Delta y = 10$ or $E_{Lab.} = 11,000$A·GeV for lead nuclei. Obviously nuclear effects, such as density increase, rescatterings, eventual phase transition or precritical behavior, etc., can modify these $p + A$ estimates essentially. At ultra-relativistic energy most of the effects one can think of act in the direction of increased stopping [47].

To assess stopping experimentally,one can basically look at the rapidity distribution of secondaries, preferably for baryons and mesons separately. The common wisdom tells us that a strongly peaked baryon rapidity distribution around the center of mass indicates strong or complete stopping, while a distribution which is flat at c.m. or if it has a minimum signals transparency.

Unfortunately to draw an accurate quantitative conclusion is not so trivial. It is true that the Bjorken model, which assumes complete transparency provides a flat baryon distribution for mesons and no net baryon charge at all in the central rapidity region,

where it is valid. We have seen, however, that contrary to the common wisdom, the Landau model—which assumes complete stopping—may produce a rapidity distribution with a dip in the middle also. (Only Landau's original approximate analytic solution yields a Gaussian, but this has limited applicability.) Similarly, relativistic one-fluid models assuming perfect fluid (no dissipation or heat conduction) may yield a bounce back of the projectile and target on each other if two highly Lorentz contracted nuclei collide centrally. This results in a dip at the c.m. in the baryon rapidity distribution also. This indicates that one needs a thorough investigation of the rapidity distribution of all particle species in order to trace down nuclear transparency in heavy ion collisions.

Experimentally the nuclear stopping in $S + S$ collisions at 200 A·GeV can be characterized as follows [48]. In order to quantify the stopped energy the average total energy loss per interacting nucleon was obtained from the rapidity and p_t of the observed protons. The enhanced stopping of the primary nucleons is reflected in $\langle E_{loss} \rangle = 5.8 \pm 0.3$ GeV for central collisions as compared to 4.7 ± 0.3 GeV for peripheral collisions (the latter being a good approximation for NN data). We obtain a total energy deposition of $54 \times 5.8 = 313$ GeV in central S + S collisions. The difference in energy loss per nucleon in central collisions has to be visible in the produced particles. However, the number of negative particles per nucleon pair goes up by 10% only when comparing central S+S with N+N data. Also their mean transverse momentum is unchanged. Therefore we are left with the conclusion that only a small fraction of the additional energy loss of the incoming nucleons is seen in the pions, both with regard to their number and their $\langle p_t \rangle$.

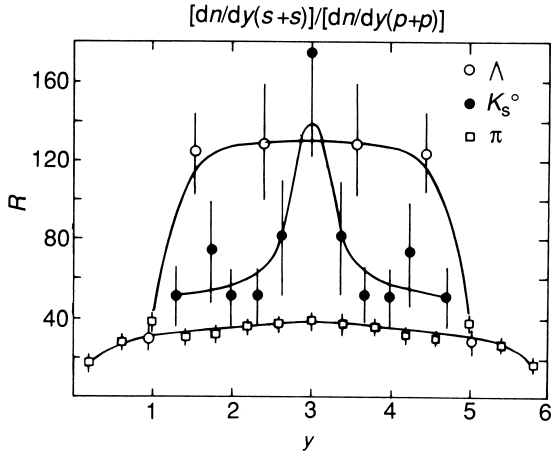

Figure 10.3: The ratio of the rapidity densities in central $^{32}S + ^{32}S$ and $p + p$ collisions. Reproduced by permission of Elsevier Science Publishers from [48].

In Fig. 10.3 the ratio $dN/dy(S + S)/dN/dy(p + p)$ is shown for negatives, K_s^0, and Λ particles as a function of rapidity. The difference in width is manifest by the inverse parabolic shape of the ratio. The average ratio is 30.6, which is 12% more than the ratio of charges in the incident particles, 27. An enhanced strange particle production is manifest in the ratios, which amount to about 60 and 55 for Λ and K_s^0, respectively. For the K's the enhancement is most prominent at mid-rapidity. Thus the additional energy

loss of the nucleons reappears in enhanced strange particle yields near mid-rapidity. We may take the present data as an indication that the enhanced strangeness production goes along with an equally enhanced baryon-antibaryon production rate in central S + S collisions. This might be understood to be the result of an enhanced production of di-quark pairs along with the strangeness enhancement. (See more details in sect. 6.6.2.)

Hence, nuclear transparency turned out to be not so important up to now. Owing to the large stopping power of nuclear matter, large baryon densities are observed even in Sulphur-Sulphur collisions at the SPS.

Expectations for higher energies

Summarizing the above discussions in p-A collisions at A≈200 the proton projectile loses approximately 2 - 2.5 units in rapidity, $\delta y \approx 2 - 2.5$. With this loss, for heavy ions the maximal stopping would occur for $\Delta y \approx 4 - 5$.

Let us assume that in the c.m. frame in a symmetric central collision the projectile rapidity is Y_0 and the target rapidity is $-Y_0$. After the collision the baryon number distribution is centered at $\pm(Y_0 \mp \delta y)$, and δy is the rapidity loss. The overall central baryon free region in rapidity thus becomes $\Delta Y_{baryon\ free} \approx 2Y_0 - 4\delta y$. Here we assumed that the spread of the decelerated baryons in rapidity is as large as their deceleration. Assuming that δy is the same in A + A collisions as for p + A, one can predict a central baryon free region of 1 - 2 units of rapidity at the BNL-RHIC and of 6 - 8 units of rapidity at the CERN-LHC. If the stopping in heavy ion reactions is $\delta y > 2.5$ it is feasible that baryon free rapidity region will be observed at LHC only. Even in this case the central rapidity regions at RHIC will be strongly dominated by mesons and baryon antibaryon pairs.

10.5.3 Stopping in theoretical models

We have seen already a few simple fluid dynamical models. Standard one fluid dynamical models assume complete stopping, and as such this is true for the Landau model and the spherical model introduced earlier. The Bjorken model is also a one-fluid model, and as such assumes complete stopping, however, the initial condition is such that the fluid dynamical regime was preceded by a nonequilibrium stage where the projectile and target baryons penetrated each other. Thus any one fluid model with a well chosen initial condition can describe the final equilibrated stages of a collision.

Two or more component fluid dynamical models, and explicitly microscopic cascade or molecular dynamics models are able to describe transparency explicitly.

String models

String models are cascade models on the quark parton level applicable at CERN-SPS and BNL-AGS energies. Soft quark-quark collisions are described by "string" formation and subsequent hadronization. First of all, we know too little about "strings" and their properties. It is also not quite certain how one should attach these strings to quarks and gluons. We also do not know what happens if many such strings overlap in space. In

available CERN experiments their density is few strings per fm^2, and it can increase to 10 per fm^2 in future lead beam experiments [49]. Thus the assumption of independent strings, what most models assume, is questionable. Even if we have independent strings, which independently produce hadrons, we certainly have rescatterings before secondaries come out of the system. Therefore, any agreement between the particle spectra obtained in such "pp-based" models (which ignore "trivial final stage interaction") can be but misleading coincidence.

Experiments do demonstrate rather nice stopping (even at CERN energies) in terms of nucleon energy loss. Pion rapidity distribution is surprisingly close to predictions of Landau hydrodynamics. Does it really mean, that there is rapid thermalization? This question is still open, for we do not have reliable estimates for the initial thermoplastic time. People use Bjorken's 1 fm/c value as a guess, although both old perturbative estimates of gluonic mean free path[50, 51] and estimates based on "color rope" model[52, 53] give something shorter, 1/2 to 1/3 fm/c.

10.6 Reaction models

Relativistic heavy ion collisions are on the borderline of applicability of different theoretical approaches. This makes this field interesting and also difficult. The problem is twofold: the smaller than macroscopic size and the short reaction time compared to microscopic equilibration.

Our primary goal is to draw conclusions on the global equilibrium features of the hot and dense matter, consequently the largest colliding systems are the most favorable. These also provide us the longest collision times. At the moment of writing this textbook no final experimental results are available yet from such reactions, the expectations based on smaller colliding systems are, however, quite reliable for some basic quantities. The final particle multiplicity is in the order of several thousand. At some stage during the reaction local thermal and mechanical equilibrium are established (not necessarily phase or chemical equilibrium), for local volume elements of the size of $\approx$ 10-100 fm^3. To describe such a complicated dynamical system in QCD is beyond our possibilities, both due to the computational scope of the problem and due to the lack of principal microscopic information that would be necessary to solve the problem. This situation is usual in most problems of statistical physics. The above estimates, however, are based on comparisons of experiments and theoretical models, and leave a wide range of possible reaction models.

Reaction models are basically belonging to two groups. Some models assume the existence of local equilibrium at some stage of the reaction (not necessarily at the initial moments), and from then on are applied with the appropriate boundary and initial conditions. These models are the different fluid dynamical models and continuum models.

Another group of models does not assume local equilibrium, but assumes the microscopic dynamics of the system: the constituents of the matter, their interactions, transitions, internal dynamics, etc. Then the transport theoretical behavior of these systems is studied, usually, by Monte-Carlo simulation.

10.6.1 Fluid dynamical results

The most simple models belong to this group, the Bjorken model (one dimensional scaling fluid dynamics) and the Landau model discussed already in chapter 5. Both models have an initial condition corresponding to a situation after the initial impact when the matter is compressed and heated up already. These initial conditions are different in the two models. At the initial state there is no kinetic energy in the Landau model, and in the c.m. system all of the available energy is in the form of internal energy of the strongly Lorentz contracted disk of matter. On the other hand the Bjorken model assumes a linear scaling expansion in the beam direction in the initial state. In a way the initial state of the Bjorken model corresponds to a later physical situation than the initial condition of the Landau model. As we have seen in chapter 5, under certain conditions the time development in the Landau model may reach a situation which is very close to the initial state of the Bjorken model. I.e., in this case the subsequent development and the final state are similar in both models. Of course, in the general case this is not true, and the final states (breakup states) of the two models are not necessarily identical.

Based on the observation that recent experiments at the CERN-SPS and particularly at BNL-AGS resemble the rapidity distributions of the Landau model it was concluded that the stopping is large at these energies. Although this observation is basically correct we cannot draw accurate quantitative conclusions from it for the initial energy or baryon density, because of the lack of knowledge of the EOS and the possible similarity of the final states of the two models. The frequent use of Bjorken's formula for the initial energy density at the present energies is not justified, and it should be considered as an order of magnitude estimate only.

The timespan from the initial impact to the Landau or Bjorken initial state is less than 1-2 fm/c.

Simple model calculations are rather successful to describe the transverse momentum spectra of several species of particles simultaneously by assuming a collective fluid dynamical expansion which is spherically and/or cylindrically symmetric [54, 55, 56, 57].

Detailed numerical models

Three dimensional detailed fluid dynamical models are also applied to describe ultra-relativistic heavy ion reactions [58]. The problem here - apart of numerical and computational difficulties - is the selection of the proper initial state for the problem and the selection of the equation of state. Obviously the study of non-central collisions is the most interesting since exactly central collisions could be described in two dimensional models. The three dimensional approach allows the study of phenomena like the collective transverse flow, which was already crucial at lower energies, and led to the most accurate determination of the stiffness of the nuclear matter.

As an example let us consider a $Pb + Pb$ collision at 160 A·GeV energy with an EOS including a strong first order phase transition to Quark Gluon Plasma [58]. If we choose the initial state as the moment of the impact of the Lorentz contracted nuclei and continue the fluid dynamical calculation from this moment on assuming immediate

local equilibrium we obtain a high temperature ($T > 400$MeV) and density 0.5 fm/c after the impact in a narrow domain, Fig. 10.4. By about 1.5 fm/c the central region is over the maximum compression, the temperature starts to decrease, but most of the central region is still in the QGP phase ($T > T_{cr}$). By this time other models, not assuming immediate local thermalization, reach a rather similar configuration, energy and density distribution.

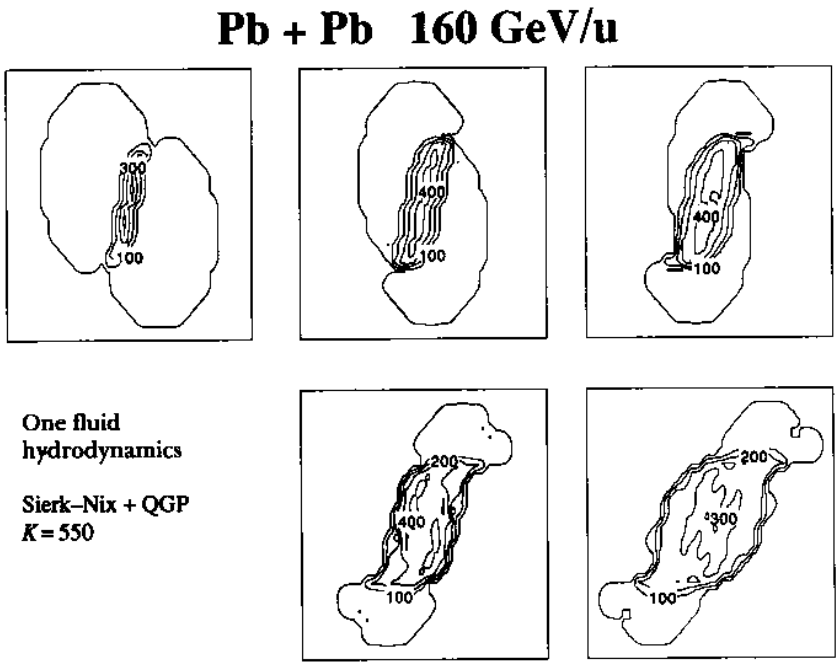

Figure 10.4: Contour lines of the temperature distribution, T [MeV], in the reaction plane of a Pb+Pb reaction of impact parameter b=4fm, at 160 A·GeV beam energy at c.m. times 0.34, 0.68, 1.03, 1.37, 1.72 fm/c. The figures are distorted for better recognizability, the size of the frame in the beam direction is 5 fm, while in the transverse direction is 20 fm. Reproduced by permission of Elsevier Science Publishers from [58].

This observation coincides with our previous conclusion that the final dynamics is similar in the Landau and Bjorken models. The final stages have two dominant features, i) the development of the collective sidewards flow, starting around 1fm/c after the impact, and ii) the final hadronization and freeze-out happening between 5-50 fm/c after the initial impact.

Due to the fact that fluid dynamical models with the initial condition described above assume equilibration earlier, compared to string models, the transverse flow is developing earlier and it is stronger by about a factor of two than in string models [58]. Nevertheless, even string models predict an observable collective transverse flow in heavy colliding systems.

The dynamics of hadronization and freezeout are more involved problems and up to now only simpler model dynamical studies are performed [28, 29].

10.6.2 Microscopic string models

A complementary set of models has been developed to describe heavy ion reactions based on microscopic Monte-Carlo simulation of the reaction. These models are in some sense the extrapolations of the lower energy Monte-Carlo cascade and Molecular Dynamics models. There are, however, important basic differences.

The models at lower energies assumed point like or compact particles (nucleons, pions, deltas, etc.) as constituents, moving in a mean field potential formed by the average density or in the force field of the sum of interaction forces of all other constituents one by one.

Hadron - hadron reactions

Already at the simulation of high energy (around 100 A·GeV or more) $p + p$ collisions it turned out that the low energy picture is not applicable at these energies. The collisions are far from being binary and a large number of reaction products are created which follow a clear systematics in the phase space: the transverse momentum spread of the secondaries is relatively limited (≈ 300MeV/c) while the beam directed distribution is widely spread between the projectile and the target and it corresponds to a nearly flat distribution in rapidity. This feature led to the introduction of composite intermediate objects, so called strings or flux tubes, with an internal structure and space-time development.

Strings

With the wider acceptance of quark-parton picture of the hadrons (i.e., that hadrons are composed of valence quarks as discussed above, plus some *see-quark* pairs) these composite objects were considered as strings or flux tubes spanned between two (groups of) quarks and the confined *chromo-electric field* between them. The large number of secondary hadrons are formed at a later proper time by pair creation from the strong field.

Thus, the microscopic Monte-Carlo models have new constituent objects, so called strings, added to the compact hadrons at these energies. These models were quite successful to describe phenomenologically all hadron-hadron collisions. The number of strings in a collision was very low and the system was a dilute system of these constituents.

Heavy ion reactions

When the same models were used to heavy ion reactions several problems became obvious in a short time. The density of constituents became so large that interactions among them became important. Although some information on hadron-hadron interactions in vacuum was available nothing was known about the interactions of strings or the modifying effects of the dense surrounding. Initially these interactions and modifying effects were neglected.

Part of these string models which allowed for interactions of secondary hadrons, and string formations initiated by secondary hadrons were rather successful in reproducing detailed experimental data on rapidity and $p_\perp$ distributions of protons, pions, K-mesons. The models without secondary scattering and secondary string formation underpredicted the observed stopping power, i.e., they failed to describe the proton rapidity distributions.

However, after a while the limits of these models were also apparent in 1991-92. The comparisons to experiments showed that the string models have two drawbacks in their original form based on hadron phenomenology: i) string-string interactions and string fusion are necessary to reproduce the formation of more massive secondaries like strange antibaryons, because single strings formed by two or three valence quarks only did not carry sufficient energy; and ii) the inclusion of hard partons is necessary to describe high $p_\perp$ phenomena, minijets, gluon jets, particularly at highly ultra-relativistic energies [59, 60, 61].

Monte-Carlo model families

(a) Naive string models: Early string models were the naive extrapolations of hadron-hadron string models, just supplemented by the baryon distributions in the nuclear projectile and target. These models are still widely used by experimentalists to simulate experimental data, for purposes of detector design etc. The most commonly used example is the FRITIOF model[62] (based on the Lund model[63]).

(b) String models with rescattering: These are more realistic models because the concept of string formation in all hadron-hadron collisions is treated the same way irrespectively of whether a hadron is originating primarily from the target or projectile nucleus or it was created during the collision. String models belonging to this category are RQMD versions without string fusion,[64, 65, 66, 67] VENUS versions without string fusion,[68, 69, 70] QGSM,[71, 72, 49] ACR,[73] Dual Parton Model versions of Ranft et al.,[74] etc. The nice feature of these models is that they are based on hadron phenomenology strictly and no additional ad hoc assumptions are involved. Consequently these models produce closely identical results although they were developed independently. In this sense these are the most sophisticated models assuming only a simple multitude of standard hadron-hadron collisions, i.e., the best *"negative"* models without any collective effects assumed (no QGP, no mass reduction of hadrons due to environment, etc.). The drawback is that these models become selfcontradictory if applied to massive heavy ion collisions like $Au + Au$ or $Pb + Pb$, at energies 200 A·GeV or higher. Then the string density becomes unrealistically high[72] and the strings will have to overlap. In this situation the assumption of independent non-interacting strings has to break down. As we mentioned above these models describe correctly the stopping power and most observables but fail to reproduce the heavy secondary production like strange anti-baryons.

(c) String models with string fusion: These are trying to find the obvious remedy to the problems of the previously mentioned family of models. The remedy is the

interaction and fusion of strings in most cases, or the formation of some heavier composite objects containing more valence quarks. The models belonging to this group are for example the RQMD versions with string fusion, VENUS versions with double strings,[75] String Fusion Model (SFM),[76] etc. Although these models are now able to describe the experiments the previous family failed to reproduce, new ad hoc parameters are introduced, like string string cross section, modification of string tension in fused strings, etc., which are not based on hadron-hadron collision phenomenology. In this way the success of these models is not surprising, but also does not provide a much more basic understanding of the problem.

(d) Parton cascade models: Particularly for higher energies, (Fermilab, RHIC, LHC) the correct description of hard parton-parton collisions is the most vital aspect of the heavy ion collision. These models may abandon the idea of strings or flux-tubes alltogether and the parton cascade is happening in the perturbative vacuum [77]. The transition from the physical vacuum to the perturbative one, as well as, the final hadronization and return to the physical vacuum is a sensitive part of these models and is still under development at the time of writing this book. Some models keep the string idea to a certain extent and the parton cascade takes place in limited clusters [59, 61]. In any case these models are allowing dynamical processes leading to the equilibration of the parton matter, and in some models the equilibration and thermalization are explicitly tested and achieved. A detailed experimental test of this family of the models is expected only when RHIC and LHC heavy ion experiments will be in progress.

Monte-Carlo models and Quark Gluon Plasma

The sequence of the previously mentioned models illustrates a gradual approach to QGP. The objects (strings) which are considered in the models are becoming larger corresponding to bigger and bigger chunks of non-equilibrated quark matter. The approach to equilibration is discussed only in some of the models of the last, D, family.

It is academic to ask if these models are supporting or are against the assumption of a Quark Gluon Plasma based on the presently available results of these models.

Each of the above string models should have a stationary equilibrium solution also, and consequently an Equation of State. In principle, however, it is possible to determine the underlying EOS for any of these Monte-Carlo models, just the model prescriptions should be applied to a large fixed container of matter, and the equilibrium properties studied. Unfortunately this is not done in any of the models up to now. Nevertheless, it cannot be excluded that these string models have a first order phase transition in their EOS, since the strings have a substantial amount of energy, which is latent, i.e. it is an internal energy and it is subtracted from the kinetic energy of the constituents leading to the pressure of the material. We expect to have answers to these questions in the next few years of research.

10.7 On some suggested signals

There are several suggestions at present to identify whether the system produced in a high energy heavy ion collision was, in its early "primordial" history, in a deconfined state or not. Essential and qualitative development is expected in the next few years in this field.

One approach is to look for primordial remnants in the observed hadron features: discontinuities in the momentum distribution of the secondaries reflecting a first order phase transition or at strangeness enhancement which is significantly larger if it arises from QGP. Another usual suggestion is to look for signals produced at early times and not affected by the subsequent hadronization. Possible observables of this type are thermal dileptons and thermal photons, which are emitted by the plasma and then escape. In the same context, one may also study the effect of the produced dense medium on the observed production of heavy quark bound states, like J/Ψ suppression or hard jets.

In the moment it is impossible to give a complete review of quark-gluon plasmas signatures here. However, one can group the quark gluon plasma signatures in the following categories:

(i) Transverse flow and thermodynamic variables measuring the Equation of State.

(ii) Strangeness and Anti-baryon enhancement.

(iii) Strangelets and other "exotic" signatures of the quark-gluon plasma.

(iv) Photons, and lepton pairs.

(v) J/Ψ suppression.

Collective flow, $p_\perp$ spectra, thermodynamic variables

The aim of this group of signatures is to measure the equation of state and thermodynamic parameters of the superdense matter. For example one wants to search for a rapid rise in the effective number of degrees of freedom, as expressed by the ratios of energy or entropy over the value in an ideal Stephan-Boltzmann gas. These quantities would exhibit a discontinuity, if there were a first-order phase transition, and if we were dealing with systems of infinite extent (see section 4.2). It is still an open question if lattice QCD calculations will predict a 1st or 2nd order phase transition or a sharp but continuous transition between hadronic matter and QGP. In real heavy ion collisions, we may expect a steep, continuous rise even if the phase transition is 1st order because only a part of the matter is converted into plasma, and this part will increase with energy.

Transverse flow is the most obvious method to measure the equation of state, pressure versus energy density and/or baryon density. When one approaches the phase transition region the equation of state becomes very soft and only small increase of the transverse flow velocity is expected. Only when the energy density significantly exceeds

that needed for QGP formation, collective flow is expected to increase noticeably again. Calculations of hydrodynamical expansion with bag-model type EOS gave predictions showing the three stages of rapid, modest and again rapid transverse flow (or average transverse momentum) increase with the increase of beam or internal energy. The existence of some "plateau" in the middle is the consequence of softness of EOS in the "mixed phase". Detailed numerical studies in the context of the hydrodynamical model have shown that this characteristic feature is rather weak in realistic models,[49] unless rehadronization occurs like an explosive process [27, 29, 78].

To observe this structured increase in nuclear collisions one has to vary the beam energy in rather small steps. In nucleon-antinucleon collisions, however, one may make use of the existence of large fluctuations in the total multiplicity even from central N - N collisions. Using this idea, the E-735 collaboration at Fermilab found a continued rise of $p_\perp$ for antiprotons and hyperons with multiplicity, reaching 1 GeV/c for the most violent events [79]. The shape of the observed multiplicity dependence was provocatively similar to hydrodynamical calculations. Lévai and Müller analyzed these data in terms of a simple model,[80] and found that the surface velocity at high dN/dy must take on quite large values for the hadrons. Studying the hydrodynamical evolution that might lead to this final state they concluded that, such a "flow" pattern can hardly be produced at the level of hadrons, because the drag exerted by the dominant pions on the nucleons is far too weak to accelerate these to such speed. So, the apparent transverse flow must be established at the quark-parton level as a consequence of expansion of a quark-gluon plasma or mixed phase. There exist other suggestions that the transverse "flow" might be generated by extended minijets. However, minijets might be the microscopic mechanism by which the transverse expansion of a quark-gluon plasma is produced.

The shape of the pion spectra: Roughly speaking, pion spectra observed in nuclear collisions at CERN can be described by two exponents, with slopes (or effective temperature parameters) of about 50 and 200 MeV, while K_s^0, ρ or Λ show the higher slope parameter only. These are transverse mass spectra divided by $\sqrt{m_T}$, so that thermal spectra should be exponential.

The concave shape of the pion p_T distribution suggests a lower break-up temperature while additional hydrodynamical motion may describe the tail [81]. The idea of one single break-up temperature is, however, not really valid. Monte Carlo Cascade or String model calculations show in fact significant contribution of the particles evaporated in the whole collision process and the low $P_\perp$ enhancement is due to resonance decays mainly. Thus transverse momentum spectra at a single beam energy do not provide sufficient evidence for a plasma or even a collective flow signal.

The space-time dynamics of nuclear collisions needs independent confirmation e.g. by particle interferometry. From two-particle correlation functions in different directions of phase space, it is possible to obtain measurements of the transverse and longitudinal size, of the lifetime, and of flow patterns of the hadronic fireball at the moment where it breaks up into separate hadrons. The transverse sizes found in heavy ion collisions are larger than the radius of the incident nuclei, indicating the fact that produced

hadrons rescatter before the final breakup. Interferometric size determinations will be possible on an, event-by-event basis when Pb or Au beams become available, and can be correlated with global parameters like $p_\perp$ and dN/dy. This will allow for much more precise study of the thermodynamic properties of superdense hadronic matter.

10.7.1 Strangeness and Anti-baryon enhancement

Enhancement of strangeness and antibaryon production is a frequently discussed signal, it is due to the reduction of the threshold for production of strange hadrons from ≈700 to ≈300 MeV and baryon-antibaryon pairs from ≈2 GeV to almost zero. The strongest signal is obtained by considering strange antibaryons which combine both effects[82, 83, 84]. The enhanced strange quark production in deconfined quark-gluon plasma leads to chemical equilibrium abundances for all strange quarks. The strangeness abundance for hadronic matter in chemical equilibrium is smaller. In a rapid hadronization the QGP strangeness abundance could almost be conserved and could even stay larger than the hadronic equilibrium abundance at the breakup. Slow hadronization and long expansion in hadronic phase before breakup will, on the other hand, reduce the strangeness abundance to the hadronic equilibrium value.

There are alternative suggestions that strange particles, and especially antibaryons, would be produced more abundantly, if their masses would be reduced in dense hadronic matter due to medium effects without QGP. However, at the expansion the hadronic matter becomes dilute, the strange hadrons regain their masses and their number should be reduced again. Thus such a process is strongly dependent on the actual timescales and dynamics of a collision.

Increase of strangeness production has been measured. Ratios like K/π and inclusive φ, Λ and $\bar{\Lambda}$ production turned out to be a factor 2-3 larger than the values in $p+p$ interaction at the same energy. Also a strong increase in multi-strange baryon production has been found. The most spectacular data are obtained by the WA85 collaboration at CERN, [85] who find the following abundance ratios at mid-rapidity and for momenta $p_T > 1\text{GeV/c}$:

$$\frac{\bar{\Lambda}}{\Lambda} = 0.13 \pm 0.03, \quad \frac{\bar{\Xi}}{\Xi} = 0.39 \pm 0.07, \quad \frac{\Xi}{\bar{\Lambda}} = 0.6 \pm 0.2, \quad \frac{\Xi}{\Lambda} = 0.2 \pm 0.4. \tag{10.29}$$

Recent calculations indicate [86] that strange baryon ratios seen by WA85 and other CERN heavy ion experiments can be consistently explained either by a quark-gluon plasma or hadronic gas with parameters $T = 220\text{MeV}$ and $\mu_B = 340\text{MeV}$. It is, however, difficult to imagine how chemical equilibrium be attained during the short life of a hadronic fireball in any other way than through an intermediate quark-gluon plasma phase.

Recently, attempts have been made to explain the enhanced A production seen by NA35 at midrapidity in terms of new mechanisms in the framework of collision models based on the string picture discussed in this chapter earlier.

10.7.2 Heavy quark bound states

Studying the spectra of heavy quark bound states can be a promising tool of analysis. J/Ψ particles formed in a collision decay electromagnetically into observable muon pairs. A suppression of the J/Ψ signal relative to the Drell-Yan di-muon continuum had in fact been predicted as a signature for deconfinement, based on Debye screening between color charges. This suppression vanishes as the transverse momentum of the J/Ψ increases. The suppression has to be distinguished from conventional absorption in dense hadronic matter with initial state parton scattering.

The ground state of the $(c\bar{c})$ pair does not exist if the color screening length, $\lambda_D = 1/gT$ is less than the ground state radius. Lattice simulations of SU(3) gauge theory show that this condition should be satisfied slightly above the deconfinement temperature (see sect. 6.3.5).

Electromagnetic probes

Photons For thermal photons, the main background at low momenta comes from the decay of hadrons, mainly π^0 and η of high momenta. There are, in addition, direct photons from Compton scattering. The observation depends very much on how well the hadron decays can be identified and eliminated.

From the experimental point of view, as far as thermal dileptons and thermal photons are concerned, no clear signal has been seen within experimental sensitivities so far.

Di-leptons

Thermal di-leptons are produced when $\pi^+\pi^-$ or $q\bar{q}$ pairs annihilate in a hot pion or quark gas, respectively. But di-leptons are produced, as well in the decay of low mass vector mesons, ρ, ω and φ, and in hard interactions between incident partons at a very early stage of the collision, leading to so called Drell-Yan pairs or to the production of heavy ($c\bar{c}$ or $b\bar{b}$) vector mesons, which subsequently decay into lepton pairs. The main competition for thermal di-leptons at high mass comes from Drell-Yan production. However, thermal di-leptons and Drell-Yan pairs have different functional dependencies on the di-lepton pair mass, M, and so, should be distinguishable. For sufficiently high energy density there seems to be a clear-cut window for high mass dileptons, between resonance decays and Drell-Yan production. The detection of low mass thermal dileptons, from $\pi^+\pi^-$ annihilation in a pion gas or from $q\bar{q}$ annihilation in a quark gas, is not so easy, since large backgrounds from π^0 and η decays and from virtual Bremsstrahlung must be subtracted.

10.7.3 Exotic signals

One could expect that the formation of quark-gluon plasma would be associated with the appearance of completely novel phenomena: there would be no ambiguity in such signatures. The most probable exotic objects that might be formed from quark-gluon plasma are strangelets[87]. These are metastable objects with baryon number $A > 2$

that contain several strange quarks. The simplest such object is the strangeness $S = -2$ dibaryon, the H-particle, which is predicted to be metastable in the original MIT bag model and might be produced in relativistic nuclear collisions. Experiments searching for strangelets produced in relativistic heavy ion reactions are in progress at BNL, and in preparation at CERN [88]. Strangelets and their hadronic counterparts, multi-hypernuclei, can be easily distinguished experimentally from ordinary fragments: they have zero or even negative charge.

10.8 Assignment 10

10.a Show that in the Bjorken model the local flow velocity, $u^\mu = \frac{1}{\tau}(t, 0, 0, z)$, is orthogonal to the $\tau =$ const. hyperbola.

10.8.1 Solution to Assignment 10

10.a The four vector tangent to the hyperbola can be written in the form $t^\mu = C(\vartheta, 0, 0, \zeta)$ where ϑ and ζ are infinitesimal displacements along the $\tau =$ const. surface and C is a normalization constant.

Since both the point $x^\mu = (t, 0, 0, z)$ and the displaced vector $x'^\mu = (t + \vartheta, 0, 0, z + \zeta)$ are on the same hyperbola

$$\tau = \sqrt{t^2 - z^2} = \sqrt{(t + \vartheta)^2 - (z + \zeta)^2} \ .$$

For infinitesimal displacements

$$\sqrt{t^2 - z^2} = \sqrt{t^2 + 2t\vartheta - z^2 - 2z\zeta} \quad \rightsquigarrow \quad 1 = 1 + (t\vartheta - z\zeta)/\tau^2 \quad \rightsquigarrow \quad t\vartheta = z\zeta \ .$$

This yields $t^\mu = C'(z, 0, 0, t)$. Consequently $t^\mu u_\mu = C''(zt - tz) = 0$.

q.e.d.

Bibliography

[1] F.E. Close: "An Introduction to Quarks and Partons" (Acedemic Press, London 1979).

[2] J.I. Kapusta: Finite-temperature field theory, (Cambridge University Press, Cambridge 1989).

[3] M. Creutz: Quarks, gluons and lattices, (Cambridge University Press, Cambridge 1986).

[4] W. Weise, in Quarks and Nuclei, Int. Rev. of Nucl. Phys. **1** (World Scientific, 1984) ed. W. Weise, p. 57.

[5] H. Kluberg-Stem, A. Morel, O. Napoly and B. Petersson. Nucl. Phys. **B220** (1983) 447.

[6] L. Susskind, Phys. Rev. **D16** (1977) 3931.

[7] H.S. Scharatchandra, H.J. Thun and P. Weisz, Nucl. Phys. **B192** (1981) 205.

[8] S. Duane, A.D. Kennedy, B.J. Pendleton and D. Roweth, Phys. Lett. **B195** (1987) 216.

[9] K. Wilson, Phys. Rev. **D10** (1974) 2445.

[10] F. Karsch, in Quark-Qluon Plasma, ed. R. Hwa, (World Sientific Publishing Co. Pte. Ltd., 1990), Advanced series on directions in high energy physics vol. **6**, p. 61.

[11] J. Engels, in Proc.: "The Nuclear Equation of State, Parts A & B; ed. by W. Greiner, and H. Stöcker, eds.) NATO ASI Series, **Peniscola**, Spain, May 21 - June 3, 1989; (Plenum, 1990) Part B, p. 17.

[12] B. Svetitsky and L.G. Yaffe, Nucl. Phys. **B210** (1982) 423.

[13] R.D. Pisarski and F. Wilczek, Phys. Rev. **D29** (1984) 338.

[14] R.V. Gavai, F. Karsch and B. Petersson, Nucl. Phys. **B322** (1989) 738.

[15] F. Karsch, J.B. Kogut, D.K. Sinclair and H.W. Wyld, Phys. Lett. **B188** (1987) 353.

[16] A. Irbäck, F. Karsch, B. Petersson and H.W. Wyld, Phys. Lett. **B216** (1989) 177.

[17] S. Gottlieb, et al., Phys. Rev. **D35** (1987) 3972.

[18] S. De Curtis and G. Pettini, Nucl. Phys. **A525** (1991) 171c.

[19] A. Barducci, R. Casalbuoni, S. De Curtis, R. Gatto and G. Pettini, Phys. Lett. **240** (1990) 429; Phys. Rev. **D41** (1990) 1610.

[20] B. Petersson, Nucl. Phys. **A525** (1991) 237c.

[21] S. Gottlieb, W. Liu, R.L. Renker, R.L. Sugar and D. Toussaint, Phys. Rev. **D38** (1988) 2245.

[22] R.V. Gavai, S. Gupta, A. Irbäck, F. Karsch, S. Meyer, B. Petersson, H. Satz and H.W. Wyld, Phys. Lett. **B241** (1990) 567.

[23] F. Karsch and H.W. Wyld, Phys. Lett. **B213** (1988) 505.

[24] R.V. Gavai, et al., Phys. Lett. **B232** (1989) 491.

[25] P. Karsch, Preprint CERN-TH-5498/89 (1989).

[26] T. Matsui and H. Satz, Phys. Lett. **B187** (1986) 416.

[27] A.K. Holme, E.F. Staubo, L.P. Csernai, E. Osnes and D. Strottman, Phys. Rev. **D40** (1989) 3735.

[28] L.P. Csernai and J.I. Kapusta, Phys. Rev. **D46** (1992) 1379.

[29] L.P. Csernai and J.I. Kapusta, Phys. Rev. Lett. **69** (1992) 737.

[30] G. Baym, H. Monien, C. J. Pethick and D. G. Ravenhall, Phys. Rev. Lett. **64** (1990) 1867.

[31] K. Kajantie, L. Kärkkäinen and K. Ruuskanen, Nucl. Phys. **B333** (1990) 100.

[32] J. Potvin, K.J.M. Moriarty and C. Rebbi, Nucl. Phys. **A525** (1991) 561c.

[33] S. Nagamiya and M. Gyulassy, Adv. in Nucl. Phys. **13** (1984) 201.

[34] L.P. Csernai, W. Greiner, H. Stöcker, I. Tanihata, S. Nagamiya and J. Knoll, Phys. Rev. **C25** (1982) 2482.

[35] L.P. Csernai and J. Kapusta, Phys. Rev. **D29** (1984) 2664.

[36] A. Barton, *et al.*, Phys. Rev. **D27** (1983) 2580.

[37] C. De Marzo, *et al.* , Phys. Rev. **D26** (1982) 1019.

[38] W. Busza and A.S. Goldhaber, Phys. Lett. **139B** (1984) 235.

[39] L.P. Csernai and J. Kapusta, Phys. Rev. **D31** (1985) 2795.

[40] L.P. Csernai and J. Kapusta, Phys. Rep. **131** (1986) 223.

[41] J. Hüfner and A. Klar, Phys. Lett. **145B** (1984) 167.

[42] R.C. Hwa, Phys. Rev. Lett. **52** (1984) 492.

[43] R.C. Hwa, Phys. Rev. **D32** (1985) 637.

[44] E. Byckling and K. Kajantie: Particle Kinematics (Wiley, New York 1973).

[45] I.N. Mishustin, V.N. Russkikh and L.M. Satarov, in "Relativistic Heavy Ion Physics", eds. L.P. Csernai and D.D. Strottman (World Scientific, Singapore 1991) Vol. 5 p. 180.

[46] L.P. Csernai, Phys. Rev.**D29** (1984) 1945.

[47] H. Satz, Nucl. Phys. **A544** (1992) 371c.

[48] H. Ströbele, Nucl. Phys. **A525** (1991) 59c.

[49] N.S. Amelin, E.F. Staubo, L.P. Csernai, V.D. Toneev, K.K. Gudima and D. Strottman, Phys. Rev. Lett. **67** (1991) 1523.

[50] V. Shuryak, Yad. Fiz. **16** 395 (1972), [Sov. J. Nucl. Phys. **16** 220 (1973)].

[51] E.V. Shuryak, Nucl. Phys. **A525** (1991) 3c.

[52] T.S. Biro, H. B. Nielsen and J. Knoll , Nucl. Phys. **B245**, 449 (1984).

[53] M. Gyulassy and A. Iwazaki, Phys. Lett. **165B**, 157 (1985).

[54] L.P. Csernai, A.K. Holme, and E.F. Staubo, in The Nuclear Equation of State, Part B; ed. by W. Greiner, and H. Stöcker, (Plenum, New York 1989) NATO ASI **216B** (1989) 369.

[55] K. S. Lee, U. Heinz and E. Schedermann, Z. Phys. **C48** (1990) 525.

[56] K. S. Lee, E. Schedermann, J. Sollfrank and U. Heinz, Nucl. Phys. **A525** (1991) 523c.

[57] J. Sollfrank, P. Koch and U. Heinz, Z. Phys. **C52** (1991) in press.

[58] N.S. Amelin, L.P. Csernai, E.F. Staubo and D. Strottman, Nucl. Phys. **A544** (1992) 463c.

[59] I. Kawrakov, H.-J. Möhring and J. Ranft, Nucl. Phys. **A544** (1992) 471c.

[60] A.S. Umar, D.J. Dean and M.R. Strayer, Nucl. Phys. **A544** (1992) 475c.

[61] Semi-Hard Collisions in Monte-Carlo Quark Gluon String Model, N.S. Amelin, E.F. Staubo, and L.P. Csernai, Phys. Rev. **D** (1992) in press.

[62] B. Andersson, G. Gustafsson and B. Nilsson-Almquist, Nucl. Phys. **B281** (1987) 289.

[63] B. Andersson, G. Gustafson, G. Ingelman and T. Sjostrand, Phys. Rep. **97**, 33 (1983).

[64] H. Sorge, H. Stöcker and W. Greiner, Ann. Phys. (N.Y.) **192** (1989) 266.

[65] H. Sorge, H. Stöcker and W. Greiner, Nucl. Phys. **A498** (1989) 567c.

[66] Th. Schönfeld, H. Sorge, A. Jahns, L. Winckelmann, R. Matiello, A. v. Keitz, H. Stöcker and W. Greiner, Nucl. Phys. **A544** (1992) 439c.

[67] R. Matiello, H. Sorge, H. Stöcker and W. Greiner, Phys. Rev. Lett. **63** (1989) 1459.

[68] K. Werner, Phys. Lett. **B208** (1988) 520.

[69] K. Werner, Phys. Lett. **B219** (1989) 111; K. Werner, Z. Phys. **C42** (1989) 85.

[70] K. Werner, Nucl. Phys. **A525** (1991) 501c.

[71] N.S. Amelin, L.B. Bravina, L.I. Sarycheva, and L.V. Smirnova, Sov. J. Nucl. Phys., **51** (1990) 535.

[72] N.S. Amelin, E.F. Staubo, L.P. Csernai, V.D. Toneev, K.K. Gudima and D. Strottman, Phys. Lett. **B261** (1991) 352.

[73] Y. Pang, T.J. Schlagel and S.H. Kahana, Nucl. Phys. **A544** (1992) 435c.

[74] K. Hahn and J. Ranft, Phys. Rev. **D41** (1990) 1463.

[75] K. Werner, Nucl. Phys. **A544** (1992) 593c.

[76] N.S. Amelin, L.V. Bravina, ... and L.P. Csernai, Phys. Rev. **D** (1992) in preparation.

[77] K. Geiger and B. Müller, Nucl. Phys. **A544** (1992) 467c.

[78] H. von Gersdorf, Nucl. Phys. **A461** (1987) 251c.

[79] T. Alexopoulos, *et al.*, Phys. Rev. Lett. **64**, 991 (1990).

[80] P. Lévai and B. Müller, Phys. Rev. Lett. **67** (1991) 1519.

[81] L.P. Csernai, A. K. Holme, and E.F. Staubo, Proc.: "The Nuclear Equation of State, Part B: QCD and the Formation of the Quark-Gluon Plasma" (W. Greiner, and H. Stöcker, eds.) NATO ASI **Peniscola**, Spain, May 21 - June 3, 1989; (Plenum, 1990) p. 369-384.

[82] J. Rafelski, Phys. Rep. **88** (1982) 331;.

[83] J. Rafelski and B. Müller, Phys. Rev. Lett. **48** (1982) 1066; (E) **56** (1986) 2334.

[84] P. Koch, B. Müller and J. Rafelski, Phys. Rep. **C142** (1986) 167.

[85] E. Quercigh, in Proceedings of NATO Advanced Study Institute on Particle Production in Highly Excited Matter, Il Ciocco Italy, July 12-21, 1992, eds. H.H. Gutbrod and J. Rafelski (Plenum Press, 1993) p. 499.

[86] J. Rafelski, Phys. Lett. **B262** (1991) 333;.

[87] C. Greiner, P. Koch and H. Stöcker, Phys. Rev. Lett. **58** (1987) 1825.

[88] S.V. Greene, in *'The Nuclear Equation of State'* NATO ASi Series B, Vol. **216B** eds. W. Greiner, and H. Stöcker, Plenum, New York, 1989, p. 117.

Chapter 11

Connections of astrophysics and Heavy Ions

High energy heavy ion physics and astrophysics are strongly connected. The physical state of matter formed in heavy ion collisions can only be compared to the matter in the early universe, in neutron or hybrid (neutron and quark) stars, and in supernovae. Here we discuss mainly the neutron and hybrid stars based on a recent review of Glendenning [1].

11.1 Neutron and hybrid stars

Stars undergo an evolution and nuclear burning during their life, where the energy is supplied by the gravitational collapse of the star. When all the energy producing nuclear reactions are over the star collapses further to a cold final state of star evolution. The final collapse is stopped either by the pressure of the degenerated ($T \approx 0$) Fermi gas pressure of the electrons leading to *White Dwarfs* as a final state, or by the degenerated Fermi gas pressure of neutrons, leading to *Neutron Stars*. The latter are massive and dense, so that the curvature of the space-time has to be taken into account for their accurate description. If the initial star is extremely massive the collapse is not stopped by any of the two processes, and the star ends up as a *Black Hole*. It might also be possible that neutron stars have a quark-gluon plasma core.

The gravitational constant, $G = 6.672 \times 10^{-8}\mathrm{cm}^3\mathrm{g}^{-1}\mathrm{s}^{-2}$, and the speed of light, $c = 2.998 \times 10^{10}\mathrm{cm/s}$, are the fundamental constants in the theory. The constant $G/c^2 = 7.423 \times 10^{-29}\mathrm{cm/g} = 1.325 \times 10^{-42}\mathrm{fm\ c}^2/\mathrm{MeV}$ is also useful since GM/c^2 is having the unit of length. If we use so called gravitational units, $G = c = 1$, both the time unit and the mass unit will be identical with the unit of length.

Nuclear and astrophysics are connected through Einstein's theory of general relativity, which connects the curvature of the space with the energy momentum tensor of the matter via Einstein's equation[2]

$$G_{\mu\nu} = -8\pi T_{\mu\nu} \quad \left(= -\frac{8\pi G}{c^4} T_{\mu\nu}\right) \ . \tag{11.1}$$

Here $G_{\mu\nu} = R_{\mu\nu} - \frac{1}{2} g_{\mu\nu} R$ is Einstein's curvature tensor, a function of the space-time metric $g_{\mu\nu}$, (it is usually given in terms of the Ricci tensor, $R_{\mu\nu}$, and the invariant scalar curvature, R). $T_{\mu\nu}$ is the matter energy-momentum tensor.

Far from any massive object the space-time is smooth and the metric tensor is $g_{\mu\nu} = \mathrm{diag}(1, -1, -1, -1)$ as we discussed in Chapter 2. In empty space outside a massive static spherical star of radius R and mass M, Schwarzschild showed that the solution of Einstein's equation has a simple form. All but the diagonal components of the metric vanish, and they are simple. The line element for $r > R$ is

$$ds^2 = \left(1 - \frac{2M}{r}\right) dt^2 - \left(1 - \frac{2M}{r}\right)^{-1} dr^2 - r^2 d\theta^2 - r^2 sin^2\theta d\phi^2 \ . \tag{11.2}$$

The metric functions in front of dt^2 and dr^2 change by an infinitesimal amount over the distance between nucleons in a star even if the star is near the limit of collapse to a black hole. Consequently in the local rest frame the matter properties and $T_{\mu\nu}$ can be calculated the same way as in the flat space-time. In other words the EOS investigated in heavy ion reactions is relevant for astrophysical situations also.

Now let us estimate the mass and radius of a star near the black hole limit. The metric becomes singular at $r = 2M$, this radius is in the interior of the star where the Schwarzschild solution is not valid. We can roughly estimate the qualitative features of a star with radius $R \approx 2M$ (or somewhat larger to avoid the collapse). Assume that the nucleons in the star are compressed to the limit of their hard core repulsion, just before they would have a phase transition to QGP, $n \approx 1/\mathrm{fm}^3$ (see Chapt. 4). Then the number of nucleons in the star is $N = nV = n \times 4\pi R^3/3$, and the mass of the star is $M = n\ m_N\ 4\pi R^3/3$, where $m_N = 939\mathrm{MeV}$ is the nucleon mass. If now we estimate the radius of the star from $R = 2M$ we get

$$R = 9.79 \times 10^{18}\ \mathrm{fm} = 9.79\mathrm{km} \ .$$

The number of nucleons in the star is 3.93×10^{57}. The mass of the star is

$$M = \frac{R}{2} = 4.9\mathrm{km} \ ,$$

and this can be expressed in terms of the solar mass, $M_\odot = 1.5$ km, as $M = 3.26 M_\odot$. So here we have an estimate of the baryon number, radius and mass of a star at the limiting nuclear density. We expect a slightly smaller mass and larger radius than the values given by the Schwarzschild relation. The typical size and mass of of a neutron star are

$$R \approx 10\mathrm{km}, \quad \text{and} \quad M = 2M_\odot. \tag{11.3}$$

The density of the nucleons is quite large in the star, so if the star would not be neutral the Coulomb force would overwhelm gravity. Thus the nucleons are mostly neutrons in such a star and that is why it is called neutron star.

In order to be able to calculate the structure of a star more precisely we need the energy momentum tensor and the equation of state (EOS) of the matter. Since the change of the metric is small in the star and even less between two neighboring nucleons

we can neglect the effects of gravitation when the EOS is calculated. Thus in the local rest frame we use the form of $T_{\mu\nu}$ =diag(e, p, p, p) introduced in Chapter 2, for perfect fluids.

In the special case of a spherically symmetric static star Einstein's equation takes a special form, the Tolman-Oppenheimer-Volkoff equation (TOV):

$$\begin{aligned} \frac{dp}{dr} &= \frac{Me}{r^2}(1+\frac{p}{e})\left(1+\frac{4\pi r^3 p}{M}\right)\left(1-\frac{2M}{r}\right)^{-1} , \\ \frac{dM}{dr} &= 4\pi r^2 e \ . \end{aligned} \tag{11.4}$$

We can easily interpret these equations. Let us consider a shell of matter in the star of radius r and thickness dr. The second equation gives the mass energy in this shell. The pressure of matter exterior to the shell is $p(r)$ and interior to it $p(r) + dp(r)$. The left side of the first equation is the pressure difference or force force acting outward on unit surface of the shell, and the first term on the right hand side is the attractive force of gravity acting on a unit size portion of the shell by the mass interior to it. This term is present in Newton's theory also. The remaining three factors are the exact corrections for general relativity. So these equations express the balance of internal pressure and gravity. The equation of state, $p = p(e)$, completes the solvable set of equations, and provides the influence of the matter on the solution.

This set of equations can be integrated from the origin with the initial conditions $M(r = 0) = 0$, and an arbitrary value for the central energy density $e(r = 0) = e(0)$, until the pressure, $p(r)$, becomes zero [4]. That point, R, defines the radius of the star, and $M(R)$ its mass. For the given equation of state, there is a unique relationship between the mass and central density, $e(0)$ (Fig. 11.1). So for each possible equation of state there is a family of stars, parameterized by the central density.

Each family has a maximum mass star, called the limiting mass, and the central density of the limiting mass star is higher the softer the equation of state. The part of the curve for which the slope is positive corresponds to stable configurations i (Fig. 11.2). For negative slope, one can readily verify that the star is unstable to radial perturbations.

If the EOS includes a phase transition to QGP the star has a special structure. The high density center is in the QGP phase, then moving outwards, we reach the phase transition density. At this density the QGP and hadronic pressures are equal in equilibrium, so we have the phase transition and the density drops down suddenly to the equilibrium hadronic density. (Fig. 11.1). This is a sharp density discontinuity at some radius like at the surface of the see on the Earth.

There are a large number of attempts to study the structure of such hybrid stars [1, 5, 3, 6, 7]. The hybrid stars are smaller, but they have approximately similar masses as the neutron stars.

The stars with mass beyond the maximum are unstable to collapse to black holes. (Fig. 11.2). It is in the limiting mass that a constraint on the equation of state arises. Obviously an acceptable equation of state must have a limiting mass at least as large as the largest observed mass. The masses of observed neutron stars are between $M = 1 - 2.5 M_\odot$.

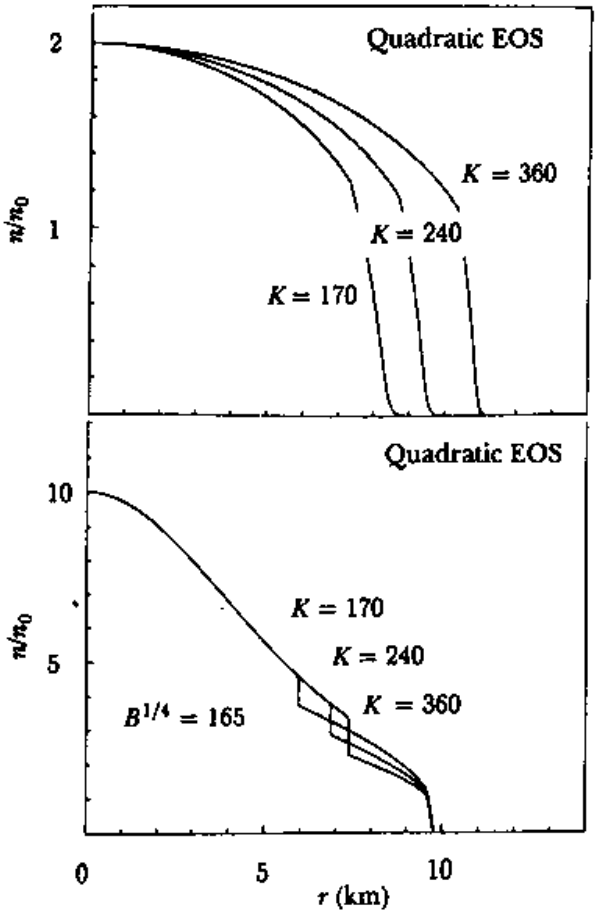

Figure 11.1: Radial baryon density profiles, $n(r)$, for a pure neutron star and a hybrid star. The upper figure shows the density profile for a neutron star with central density of $2n_0$, calculated from a so called "Quadratic EOS" with different compressibilities indicated. The lower figure displays a hybrid star profile with a central density of $10n_0$ for the same nuclear EOS as above and a QGP EOS with a bag constant $B^{1/4} = 165$MeV and $\alpha_s = 0.4$. The discontinuities of $n(r)$ at the radii around 6-7.5 km reflect the first order phase transition between the quark core and the outer layer of neutron matter. Reproduced by permission of Springer-Verlag from [3].

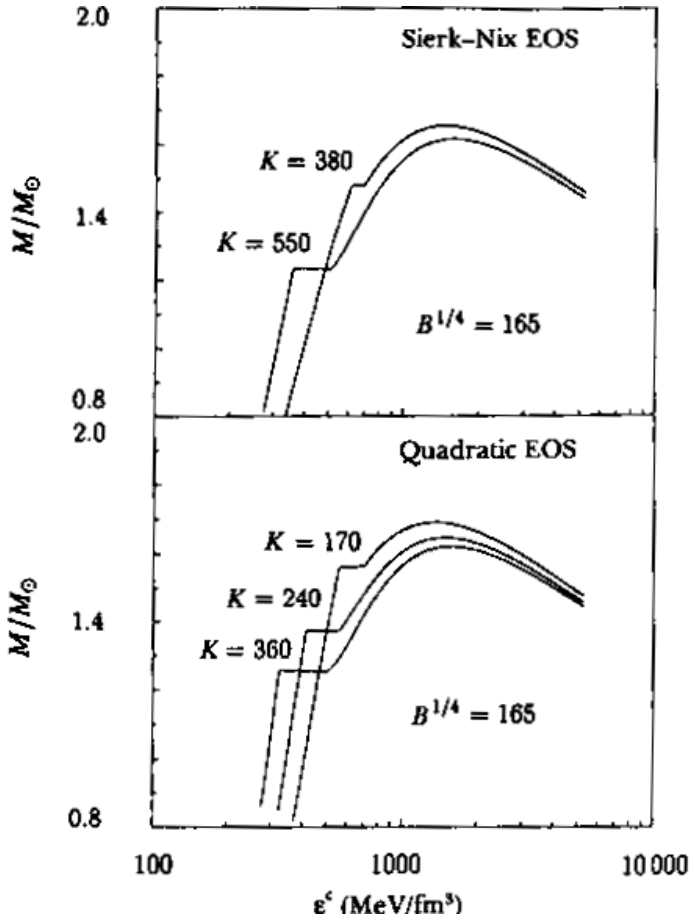

Figure 11.2: The mass of hybrid (quark-neutron) stars as a function of the central density for different nuclear and QGP equations of state. Note that positive slope is required for stability against gravitational collapse. Reproduced by permission of Springer-Verlag from [3].

The stability of stars requires that the mass and the radius of the star should increase with increasing central density. Furthermore the mass of the star should increase with increasing star radius. This latter requirement makes pure quark stars unstable against collapse to black holes according to most model calculations.

11.1.1 Pulsars and neutron stars

Since the first discovery of a pulsar in the pulsed signals of a radio-telescope in 1967 about 400 pulsars have been observed. The period of the pulses ranges from milliseconds to seconds, and is interpreted as the period of the star rotation.

Ordinary stars have magnetic fields and rotate. When they collapse from a radius of $\approx 10^6$ km to 10 km, both the rotation frequency and field are scaled up by the conservation laws of angular momentum and magnetic flux. It can be shown that these conservation laws provide the rotation frequency observed in the pulsars, (see, for example, ref. [1].)

11.1.2 Supernova explosions

The maximum mass of the neutron and hybrid stars is not too large, $1 - 2.5 M_\odot$, so a massive star due to smooth burning and collapse would not be able to end up in a neutron star, because the loss of mass during these processes is not very large. Consequently smaller stars end up as White Dwarfs, while massive stars, above 5-20$M_\odot$ or larger, collapse into black holes.

The most generally accepted way to produce a neutron or hybrid star is going through an explosive process, the supernova explosion, where the outer crust of the star is blown away by an explosion and the internal core collapses to a neutron star. The most dominant causes of such an explosion are the shock wave propagating outwards after a collapse of the core to a dense degenerated state, and the intense neutrino flux arising from the collapse when the protons are converted into neutrons.

However, the physics of supernova involves so many factors of comparable importance but high uncertainty, that they cannot be said to provide any constraint on the nuclear EOS at the present time. It is not known whether supernovas can always explode by the prompt bounce mechanism. Only a small part of supernova remnants contains a neutron star and very little observational information on the explosion mechanism is available even in the best studied case (SN 1987A). We know that some supernovas leave neutron stars behind and that the kinetic energy of the ejecta is typically around 10^{51}erg. It is possible that only those stars can explode by the prompt shock wave mechanism which possess a significant amount of angular momentum initially. Nevertheless, there is little doubt that soft (supra-nuclear) equations of state favor prompt explosions, at least for non-rotating models.

11.2 Implications on the early universe

Einstein's equations (11.1) cannot provide a static solution for the whole homogeneous and isotropic universe. Initially this was thought to be a problem of the theory and Einstein did introduce a small extra repulsive term the so called *cosmological constant* to the Einstein equation, $\Lambda\, g_{\mu\nu}$, added to the energy momentum tensor.

Later Friedmann has found a time dependent solution and it turned out that it actually agrees with all observations. According to this solution the universe started from a singularity at time zero, and then it is expanding. This is the so called Big Bang theory. For a closed universe the metric of the space time is

$$ds^2 = dt^2 - R^2(t)\left[\frac{dr^2 + r^2(d\Theta^2 + \sin^2\Theta d\phi^2)}{1 + r^2/4}\right]. \tag{11.5}$$

The curvature radius of the universe, $R(t)$, can be obtained from the Einstein equations if the equation of state of the matter of the universe is known.

High energy heavy ion physics can provide experimental information of the equation of state of the early universe. This EOS clearly influences the early development of the universe. Phase transitions in the EOS are leading to rapid expansion of the early universe, to the *inflation*.

The energy domain studied in heavy ion reactions is relevant in the first few seconds of the universe (see Table 11.1, [1MeV = 1.16045 $\times 10^{10}$ ^{o}K if $k_B = 1$]).

time	Temperature [^{o}K]	Temperature [MeV]	
10^{-6} s	10^{15}	10^5	QGP
10^{-4} s	10^{12}	100	QGP hadronization
1 - 2 s	10^{10}	1	$e\bar{e}$ annihilation
1.5 min	10^9	0.1	d formation

Table 11.1: *Time and temperature scale of the early universe*

Thus the hadronization of quark gluon plasma and the initial expansion of dense nuclear matter happens between a few seconds and a minute in the early universe. Here the entropy per baryon charge or particle number per baryon charge is about 10^9-10^{10}, so that only the mid rapidity region of highest energy heavy ion collisions at the CERN - LHC or the BNL - RHIC, with near to complete transparency are relevant from this point of view.

Possible signatures of the quark-hadron transition are strangelets as candidates for the dark matter (i.e. of matter that contributes to the gravitation but optically not observed in the universe), or consequences in cosmological nucleosynthesis[8].

At the time of the QGP hadronization at $\approx 10^{-6} - 10^{-4}$ s, the horizon mass was less than a solar mass, so fluctuations arising from the hadronization of QGP are unlikely to affect directly anything larger than a solar mass size system. Consequently the galaxy cluster structure or the galaxy structure is not likely to be connected with the QGP phase transition[8].

11.2.1 Strangelets

One form of debris possibly formed in the QGP hadronization is strange quark nuggets or strangelets. If in QGP not only u and d, but also s quarks are present the Pauli exclusion effect will be decreased in dense matter. High density of strange quarks may be present in a final state if the Fermi level is above the strange quark mass.

During the rehadronization of QGP strangeness and antistrangeness may be separated [9]. This may happen in the early universe as well as in heavy ion collisions. The total strangeness charge is zero for the total system, but it is not necessarily so in both phases separately in a mixed phase system. It is shown that if the system has a net (positive) baryon charge the strangeness and anti-strangeness will be separated during the hadronization, so that the strangeness will be retained in the QGP while the newly formed hadronic phase will carry more anti-strange quarks.

We assume that the reaction rate is sufficiently fast to maintain thermal, mechanical, and chemical equilibrium during the phase transition. In such a case the system follows the Maxwell construction closely, and the extra entropy production is small. Therefore the thermodynamical intensives should be equal during the phase transition: $T_H = T_{QGP}$, $P_H = P_{QGP}$, $\mu_H^{(B)} = \mu_{QGP}^{(B)}$ and $\mu_H^{(s)} = \mu_{QGP}^{(s)}$. This last condition indicates that not the strangeness density but the corresponding chemical potential is continuous during the transition. Given the total energy, volume, strangeness, and baryon charge for the combined system of the two phases the intensives can be determined. It is important to emphasize that even if the total strangeness is zero, the strange chemical potential and the net strangeness in the two phases will not be zero in phase equilibrium. For vanishing total strangeness in a pure single QGP phase system the strangeness chemical potential is zero, but in a pure hadronic system it is not if our system has a net baryon charge. In ref. [9] the development of strangeness abundance was calculated in the Bjorken model assuming phase equilibrium and adiabatic expansion. The ratio of net strangeness density versus baryon density in the plasma was increasing during the collision and it reached 0.4-0.5 by 4-5fm/c time.

The excess strangeness in the remaining plasma droplets will then contribute to massive strange objects which are larger than conventional strange hadrons, i.e. to massive strange objects, strangelets or strange nuggets. Some suggested observable candidates are: multistrange hadrons with baryon charge B$\geq$2, the H-dibaryon (uuddss), or multistrange hypernuclei [10].

Even if the reaction rate is not sufficient to establish chemical equilibrium exactly at each stage of the hadronization [11, 12], the hadronization will tend to develop a strangeness, anti-strangeness separation, although (usually) somewhat smaller than in a chemical equilibrium process.

Bibliography

[1] N.K. Glendenning, in The Nuclear Equation of State, Proc. of the NATO Adv. Study Inst., May 22 - June 3, 1989, Peniscola, Spain, eds.: W. Greiner and H. Stöcker (Plenum, 1989) p. 751.

[2] L.D. Landau and E.M. Lifshitz: Classical Field Theory (Nauka, Moscow, 1973).

[3] A. Rosenhauer, E.F. Staubo, and L.P. Csernai, Z. Phys. **A342** (1992) 235.

[4] L.P. Csernai, D. Kisdi, J. Nemeth, Acta Phys. Hung. **38** (1975) 89.

[5] A. Rosenhauer, E.F. Staubo, L.P. Csernai, T. Øvergård and E. Østgaard, Nucl. Phys. **A540** (1992) 630.

[6] J.I. Kapusta and K.A. Olive, Phys. Rev. Lett. **64** (1990) 13.

[7] J. Ellis, J.I. Kapusta and K.A. Olive, Nucl. Phys. **B 348** (1991) 345.

[8] D.N. Schramm, B. Fields and D. Thomas, Nucl. Phys. **A544** (1992) 267c.

[9] C. Greiner, P. Koch and H. Stöcker, Phys. Rev. Lett. **58** (1987) 1825.

[10] C. Greiner, D. Rischke, M. Rufa, B. Müller, H. Stöcker, J. Maruhn, W. Greiner, P. Koch and P.G. Reinhard, Nucl. Phys. **A479** (1988) 295c.

[11] L.P. Csernai and J.I. Kapusta, Phys. Rev. **D46** (1992) 1379.

[12] L.P. Csernai and J.I. Kapusta, Phys. Rev. Lett. **69** (1992) 737.